UNIVERSITA' DEGLI STUDI DI NAPOLI "FEDERICO II"

Di.S.T.A.R. - Department of Earth Sciences, Environment and Resources

Doctorate School in Analysis of Environmental Systems - XXVI Cycle

UNIVERSITAT POLITÈCNICA DE CATALUNYA

R.S.Lab. - Remote Sensing Laboratory - Signal Theory and Communications Department

Doctoral Program in Signal Theory and Communications

Application of DInSAR techniques to the monitoring of ground deformations

---

Ph.D. Thesis

Serena Tessitore

Advisors

Prof. Domenico Calcaterra

Prof. Jordi J. Mallorqui

Co-Advisor

Prof. Massimo Ramondini

Ing. Gerardo Herrera Garcìa

Coordinators of the Doctorate Schools

Prof. Maurizio Fedi

Prof. Carlos López-Martínez

"Tu patria son tus amigos"

Alfredo Bryce Echenique

Contents

Abstract

Subsidence is a natural hazard which affects wide areas in the world causing important economic losses annually. This phenomenon has occurred in the metropolitan areas of Murcia City (Spain) and of Telese Terme (Italy), causing relevant economic damage to structures and infrastructures. In Murcia city, subsidence is the result of groundwater overexploitation; due to the intensity of the phenomenon, institutions requested detailed studies since the '90, to understand its cause-effect mechanisms. For this reason a monitoring network of extensometers and piezometers has been installed and implemented during the years. Telese Terme has been affected by subsidence due to its geological and hydrogeological settings. Here, in fact, the underground water circulation provokes piping phenomena in the surficial fine-grained soils and, because of chemical characteristics and physical properties of the water, may also activate processes of accelerated travertine's corrosion. In this case, a monitoring network is not available and the only evidences of the phenomenon occurrence are the structural damage to buildings. These two study areas have been chosen to test the applicability of the innovative Advanced DInSAR techniques in the natural risk mitigation related to subsidence phenomena. In particular, these techniques can complete a monitoring network where available (as in the case of Murcia city) and partially replace it in case of its absence (as in the case of Telese Terme). In the first case, such techniques allowed to implement an integrated monitoring system based upon satellite DInSAR monitoring, in situ monitoring and geotechnical data. In particular, the correlation of the temporal evolution of ground surface displacement measures (radar and in situ) and the piezometric groundwater level variation have been analyzed to determine mechanisms and critical states of failure; this has permitted to implement a finite element model (FEM) of the phenomenon. The proposed numerical model will allow the prediction of possible future deformations and the consequences of any piezometric level variation in the study area. This is regarded as necessary to better plan the subsequent water resources exploitation and the land use management. In the Telese Terme case study, radar measured displacements allowed to understand the spatial extension of the phenomenon, its magnitude as same as its historical development. In fact, a remote sensing monitoring system allows the knowledge of unmonitored phenomena also in the past. This has permitted the individuation of the causes which provoked damage for some "test buildings". For one of them, a structural model has been implemented; in this case, radar data have been used to verify whether its structural response to the displacements detected by SAR corresponds to the overpassing of the limit states. In conclusion, it has been argued that the proposed approaches could be applied to other scenarios affected by similar phenomena.

Keywords

Subsidence, uplift, DInSAR, modelling, monitoring, prediction, validation.

Acknowledgements

Many people have given their support to my PhD research and I am deeply grateful to all of them.

I have had the luck to collaborate with many research groups which have shared with me their high-professional technical competence, and above all they have always made me feel like at home, with their warm welcome and kindness.

I truly feel that all the thesis acknowledgements are not directed to collaborators, but to friends. After only one year spent in Spain, I feel to belong to two countries and the dedication *"Tu patria son tus amigos"* (your country are your friends) has been the perfect way to dedicate this thesis to all of them.

First of all, I want to thank my supervisors which have provided me this opportunity of great professional and personal growth.

Prof. Domenico Calcaterra (University of Naples) for his guidance and precious suggestions. I am very grateful to him for being my tutor and for having put his trust in me.

Prof. Jordi J. Mallorqui (UPC - Barcelona) for welcoming me and for his constant support.

Dr. Ing. Massimo Ramondini (University of Naples), for his endless helpfulness. He has been my reference point in every moment and at every hour both of night and day, my omnipresent technical and moral support!

Dr. Ing. Gerardo Herrera (IGME – Madrid) because, without him, this research would have not been possible. I have not enough words to adequately thank him. He has been first of all a friend and after a tutor, a guide and a constant support.

I would also like to show my gratitude to ***Prof. Filippo Barattolo*** and ***Prof. Maurizio Fedi*** (University of Naples), coordinators of the PhD School, which allowed me to enrich my studies with a challenging international experience.

Then I would like to thank all the people which have collaborate to this work; in particular:

Dr. José Antonio Fernandez Merodo (IGME – Madrid) for sharing with me his knowledge and time, allowing the geotechnical modelling of the subsidence phenomenon in Murcia city.

Dr. Carolina Guardiola Albert and ***Dr. Margarita Sanabria Pabón*** (IGME – Madrid) for their inestimable support in geostatistical applications and their kindness and willingness;

Dr. Giuseppe Centolanza, Dr. Dani Monells, Dr. Ruben Iglesias (UPC – Barcelona), for the great help in the SAR processing learning and to be always patiently available to solve all the occurred issues;

Dr. Diego Di Martire (University of Naples) for his help during my PhD, especially for his explications concerning the SAR processing in an "Italian version"!

Dr. Alessandro Novellino (University of Naples) for his geological revisions and help, always provided with a smile and to ***Dr. Ahmed Ali*** for his help in the bibliographic research;

Mirko Iannarone for his support in the structural modelling;

Dr. Vincenzo Fuschini for the know-how regarding the geological and hydrogeological settings of Telese Terme and for the data feedback;

Dr. Joaquín Mulas (IGME - Madrid) for his kindness, precious suggestions and for 20 years of shared knowledge about Murcia case study;

Dr. Gabriella Castiello for the geophysical support;

Dr. Gabriella Tessitore (Bochum University), my sister, friend and colleague for her help in the English revisions, for our interesting mathematical debates and simply for being her!

Finally, I would like to acknowledge the referees of the thesis, ***Prof. Roberto Tomás*** and ***Prof. Kurosch Thuro*** for the important contributions to the work improvement.

Other kind acknowledgements have to be given to all those people who have made this experience unforgettable. A limitless thanks to all the IGME's and the UPC's teams (***Diana, Robert, Marta, Esther, Esther, Virginia, Josè, Imma, Rosa, Raul, Dani, Ruben, Giuseppe, Alberto***) and to the "*IGME's little Italy*" for welcoming me with open arms and for being my Spanish family.

In particular, thanks to ***Diana Ponce de León*** and ***Roberto Sarro Trigueros*** for their "*rutas culturales y non*" of the wonderful Madrid, to ***Silvia Bianchini*** for all the "*que si*" adventures and for being my Spanish "*professora*", to ***Dani Monells*** for the Catalan lessons and to ***Ruben Iglesias*** for teaching me "the other side of the Spanish language"!

A big thanks to ***Virginia Zamparelli*** and ***Silvia De Simone*** for all the wonderful moments spent together in the beautiful Barcelona and for all the help they have provided me.

Another kind thanks to ***Rosa Maria Mateos, Immaculada Garcìa, Curro Roldan*** and ***Josè Miguel Azañón*** to the best tour (geological, cultural and gastronomical) of Granada and Mallorca ever!

A big thanks to ***Francesca Dalènz*** for her help in the thesis' summary Spanish translations and to all the group of Italian friends which enjoy my stay in Madrid (***Silvia, Roberta, Stefano, Ivan, Elisa***, thanks for all).

The greatest thanks is for my family, my endless and unconditional support ever: to my parents and all the uncles and friends which have never leave me alone and to my soul, ***Danilo***, for having always been near to me despite the distance and hold up my choices, being my main fan, my happiness, my peace.

Thanks, gracias, grazie, gràcies.

The SAR images used in this work for Murcia city were provided by the European Space Agency (ESA) in the framework of the EO CAT11 project 2494. The TerraSAR-X images were provided by DLR in the framework of the scientific project GEO0389: "High resolution DInSAR monitoring of subsidence induced by aquifer exploitation in the Vegas Baja and Media of the Segura river, SE, Spain". Furthermore, the ESA Terrafirma project has funded all the SAR data processing with the SPN technique.

For the Telese Terme area, the ENVISAT images for the period 2002-2010 and the SAR data processed with PSInSAR technique were provided thanks to a specific agreement between the Department of Hydraulic, Geothecnical and Environmental Engineering of the University of Naples and the Italian Ministry of Environment (MATTM)

The Spanish Geological and Mining Institute (IGME), EMUASA, the Hydrographic Confederation of Segura (CHS), the company "Aguas de Murcia" and the Regional government of Murcia were so kind to provide piezometric and hydrological data. The extensometric data were provided by the Regional government of Murcia and by IGME. The Cartographical Service of Murcia (CARTOMUR) has provided DEM data and aerial photographs used in this work.

The software used for the SAR image processing has been implemented at the Remote Sensing Laboratory (RSLab) of the Technical University of Catalonia (UPC).

CHAPTER I

Introduction

Chapter I. Introduction

Subsidence is a gradual settling or sudden sinking of the Earth's surface owing to subsurface movements of Earth materials. It represents a natural hazard, causing relevant economic damage and social alarm. It can affect wide areas over variable time periods, with deformations which can vary from a few millimetres to several meters. It may be due to several causes, both natural and anthropic, like compaction of soil materials, fluid withdrawal (oil, water, gas), deep material dissolution, excavation of tunnels or mining galleries, deep erosion (piping), lateral soil creep, or tectonic activity.

Therefore, subsidence risk assessment and prevention is a key-point for a correct territory management. For this reason, it is necessary to determine mechanisms and critical states of failure, and to evaluate, knowing the causes, possible corrective measures and their effectiveness (Tomás et al., 2005a). Thus, an effective monitoring system represents the starting point for the decision-making and the problem solving processes (Thuro and Schubert, 2009).

The development of subsidence monitoring techniques has allowed passing from the traditional topographic surveys, to the instrumental methods (i.e. extensometer), yielding to punctual measures of the ground deformations.

An effective monitoring system should be well distributed in the subsiding area and provide measures in the whole period of the phenomenon occurrence to reach a correct analysis of its evolution. This implies the necessity of a great number of instrumental installations, often resulting in high costs. Furthermore, the displacement measurements have to be matched with other physical factors, related to the examined phenomenon causes (i.e. piezometric level variation), also leading to additional costs.

The technological progress has provided new techniques for deformation measurements. In particular, *Remote Sensing techniques* have demonstrated to be powerful investigation tools for their high spatial and multi-temporal coverage, fast data acquisition, and overall low costs. Thanks to the recent development of the sensor technology, it has been employed as a monitoring system for various instability phenomena, such as volcanic eruptions, earthquakes, landslides, subsidence, sinkholes, and it has been proficiently used for the related risk assessment.

In fact, among the various radar sensors, the modern *Synthetic Aperture Radar* (SAR) devices are able to irradiate the observed areas with microwaves, resulting in the transparency of the clouds. Therefore, they are able to operate 24-hour a day, and in any cloudiness condition. In particular, through the innovative *Advanced DInSAR Interferometry* techniques, it is possible to evaluate the ground deformations, projected

along the sensor *Line of Sight* (LOS), by calculating the differences of images referred to the same area, but detected in different times. The use of these techniques yields to a monitoring of wide areas (for the whole images acquisition period) characterized by a millimeter accuracy (function of the radiation wavelength) and it results to be particularly effective if these areas show deformations with a predominant vertical component, as in the case of subsidence and sinkholes.

A remote sensing monitoring system allows the integration of conventional techniques, if available, and the knowledge of unmonitored phenomena also in the past. The so obtained information about the historical development of a given phenomenon, permit to understand its cause-effect mechanism or to correlate the measured deformations with other monitored variables, if directly correlated with the phenomenon occurrence.

The details of the historical time evolution achieved through these techniques are function of the time elapsed between observations of the same point (revisit time: 4-8 days in the case of the recent COSMO Sky-Med and Terrasar-X satellite constellations vs. 35 days for ERS and ENVISAT). As to obtain comparable results, a long and continuous monitoring through traditional field surveys is required, also if often impossible to perform over wide areas, and highly costly and time-consuming.

The processing results, however, could not be conveniently used without their validation, necessary also to discretize the millimeter displacements detected by the SAR. In fact, displacements measured by radar could represent, for example, a structural response to the soil settlement and not directly its deformation.

Therefore, it is necessary to define the so-called "*ground truth*", through the complete knowledge of the phenomenon characteristics. To this aim, the reconstruction of the geological and geotechnical model of the study area, based on the well-established field surveys and in situ instrumental monitoring is requested.

For the above reasons, implementing an integrated monitoring system of in situ and radar data could be employed to obtain reliable information of a phenomenon, in points not covered by the monitoring network or in achieving measures of variables related with the subsidence causes. In this case, displacement measurements could also give an estimation of an unmonitored variable (or unmonitored only in a part of the observation period), related with the observed phenomenon (i.e. water table levels), through a back-analysis procedure.

At the same time, the experienced use of radar data permits to reconstruct the evolution of a phenomenon also in the past. This allows, in many cases, to analyze the beginning and initial development of an instability phenomenon, when the requirement of an in situ monitoring network has not yet been manifest.

1.1. Structure of the thesis

The thesis develops in seven chapters.

1. The first chapter includes the thesis objectives, material and methods.
2. In the second chapter the subsidence definition, several historical cases, and the related social problems are introduced.
3. The third chapter illustrates the different subsidence monitoring systems.
4. In the fourth chapter, the DInSAR techniques are described.
5. The fifth chapter tackles the theme of the geotechnical and hydrogeological explication of the subsidence phenomenon.
6. The sixth chapter shows the application of DInSAR techniques to the study areas (Murcia city, SE Spain; Telese Terme, SW Italy). In particular, the processing results have been used to the implementation of an integrated monitoring system based upon satellite DInSAR, conventional field techniques and geotechnical data.
7. The seventh and last chapter reports the work's conclusions and provides a critical analysis of the obtained results. Furthermore, it identifies possible developments of the research.

1.2. Objectives

The present thesis is devoted to the implementation of an integrated monitoring system based upon satellite DInSAR, conventional field techniques and geotechnical data. In particular, the aim is to test the applicability of A-DInSAR results to the natural risk mitigation related to the subsidence phenomenon.

For this reason, two test sites have been chosen, both located within alluvial plains and affected by subsidence phenomena (Fig. 1.1):

- *Murcia city* (SE Spain);
- *Telese Terme* (Benevento Province) in Campania Region (SW Italy).

Figure 1.1: Study areas location

In the first case, DInSAR results have been used to model the subsidence phenomenon occurred in the metropolitan area through their integration with in situ monitoring and geotechnical data.

In the second case, DInSAR data have been employed to analyse the subsidence effects on structures. In particular, in an area where a monitoring network does not exist, they have been useful to verify whether the structural response of some buildings to the displacements detected by SAR overpassed the limit states.

Therefore, these two areas have allowed to test different approaches in using DInSAR results. Moreover, they can complete a monitoring network where available (as in the case of Murcia city) and partially replace it in case of its absence (as in the case of Telese Terme).

These two test sites have been chosen considering as discriminating factors the typology and the

magnitude of the instability phenomena. In fact, in Telese Terme and in the metropolitan area of Murcia City, subsidence has provoked damage to structures and infrastructures, which, for the second case of study, have been estimated to be more than 50 million euros in the '90s.

Murcia city represented the first case in Spain of subsidence due to aquifer system consolidation, in turn induced by ground water overexploitation (Tomas et al., 2011). Subsidence affects the first 5-30 m of fine-grained soils overlying a gravel layer where the pumping takes place. It has arisen in the flood plain of the Segura River, also known as the Vega Media (where Murcia city is located), since 1992. Consequently, a monitoring network of extensometers and piezometers has been installed and implemented during the years, in order to understand the cause-effect mechanisms of this phenomenon and to better plan the subsequent water resources exploitation and the land use. In particular, the temporal evolution of the subsidence in Murcia city has been monitored by an extensometer network since 2001 (Mulas et al., 2001, 2004, 2005; Peral et al., 2004), while since 1974 groundwater table variations (Aragón et al., 2004) have been recorded through a spatially dense piezometric network. The availability of the up-to-date extensometer measurements until November 2012, has allowed a complete analysis of the soil behaviour, including not only the subsidence phases occurred in the study area, but also the soil response to the last water level up-lift phase.

Moreover, the great amount of available field surveys and boreholes have allowed the implementation of a geotechnical model of the surficial aquifer. To this aim, the geotechnical and hydrogeological characterization performed by Mulas et al. (2003) and updated by Mulas et al. (2010) for the materials of the Vega Media of the Segura river (VMSR) has been adopted.

Subsidence has been analysed through the application of different Advanced DInSAR techniques. In this regard, the processing of the available SAR images has been performed through the *Coherent Pixels Technique* (CPT, Mora et al. 2003) and the results have been compared with other DInSAR data carried out with other techniques.

The displacement time series estimated through these techniques represent the whole deformation of the stratigraphic column and, for this reason, have been compared with the results of the model implemented up to the base of the surficial gravel layer (where the pumping takes place). These comparisons have allowed the individuation of local anomalies of the stiffness values, and have permitted a best model calibration.

Furthermore, the comparison between displacements calculated through the achieved model up to the extensometers depth and their time series has showed the occurrence of vertical anisotropies of the permeability. This hypothesis has been verified, analysing the available Lefranc's tests and the most

detailed stratigraphic columns and a new model has been proposed.

Therefore, the integration of in situ measurements and DInSAR displacement estimates has permitted the calibration and the validation of a numerical model. Through the achieved validated model, it will be possible to predict future deformations of a given monitored area, finding the consequences of any variation of the imposed boundary conditions.

Today, several piezometers, installed in the study area, continue to supply data every 8 hours; considering that the extensometer measurements are taken about three times a year, the up-to-dated model results (achieved considering the real-time water level variation) could be very useful to the natural risk mitigation. At the same time, a future continue monitoring of the study area could be performed through the update of the achieved processing of the SAR images acquired by the high-resolution Terrasar-X radar satellite constellation. It is characterized by a revisit time of 11 days that could facilitate the risk management.

Using the model results, it has also been possible to obtain 2D maps of deformations, (performed with different geostatistical techniques) in order to well analyse the spatial evolution of the phenomenon. The 2D maps, then, have been used in the A-DInSAR processing to correct the differential linear part of the interferometric phase (related to the soil deformation) and to better estimate its non-linear part.

In the Telese Terme case, the purpose of the project regards the utilization of multi-pass DInSAR algorithms (Sanabria et al. 2013) to control the evolution of the structural damage in buildings located in a subsiding urbanized area. Then, a structural model of a building affected by severe damage has been performed. The differential settlements measured by SAR have been used to verify the structure. The model results have been then compared with the forensic analysis achieved in situ.

This could allow to mitigate the risk in an area where a monitoring system does not exist, by using this remote sensing technique as a complementary tool for the forensic analysis of building structures.

Similar approaches could be tested in different areas to demonstrate the possibility of their application to the risk mitigation in other test sites affected by similar phenomena.

1.2.1. Thesis history

The thesis project began in April 2011 and the original aim was to use A-DInSAR techniques to analyse phenomena characterized by a predominant vertical component (subsidence and sinkholes). The first choice of the study areas, supported by the bibliographic research, was obtained taking into account as discriminating factors: amount and quality of available data; typology and magnitude of the instability phenomena. In particular, a specific attention was given to these areas where both subsidence and sinkholes phenomena could be analysed.

Starting from a first list of Italian areas, including San Vittorino plain (Rieti province), Contursi (Salerno province), Telese Terme (Benevento province), Bottegone (Grosseto province), Palermo, the choice was subjected to substantial changes during the years. This was due to the unavailability of financial aid to the research which limited the acquisition of the in situ ancillary data necessary to the DInSAR results validation for most of the selected areas. Therefore, the exposed research project has been carried on with the help of external collaborations provided by some colleagues.

For this reason, two areas were chosen, located within alluvial plains: Telese Terme (Benevento Province) and Castelvolturno (Caserta Province), both in Campania Region (Italy), which resulted suitable to implement an integrated approach, based on the traditional “in situ” techniques (geological-geomorphological, topographic and geophysical monitoring) and on the innovative Advanced DInSAR Interferometry Techniques (A-DInSAR).

Thanks to a specific agreement with the Italian Ministry of Environment (MATTM) ERS and ENVISAT SAR images of Telese Terme and Castel Volturno have been obtained, for the periods 1992-2000 and 2002-2010 respectively.

In the Telese Terme case, two sinkholes occurred in the metropolitan area, but the available C-band SAR images did not allow to detect them because of the resolution and the phenomena date; in fact, radar images were acquired before the occurrence of the phenomena and after its filling. Therefore, in the Telese Terme case, the research aim passed from the sinkhole to the subsidence analysis; in particular, focusing the attention to the applicability of SAR results to the structural monitoring. Also in this case, the availability only of C-band images have considerably reduced the analysis possibilities. In fact, the use of X-band image processing results would provide a higher density of points (where the SAR-detected displacement information would be available) to improve the analysis and to achieve a better estimation of the structural response.

However the high cost of the X-band images was not compatible with the available budget.

Therefore, the only possibility to obtain X-band images regarded the participation to projects devoted to their use to researches aimed to the natural risks mitigation. Unfortunately the time to obtain the images has not resulted compatible with the thesis duration.

For one of the originally chosen test sites (Palermo, Sicily), the X-band PS data were available thanks to the collaboration within the "Extraordinary Plan of Environmental Remote sensing (EPRS-E), lot 2: Analysis and assessment of the results achieved from the interferometric processing of Cosmo-SkyMed radar data in the test areas". However, after a first analysis of the phenomena affecting the area of Palermo, this case study resulted of great interest to test the potentiality of DInSAR data to landslide monitoring only. In fact, in situ data have not resulted sufficient to the subsidence analysis; moreover, the sinkholes detected in Palermo city turned out to have an anthropic origin and little magnitude and their collapse characteristics were not compatible with the satellite revisit time.

Also in the case of Castel Volturno, the in situ data were not sufficient to implement an integrated monitoring system with radar data.

During the second PhD year, thanks to a collaboration with the *"Instituto Geológico y Minero de España"* (IGME), the area of Murcia city has been chosen. The great amount of in situ data (piezometers and extensometers) and of DInSAR data have permitted to fulfil the predetermined tasks. Furthermore, the co-tutorship established with the Signal Theory and Communications Department (TSC) of the UPC of Barcelona has allowed also to carry out the processing of C- and X- band SAR images.

1.3. Materials and methods

The present study has been focused on the application of the so called *Advanced DInSAR Interferometry Techniques* (A-DInSAR) to the ground deformation monitoring and on the analysis and interpretation of the obtained results.

Remote sensing represents the technical–scientific discipline which allows to obtain quantitative and qualitative information about targets located far from a sensor, through measurements of an electromagnetic radiation (emitted, reflected or transmitted) that interacts with the involved surfaces. Forty years of progresses in the sensors technologies and in developing tools able to observe the environment in different spectral bands, have considerably improved the effectiveness of the Earth observation through these techniques. In particular, in addition to the passive sensors which measure the energy emitted by an external source and reflected by the observed target, there are the active ones, that illuminate the scene and measure the backscattered signal. The first ones allow a qualitative observation of an area, working mainly with optical data; in this case the electromagnetic energy is characterized by wavelengths belonging to the visible up to the infrared in the electromagnetic spectrum. On the other hand, active sensors achieve quantitative information of an observed phenomenon working with wavelengths of the L-, C- or X- band. In particular, radars are active sensors that use electromagnetic waves in the radio wavelengths and determine the distance of an object (registering the two-way travel time of the pulse) and its physical quantities measuring its backscatter intensity. In the development of the radar technology, a considerable limitation has been represented by the achievable resolution of the pixels that did not allow the applicability of simple radar sensors on satellite platforms to the displacement measurements. This limitation was overcome through a Synthetic Aperture Radar where signal processing is used to improve the resolution beyond the limitation of physical antenna aperture (Curlander et. al., 1991). In others words, SAR “synthesizes” a very long antenna playing on the forward motion of the physical antenna. This innovation changed the possibilities in the remote sensing application, because these instruments, using microwaves, do not feel the effect of clouds and could achieve measures 24 hours a day obtaining radar images of wide areas.

Radar images are pixels matrixes: to each of them, it is associated a value of the phase and the amplitude relative to the wave emitted by the antenna and backscattered from the targets. Using two images referred to the same area, acquired at different times (*temporal baseline*) and in different orbit positions (*spatial baseline*), it is possible to calculate images in which each pixel is associated to the difference of the phases, called *interferograms*. The so obtained interferometric phase contains various contributions among which the topography of the observed scene, and the possible soil deformation occurred in the interval of time

between the two acquisitions. Subtracting the topographic component it is possible to estimate the component due to the displacement. Therefore, from a processing of the interferometric phase, compared with the ground topography, it is possible to obtain two kinds of results:

- High resolution Digital Elevation Models (DEMs);
- Deformation maps characterized by millimetre resolution.

In the last two decades, the development of the interferometry has led to techniques that permitted the knowledge of the temporal evolution of displacements in an observed period, called Advanced DInSAR Interferometry techniques. Among them, it is possible to cite the following approaches: PSInSAR (Ferretti et al., 2001), SBAS (Berardino et al., 2002), SPN (Arnaud et al., 2003), CPT (Mora et al., 2003), IPTA (Duro et al., 2005), PSP-IFSAR (Constantini et al., 2008), SqueeSAR (Prati et al., 2010). Through the innovative A-DInSAR techniques it is possible to evaluate ground deformations, projected along the sensor Line Of Sight (LOS) by calculating the differences of the images referred to the same area, but detected in different times. Using images acquired at different times (*temporal baseline*) and in different orbit positions (*spatial baseline*), processing may be affected by errors, which lead to additional contributions to the interferometric phase and may severely reduce the accuracy of the technique.

Among the various methods cited above, the approaches employed to overcome these issues are essentially two: the so called "*Coherence-based*" approaches, among which the DInSAR SBAS (*Small BAseline Subset*) technique can be mentioned, and the *Persistent Scatterers* (PS) technique.

In particular, SBAS techniques only use interferograms characterized by a small temporal and spatial baseline, obtaining a high areal density of coherent pixels (where the mean coherence, computed considering all the selected interferograms to the processing, overcome an imposed threshold value).

The second approach is the *Persistent Scatterers* (PS) technique, based on the observation of a small subset of radar targets (the PS), constituted by parts of buildings, metal structures, outcropping rocks, showing negligible electromagnetic characteristic variations among the various acquisitions.

In the present work, the SBAS "Coherent Pixels Technique" (CPT) algorithm implemented by Mora et al. (2003) at the Remote Sensing Laboratory (RSLab) of the Universitat Politècnica de Catalunya (UPC) has been used to process all the available SAR images of the study area. Here, for the Murcia case study, 151 C-band images between 1995 and 2010 and 128 X-band images in the period 2008-2013 have been processed. X-band images have a high pixel resolution (about 2x3 m - azimuth-range) against the 5x20 m of C-band images; this allows to obtain a very high spatial and temporal density of measured displacements. Furthermore, thanks to a specific agreement with the Italian Ministry of Environment (MATTM), ERS and

ENVISAT SAR images of Telese Terme were available respectively for the periods 1992-2000 and 2002-2010 and are being processed too.

In the case of Murcia, 129 SAR images acquired from the European Space Agency (ESA) ERS-1/2 and Envisat ASAR sensors) covering two periods, July 1995-December 2005 and January 2004-December 2008, have been processed through the SPN technique (Arnaud et al., 2003) from Altamira Information. In the case of Telese the interferometric data elaborated by the PODIS Campania through the PSInSAR technique have been used.

CPT results obtained for the two study areas have been compared and validated through the comparison with other available PS DInSAR data.

CHAPTER II

Subsidence

Chapter II. Subsidence

2.1. Definition and classification

Subsidence is a gradual settling or sudden sinking of the Earth's surface owing to subsurface movement of earth materials. It may be classified in function of its causes (Scott, 1979), which can be natural or anthropic. In particular, it can be due to the compaction of soil materials, fluid withdrawal (oil, water, gas), deep material dissolution, excavation of tunnels or mining galleries, deep erosion (piping), lateral soil creep, or tectonic activity.

As referred by Tomás et al. (2013), following Prokopovich's genetic classification (1979), subsidence can be:

- "*endogenic*" if associated with internal geological processes, such as faulting, folding, isostatic adjustments and volcanism; and
- *"exogenic*" if related to anthropogenic or natural processes involving the creation of cavities and/or the removal of material from the subsurface.

2.2. Importance of the phenomena: social hazard and historical cases

Subsidence is a natural hazard, usually characterized by slow movements and, for this reason, it rarely turns out to be dangerous for the human life. However it can interest wide areas over variable time periods, causing deformations that vary from a few millimeters to several meters. Therefore, if it affects metropolitan areas, can causes important damages to structures and infrastructures with consequent high costs.

As referred by Tomàs et al. (2013), subsidence constitutes a hazard for bridges, roads, railways, storm drains, sewers, canals, levees, buildings and well pipes, increases the susceptibility to tidal flooding in low-lying coastal areas, Wu (2003) and can involve multi-million dollar losses (e.g. Kappel et al. 1999; Autin 2002; Gutièrrez et al. 2009; Mancini et al. 2009).

A lot of cities throughout the world have been experiencing subsidence problems. Most of them are coastal cities, like London, Houston, and Venice, or are built on river flood plains and deltas, like New Orleans, Baton Rouge, and the San Joaquin Valley of central California or on former lake, like Mexico City.

Hu et al. (2004) estimated that more than 150 cities in the world are affected by subsidence due to excessive groundwater withdrawal. In particular the most famous cases include the Po Valley, Venice and Ravenna (Italy), Mexico city, Santa Clara and San Joaquin Valleys, Antelope (USA), Bangkok (Thailand),

Murcia city, Barcelona, Granada, Almeria (Spain) and many other areas in the world. Some references are reported in Tab. 2.1.

Mexico City	Po river delta	Venice	Tokyo
Figueroa and Germán, 1977	*Schrefler et al., 1977*	*Gambolati and Freeze, 1973*	*Ricceri and Butterfield, 1974*
Carbognin et al., 1978	*Carbognin et al., 1978*	*Ricceri and Butterfield, 1974*	*Bouwer, 1977*
Scott, 1979	*UNESCO, 1984*	*Bouwer, 1977*	*Ishii et al., 1977*
UNESCO, 1984.	*Placzek, 1989*	*Carbognin et al., 1977*	*Carbognin et al., 1978*
Placzek, 1989	*Ricceri and Favareti, 1992*	*Carbognin et al., 1978*	*Scott, 1979*
		Carbognin et al., 1979	
Birkle and Schneider, 1998	*Lewis and Schrefler, 1998*	*Corapcioglu, 1984*	*Corapcioglu, 1984*
Strozzi and Wegmüller, 1999	*Gambolati et al., 1999*	*UNESCO, 1984*	*UNESCO, 1984*
	Bitelli et al., 2000	*Placzek, 1989*	*Akagi, 1992*
	Carminati and Martinelli, 2002	*Ricceri and Favaretti, 1992*	*Yamamoto, 1996*
	Teatini, 2011	*Lewis and Schrefler, 1998*	*Sato et al., 2003*
		Gambolatti et al., 1999	
		Alberotanza et al., 2002	
		Strozzi et al, 2003	
		Teatini, 2005b	

Ravenna	Bangkok	Osaka	Bologna
Carbognin et al., 1979	*UNESCO, 1984*	*Carbognin et al., 1978*	*Ricceri and Favareti, 1992*
UNESCO, 1984	*Bergado et al., 1987*	*UNESCO, 1984*	*Folloni et al., 1996*
Lewis and Schrefler, 1998	*Prinzl and Nutalaya, 1987*	*Akagi, 1992*	*Wegmüller et al., 1999*
Gambolati et al., 1999		*Yamamoto, 1996*	*Bitelli et al., 2000*
Carminati and Martinelli, 2002		*Nakagawa et al., 2000*	*Carminati and Martinelli, 2002*
Teatini 2005 a, 2006			

Table 2.1: Historical cases of subsidence

In some cases, subsidence can manifest itself as catastrophic collapsing, called *sinkholes*, often dangerous for human life (Guerrero et al. 2008; Gutiérrez et al., 2008, 2009, 2011; Galve et al. 2009). They can be provoked by karst processes (consisting in the dissolution of limestone, dolomite, marble, or any other water-soluble rocks) or by piping phenomena. In the first case, between the countries affected by these kind of phenomena, it is possible to cite Florida, Texas, Mexico, but also several areas in Italy (Nisio, 2004; Caramanna et al., 2008), like the Salento Peninsula (Polselli, 2005; Castiello, 2010), Toscana region (D'Amato Avanzi, 2004), Campania region and the famous S. Vittorino plain (Rieti).

The phenomenon of "*soil piping*" consists of the excavation of tunnels and cavities along the water preferential flow paths. The most famous cases of piping sinkholes are that occurred in Guatemala City in 2007 and 2010 in the Quaternary volcanic deposits. Here the leaking water mains progressively eroded and removed coarser materials, creating large underground voids. Other examples of piping sinkholes occurred in Italy in 2002 and 2006 in Telese Terme (Calcaterra et al., 2009).

Sinkholes can also have an anthropic origin and be correlated to land-use practices, like in the case of Palermo (Sottile, 2010) and Naples (South Italy) where are due to the presence of anthropic cavities; or they can be originated by groundwater pumping and by construction and development practices; i.e. mining activities, (Pipia, 2007a; Yerro et al., 2014).

2.3. DInSAR monitoring of subsidence phenomena

The Advanced DInSAR Interferometry techniques has been used to monitor subsidence phenomena in many works (e.g.: Teatini, 2005; Cascini et al., 2006, 2007a,b; 2013; Marturià et al., 2006; Galloway and Hoffmann, 2007; Stramondo, 2008; Herrera et al., 2009; Ashrafianfar et al., 2011; Calderhead et al., 2011; Gutiérrez et al., 2011; Tomás et al., 2010, 2012; Raspini, 2013; Yerro et al., 2014). In particular, SAR processing results, obtained through various A-DInSAR algorithms, proved to be helpful to the phenomenon analysis and to the related risk mitigation.

In the case of subsidence due to groundwater withdrawal, DInSAR displacement estimation resulted particularly effective to the phenomenon analysis and to achieve comparisons between the water level measures and the consequent produced displacements. In many case, DInSAR data allowed the calibration of subsidence models: hydrological, geotechnical and structural models.

2.3.1. Hydrological models

In Galloway and Hoffmann, (2007) DInSAR, data have been used in a hydrogeological application, resulting very effective in the analysis, monitoring and simulation of the groundwater flow, of the aquifer-system compaction and of land subsidence. In particular, DInSAR displacements reached to define the material and hydraulic heterogeneity of deforming aquifer-systems and to estimate system properties (e.g. storage coefficients and hydraulic conductivities).

The storage coefficients represent physical properties that characterize the capacity of an aquifer to release groundwater. In particular, S_k is the aquifer system skeletal storage; it is function of the thickness of the aquifer system b (eq. 2.1) and of the skeletal specific storage S_{sk}

$$S_k = S_{sk} \cdot b \tag{2.1}$$

and represents the volume of water released from storage per unit decline in hydraulic head in the aquifer, per unit area of the aquifer. In other words, it represents the deformability of the aquitard, varying with the stress state and can be defined for the elastic and inelastic ranges of stress.

In the case of water overexploitation, the water level could exceed under the historical minimum (h_p) and, consequently, the pre-consolidation pressure, by means of the highest pressure suffered by the soil along its life, could be overcome. In this case, a part of the produced deformation is not recoverable and the water released from storage derives from an inelastic compaction of the aquitard. Fine-grained sediments that constitute the confining and interbedded aquitards may deform both elastically and an-elastically.

The aquifer skeletal storage S_k can be calculated (Riley, 1969) as:

$$S_k = \frac{\Delta b}{\Delta h} \tag{2.2}$$

Where Δb represents the change in the aquifer thickness (by means the subsidence) and Δh the water level variation. Riley proposed a graphical methodology to the skeletal storage computation, consisting in the determination of the slope of the branch of the stress–strain curve (elastic or anelastic). This methodology has been used by several authors (Hoffman, 2003; Hoffmann et al., 2003; Schmidt and Bürgmann, 2003; Galloway and Hoffmann, 2007; Tomas et al., 2010), where, in particular, Δb computation, obtained from the DInSAR displacement measurements in conjunction with piezometer ones, allowed to find spatially variation of storage coefficients and verify the elastic behaviour of the aquifer.

As reported from Tomas et al. (2010), this approach permitted to implement a numerical model for the subsidence prediction in Murcia city and, in particular, to achieve an-elastic coefficient from the strain-stress curve

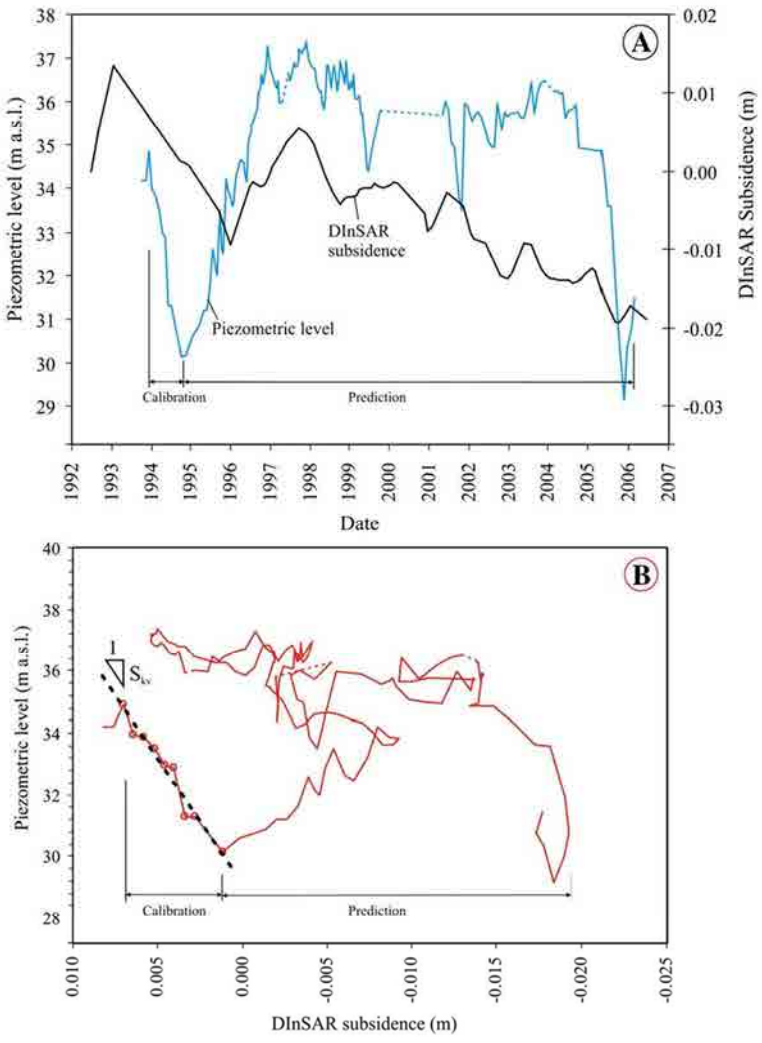

Figure 2.1: A) LOS-projected subsidence and piezometric data used for the calibration and prediction. B) Strain–stress curve and graphical construction for an-elastic coefficient computation (Tomas et al., 2010).

(Fig. 2.1), obtained thanks to the DInSAR displacements. It is showed a water level drought, occurred in the period 1993-1995, produced displacements measured through SAR data. The CPT displacement time series corresponding to the 1993–1995 period were used to calibrate a one-dimensional subsidence model and to retrieve the soil physical parameters. In this period the historical piezometric minimum was overpassed, so the an-elastic storage coefficient has been achieved. Using 139 oedometric tests performed following the UNE 103-405-94 (UNE, 1994) procedure, the elastic storage coefficient was computed as a percentage of an-elastic storage coefficient (S_{kv}). In fact, the ratio (which resulted equal to 15% on average) between the swelling index C_s (slope of the oedometric unloading–reloading branch) and the compression index C_c (slope of the oedometric virgin compression branch), could be considered as that of the S_{ke} and S_{kv} parameters. The so obtained model was successfully used to predict the deformations for the period 1993–2007.

2.3.2. Geotechnical models

DInSAR measured displacements has demonstrated to be useful also for the calibration or validation of more sophisticate subsidence geotechnical models, like referred by Herrera et al. (2009a;b), Calderhead et al. (2011).

In Herrera et al. (2009b), in particular, it was demonstrated that the consolidation process is the most important phenomenon to be simulated in Murcia city. Here, the elastic constitutive relation proposed by Biot (1941) was chosen to model the soil behavior and the possible occurrence of plastic deformations was not taken into account. Through the comparison between the model results and DInSAR displacement time series, an average absolute error of 5.5 ± 4.7 mm (in the period 1995-2007) was achieved.

This result demonstrated the potential of A-DInSAR techniques to validate subsidence prediction models as an alternative to using instrumental ground-based techniques for validation.

2.3.3. Structural monitoring

Some other interesting applications of DInSAR displacement measurements have provided the monitoring of buildings affected by structural problems related to the subsidence, due to water over-exploitation. In particular, Cascini et al. (2006, 2007b, 2013), Tomás et al. (2012), used geotechnical criteria to characterize potentially risky situations, identifying buildings where damage related to the DInSAR measured settlements could occur.

In Cascini et al. (2006), in particular, DInSAR results allowed to investigate the relationship between the magnitude of absolute and differential settlements and the occurrence of building damage. In Figure 2.2 the magnitude of the deformation gradient has been compared with the localization of recorded damages.

Above all, it has been noted that the main directions of damage, often consisting of vertical cracks, seemed to be almost normal to the gradient deformation direction.

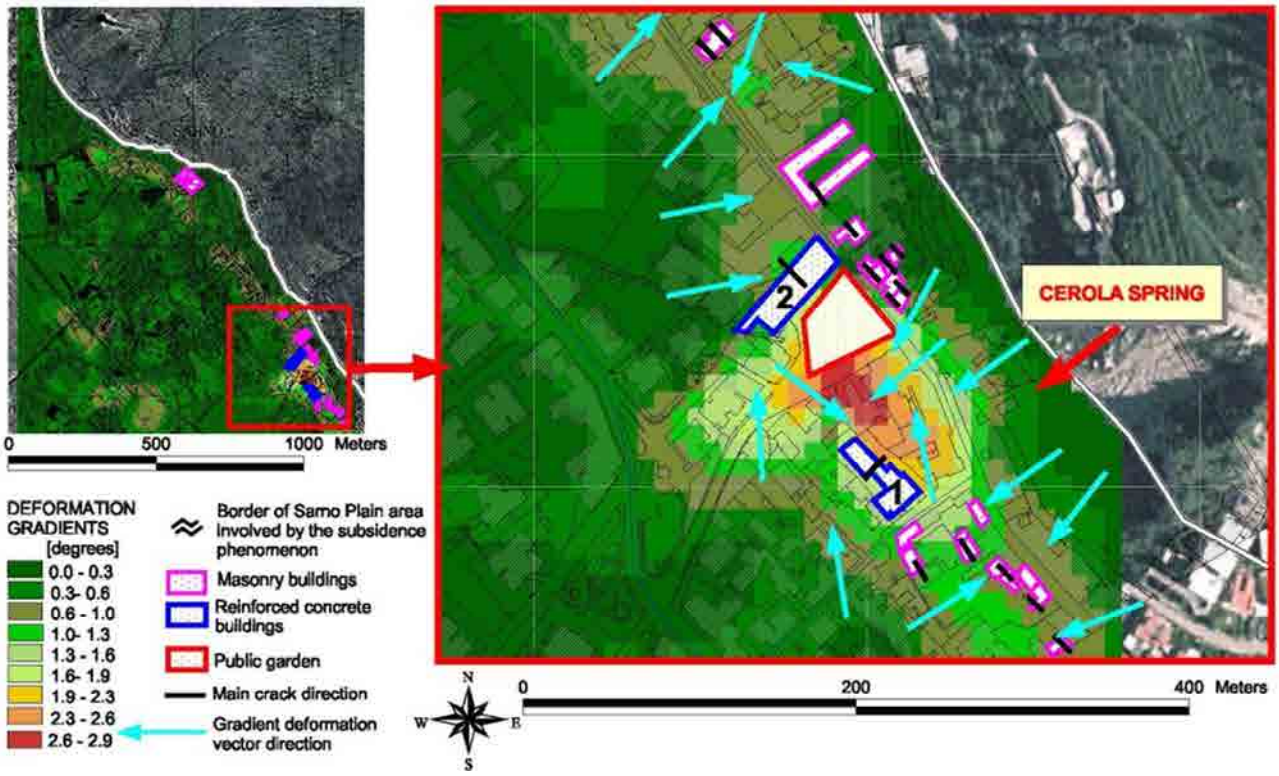

Figure 2.2: Deformation gradient map of the investigated area and spatial distribution of damaged buildings (Cascini et al. 2006).

In Tomàs et al. (2012), DInSAR data were used to understand the mechanism that affects the Santa Justa and Rufina Church in Orihuela city (Spain), related to the subsidence due to groundwater withdrawal. The geotechnical characterization of the substrate properties and geometry beneath the church, linked to a detailed forensic analysis and examination of the historical reports concerning the church pathologies, allowed to interpret the DInSAR interpolated map.

In particular, this map permits to estimate the high surface deformation gradients and the angular distortions that are related to the presence of anisotropic stresses in a building. In this way, it is possible to individuate the buildings that have a greater propensity to damage and analyze the single cases with a more accurate structural analysis.

2.3.4. DInSAR monitoring of subsidence phenomena in Italy

An important contribution to discover the potentiality of DInSAR monitoring systems was brought by the "The Extraordinary Plan of Environmental Remote sensing" (EPRS-E, 2009). In this project, the available ENVISAT images have been processed in the whole Italian territory and made available through the website of the National ministry of environment (MATTM). Furthermore, the processing of high resolution Cosmo Sky-med images acquired by last generation sensors has been achieved for three test sites Bologna, Venice and Palermo to analyse advantages and limits of this technique.

Venice, is affected by subsidence due to the water overexploitation. In order to monitor the displacements a levelling network was installed in 2007 and implemented in the last years, introducing, recently, also a DGPS network (Tab. 2.2).

An area of 5x3 Km has been chosen to test the DInSAR data, achieved from the processing of X-band Cosmo Sky-med images through the Persistent Scatterer Pairs (PSP)-IFSAR technique (Costantini et al. 2008).

Here, 38 images acquired in ascending orbit and 50 in descending orbit in 2009-2011 (having a revisit time of 11 days) have been processed.

The comparison between in situ and radar data has been carried out considering a buffer of 100 m from the 18 GNSS network vertex and computing the average velocity between the PS within the buffer.

Nome	VEL GNSS (mm/anno) LOS ASCENDING	VEL PS (mm/anno) LOS ASCENDING	Delta GNSS - PS (mm/anno) ASCENDING	VEL GNSS (mm/anno) LOS DESCENDING	VEL PS (mm/anno) LOS DESCENDING	Delta GNSS - PS (mm/anno) DESCENDING
CN06	1,1	1,7	-0,6	0,7	0,7	0,0
CN07	0,9	1,1	-0,2	0,7	0,9	-0,2
CN08	0,2	0,8	-0,6	0,2	0,1	0,1
CNA01	1,2	1,4	-0,2	0,9	1,0	-0,1
CS09	0,9	0,2	0,6	0,8	0,6	0,2
CS16	-0,7	-0,2	-0,5	-1,0	0,1	-1,1
CSA02	1,2	1,2	0,0	0,8	1,0	-0,2
CSA07	1,0	0,9	0,2	0,7	0,7	0,0
CSA08	0,6	0,9	-0,3	0,4	0,5	-0,1
DD08	1,0	1,3	-0,2	0,7	1,2	-0,5
DD09	-0,7	0,8	-1,5	-1,0	0,8	-1,9
DDA02	0,9	1,1	-0,2	0,5	1,2	-0,7
DDA05	0,8	1,0	-0,2	0,6	1,2	-0,6
DDA07	0,8	0,7	0,1	0,6	0,2	0,4
SC06	1,3	1,6	-0,3	1,1	-0,3	1,3
SCA04	0,8	1,1	-0,4	0,6	1,3	-0,7
SMA02	0,9	0,7	0,2	0,5	0,9	-0,4
SPA01	1,0	0,9	0,2	0,6	0,8	-0,2

Table 2.2: Comparison between mean velocities of the displacements measured by SAR and in the 18 vertex of the GNSS network of Venice (EPRS-E, 2009).

The reported velocity values have been compared with that of the topographic surveys obtaining an error of 0.5 mm/year and 1.3 mm/year for the ascending and descending acquisition geometry.

Bologna is affected by subsidence due to the water overexploitation. Also in this case, it has been chosen to test the Cosmo Sky-med products because of the great amount of in situ monitoring data. Here, in fact, topographic measurements (GNSS network, Tab. 2.3) have been achieved between 1993 and 2001 and after 2007 (ERGPS7). Starting from these networks, a topographic campaign has been performed in an area of 165 Km^2 (21x12 Km).

Here, 36 CSK images acquired in ascending orbit between 2009 and 2011 and 40 CSK images in descending orbit between 2008-2011 (having a revisit time of 24 days) have been processed through the SqueeSAR™ technique (Prati et al. 2010).

Using the same criteria described in Venice case study, an error of 2.6 mm/year and 2.3 mm/year for the ascending and descending acquisition geometry have been obtained.

Nome	VEL GNSS (mm/anno) LOS ASCENDING	VEL PS (mm/anno) LOS ASCENDING	Delta GNSS - PS (mm/anno) ASCENDING	VEL GNSS (mm/anno) LOS DESCENDING	VEL PS (mm/anno) LOS DESCENDING	Delta GNSS - PS (mm/anno) DESCENDING
BO014	-14,0	-15,0	1,1	-11,6	-14,2	2,6
BO017	2,2	1,6	0,6	2,5	2,1	0,4
BO045	-1,9	-2,9	1,0	-1,6	-0,9	-0,7
VIACADRIANO	0,8	0,5	0,3	0,9	0,2	0,7
VIAGANDOLFIGRANAROLO	-1,3	-1,7	0,4	-1,2	-1,2	-0,1
VIAGRANDICASTELMAGGIORE	-3,1	-6,3	3,2	-2,7	-4,8	2,1
VIALIPPARINI	-1,0	-2,7	1,7	-0,8	-0,2	-0,7
VIAVIADAGOLA	-1,3	-2,7	1,4	-1,2	-0,5	-0,7
PARCOFUNAKOSHI	-4,9	-6,3	1,4	-4,1	-6,5	2,4
ARCOVEGGIO	-5,8	-5,2	-0,6	-5,8	-5,1	-0,7
VIAGOBETTI	-1,4	-2,1	0,7	-1,1	0,0	-1,2
ROSALUXEMBURG	-4,3	-6,8	2,5	-3,6	-5,8	2,2
PIAZZASTADIO	-2,1	-2,4	0,4	-1,7	-1,7	0,0
VIAMARCOPOLO	1,5	0,7	0,8	1,7	1,0	0,7
VIASTALINGRADO	2,0	2,2	-0,2	2,6	2,2	0,4
CARICCHI	1,8	1,0	0,8	2,3	1,2	1,1
CENTROPARADISO-SANLAZZARO	-1,1	-1,9	0,8	-0,9	-1,2	0,3
DUEMADONNE	-3,7	-5,8	2,1	-3,1	-3,5	0,4
LUNETTAGAMBERINI	-3,9	-3,9	0,1	-3,3	-2,8	-0,4
ROVERI	2,2	1,2	1,0	2,8	2,8	0,0
VIADELTERRAPIENO	-1,9	-4,3	2,4	-1,5	-2,1	0,6
VIALARGA	0,8	-1,9	2,7	1,0	-0,3	1,3
PARCOVIGANO	-1,9	-3,0	1,1	-1,6	-2,4	0,8
VIAINDUSTRIA	0,9	1,3	-0,5	1,1	1,1	0,0

Table 2.3: Comparison between mean velocities of the displacements measured by SAR and in the 24 vertex of the GNSS network of Bologna (EPRS-E, 2009).

All the previous described case studies, shows that A-DInSAR results could be useful tools in the natural risk mitigation if used expertly, knowing the limitations related to the SAR images processing and validating these results with the "*ground true*" previous reconstruction.

For this reason, their use is normally coupled with the *"in situ"* monitoring to perform an integrated monitoring system. Several other examples can be found in Avallone et al. (1999); Baldi et al. (2009); Teatini et al. (2006; 2011).

Referring to Avallone et al. (1999) they used DInSAR method for measuring the ground displacement changes in Neapolitan volcanic area. The DInSAR method, applied to radar images in the period comprised between 1993 and 1996. It confirms the significant subsidence still occurring in the Campi Flegrei area after the last 1982-1984 seismic and inflation sequence. This subsidence is also observed by classical levelling surveys. The best interferogram, corresponding to the 1993-1996 period shows that the centre of the Campi Flegrei caldera subsided by about 26±9 mm/year during this three years interval. This result is consistent with the value of 100±5 mm obtained from the routine levelling surveys carried out by observatories Vesuviano in the same area. The modelling of the fringe pattern using the Mogi's model predicts a source centred offshore eight hundred meters Southwest of Pozzuoli at about 2.7 km depth. The modelled volume decrease at depth is 0.8x106 m^3/year and the maximum subsidence predicted by the model is 78 mm.

The other important subsidence case study in Italy is represented by Ravenna.

Ravenna is affected by subsidence provoked by the aquitard and reservoir compaction; this is caused, respectively, by extensive groundwater withdrawals from the unconsolidated Quaternary basin and gas production from a number of pre-Quaternary pools scattered over the area. Water pumping paralleled the post-war industrial development of Ravenna until the middle seventies when consumption was drastically curtailed owing to the economic crisis and the activation of a new aqueduct.

The discovery (made in 1952) of several underground gas pools and the construction of a big commercial port promoted rapid industrial and agricultural development in the neighbouring area. Therefore, after the Second World War, Ravenna experienced a new flourishing era. The major environmental cost paid for this outstanding growth has been a pronounced land settlement as a direct consequence of groundwater overdraft and gas removal. Subsurface water has been extensively withdrawn since 1950 to cope with the growing demand for fresh water for civil, industrial and agricultural use. The problem became critical in the middle 1970s because of obvious large damage to the infrastructure and the monumental heritage that was increasingly subject to flooding during the most intensive meteorological events, the highest Adriatic tides and the longest rainy periods. One major controversial issue was apportioning the responsibility for land subsidence between gas and water pumping. Overall geodetic evidence pointed out a joint responsibility. However, the respective magnitude and extent were unclear (Gambolati et al. 1991).

The extraction of gas in Ravenna Terra field reaching a peak withdrawal of about 7 million Sm^3 per day in 1966 and being practically stooped in 1982. Water has also been heavily extracted from the upper aquifers in the period 1950-1973. After that pumping was drastically reduced and finally stopped. Both extractions have contributed to surface settlement, however the one caused by gas extraction decreases rapidly away from the reservoir, while that due to water withdrawal is spread all over the area (Schrefler et al. 2008). They concluded that there is direct and indirect evidence that the reservoir sands of this region show the typical features of soils in presence of capillary forces.

The exploitation of several reservoirs is currently under way and the search for new fields is still in progress. Geodetic records indicate that the maximum cumulative subsidence over the period 1950-1986, including a natural geologic settlement of perhaps 2 mm/yr, has been 1.30 m in the industrial zone of Ravenna. In 1980 the municipality promoted a reconnaissance study with the primary aim of providing the information base needed to reconstruct the actual occurrence, understand correctly the physical behaviour and produce the essential input data to a mathematical model which realistically relates the subsidence of the city to groundwater withdrawal and gas removal with an emphasis on their respective influences.

All of the previous studies on the Ravenna subsidence are dealing with mathematical 3D models, geodetic, hydrogeological, seismic and environmental measurements. Gambolati et al. (1991) reported that a borehole (RA1) drilled down to 500 m by AGIP (Italian National Oil Company) and Ravenna municipality give a detailed lithological description. Several analyses have been performed on the borehole core samples, including sediment grain size analysis, specific weight of the porous bulk, specific weight of the grains, Atterberg limits, natural water contents, oedeometer tests on soil consolidation, and permeability tests with either constant or variable load. The oedeometer tests were performed on cohesive as well as granular sediments to assess the vertical soil compressibility. The range of stress explored was between 0.5 and 82 kg/cm 2, taking care to exceed the in situ consolidation stress by at least 2 times. Gambolati et al. (1991) noted that the compressibility decreases with depth and the difference between the sand and clay compressibilities become smaller for larger values of depth. Values of compressibility appear to be between 4×10^{-3} and 6×10^{-5} Kg/cm^2.

The results from the three-dimensional numerical simulations, performed with the aid of mixed finite element, finite difference and integral models, show that the primary responsibility for the regional land sinking should be placed on the subsurface water overdraft which occurred until the middle 1970s. Gas withdrawal plays a role restricted to the area overlying each reservoir with a magnitude depending on the depth of burial, thickness of mineralized rocks and overall volumetric production. A major environmental impact may be expected where the gas subsidence bowl is intersected by the Adriatic coastline (Gambolati et al. 1991).

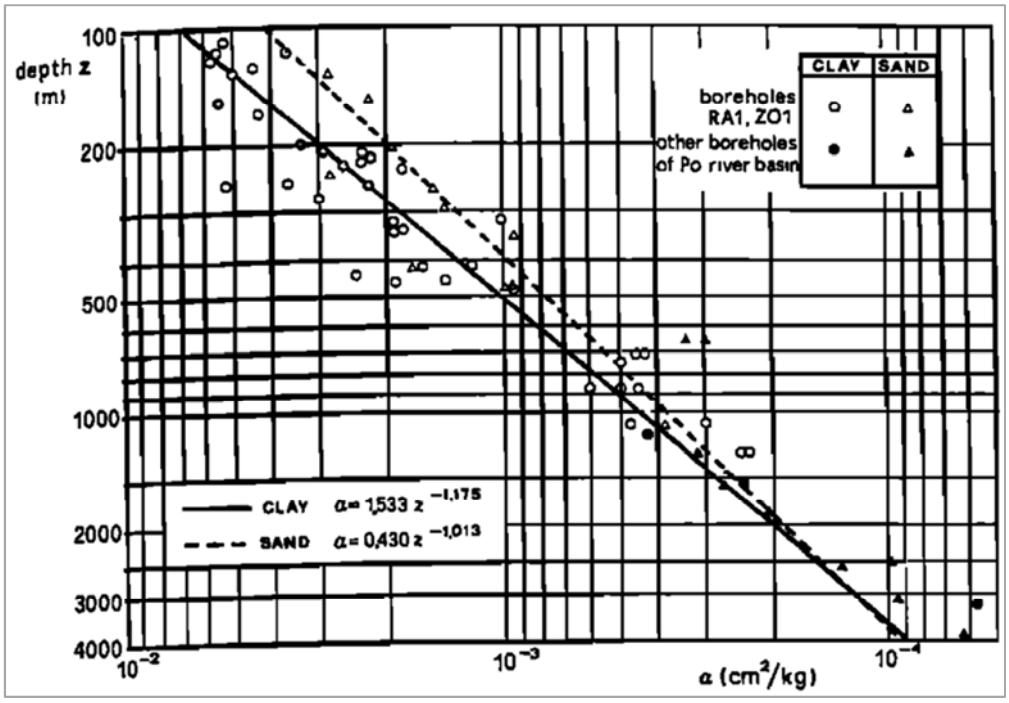

Figure 2.3: Vertical soil compressibility versus depth as obtained from oedometer tests carried out on core samples RA1 (after Gambolati et al., 1991).

Teatini et al. (2005) studied the Ravenna land subsidence by implementing the levelling measurements carried out since 1987 in a GIS environment. They noted that land subsidence increased in the last decades due to groundwater withdrawal from a well-developed multi-aquifer system underlying the coastland and, subordinately, to gas extraction from deep reservoirs scattered through the area and still productive nowadays. Land settlement occurred at an average rate of about 5 mm/year until World War II, increased greatly up to an order of magnitude in the Ravenna industrial area, mainly due to the aquifer over-draft in connection with the post-war economic growth. The construction of new public aqueducts using surface water during the late 1970s and 1980s has significantly reduced the subsurface water consumption and the settlement rates to the pre-war values. However, local areas of significant land subsidence are still present because of local groundwater pumping and the development of deep gas reservoirs. The cumulative land settlement, accounting for both the natural and the anthropogenic components, has achieved the alarming value of 1.6 m from 1897 to 2002 in the industrial area located between the city and the seashore, with the coastland and the historical centre settled by more than 1 m. Although the mainland appears to be substantially stable to date, subsiding rates up to 15 mm/year recorded between the Lido Adriano and Lido di Dante villages facing Ravenna and in the northern area separating the Comacchio Lagoon from the Adriatic Sea raise concern for the sustainability of an environment already greatly affected by the past occurrence.

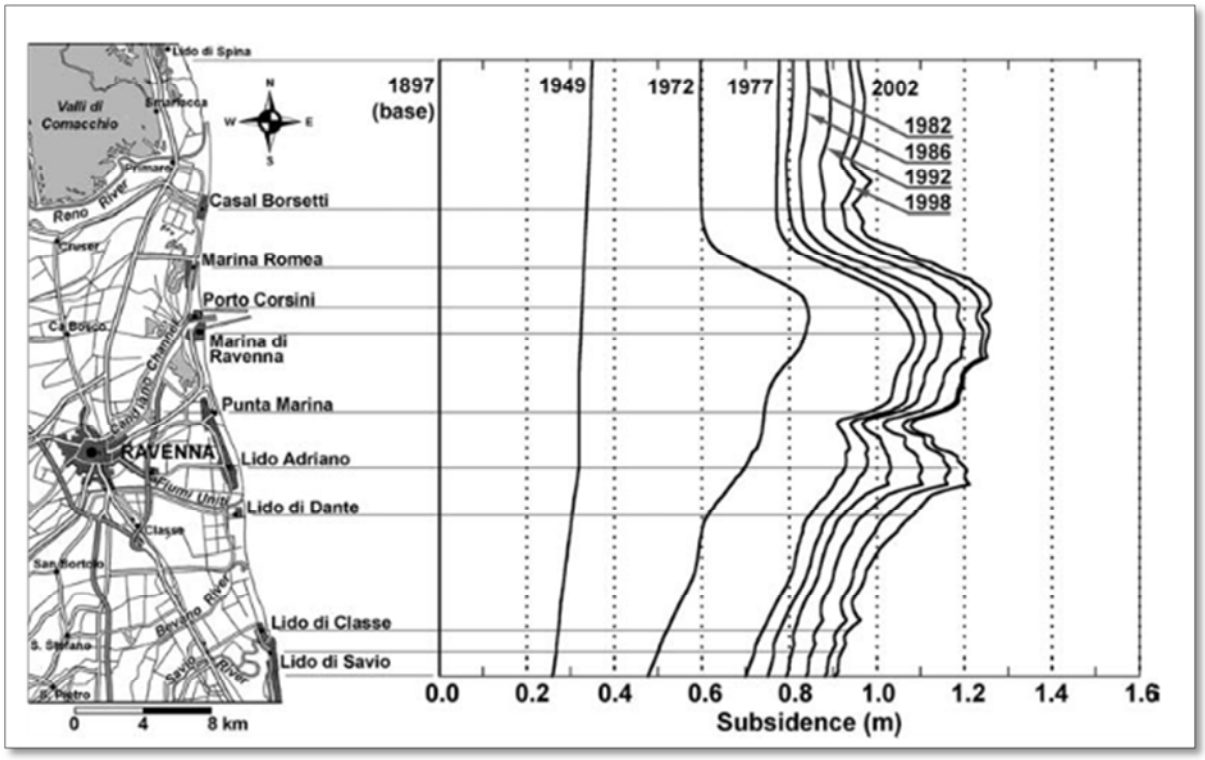

Figure 2.4: Land subsidence versus time along the shoreline of the Ravenna Municipality obtained from the GIS slicing of the levelling data (Teatini et al., 2005).

As referred by Teatini et al. (2006) mentioned that Anthropogenic land subsidence due to groundwater overdraft has caused serious and costly damages to the Emilia-Romagna coastland, a low-lying area facing the Adriatic Sea south of the Po River delta, Italy. Both areal pattern and time behaviour of the occurrence are reconstructed over the last 50 years and predicted until 2016 by a 3-D FE model. The model addresses the pumping-related hydrodynamics of the complex multi-aquifer system underlying the study area and predicts ground surface displacements. The simulations have been performed using the most recent and advanced 3-D interpretation of the aquifer geology. However, the paucity of data on the pumping rate distribution does not allow for local in-depth investigations. The aquifer/aquitard hydraulic conductivity and compressibility have been estimated by in situ and laboratory tests and calibrated by a coupled iterative procedure matching the historical piezometry, land subsidence, and multi-aquifer system compaction over the study area. The hydrologic and geo-mechanical models have been calibrated over, 1976-1946 when an almost continuous pressure decrease occurred, and validated over 1976–2001, when a general pressure recovery was experienced by the sandy formations because of a significant curtail of groundwater withdrawal. A hysteretic partially recoverable constitutive relationship is implemented for the rock compressibility to account for the different behaviour in loading and unloading conditions. Groundwater withdrawal from the upper multi-aquifer system is the main responsible for the

anthropogenic land subsidence experienced by the Emilia-Romagna coast land after World War II. Over the last two-three decades, when a general head recovery has been observed within the pumped formations, residual land settlement measured all over the region appears to be accounted for by the delayed aquitard consolidation.

In the same article it has been mentioned that a most fundamental parameter for a reliable modelling of land subsidence due to fluid withdrawal is the uniaxial vertical compressibility (CM) which controls the amount of vertical soil compaction caused by pore pressure drawdown. Pumping tests can provide some in situ estimates of the aquifer elastic storage *S*. As reported in eq.2.1, dividing the S values by the aquifer thickness, a specific elastic storage S_s is obtained. In this case, a specific elastic storage between 10^{-4} -10^{-5} m^{-1} has been found. S_s is related to the vertical compressibility by the relationship:

$$Ss = \gamma(CM + \varphi\beta) \tag{2.3}$$

Where γ and β are, respectively, the groundwater specific weight and volumetric compressibility (β = 0.432 X 10^{-8} kg/m^2) and φ = 0.3 the medium porosity. Hence the in situ measurements provide a sand compressibility that is from 5 to 10 times smaller than that found from laboratory tests, displayed in Figure 2.3, consistent with the most recent findings that laboratory tests tend to overestimate the actual CM.
Teatini et al. (2006) concluded that Groundwater withdrawal from the upper multi-aquifer system is the main responsible for the anthropogenic land subsidence experienced by the Emilia-Romagna coastland after World War II. Over the last two-three decades, when a general head recovery has been observed within the pumped formations, residual land settlement measured all over the region appears to be accounted for by the delayed aquitard consolidation.

Baldi et al. (2009) studied the land subsidence in the Po plain using regional and local networks of continuously operating GPS stations (CGPS) distributed in the northern-central part of the Italian peninsula. They mentioned that over the last century the Ravenna area has been affected by a widespread land subsidence of both natural and anthropogenic origins; initially, it was of the order of a few mm/yr, but the extensive groundwater withdrawals started in the early 1950s and the beginning of gas production from onshore and offshore reservoirs, discovered in the area in 1952, increased the subsidence up to 110 mm/yr (Gambolati et al., 1991). Following the late 1970s, the water withdrawal was drastically reduced due to the economic crisis and the activation of a new aqueduct, inducing an abrupt decrease in the land subsidence rate to an average of 10 mm/yr. At the beginning of the 21st century data indicate an average yearly rate generally smaller than 10 mm/yr in the city area and in the industrial zone of Ravenna whereas in the

coastal area close to the gas reservoirs a maximum of 10–15 mm/yr was recorded (Teatini et al., 2005). The present vertical velocity in the city area observed in the RAVE and RAVS sites indicates a subsidence rate of about 3 mm/yr (Table 2.4).

Teatini et al. (2011) used radar Interferometric Point Target Analysis (IPTA) with previous geomorphological investigations on aerial/satellite images and seismic surveys, geochronological data from core samples and geomechanical in situ tests, to assess the current sinking of the Po River delta and to understand the processes controlling the vertical movement. They concluded that the consolidation of late Holocene sediments is the major cause of the present land subsidence in the Po River delta.

Site	Code	LL	DinSAR	GPS
Bologna	BOLG	−18		−3.2 ± 1.9
Codigoro	CODI	−6	−8	−1.7 ± 1.1
Collecchio	COLL		−1	−2.2 ± 0.6
Conselice	CONS		−8	
Ferrara	UNFE	−3		−1.1 ± 0.7
Finale Emilia	MO05		−4	−1.9 ± 1.2
Guastalla	GUAS		−1	−4.0 ± 0.6
Imola	IM01	−3		−0.1 ± 1.1
Medicina	MEDI		−5	−0.5 ± 0.4
Mirandola	MO04		−2	−1.0 ± 1.1
Modena	MO01	−3		−15.7 ± 0.8
	MODE	−2		−12.5 ± 1.1
	MOPS	−2		−15.1 ± 1.2
Molinella	BO03	−6		−4.9 ± 0.9
Parma	PARM		−1	−0.4 ± 1.1
Piacenza	PIAC		0	−0.2 ± 1.1
Ravenna	RA01	−6		
	RAVE	−6		−2.1 ± 0.7
	RAVS	−5		−4.7 ± 0.8
Reggio Emilia	REGG	−1		
Rimini	ITRI	−6	−4	
San Giovanni in Persiceto	SGIP	−7		−7.0 ± 0.8

Table 2.4: comparison between in situ (topographic levelling and GPS) and DInSAR measured displacements (ARPA, Emilia Romagna region); in the table are reported the vertical velocity (mm/yr) estimated by levelling (LL) from 1999 to 2005 on selected benchmarks located near the CGPS (maximum distance of some hundred meters), or inferred by the DInSAR analysis (2002–2006) (Baldi et al., 2009).

All these studies concerning the comparisons between DInSAR data and in situ measurement are very usefull to understand the accuracy of these innovative techniques to the monitoring of ground deformations. In particular, as reported in Herrera et al. (2009), some recent validation experiments available in the scientific literature (Strozzi et al., 2001; Hanssen, 2003; Colesanti et al., 2003; Casu et al., 2006; Crosetto et al., 2008; Herrera, 2008, 2009; Tomás, 2009) have found that the error of the deformation time series, estimated with different A-DInSAR techniques, compared with "*ground truth*" measurements was within the ±6.9 mm interval.

CHAPTER III

Subsidence monitoring

Chapter III. Subsidence monitoring

3.1. Subsidence monitoring techniques

Subsidence phenomena can be characterized by planning an effective monitoring system both of deformations and of their causes. For this purpose, it is necessary to measure several parameters, as the relative displacements between two points, absolute, inclinations, settlements occurred in a specific direction, deep movements and so on.

Furthermore, the accuracy measurement of the ground deformation and its temporal and spatial scale are the principal parameters to implement a subsidence monitoring system.

Therefore, the monitoring system has to take into account the phenomenon characteristics and development; in particular, it has to be performed in function of the phenomenon extension, magnitude, frequency of the necessary measures and, of course, the availability of the economic resources.

The principal methods to the displacements monitoring (*extensometers, topographic levels, GPS, total stations, theodolites, Laser systems, radar interferometry, …*) can be classified into two principal categories: "*in situ*" techniques and "*Remote sensing detection*".

Among these branches is possible to distinguish:

- *In situ techniques:* ***Instrumental methods:***
  - → **Extensometers**
  - → **Inclinometers**
  - → **Micrometers**
- *Remote sensing detection:*
  - → **Topographic conventional methods**
  - → **Geodesic *methods***
  - → ***Photogrammetric* methods**
  - → **Radar remote sensing *techniques***

3.1.1. In situ techniques: Instrumental methods

Instrumental methods include all the techniques to measure *"in situ"* surficial or deep displacements. The measurements can be lineal or angular and can be managed in one, two or three perpendicular directions.

The most used instruments for the subsidence monitoring are *extensometers, inclinometers and micrometers*.

3.1.1.1 Extensometers

Extensometers are truly common instruments for site-specific measurements of subsidence. However various typologies exist, only the rod and differential extensometers are described in the following, as they have been used for the measurements considered in the present thesis.

3.1.1.1.1. Rod extensometers

Borehole rod extensometers consist of anchors set at specified depths, rods inside to the protective pipe, and a reference head. Therefore, they are used to monitor the movements of "*measuring points*", permanently installed in the borehole at selected depths. The absolute deformation profiles is so determined by knowing the extensometer position respect to a fixed reference.

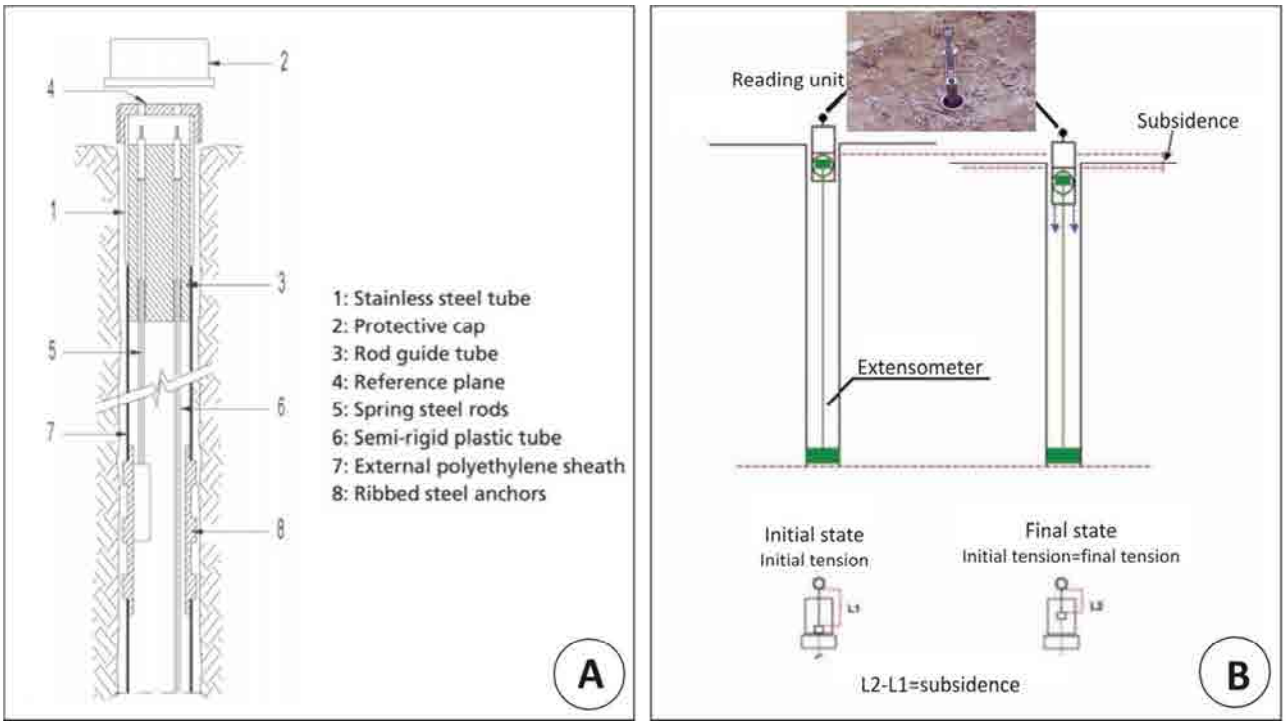

Figure 3.1. A: Rod extensometer (http://www.roctest.com); B: measurement principle (Mulas et al., 2010).

In particular, WR-FLEX boreholes extensometers (Fig. 3.1) have been used to monitor the subsidence in the metropolitan area of Murcia city. As showed in Fig. 3.1, the rod extensometer is constituted by a protective cap (2) from which a stainless steel tube (1) and a guide tube to the rod of the extensometer (3) start. The plain part of the cap is the reference basis on which the reading unit is installed. Anchors are spaced along a protective plastic tube, located at elevations at which displacement measurements are required. One end of a spring-steel measuring rod (5) is attached to the inner part of each anchor. In soft soils, mechanical leaf-spring anchors are used. The rods extend through the protective tube (6) and terminate within the head assembly. Rods and protective plastic tube are protected by an external polyethylene sheath (7) which is in contact with the casting cement that prevents system movements and blocks the steel anchors (8). The rods are free to move within the head assembly and the protective plastic pipe. As a relative displacement between the anchors and head assembly occurs, the location of rods free ends in the head assembly undergoes an equal shift. By measuring the displacement between the free ends of the head assembly (fig. 3.1b), the displacement of the anchors relative to the head assembly is obtained. Displacement can be measured either manually, using a depth gauge, or remotely, by converting the head in an electrical head assembly and installing linear potentiometer displacement transducers. Moreover, referred to figure 3.1b, a tensor and a micrometer have been used to measure rod deformations.

3.1.1.1.2. Differential extensometers

Instead, a differential extensometer is constituted by two deep anchored reference bases to control the movements.

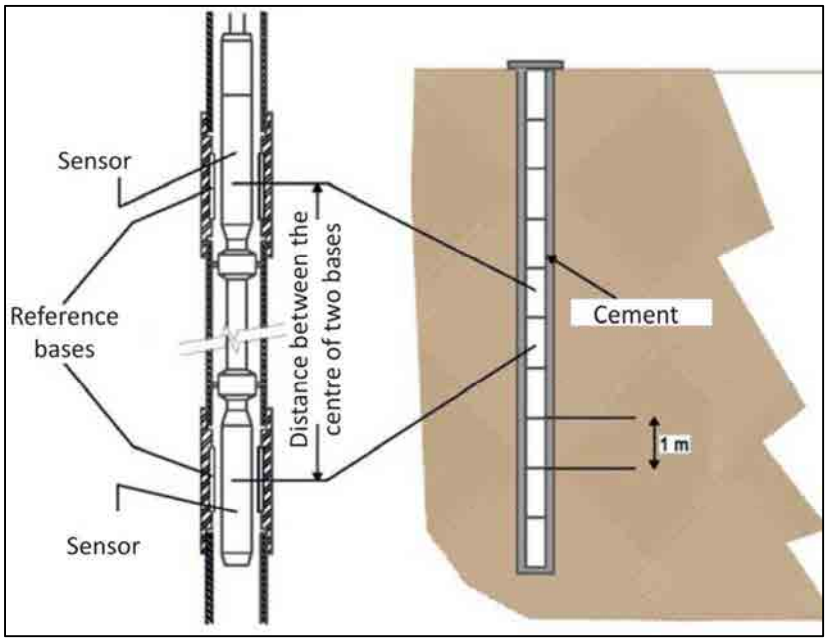

Figure 3.2. Differential extensometer (Mulas et al., 2010)

In addition to the rod extensometers, in Murcia city, differential extensometers having the scheme reported in figure 3.2 have been used. These extensometers are constituted by a probe, a reading unit and a PVC tube (of 1 m) having paramagnetic bases put up in the borehole.
The measures consist in introducing the probe into a PVC tube and align it to two consecutive bases. Since the inductive sensors for the displacement measurement in the probe are at an invariable distance, any variation of the distance between two consecutive bases is due to the ground deformation. This displacement is read as a variation of the magnetic field induced by the surface variation of the coil in the tube. Two steel rods (having a diameter of 12 mm) and a steel corrugated bar facilitate the anchorage in the soil through its cementation. Soil displacements are controlled through the length variations from the upper extremity of each rod up to the reference bases. The instrument used for these measurements is a digital micrometer (MITUTOYO) with a resolution of 0,01 mm.

According to Mulas et al. (2010) both types of extensometers provide measurements with 0.1 mm accuracy.

3.1.1.2. Inclinometers

Inclinometer surveys consist in the measurement of inclination variations respect to the vertical direction. They yield to evaluate the displacement direction (azimuth) and its components. Inclinometer can be fixed or mobile and the measurement configuration usually involves the use of an inclinometer probe in a cased borehole (fig.3.3a). The case of vertical displacement measurements is more rare and provide the employment of a horizontal probe (fig. 3.4), usually used to monitor the foundations displacements.

Inclinometric casing have four grooves which allow to keep in place the probe and to maintain constant the azimuth reference. The probe is constituted of a cylindrical body equipped with two carriages that can be inserted into the grooves. In the body probe, the servo-inclinometer sensor measures the inclination in the orthogonal plains 1-3 and 2-4 of figure 3.3b. In this way, it can furnish the angular measurement of soil real movements at different depths. During a survey, the probe is driven upwards from the bottom of the case to the top, blocked during its motion at 0.5 m intervals for tilt readings. The inclination of the probe body is measured by two force-balanced servo-accelerometers (which are inside the probe). One accelerometer measures the tilt in the inclinometer wheels plane, which track the longitudinal grooves of the casing. The other accelerometer measures the inclination in the plane perpendicular to the wheels. Inclination measurements are converted to lateral deviations, as shown in figure 3.3c. The obtained measurements are related to the initial reading (called *"zero reading"*), which consists of four cycles of measures in which the probe is rotated of 90° to minimize the systematic errors. Therefore, changes in deviation, determined by

comparing current and initial surveys, indicate ground movements. Through the numerical integration of the angular measurements carried out at different depths, it is possible to obtain horizontal and vertical displacements (fig.3.3c).

Casing is installed into sub-vertical holes embedded into the ground (up to the bedrock) and can follow the soil movement. The accuracy of the measurement is of the order of ± 0.02 mm for every 3 m depth.

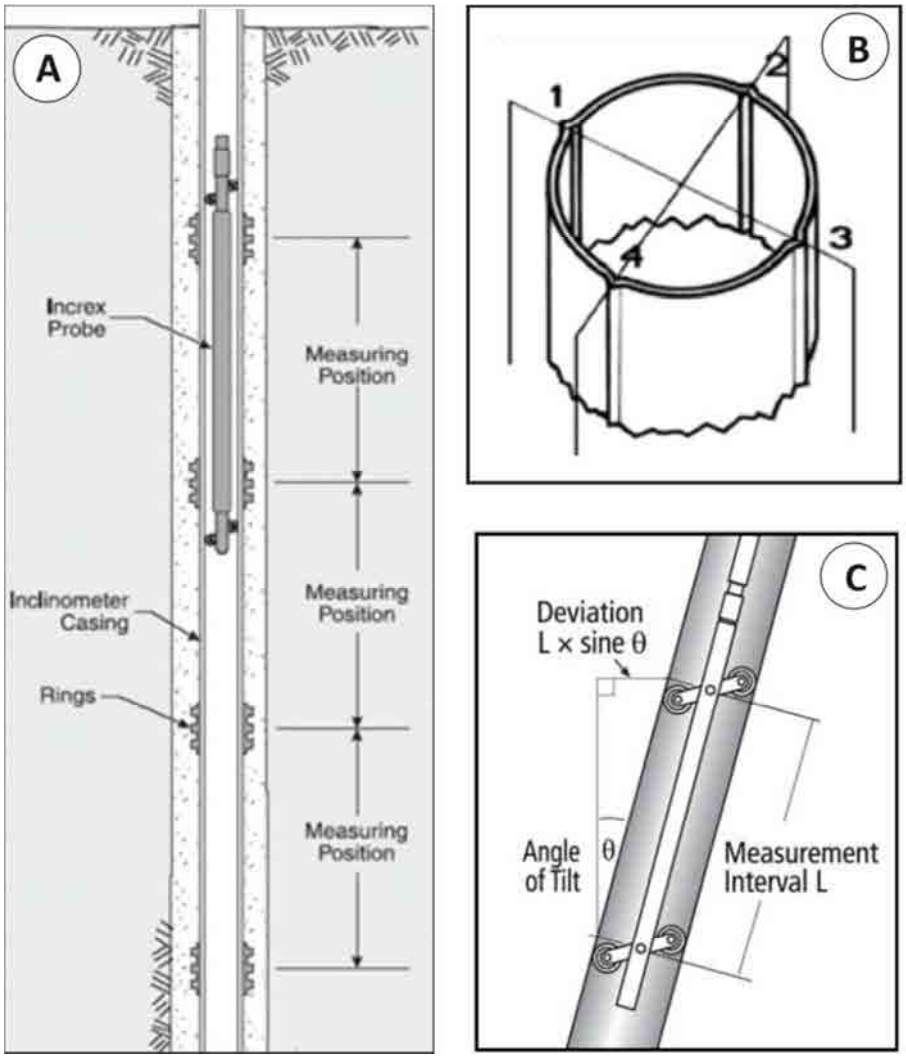

Figure 3.3: Inclinometer section (a); inclinometric groves (b); angular measurements (c); (http://www.howland.co.uk/)

Inclinometers are more frequently used to determine subsurface movement of landslides (Mihalinec and Ortolan 2008, Yin et al., 2008). They are installed in boreholes located within the landslide.

In the horizontal inclinometers case, casing is installed in an horizontal trench or borehole with one set of grooves alligned to the vertical direction. In this system, the carriages are constituted of two pairs of wheels; the first pair is fixed and the second one is swing and the probe is available only with high accurate

servo-accelerometer sensors. If the far end of the casing is not accessible, a dead-end pulley and cable return pipe are installed within the casing (fig. 3.4). Also in this case, a zero reading allows to estabilish the initial profile of the casing, while the subsequent surveys reveal changes in the profile if a ground movement occurs.

The servo-acelerometer in the probe allows to measure tilt in the plane of the probe wheels. Tilt measurements are usually achieved at half-meter intervals. In order to eliminate systematic errors, after the first measurement, the probe is reversed and driven through the casing a second time.

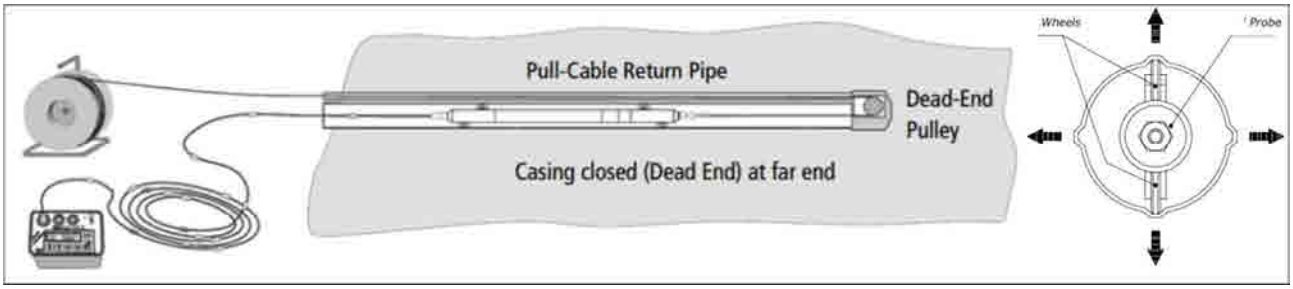

Figure 3.4: horizontal inclinometer (http://www.slopeindicator.com/)

Settlement and heave are calculated as $L(\sin(\vartheta_1)-\sin(\vartheta_0))$, where L is the measurement interval, ϑ_1 is the current tilt and ϑ_0 is the initial tilt. Settlemets profiles are generated by summing displacements and plotting them.

3.1.1.3. Micrometers

A sliding micrometer is a high precision strain meter to determine the complete distribution of strains and axial displacements along a measuring line in rock, concrete or soil. The axes of the measuring lines can have any arbitrary direction and this makes the micrometer a very useful tool to the subsidence monitoring and to facilitate the determination of the compressible layers. A measuring tube to accommodate the measuring probe, consisting of measuring marks and plastic connecting tubes, is grouted into a borehole and can follow the three-dimensional deformations free of hysteresis. It is a portable device to monitor the strain distribution along a straight line with an accuracy of measurement better than ± 0.002 mm/m.

Moreover, it has the advantage of being usually combined with a mobile inclinometer or with trivec surveys, which means that it can determine the three components of motion. In fact, Trivec measures the three orthogonal components *Δx, Δy, Δz* of the displacement vectors along the vertical measuring lines, while the Sliding Micrometer measures displacements along an arbitral direction. The accuracy of measurement of this system is of the order of ± 0.04 mm/m for the *Δx* and *Δy* measurements and of ± 0.002 mm/m for *Δz*.

The probe uses the ball-and-cone positioning principle (fig.3.5b) in the measuring marks of the measuring tube. This principle consists of a probe with a spherical shaped heads and measuring marks having the shape of circular cones. This guarantees the precise positioning of the 1 m long probe during measurement.

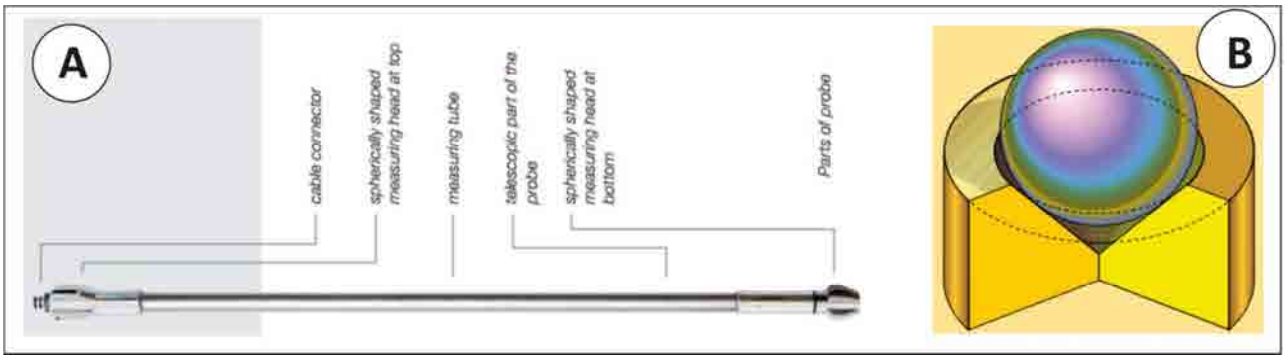

Figure 3.5: sliding micrometer (A); ball-and-cone positioning principle scheme (B); (http://www.epc.com.hk)

Another kind of micrometer is the fixed installable micrometer (FIM), used for the continuous measurement of stationary axial deformations in boreholes. Also the FIM is based on the cone-ball contact principle, like the Sliding Micrometer and the Trivec. Boreholes measuring lines, in which deformations measurements are already being registered with the Trivec can be fitted out from time to time with one or more FIM for further continuous data acquisition. For this purpose, the FIM can be temporarily inserted into the borehole between two measuring marks and connected to the data acquisition system.

3.1.1.4. Instrumental methods to the cracks monitoring

These instruments allow the monitoring of surficial cracks, which can be in soil or on a building. In both cases, it is important to analyse cracks geometry and propagation time, because they represent the consequence of an active phenomenon (i.e. a landslide or a subsidence). In case of presence of cracks on a building, their inclination and location can help to individuate, for example, a differential displacement as their cause. In this case, if they correspond to a structural failure, their monitoring and analysis allow to understand the risk grade as habitation.

The most simple crack monitoring consists in a piece of glass which is fixed through lime across the crack (fig. 3.6). If the glass is broken it is a proof that the crack moved. Nevertheless, this method allows only to visually understand where the cracks are increased but not to quantify their widening.

Another system to the structural crack monitoring is the so called *"Tell tales"* (fig. 3.6) which overcome this limit. It consists of two slips of overlapping plastic plates with a red cross on one and a marked grid on the other.

Once this monitor is fixed in position, an initial reading is taken. Then more readings are gotten at regular intervals to establish if the movement is occurring and if so, at what rate.

By comparing the different rates of movement for cracks at different locations in a building, the cause and location of the weakness can be established. The monitors should be left in the same place for as long as possible (because it doesn't get broken, being constitute of two separated parts) to establish whether the crack is moving or not.

In the present thesis, for some building affected by structural failures in the subsiding area of Telese Terme, these two simple methods have been used, inside and outside a building (figs. 3.6 and 3.7) that has been evacuated for the magnitude and the rapidity in the evolution of the phenomena.

Figure 3.6: glass cracks monitoring system (left); "tell tales" cracks monitoring system in Telese Terme (right)

At first, many glasses have been installed in March 2010, June 2011, April 2012 and January 2013 and always get broken (fig. 3.7) and some "tell tales" have been used (fig. 3.6-right).

A broad number of electrical gage types exists, but most of them are based on an arrangement of pins attached on opposite sides of a joint or crack, with the pins connected by sliding extension rods. Their relative differential movements are detected by a built-in transducer.

The most common transducer is the linear variable displacement transformer (LVDT) that consists of a movable magnetic core passing through one primary and two secondary coils.

Figure 3.7: example of cracks monitoring in Telese Terme

3.1.1.4. Crackmeter

Crackmeter is used to detect differential movement between two points. Anchors are typically installed on opposite sides of the crack (fig. 3.8). It can incorporate a displacement transducer mounted across the anchors. A change in the distance across the crack causes a change in the frequency signal produced by the displacement transducer if excited by the readout or data logger. The initial reading is used as a datum. Subsequent readings are compared to the previous datum to calculate the magnitude, rate, and acceleration of movement across the crack.

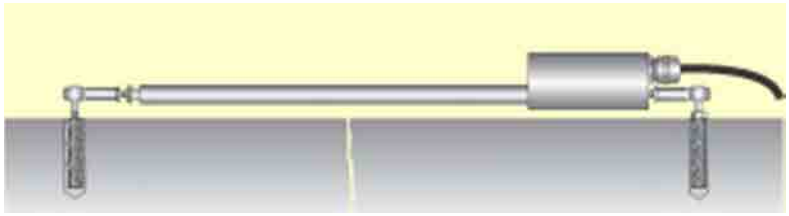

Figure 3.8: Crackmeter (http://www.slopeindicator.com/)

3.1.2. Remote sensing detection:

Remote sensing represents the technical–scientific discipline which allows to obtain quantitative and qualitative information about targets located far from a sensor, through measurements of the electromagnetic radiation (emitted, reflected or transmitted) interacting with the involved surfaces. Forty years of progresses in the sensors technology and in developing an always higher number of tools, able to observe the environment in different spectral bands, have considerably improved the effectiveness of the Earth observation through these techniques. In fact, in addition to the passive sensors, which measure the energy emitted by an external source and reflected by the observed target, there exist the active ones which generate electromagnetic waves, illuminate the scene and detect the backscattered signal. The first ones allow a qualitative observation of an area, exploiting mainly optical data; in this case the electromagnetic energy is characterized by wavelengths belonging to the visible up to the infrared in the electromagnetic spectrum (Fig. 3.9).

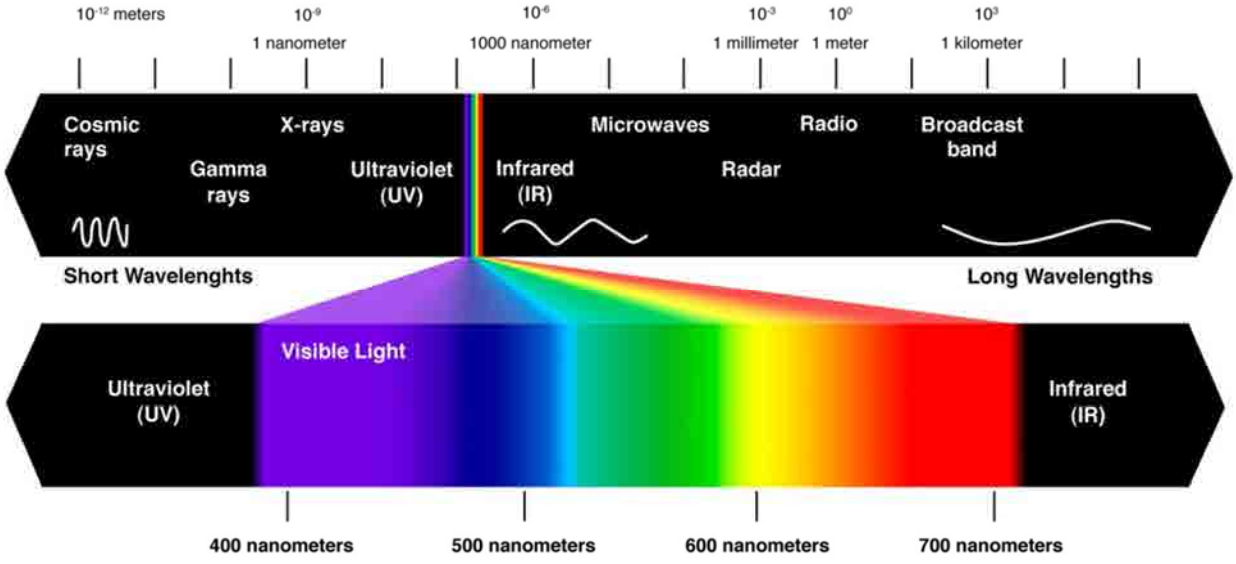

Figure 3.9: electromagnetic spectrum

In particular, it is possible to distinguish non-imaging passive sensors which are microwaves radiometers or magnetic sensors from Imaging ones which are cameras, optical mechanical scanners, spectrometers, microwave radiometers). On the other hand, active sensors yield to quantitative information of an observed phenomenon, working with the wavelengths reported in table 3.1 (especially with the L, C or X bands). Moreover, radars are active sensors which use electromagnetic waves in the radio wavelengths and determine the distance of an object (registering the two-way travel time of the pulse) and its physical properties, measuring its backscattered intensity.

On account of this, among the remote sensing techniques there are the *topographic levelling, the photogrammetric, the laser and radar techniques*.

Each technique can be classified respect to the platform where the instrumentation is gotten on.

Photogrammetry, for example, can be distinguish in *terrestrial, aerial and satellite*.

In the same way, among the laser techniques, they can be found the Terrestrial Laser Scanner (if it is on a terrestrial platform) or LIDAR, ALS and ALTM, if on an aerial platform.

To the radar techniques belong the Ground Based Synthetic Aperture Radar, GB-SAR (which is a terrestrial radar), the Airborne Radar (on aerial platform) and Spaceborne Radar (satellite platform).

3.1.2.1. Topographic conventional methods

The term topography includes all the techniques of earth cartography, traditionally used by surveyors to monitor and quantify land surface deformations.
Starting from topographic basis, which are points having known coordinates, those ones for the monitoring points (called "*control points"*) at the beginning of the monitored period (x_0, y_0, z_0) have to be achieved. After that, reference system variation components are performed, measuring the control points x, y and z changes [$dx(t_i)$, $dy(t_i)$, $dz(t_i)$] in different times (t_i).

Topographic methods can be divided in *altimetric* and *planimetric*.

The first ones, allow to obtain the control points height variations respect to a reference horizontal surface (usually the sea surface).
In particular, optical levelling is a traditional surveying technique for determining the elevations of points on the Earth's surface relative to some starting point or height datum. Surveyors place points or monuments, referred to as "*benchmarks*", in or on the ground, and make repeat measurements over a certain period of time to measure changes in height. The used instrument is the optical level. Generally mounted on a tripod, the optical level enables the observer to sight along a horizontal line, perpendicular to the local gravity vector. By reading the height of benchmarks below this horizontal line, using a precise ruler commonly known as a "staff", the relative heights of different benchmarks can be determined. By repeating this process in a leapfrog manner and adding up all the differences in height, the total difference in height between two distant points can be calculated. If the first point is a tide gauge or a benchmark

where Mean Sea Level height has been previously established, then all the points measured in the survey will have known heights above Mean Sea Level.

Appling the planimetric topographic method results in obtaining the horizontal projection of the control points which are defined through their cartographic coordinates (x, y). The most important are the intersection methods which consist into the determination of the coordinates of the vertex of a triangle, knowing the other two vertexes coordinates and the geometric characteristics.

Depending on the topographic used technique, the height measures accuracy can vary between ±0.1 mm/Km (achievable with the precision geometric levelling) and 20 mm of the trigonometric levelling. However, they are labour-intensive and best suited to small regions only.

Using a *Total Station*, measurement of distance is accomplished with a modulated microwave or infrared carrier signal, generated by a small solid-state emitter within the instrument's optical path, and reflected by a prism reflector or the object under survey. The modulation pattern in the returning signal is read and interpreted by the computer in the total station. The distance is determined by emitting and receiving multiple frequencies, and determining the integer number of wavelengths to the target for each frequency. This technique reaches to very accurate results, the angles are measured with a precision of 1'' while distances with a standard mode, with a precision of 1 mm + 1.5 ppm. Depending on weather conditions (temperature, humidity and pressure), that influence the resulted accuracy, this instrument allows measurements on very long distances, up to 3 km.

3.1.2.2. Geodesic methods

Geodesy is the scientific discipline that deals with the measurement and representation of the Earth, including its gravitational field, in a three-dimensional time-varying space. It reconstructs the Earth shape through points distributed on its surface, called geodesics; furthermore, it permits to know the coordinates of their projection on the earth reconstructed surface, as the same as their height upon see level (geoid). In the last century, a new branch of this discipline, called Spatial Geodesy, revolutionized the earth observation systems.

Among the various techniques of the Spatial Geodesy, the principal are the **GPS (Global Positioning Systems)** and the **DGPS (Differential Global Positioning Systems)**. They consist in a radio-location system that, through connections established with some satellite constellations, yield to the three-dimensional coordinates of the points. GPS systems allows to perform both occasional, repeated over time, and real-

time measurements, allowing studies both in small and large scale. The main advantages, with respect to the terrestrial instrumentation, are the possibility to work in any condition of visibility and weather. It is nevertheless required a certain satellite "visibility" from the monitored points. As referred by Di Martire, (2013), several experiments conducted in the field of monitoring of surface deformation estimated an error of about ± 5 mm for ranges of 50 km in diameter in the absolute positioning of the point. While, as far as the evaluation of displacements is concerned, they are characterized by a standard deviation of about 3 mm for the horizontal component and 1.5 times the horizontal to the vertical. To achieve the measure, the minimum number of satellite constellation to which the system has been connected is 4, with a maximum of 12 upon the horizon.

Figure 3.10: GPS sensor

Differential Global Positioning System (fig. 3.11) provides an increment in the precision achievable through the classic GPS, based on a reference station located on the earth having a known position (B2). In this way, systematic errors in B1 movement computation are corrected.

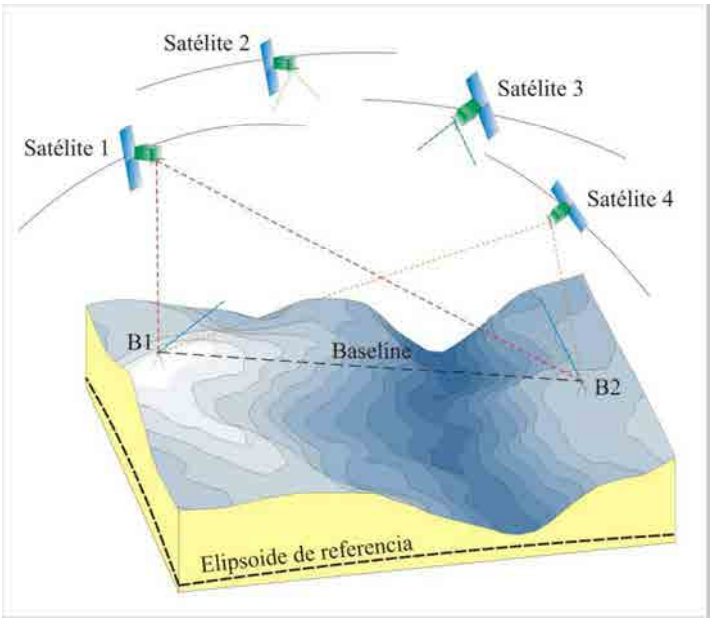

Figure 3.11: Differential Global Positioning System scheme (extract from Tomàs, 2009)

As referred by Tomás, (2009), GPS techniques have been efficaciously used to subsidence monitoring in several case studies, like Wegmüller et al 1999; Strozzi et al., 2003; Sato et al., 2003.

3.1.2.3. Photogrammetric methods

Photogrammetry is a technique employed to obtain a three-dimensional scene through its acquisition by couples of photos, having a different capture angle, called photograms. Among the various techniques, for the "*Aerial Photogrammetry*" the camera is mounted in an aircraft and is usually pointed vertically towards the ground. Multiple overlapping images (in the visible spectrum) of the ground are taken as the aircraft flies along a flight path. These photos are processed by an instrument that lets an operator see two photos at once in a stereo view called stereo-plotter. These photos are also used in automated processing for Digital Elevation Model (DEM) creation. Comparing DEMs obtained for the same study area in different times, is possible to obtain the occurred changes but with a bad resolution (±100 mm).

3.1.2.4. Radar remote sensing techniques

Radar (*RAdio Detection And Ranging*) is an active remote sensing system operating at the microwave wavelength. The sensor transmits a microwave (radio) signal, (specifically in the frequency interval from 40.000 to 300 megahertz (MHz) of the electromagnetic spectrum) towards a target and detects the backscattered radiation. The strength of the backscattered signal is measured to discriminate between different targets and the time delay between the transmitted and reflected signals determines the distance (or range) to the target. The latter frequency extends into the higher frequencies of the broadcast-radio region.

Commonly used frequencies in radar remote sensing and their corresponding wavelengths are specified by a band nomenclature, as reported in Table 3.1

Band	Frequncy (MHz) f	Wavelength λ (cm)
Ka band	40000-26500	0.8-1.1
K band	26500-18000	1.1-1.7
Ku band	18000-12500	1.7-2.4
X band	12500-8000	2.4-3.8
C band	8000-4000	3.8-7.5
S band	4000-2000	7.5-15.0
L band	2000-1000	15.0-30.0
P band	1000-300	30.0-100.0

Table 3.1: Microwave bands (Frequncy and Wavelength) commonly used in radar remote sensing

In particular:

- **Ka**, **K**, and **Ku bands** are characterized by very short wavelengths; in the last years the K-band is also used for Ground Based SAR;
- **X-band** is used extensively on satellite (TerraSAR-X-1, COSMO-Skymed) and airborne systems for military terrain mapping;
- **C-band** is common on many airborne research systems (CCRS Convair-580 and NASA AirSAR) and spaceborne systems (including ERS-1/2 SAR, RADARSAT-1/2, ENVISAT ASAR,RISAT-1);
- **S-band** is used on board the Russian ALMAZ-1 satellite;
- **L-band** is used on-board ALOS PALSAR, American SEASAT and Japanese JERS-1 satellites and NASA airborne system;
- **P-band** has longest radar wavelengths and is used AIRSAR satellite on NASA experimental airborne research system.

The advantages respect to optical remote sensing can be synthetized in the following points:

→ all weather capability (small sensitivity of clouds, light rain)
→ day and night operation (independence of sun illumination)
→ no effects of atmospheric constituents (multitemporal analysis)
→ sensitivity to dielectric properties (water content, biomass, ice)
→ sensitivity to surface roughness (ocean wind speed)
→ accurate measurements of distance (interferometry)
→ sensitivity to man-made objects
→ sensitivity to target structure (use of polarimetry)
→ subsurface penetration

In the development of the radar technology, a considerable limitation was represented by the achievable resolution of the pixels that did not allow the applicability of simple radar sensors on satellite platforms to the displacement measurements. This limitation was overcome through a Synthetic Aperture Radar, in which signal processing is used to improve the resolution beyond the limitation of physical antenna aperture. This innovation changed the possibilities in the remote sensing application, because these instruments, using microwaves, are not affected by the presence of clouds and could achieve measures 24

hours a day obtaining radar images of wide area. Furthermore, during the last twenty years many satellite constellations have been launched. Among them, ERS1/2 and ENVISTAT ASAR (European Space Agency), JERS-1 SAR (Japanese Aerospace Exploration Agency), RADARSAT-1/2 (Canadian Space Agency), TerraSAR-X and TanDEM-X (Infoterra (Germany)), and COSMO-SKYMed (Italian Space Agency) can be mentioned (Fig. 3.12).

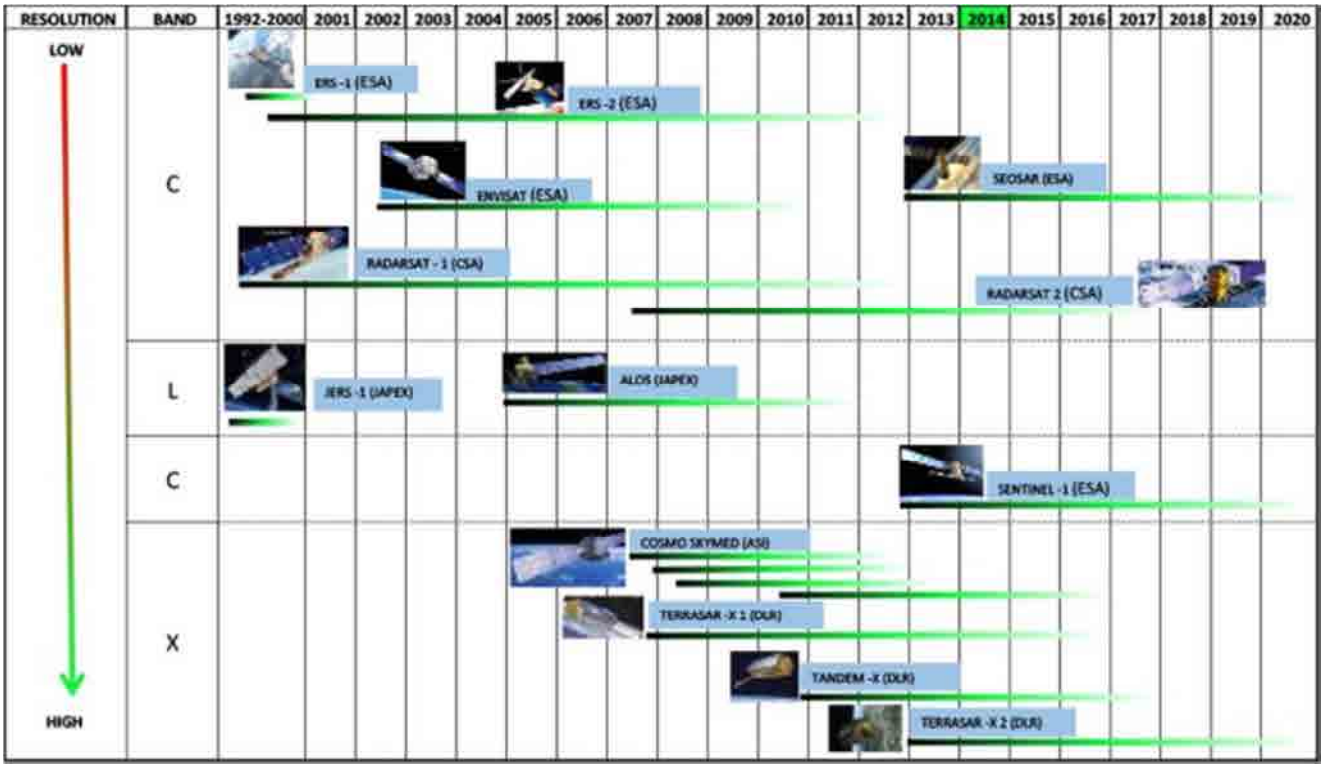

Figure 3.12: Temporal schedule of the most important SAR missions (modified from ESA)

The great amount of SAR images has so guaranteed the improvement of research studies in algorithms implementation for their processing, reaching a very high precision in the natural hazard assessment. SAR techniques can also be classified respect to the algorithm used to the images processing in Conventional and Advanced Differential Interferometric SAR techniques (which will be treat in the chapter V).

Among the radar remote sensing techniques, there are the *Ground Based Synthetic Aperture Radar*, GB-SAR (terrestrial radar), the *Airborne Radar* (aerial radar) and the *Spaceborne Radar*.

3.1.3.4.1. GB-SAR

Ground based radar with synthetic aperture and interferometric technique (GBInSAR) is an innovative type of remote detection that furnishes a very accurate movement measurement of the ground over large areas. It employs a combination of devices and methods that can generate raster maps of two-dimensional deformations (and/or velocity) of a slope irradiated, from a remote location, with electromagnetic waves covering an area of several square kilometers and obtaining a sub-millimetric precision (equivalent or even better than traditional topographic and geotechnical instrumentation). The output maps are made up by thousands or tens of thousands of pixels, each with its own time series of displacement. Various reasons make GBSAR an attractive device: it provides displacement measurements with sub-millimetric precision on areas large up to a few square kilometers; it acquires images with "high" frequency; it has a ground resolution of a few meters and it is able to monitor also relatively fast movements. This large amount of information and the spatial distribution of data are typically useful for understanding the phenomena, for real time monitoring, and, finally, for the decision-making process. Periodic monitoring of landslides phenomena with GBInSAR represents a promising approach for the long-term evaluation of instability conditions, especially in those areas where property and infrastructure are exposed to risk. It is effectively used in the subsidence monitoring (Pipia et al., 2007a; 2007b).

3.1.3.4.2. Airborne Radar

Also in this case, it is constituted by an active radar and is mounted on a plane. The problems related to this technique are due to the difficulty in eliminating the errors phase contribution due to atmospheric turbulence. The backscattered signal time, in fact, provides the target position, function of that of the plane which is not stable like the satellites ones. In the last years, the research development also in this field, has permitted to focus SAR images acquired on planes, (as showed in several publications like Perna et al., 2013) which, thanks to the littler distance from the target respect to that of satellite platforms, corresponds to an high pixel resolution.

In addition to the radar remote sensing technique, there are the laser ones and, in particular, Airborn Laser scanner represented a very useful tool to the subsidence monitoring (Bock y Tom, 2001; Oppikofer, 2008; Travelletti et al, 2008).

CHAPTER IV

Radar remote sensing techniques

Chapter IV. Radar remote sensing techniques

4.1. Introduction: Radar acquisition geometry and images characteristics

As introduced in paragraph 3.1.2.4, radars are active sensors which use electromagnetic waves in the radio wavelengths. Radar acquisition geometry is represented in Fig. 4.1.

According to this scheme, the projection of the spacecraft orbit on the Earth surface is known as *ground track* or *sub-satellite track* and *Nadir point* represents the radar position projected on the ground. The SAR sensor, housed on carrier (aircraft or spacecraft) platform, usually points perpendicularly to the flight direction, along the so called *across-track* or *ground range* direction. Taking into account the image 4.1b (Chan and Koo, 2008), radar beam enlightens (with a certain inclination respect to the *nadir* direction) a portion of the earth surface, called *swath*. In the case of Fig. 4.1b, the swath width is the distance between the points A and B. The distance between a point (within the swath area) and the radar is called its *slant range* and that between a point (within the swath area) from the nadir point is called its *ground range* (ESA glossary). The perpendicular line to the trajectory orbit and the look line form an angle called *look angle*. A satellite can observe the same area from slightly different look angles. This operation can be made with the help of two sensors applied on the same platform (for instance the NASA SRTM mission), or in different periods with the aid of images captured on different satellite orbits. Satellites cover ascending and descending orbits and traditionally an area can be enlightened from East during descending orbits (from North to South) or from West during ascending ones. New satellites, like COSMO-Skymed, can now acquire images at both right and left side of the satellite ground track.

Targets on the Earth surface (on the *ground-range plane*) backscatter the pulse allowing the identification of their position and physical quantities (through the detection of the two-way travel time of the pulse and its intensity). Specifically, the emitted pulse having a duration τ, covers a distance R_0 to reach the target. The backscattered radiation will reach the satellite after a delay $t_r = 2R_0/c$ from its emission (where c is the speed of light).

In particular, the returning echoes of the energy pulses providing information on:

- → *target distance* (time interval between pulse emission and return from the object)
- → *phase*
- → *magnitude*
- → *polarization*
- → *Doppler frequency*

Radar images are pixels matrices where, to each of them, is associated a value of the phase and the amplitude relative to the wave emitted by the antenna and backscattered from the targets. The targets detected information are projected in the sensor's acquisition plane, namely in the *slant-range plane*.

The two types of imaging radars most commonly used are the Real Aperture Radar (RAR) and the Synthetic Aperture Radar (SAR) which are *side-looking* systems with an illumination direction in the ground range one as shown in Fig. 4.1. This means that they enlighten just a side of ground range.

RAR (also called Side Looking Airborne Radar, SLAR) and SAR, differ in the resolution along the direction of the satellite's movement (the so called *along-track*, or *azimuth direction*).

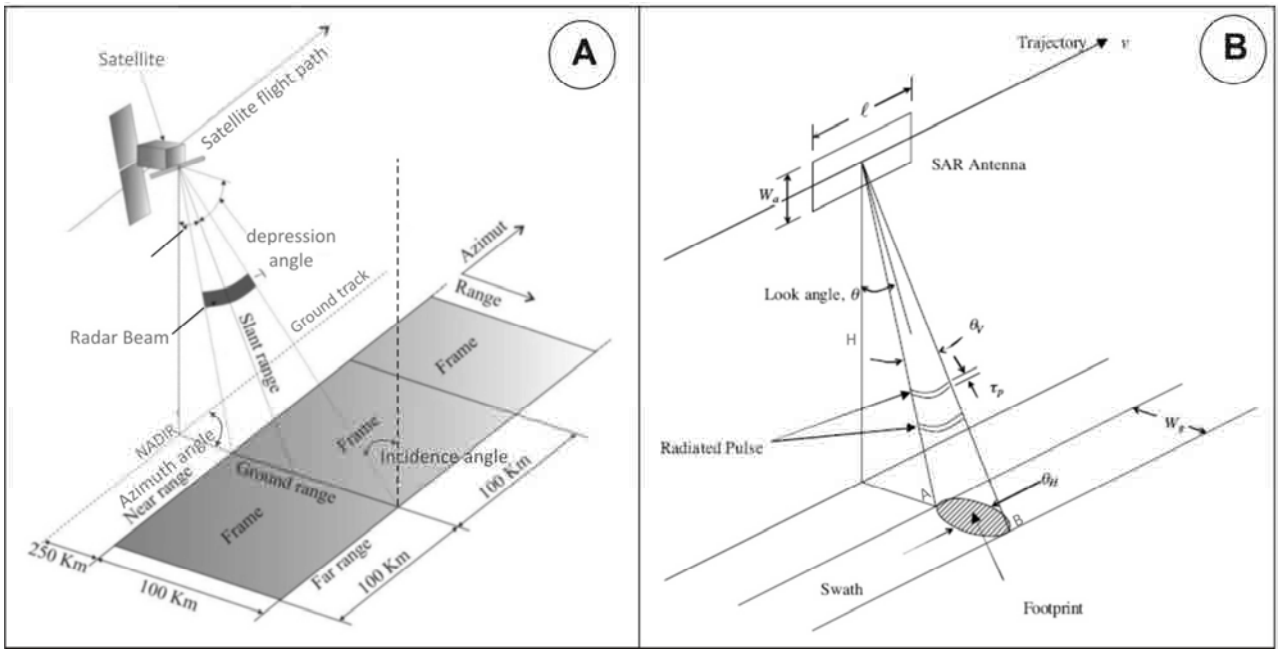

Fig. 4.1: radar acquisition geometry (image credit: NASA/JPL)

Real Aperture Radars have an azimuth resolution determined by the antenna beam-width, so that it is proportional to the distance between the radar and the target (*slant-range*).

Ground range resolution (R_g) is defined as the capability of the sensor to detect two targets on the ground.

It is function of the pulse duration of the transmitter (t_p) and of the incidence angle (also called "look angle", θ), but it is independent from the carrier height (eq. 4.1).

To improve range resolution, radar pulses should be as short as possible, but, at the same time, their amplitude has to be increased; in fact they have to transmit enough energy to allow the detection of the backscattered signals.

The building of a similar equipment, which transmits a very short, high-energy pulse, is very difficult.

In practice, chirp signals are used as they are long in time but also long in frequency (*bandwidth*, B). They can be compressed during the data processing step and thus provide a resolution which depends on the transmitted bandwidth.

Therefore, R_g can also be expressed in function of B; see eq. 4.1.

$$R_g = \frac{c \cdot t_p}{2sin\theta} = \frac{c}{2Bsin\theta} \quad (4.1)$$

The Incidence angle represents the angle between the vertical to the terrain and the line going from the antenna to the object (Fig. 4.5).

The azimuth resolution is the minimum distance on the ground in the direction parallel to the flight path of the platform by which two targets (at the same range) must be separated in azimuth to be distinguished by a radar set. It is equal to:

$$R_a = \frac{H \cdot \lambda}{l \cdot cos\theta} \quad (4.2)$$

where λ is the wavelength of the transmitted pulses, *H* is the height of the antenna (height of the airplane), is the geometric length of the antenna and θ is the look angle

This equation states that the azimuthal resolution decreases with the altitude (H) increase. Only to have an order of magnitude of the azimuthal resolution achieving through a RAR system, considering the following values: λ = 1 cm, *l* = 3 m, *H* = 700 km, θ = 23°, the dimension of the pixel on earth results to be of about 2.5 km along the satellite orbit direction.

For this reason RAR systems cannot be used on satellite platform to the displacements assessment because to obtain a good resolution from a satellite, a very long antenna would be required.

In the development of the radar technology, *Synthetic Aperture Radar (SAR)* represented the innovative solution to this limit.

4.2. Synthetic Aperture Radar

Synthetic Aperture Radar (SAR) is a radar which uses signal processing to improve the azimuthal resolution overcoming the limitation of physical antenna aperture (Curlander et. al., 1991). In other words, SAR "*synthesizes*" a very long antenna playing on the forward motion of the physical antenna , in particular, by operating on a sequence of signals recorded in the system memory.

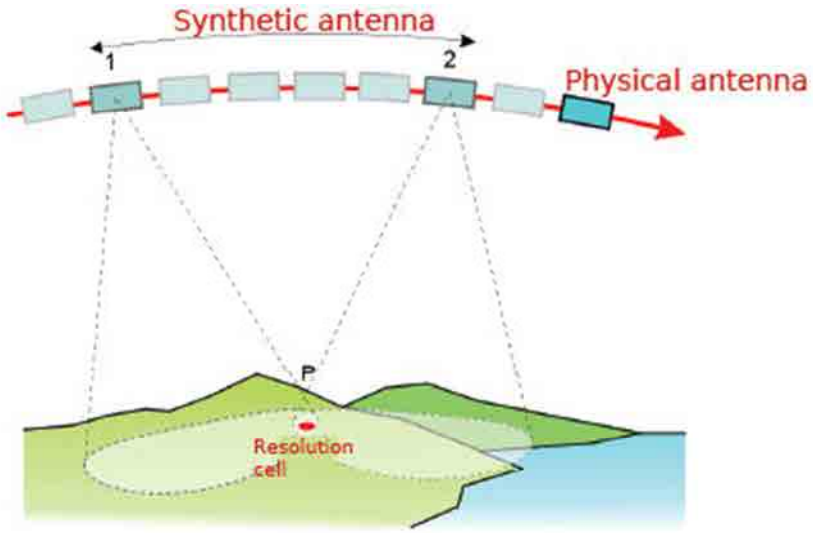

Fig. 4.2: Synthetic Aperture Radar

In an instant t_0 the radar beam starts "enlightening" a point P. The SAR transmits a series of waves that, from an initial time t_1 to an instant t_2, beat P (Fig. 4.2). During this interval, the real antenna (having an aperture D) occupies a series of positions from which sends a pulse to the target.

Considering Fig. 4.3, the real antenna defines, along the direction of the azimuth, a synthetic one L_s which can be expressed as:

$$L_s = \frac{\lambda}{D} \cdot h \tag{4.3}$$

where *h* is the satellite height.

The azimuth resolutionΔL_s, can be calculated as the following:

$$\Delta L_s = \beta_s \cdot h = \frac{D}{2} \tag{4.4}$$

where β_s is the angular resolution, equal to:

$$\beta_s = \frac{\lambda}{2L_s} \tag{4.5}$$

These systems have azimuth resolution that, differently from the RAR, is independent from the distance between the antenna and the target.

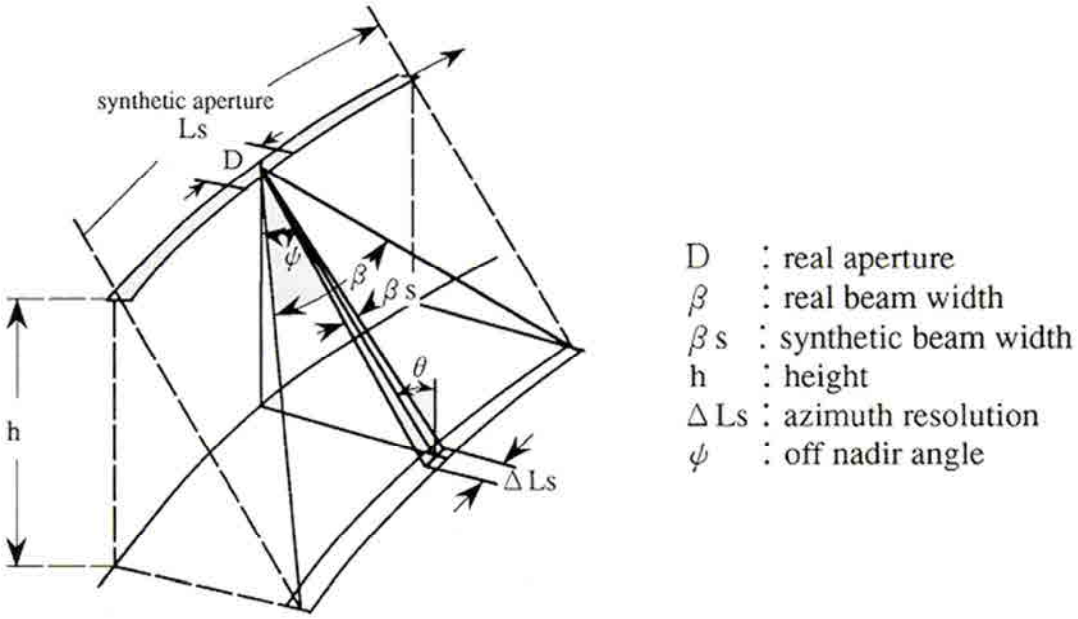

Fig. 4.3: Relation between real aperture and synthetic aperture radar (http://www.wtlab.iis.u-tokyo.ac.jp)

This innovation changed the possibilities in the remote sensing application, because these instruments, using microwaves, do not feel the effect of clouds and could achieve measures 24 hours a day obtaining radar images of wide areas.

It is important to describe how SAR data are recorded. Radar pulses, sent out by the radar, are scattered upon contact with the earth's surface. The way in which the energy contained in the pulse is distributed is known as *scattering mechanism*. A radar can only measures the energy scattered back towards it, (i.e. the backscatter) which will depends on the scattered surfaces characteristics, the pulse incidence angle and the frequency band used.

In this regard, according to the Fig. 4.4, it is possible to define two angles: the local incidence angle (α) and the incidence angle θ (Fig. 4.4).

They represent the angle between the radar beam and, respectively, the local normal to the surface and the vertical to the Earth surface. It is evident that the local incidence angle is subjected to some changes according to the ground slope.

Considering the Fig. 4.4 , when an electromagnetic wave is scattered from a point on the ground *P(x,y)*, the features of the ground cause changes both in the angular phase *φ(x,y)*, and in the amplitude *A(x,y)* of the electromagnetic wave. After the focusing process, the SAR image is complex.

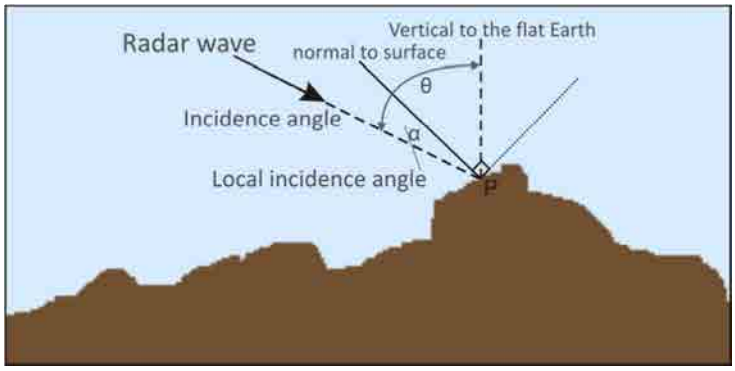

Fig. 4.4: The relationship between radar incident angle, true vertical, and local slope angle (after Henderson and Lewis, 1998).

The amplitude, which represents the modulus, depends on the scene reflectivity (to the "*backscattering coefficient*" as described below) while its phase is proportional to the two-way distance from satellite to ground and therefore to the geometry of the scene.

It is possible to introduce three principal scattering mechanism (Fig. 4.5) in function of three surfaces:

- *Smooth surface*
- *Rough surface*
- *Double-bounce and triple-bounce*

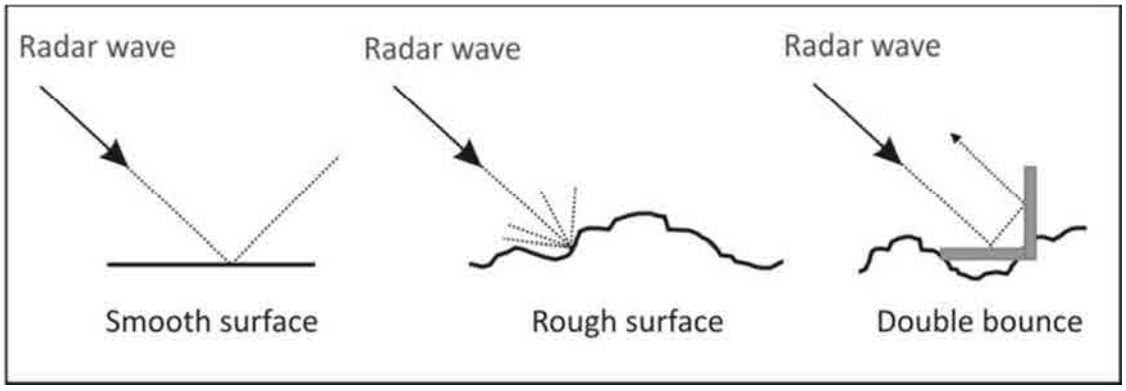

Fig. 4.5: Scattering mechanisms

The rough surface mechanism differs from the smooth surface one because its scatter occurs in all the directions. Some fraction of the energy of the transmitted pulse is reflected back towards the radar. In the smooth case, the backscattered energy can be very high if the surface is almost orthogonal to the beam, but, as in the case in Fig. 4.5, it can also occur that a very small fraction of the energy in the transmitted pulse is reflected back towards the radar. As it possible to note in Fig. 4.5, a smooth surface generates a dark pixel in the SAR image since all the power is reflected in the specular direction, i.e. the foreword one.

The third type of scatter is the so called double-bounce. In this case, most of the power is backscattered towards the sensor. The double-bounce backscatter will tend to be fairly high and will appear bright in the radar image. Double-bounce scattering occurs commonly in urban areas, where there are plenty of vertical surfaces (the sides of buildings) and horizontal surfaces (sidewalks, streets). It represents also the mechanism on which are based the *"Corners Reflectors" (double or triple bonce)*; these represent artificial reflectors which influence the scattering mechanism, the radar geometry acquisition (incidence angle) and the slope geometry (local incidence angle, or local slope). An example of their effectiveness, demonstrated by several studies (Sarabandi et al., 1995, Xia et al., 2004, Ferretti et al, 2007, Doerry, 2008, Di Martire et al., 2013) has been reported in Fig. 4.6; moreover, they are very cheap and simple to install.

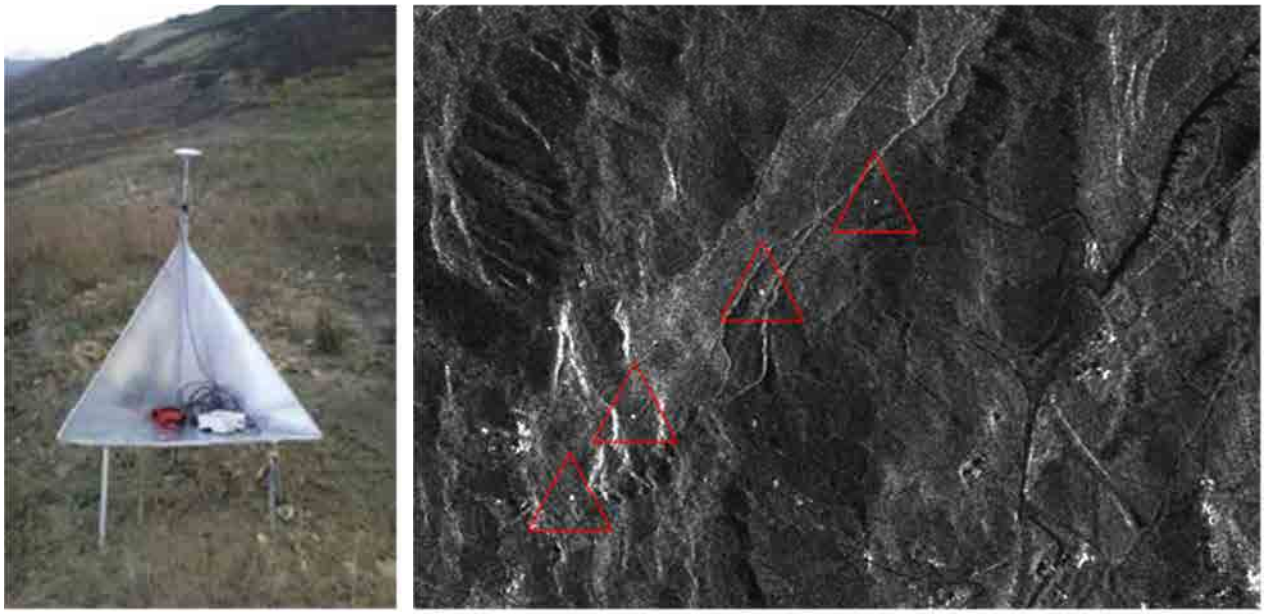

Fig. 4.6: Corner reflector installed in Agnone (Isernia province, Italy) on the left; example of reflectivity increase using the corner reflectors on the right (Di Martire PhD thesis, 2013)

In the following paragraph are described the factors that influence the radar backscattering and contribute to the distortion of the images. These factors include:

- Changes in the attitude, velocity and altitude of the sensing platform.
- The forward motion of the platform which causes scan skew.
- The radar oblique viewing geometry
- The geometry of the images, affected by the earth's rotation, its curvature and atmospheric refraction.
- Sensor "noises", due to poor calibration between detectors, to the atmosphere (e.g. presence of aerosols and scattering effect) and to the scene itself (e.g. effect of relief on reflection and type of reflection of the object).

All these parameters have to be taken into account for a preliminary analysis that is necessary to choose the best system to use; in fact it has to be chosen in function of the phenomena to observe. In particular, it is very important to analyse the geomorphological settings of the study area, the presence of vegetation, the scene aspect respect to the satellite *line of sight (LOS)*, the presence of building, etc.

This allows a correct use of the SAR system, which represents a useful tool in the natural risk mitigation if used expertly, namely knowing the limitations related to the SAR images acquisition and following processing.

4.3. SAR limitations: parameters affecting radar backscatter and distortions

4.3.1. Parameters affecting radar backscatter

The backscatter response of microwave energy is a complex mix of a variety of influences: surface roughness, dielectric constant, penetration depth, subsurface features, presence of liquid water, frequency, azimuthal modulation, viewing geometry (incidence and local angles, Fig. 4.6), surface slopes, fan-beam, etc.

According to Jensen, (2000), the strength of the signal received by RADAR antenna for a given ground resolution cell (represented by the so called *"radar backscatter coefficient"* σ°) is mainly a function of the wavelength of the microwave energy, the characteristics of the imaged feature, and the geometry of the image acquisition.

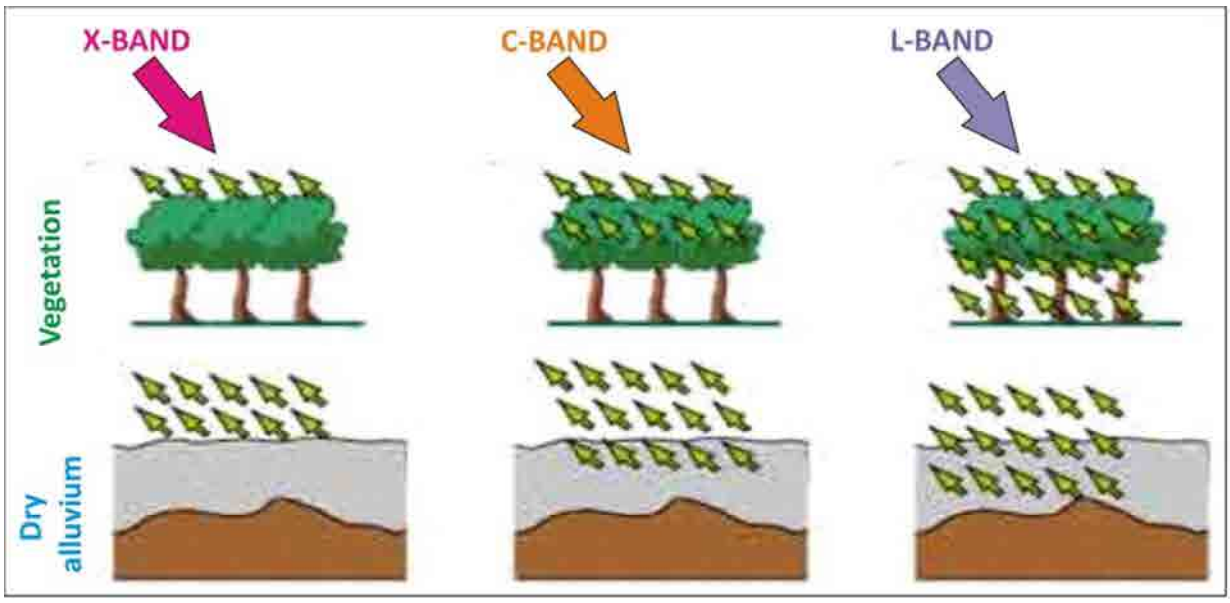

Fig. 4.7: Radar backscattering (http://www. earth.esa.int)

This means that the parameters which influence the radar backscattering regard the emitted waves and the enlighten surface characteristics.

Specifically, the radar observation ones are the frequency f, the polarisation p and the incidence angle of the electromagnetic waves emitted, while the surface parameters are the roughness, the geometric shape and the dielectric properties of the target.

→ *Frequency of the incident radiation:* the penetration depth for the target imaged results longer with longer wavelengths and the relative roughness of the interested surface.

→ *Moisture and water content of the target*: the electromagnetic wave penetration in an object is an inverse function of water content and microwaves can penetrate water only for few millimetres. In the case of vegetation or dried soils, penetration depth strongly depends on moisture (in the vegetation case, also on density and geometric structure of the plants). In particular, to a moisture increase, corresponds the increase of radar reflectivity due to the important variation of the natural materials dielectric properties.

→ *Polarization*: the penetration depth varies with the chosen polarization. This parameter describes the orientation of the electric field component of an electromagnetic wave. The polarization configuration most frequently used are the “linear” (HH, VV, HV, VH, where X stands for X-band, H for transmit, and V for receive). The first term corresponds to the polarization of the emitted radiation, the second term to the received one.

→ *Roughness and incidence angle:* the influence of these two parameters on the radar backscattering is not independent. In fact, roughness is a relative concept which depends on wavelength and incidence angle. A surface is considered "*rough*" if, according to the Rayleigh criterion, results $h > \lambda/cos\theta$ (where *h* is the mean height of surface variations); that is to say if its surface structure has dimensions that are comparable to the incident wavelength. In some cases, has been demonstrated Ulaby et al., 1982 that the roughness of the field can make the backscattering almost independent from the local incidence angle (fig. 4.7).

The synthesis of all the parameters influence, make that different surface features exhibit different scattering characteristics; for example, the urban areas are characterized by a very strong backscatter, the forest an intermediate backscatter, the calm water (having a smooth surface) a low backscatter.

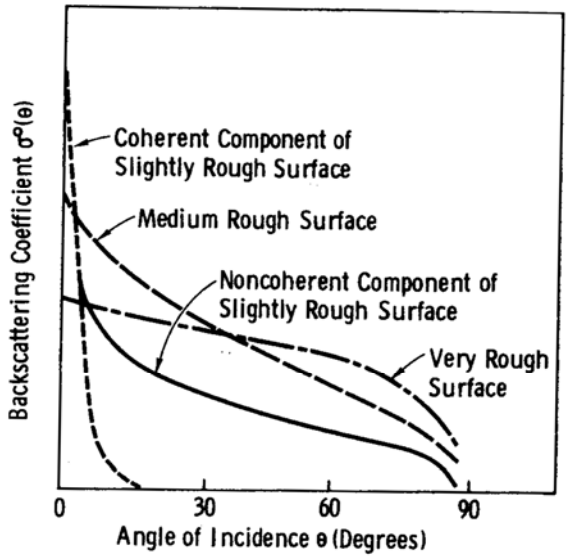

Fig. 4.8: Angular variation of backscatter for different roughness conditions (Ulaby et al., 1982)

4.3.2. Distortions

Radiometric distortions

Radiometric distortions represent an error which influences the radiance or radiometric value of a scene element (pixel).

These are due to the:

- *System characteristics and illumination geometry*
- *Interactions between radar signal and atmosphere*
- *Sensor failures or system noise*
- *Terrain which influences radiance*
- *Seasonal changes (which affect radiometric values)*

Principal distortions are *speckle noise* which is caused by coherent radiation used by radar systems; it occurs because each resolution cell, associated with an extended target, contains several scattering centres whose elementary returns, by positive or negative interference, originate light or dark image brightness.

This means that the energy registered by the sensor can come from several objects whose backscattering

energies are combined together.

In fact, as said above, SAR image is complex where the amplitude, which represents the modulus, depends on the scene reflectivity while its phase depends to the target distance and to the scene geometry. The amplitude image usually allows to distinguish the structures (houses, rivers, rock formation, …) which are in the picture; also if they are extremely speckling, can be easily interpreted. On the contrary, the phase image is affected by interference among waves coming from the different objects which cannot be distinguished inside the pixel. If in a pixel are k discrete scatters in a pixel, the return signals to be amplified or weakened according to the related phase. In fact results:

$$Ae^{i\varphi} = \sum_{K=1}^{N} A_k{}^{t\varphi_k} \tag{4.6}$$

Radiometric distortions can be reduced by a multi-look processing or by filtering. As for multi-look processing, the observation period of the returns is divided in shorter sub-periods. During every sub-period the instrument gets *"a look"* on the object. Using the average of these intervals we obtain the final image. This operation, however, reduces the spatial resolution. Furthermore, filters must preserve the average scattering value, maintain sharp edges between adjacent objects and preserve spatial variability (textural information) of the scene.

Geometric distortions

SAR images differ from the optical ones mainly because of the acquisition geometry.

When terrain is imaged using an optical sensor such as a camera, the image can be thought of as a central perspective projection (Fig. 4.8a). In this case, all the terrain points have projection lines passing through a central point on their way to their corresponding image points, as in Fig. 4.8a. On the other hand, for a SAR images, ground objects will be placed into locations on the image line as a function of their distance from the antenna.

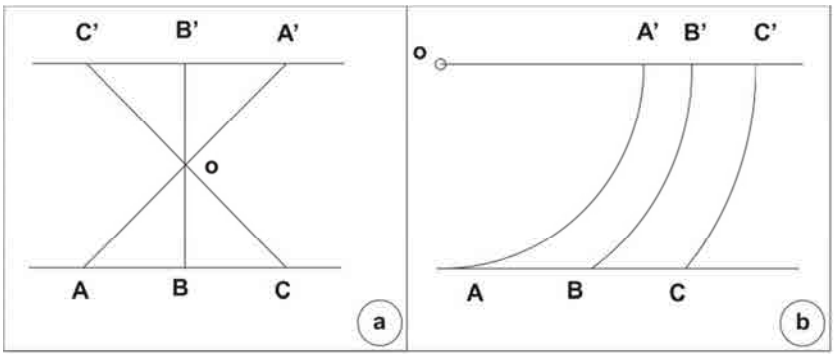

Fig. 4.9: Image projections for (a) optical and (b) SAR imaging systems (http://www. www.geo.uzh.ch)

The radar, in fact, is measuring the distance to features in slant-range rather than the true horizontal distance along the ground. Because of the radar is side-looking, ground elevation will result in geometric distortions in the SAR image. This results in a varying image scale, moving from near to far range.

The image distortions caused by the oblique viewing geometry are *foreshortening*, *layover*, and *shadowing* (Fig. 4.9).

- *Foreshortening* occurs when the radar beam reaches the base of a tall feature tilted towards the radar (e.g. a mountain) before it reaches the top. Because the radar measures distance in slant-range, the slope (from point a to point b) will appear compressed and the length of the slope will be represented incorrectly (a' to b') at the image plane.

- *Layover* occurs when the radar beam reaches the top of a tall feature (b) before it reaches the base (a). The return signal from the top of the feature will be received before the signal from the bottom. As a result, the top of the feature is displaced towards the radar from its true position on the ground, and ”layover” the base of the feature (b' to a').

- The *shadowing* effect increases with greater incident angle θ, just as our shadows lengthen as the sun sets.

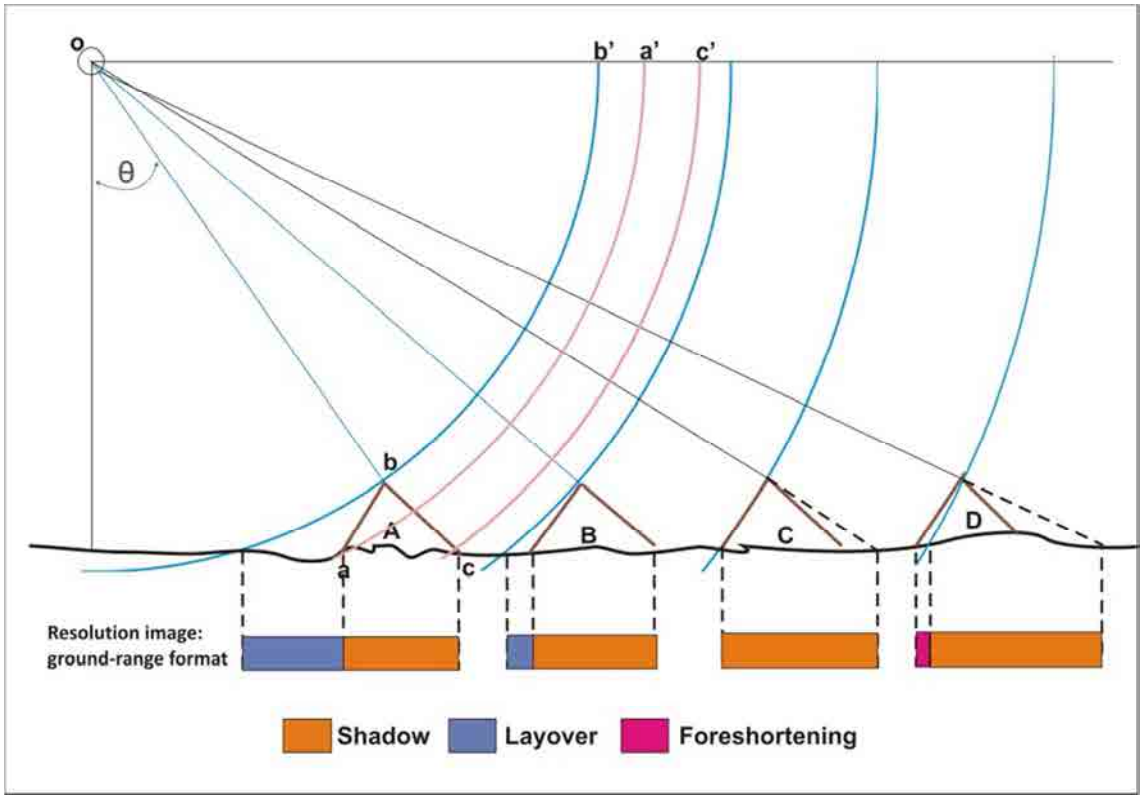

Fig. 4.10: slant-range distortions (image adapted from A.J. Lewis, 1976)

In topographic feature A, the beam reaches the top of the slope facing the wave front before it reaches the slope base. Thus the upper beam is reflected to the receiving antenna before the lower beam, producing the layover effect.

This is most pronounced in near range encounters and decreases as the beam encounter tend towards far range; thus layover has decreased in feature B. Foreshortening begins where the facing slope is less steep than the impinging wave front causing a distortion of the slope size.

The angle of the opposing face (back side) relative to the look angle produces a third phenomenon known as radar shadowing. Shadow length and darkness increases from feature A through D as the look angle becomes progressively less than the fixed back slope angle.

A typical example of the layover phenomena is the SAR detection of the Eiffel Tower (Fig. 4.10).

The beam is directed from top to down in Fig. 4.10. Since the sensor is located in every moment along a flying line, and since it gathers data even at a certain distance from it, the image given will show different scales moving from the area underlying the flying line to farther and farther areas.

The objects of the image near to the flying area (near range) will appear compressed towards ground range, if we compare them to the farther objects (far range). It is clear that the layover effect generates a variation of the image scale and of the tower geometrical characteristics.

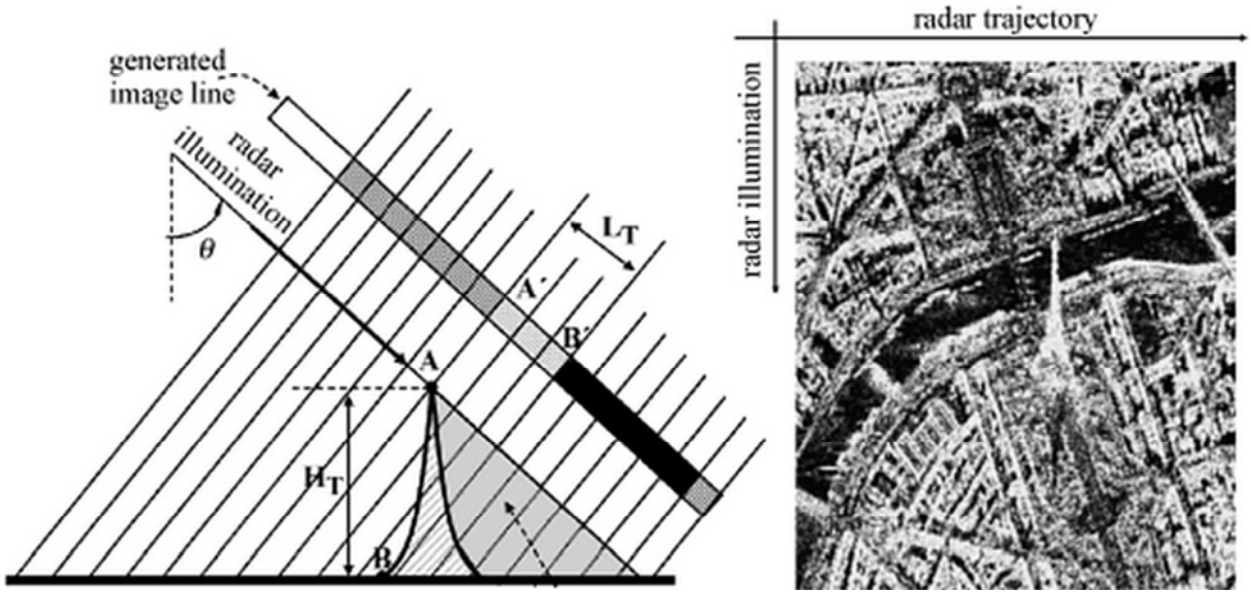

Fig. 4.11: Layover effect in the Eiffel Tower SAR detection (http://www.geo-informatie.nl/)

Another common example is that of radar images of mountainous terrain. The visual pattern gives the impression that the mountains, whose opposing surfaces have similar angles, are analogous to the special topographic feature known as "*flatiron*" form (hogbacks along the Rocky Mountain Front resulting where rock units are dipping in one direction are this geomorphic type).

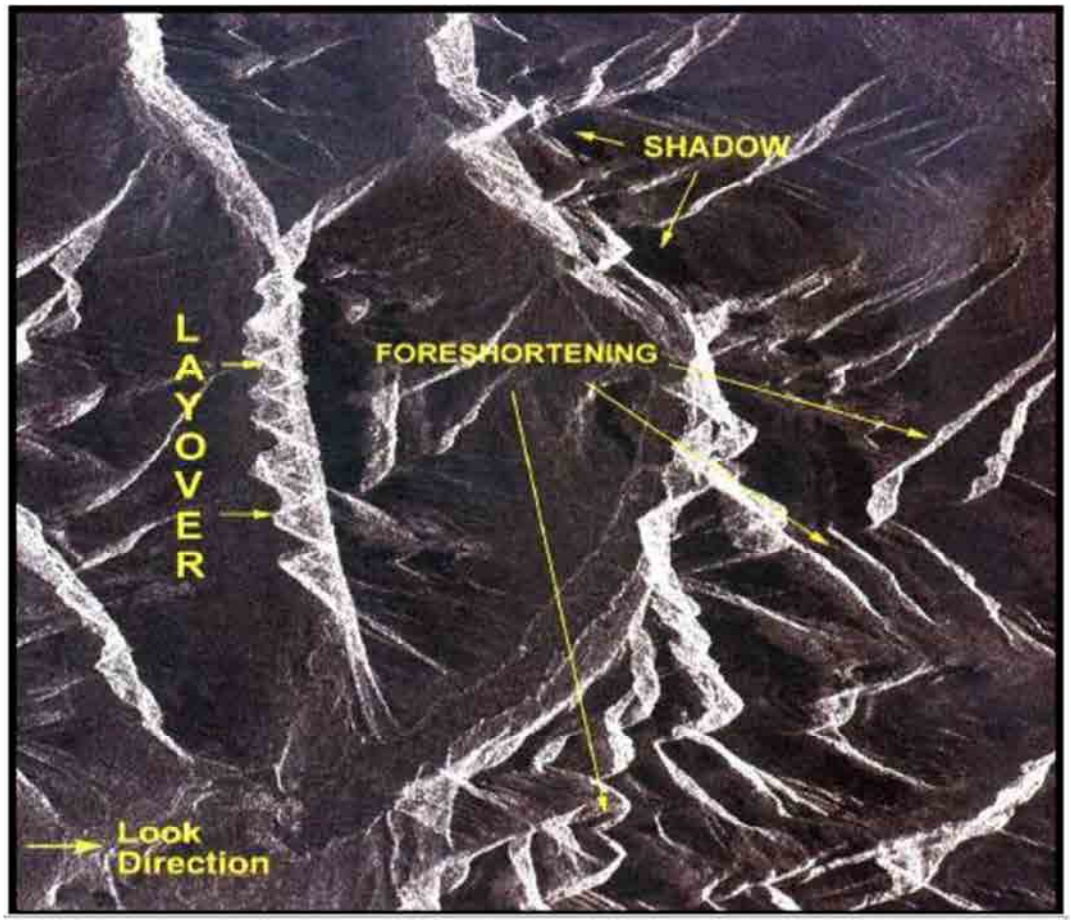

Fig. 4.12: Example of geometrical distortions, from RADARSAT Geology Handbook (RADARSAT International).

The geometric correction has to involve several levels of pre-processing. Various techniques have been developed based on the use of several images in order to have different view angles and digital elevation models (DEM).

The data has first to be corrected for earth curvature, earth rotation and satellite attitude errors. After this, the image may still contain geometric distortions, with the centre of the scene located to an accuracy of only a few kilometres.

To improve this, a sufficient number of ground control points, which are readily identifiable on the image and on a map, are selected for calculations of a least-square fit, and the results are then used to adjust the image to the map coordinates.

4.4. SAR interferometry

Interferometric Synthetic Aperture Radar (*InSAR*), was first described by Gabriel et al., 1989 and its first applications was described in Massonnet y Rabaute, 1993. It concerns upon the measurements over time of single or few signal phase changes ("*interferences*"). This allows to obtain information about deformations of the earth surface.

As said in the previous, a SAR image, differently from the simple optical data, contains useful information about the scene backscattering coefficient (related to the image amplitude) and about the targets distance (related to the phase information). However this information contained in one image is useful only if used together with another image. When a point on the ground moves, the distance between the sensor and the point on the ground also changes and so the phase value recorded by a SAR sensor flying along a fixed orbit will be affected, too.

SAR interferometry is based on the principle that, using two images referred to the same area, is possible to calculate an image called "*interferogram"* sensible to changes in the scatters position inside the resolution cells (ground pixel).

An interferogram is obtained by multiplying one image by the complex conjugate of the other, on a pixel by pixel basis. Their amplitude is an important parameter to the images correct coregistration. One of the images, called "*master"*, is taken as a reference (usually the first according to a chronological order), while the other will be called "*slave"*. The deriving obtained complex image will have amplitude *ΔA* equal to the one of the first image multiplied for the second, while the phase will be the difference between the two.

$$\Delta A e^{i\cdot\Delta\varphi} = A_1 \cdot e^{i\cdot\Delta\varphi_1} \cdot A_2 \cdot e^{i\cdot\Delta\varphi_2} == A_1 \cdot A_2 \cdot e^{i\cdot(\varphi_1-\varphi_2)} \tag{4.7}$$

Through the amplitude information, is possible to achieve high resolution images of an area, like that shown in Fig. 4.13 referred to the area of Murcia city (SE Spain), having a pixel resolution of 5x5 m which have been obtained through 128 Terrasar-X images.

If the two images of the same area are detected at the same time (this can be obtained if two sensors are installed on the same platform with a small shift in the look angle) the phase difference allows to obtain the three-dimensional position of the pixel and, therefore, to achieve a Digital Elevation Model of the area.

If the satellite acquires two images passing on the same area in two different times (*temporal baseline*) and in different orbit positions (*spatial baseline*), the phase difference contains various contributions among which the topography of the observed scene, and the possible soil deformation occurred in the

interval of time between the two acquisitions. Subtracting the topographic component is possible to estimate the component due to the displacement.

Fig. 4.13: Amplitude high resolution image obtained using 121 available X-band images of Murcia (pixel resolution 1.5x1.9 m)

Therefore, from a processing of the interferometric phase, compared with the ground topography, it is possible to obtain two kinds of results:

- *High resolution Digital Elevation Models (DEMs);*
- *Deformation maps characterized by millimetre resolution.*

So, the Interferometric technique employs the phase measures to infer the *differential range* (difference between distances perceived by the radar sensor to the same target on two different points of view) and the *range change* (difference between a couple of images, proving that a target transfer took place between the two acquisitions).

The phase of the SAR image response of a point scatterer is proportional to range (and to the used wavelength λ) plus a possible shift due to the scatterer itself $\varphi_{scattering}$. The $\varphi_{scattering}$ is a random variable having a uniform distribution between 0 and 2π and, for this reason, the phase image is noisy and useful only if compared with another one referring to the same scene. The phase is proportional to the two ways travel path $2k \cdot r$ and results:

$$\varphi = -\frac{4\pi}{\lambda} \cdot r + \varphi_{scattering} \tag{4.8}$$

where the term $4\pi/\lambda$ (called *"Propagator"*) depends on the sensor-radar target distance, while $\varphi_{scattering}$ depends (eq. 4.9) on the reflectivity of the radar target ψ, on the atmospheric phase contribution α and on the noise ν.

$$\varphi = -\frac{4\pi}{\lambda} \cdot r + \psi + \alpha + \nu \tag{4.9}$$

If in the two images (1 and 2) morphology results the same and surface changes does not occur, it is possible to assume that the scattering phases (eq. 4.10), are the same in both images; this means that $\varphi_{scattering1} \approx \varphi_{scattering2}$.

$$\begin{aligned} \varphi_1 &= -\frac{4\pi}{\lambda} \cdot r_1 + \varphi_{scattering1} \\ \varphi_2 &= -\frac{4\pi}{\lambda} \cdot r_2 + \varphi_{scattering2} \end{aligned} \tag{4.10}$$

Therefore, the interferogram phase $\Delta\varphi_{\text{int}} = \varphi_1 - \varphi_2$ results a very sensitive measure for the range difference and is equal to (Mora, 2004):

$$\Delta\varphi_{\text{int}} \approx \frac{4\pi}{\lambda} \cdot (r_2 - r_1) \tag{4.11}$$

It is function of the distances difference between the target and sensors in the two considered images (eq. 4.11 and Fig. 4.14).

As said in the previous, the most important factor affecting the phase regards the wave interaction with the ground surface. The phase of a backscattered wave change in function of the target characteristics; if changes do not occur on the ground, the contributions of each target are the same. This allows to remove this effect from an interferogram. Once the ground effects have been removed, the orbital effects represents the main contribution in the interferometer phase. For this reason, to obtain good results from the interferometric techniques, the images have to be acquired by satellites having a little distance, which move on the same orbit. This orbital distance influence the phase, provoking an orbital effect which can be removed and altering the distortion due to the topography (namely, an extra phase difference, introduced by a stereoscopic effect).

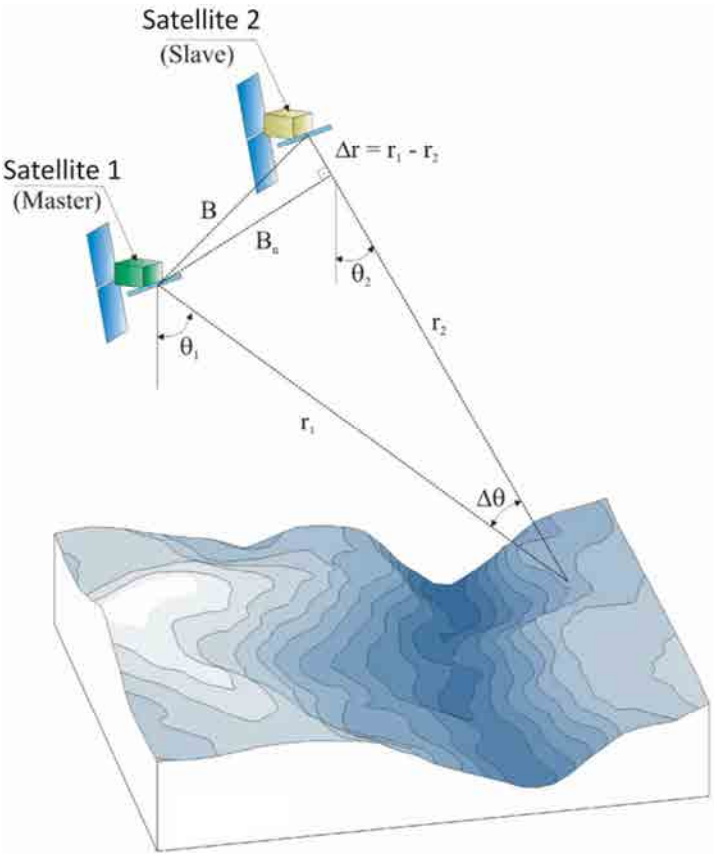

Fig. 4.14: SAR acquisition geometry (extract from Tomàs, 2009)

Considering the two SAR sensors (S_1 and S_2) of Fig. 4.14, their distance on the perpendicular plane to the orbit direction, the so called *interferometer baseline*, is indicated with B_r, while the latter one component projected the slant range direction, called *perpendicular baseline*, with B_n. According to the Fig., the relative displacements of two point scatterers A and B have been indicated with r_p and n_p (respectively parallel and normal to the slant range direction).

The positions of S_1 and A with their relative distance r_1 have been assumed as reference.

Consequently to a change in the sensor and target positions, respectively of (B_n, B_r) and (r_p, n_p), the sensor-target distance becomes:

$$r = \sqrt{\left(r_1 + r_p - B_r\right)^2 + \left(n_p - B_n\right)^2} \tag{4.12}$$

Since the distance between the two SAR sensors is generally smaller than the sensor-target distance r_0 (a few hundred meters compared with 800 km, in the ERS-1 case), the following expression of the interferometric phase variation holds:

$$\Delta\varphi = \frac{4\pi \cdot B_n \cdot n_p}{\lambda \cdot r_1} \tag{4.13}$$

This result shows that, if the relative displacement of the two orbits normal to the slant range (B_n), the distance r_1 and the value of the SAR wavelength λ are known, then the phase difference Δφ depends only on the n_p value, (i.e. the elevation difference between the points displayed in Fig. 4.14, measured in the direction normal to the slant range axis).

This factor can be decomposed to correlate the phase with the topographic differences among the observed points (Δh, eq. 4.14).

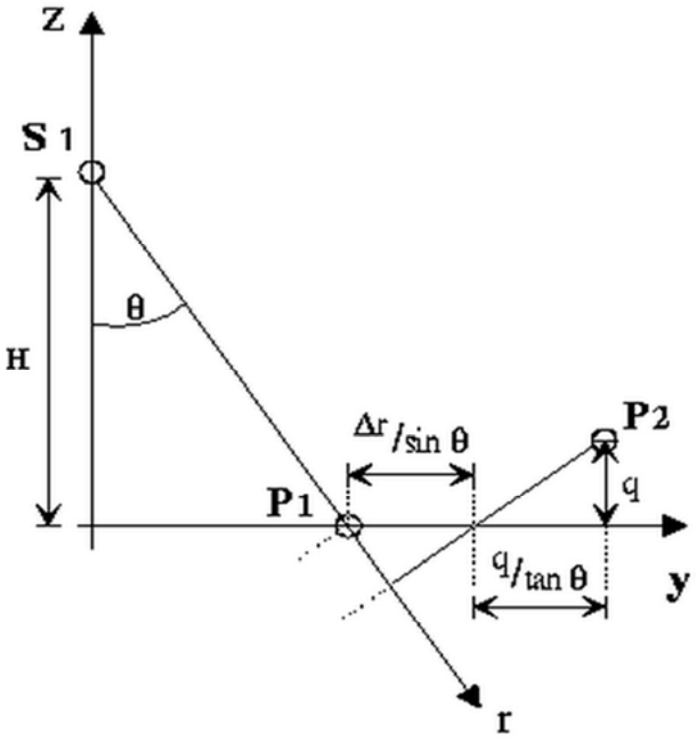

Fig. 15: cross section of the SAR system geometry, normal to the azimuth direction (http://www. http://astrogeology.usgs.gov/)

The interferometric phase, out-coming from the path difference of the slant-range signal between two acquisitions, in theory would only depend on the elevation differences between the two images and the deformation related to them. Basically, however, such a signal will see the contribution of other different factors (better explained in the paragraph 4.5), which can be summed up to form the interferometric phase.

Therefore, considering a deformation occurred between the two acquisition times, whose component in the slant-range direction is indicated with Δρ, differential phase can be calculated (eq. 4.14, Mora, 2004), in the most general form:

$$\Delta\varphi_{\text{int}} = \frac{4\pi}{\lambda \cdot r_1} \cdot \frac{B_n \cdot \Delta r}{\tan\theta} + \frac{4\pi}{\lambda \cdot r_1} \cdot \frac{B_n \cdot \Delta h}{\sin\theta} + \frac{4\pi}{\lambda} \cdot \Delta\rho + \Delta\varphi_{atm} + \Delta\varphi_{noise} \qquad (4.14)$$

where: $\Delta\rho$=measured deformation in the slant range direction, θ=incidence angle, B_n=perpendicular baseline (distance between two SAR acquisitions along the orthogonal direction to the incidence angle), Δh=altitude difference between two points in the image, Δr=increase of the distance satellite-target relative to two points of the image.

So, according to the equation 4.14, the interferogram phase is function of:

- **"*Flat earth phase*":** this component is function of the displacement of the radar target (Δr) and is intrinsic of each interferogram. It represents the phase difference measured in the absence of any topography.

- ***Topography*:** topographic distortions arising from slightly different viewing angles of the two satellite passes. This factor contains the information relative to the scene topography (Δh) and is function of the perpendicular baseline (B_n).

- ***Deformation*:** depends to the deformation ($\Delta\rho$) occurred between the two acquisitions

- **Atmospheric effects:** arising from the wavelength distortion that occurs when signals enter and leave a moisture-bearing layer. This factor provokes phase patterns in the interferograms and is due to the changes in the atmospheric conditions existed during the images acquisition.

- **Noises:** it includes all the elements that provokes decorrelation

4.5. Differential Interferometry

The aim of the Differential Interferometry SAR (*DInSAR*) consists in the elimination (or at least the minimization) of the terms affecting the interferometer phase introduced in the equation 4.14, to obtain an estimation of the ground deformation occurred between the two SAR acquisitions. It is possible to classify DInSAR techniques in Conventional and Advanced. To the first group belong the "*two-pass method*" (with two images and an external DEM), "*three-pass method"* (with three images) and the "*short baseline method*", (Mora, 2004). In this three cases, a simulation of the topographic contribution (considering B_n known from orbital data) allows the estimation of the total deformation (Δρ) projected along the slant range direction (or *line of sight, LOS)*; through the DInSAR techniques is only possible to estimate this component of the total displacement.

The topographic contribution of the equation 4.14 can be simulated using an external DEM or obtaining the DEM from an independent interferogram. If a DEM with an adequate precision is available, the contribution of the known topography can be almost completely removed from the interferometric phase but others "*error sources*", (described in the following paragraph), have to be considered. Using an external DEM, the topographic contribution in the equation 4.14 is equal to:

$$\Delta\varphi_{topo_{est}} = \frac{4\pi}{\lambda \cdot r_1} \cdot \frac{B_n \cdot \Delta h_{DEM}}{\sin\theta} \tag{4.15}$$

and the error relative to its estimation depends on the DEM and the perpendicular baseline precisions.

When an external DTM is not available, it is possible to use a third independent image to generate a second interferogram (called "*topographic interferogram*"). It has to have a short temporal baseline and a high spatial baseline to achieve a good precision of the topographic component.

The second "deformation interferogram" is achieved from two of the three available images, without limitations in the temporal baseline (in this case, the two images have to be referred to a period when a ground deformation occurred to obtain a sufficient residual phase due to deformation).

The "*short baseline technique*" is based on the assumption that the topographic component of the interferometer phase only depends to the perpendicular baseline B_n (eq. 4.14). When the baseline is short, is possible to consider the topographic factor negligible respect to the deformation one.

In this case, it is possible to consider a part of the image having a short spatial baseline, and through the information about the satellite orbits, bring a correction of the flat earth phase.

$$\Delta\rho_{est} = \frac{\lambda}{4\pi_1} \cdot \Delta\varphi_{dif} \tag{4.16}$$

$$Error_{\Delta\rho_{est}} = \frac{B_n \cdot \Delta h}{r_1 \cdot \sin\theta} + \frac{\lambda}{4\pi} \cdot \Delta\varphi_{atm} + \frac{\lambda}{4\pi} \cdot \Delta\varphi_{noise} \tag{4.17}$$

The error of the estimated displacements achieved through the described methods is also function of the left out atmospheric and noise components.

4.5.1. Error sources

The interferometric phase model equation (eq. 4.14) can be written as follows (Hanssen, 2001; Mora, 2004):

$$\Delta\varphi_{\text{int}} = 4\pi \cdot \frac{r_1 - r_2}{\lambda} = \Delta\varphi_{flat} + \Delta\varphi_{topography} + \Delta\varphi_{moving} + \Delta\varphi_{atmosphere} + \Delta\varphi_{noise} \quad (4.18)$$

Besides the factor ($\Delta\varphi_{topo}$), which represent the contribution of the topography and the deformation one ($\Delta\varphi_{mov}$), others three factors contribute to the definition of the interferometric phase for a given scatter:

$\Delta\varphi_{flat}$ the parameters which identify the satellite position during the acquisition of the image on the ground are called "*orbital parameters*", and they are made up of a series of points on the satellite orbit path, whose position and speed are known. This information is usually given by the service supplier. In order to minimize the error, more accurate state vectors (position and speed) are needed. These data were obtained from the European Space Agency and from other institutions and universities, several months after the satellite acquisition. The flat term will be the phase pattern generated by a flat terrain. The separation with the topographic term is just from the mathematical `point of view as both depend on the spatial baseline. The former can be mathematically calculated with the orbital information and the latter if a DEM is available.

$\Delta\varphi_{atm}$ when two SAR images are acquired in different dates, the travelling speeds of the electromagnetic waves are different due to the atmosphere variations. This signal disturbance can take place due to variations in humidity, temperature and pressure in the air. This effect usually arouses a phase shift included inside a single cycle 2π, with a gradual variation inside the image. Usually, the images at one's own disposal have very different conditions of acquisition; for this reason, to eliminate a part of this disturbance it is possible to relate every one of them to only one master image, following the APS pattern (Atmospheric Phase Screen) for the spreading in atmosphere. Another possibility can be to use atmosphere patterns specifically realized for the area of interest, which are also able to determine a phase shift contribution due to the tropospheric refractivity when the signal passes through.

$\Delta\varphi_{noise}$ Atmospheric effect is not usually predominant in the phase noise, but the latter is the sum of several distributed factors, which can vary considerably through time between two acquisitions. As we said before, the elements which create a phase interference of phase speckle are mainly:

- *Variation of the scatters*, mainly for densely lush reservoirs and areas densely lush, which change in few milliseconds, the response on earth of the signal will hardly supply comparable values, even if it is acquired in a short time. This factor can be defined temporal decorrelation.

- *Variation of the incidence angle*, which has as a main consequence the variation of the critic baseline, beyond which the response is only noise. This factor depends on the dimensions of the pixel on earth, and the ground formation, on the radar frequency and the distance from the sensor – target. In order to reveal this special contribution to the noise we can use the term spatial decorrelation.

- *Volume scattering*, when there is a volumetric distribution of scatters on the resolution cell, the incident signal can carry out different paths inside it, with a different number of rebounds, return time, and so on. As the previous, this decorrelation source depends on the critical baseline too.

$\Delta\varphi_{mov}$ represents the earth surface motion and is constituted by a linear and a non-linear part.

$$\Delta\varphi_{mov} = \Delta\varphi_{lin} + \Delta\varphi_{non-lin} \tag{4.19}$$

The so obtained displacement information represents only a component of the total displacement because can be estimated along the LOS direction. Through these methods, in fact, it is not possible to estimate deformation in the direction perpendicular to the LOS direction.

In order to reduce the errors related to these methods, some algorithms have been implemented.

The first performed algorithms (Peltzer et al., 2001) were focused on the reduction of the effects of the phase *atmospheric artefacts* due to changes in the atmospheric conditions between the acquisition SAR pairs and/or those due to the uncertainties in the sensor orbit information (*orbital artefacts*).

These techniques, (called "*stacking techniques*") essentially calculate a weighted average of all the deformation velocities computed from single interferograms (the weights being the corresponding time spans) and allow providing an improved estimate of the mean deformation rate of the investigated area.

4.6. Advanced DInSAR Interferometry techniques

The development of DInSAR techniques has permitted to pass from the methods introduced in the paragraph 4.5, (which allow to calculate displacements occurred between two images acquisition dates), to multi-pass methods which take into account all the SAR images available for an area. In this way permit to obtain information on the historical time evolution of an instability phenomenon (using at the least 20–30 images), whose detail is function of the time elapsed between observations of the same point (revisit time) (4-8 days in the case of the recent COSMO Sky-Med and Terrasar-X satellite constellations vs. 35 days for ERS and ENVISAT).

As to obtain comparable results, only a long and continuous monitoring through the traditional field surveys could help, which very often cannot be performed over wide areas.

As introduced in paragraph 4.5.1, using images acquired at different times (temporal baseline) and in different orbit positions (spatial baseline), processing may be affected by errors, which lead to additional contributions to the interferometric phase and may severely reduce the accuracy of the technique.

For this reason, several algorithms have been performed to overcome these limits.

Among the various methods, the "*Coherence-based*" approaches, (among which the *DInSAR Small BAseline Subset* –SBAS- belongs) and the *Persistent Scatters* (PS) techniques can be mentioned.

Coherence-based techniques only use interferograms characterized by a small temporal and spatial baseline, obtaining a high areal density of consistent points, i.e. targets, selected on the bases of their coherence in all the used interferograms. On the other hand, the Persistent Scatters (PS) technique is based on the analysis of the images amplitude dispersion. In particular, it is based on the observation of a small subset of radar targets (the so called PS), constituted by parts of buildings, metal structures, outcropping rocks, showing negligible electromagnetic characteristic variations among the various acquisitions.

Among these two principal approaches, several different algorithms belong; in particular, it is possible to cite that implemented by Ferretti et al., 2000; Werner et al., 2003; Arnaud et al., 2003; Hooper et al., 2004; Duro et al., 2005; Costantini et al., 2008; Iglesias et al., 2012, which are part of the Persistent Scatterers (PS) methods and that performed by Berardino et al., 2002; Mora et al., 2003; Lanari et al., 2004; Prati et al., 2010), which belong to the Small BAselines Subset (SBAS) methods; furthermore, also a solution that incorporates both the PS and SBAS approaches has been recently proposed (Hooper, 2008).

The DInSAR processing consists of several steps through which to perform the displacement information. The so called "*co-registration phase*", using all the SAR images referred to the same area and having the same dimensions, is common also to the other techniques.

Here one image, called supermaster (Hanssen 2001), is selected and used as reference to have all the other images with the same geometry. Using all the co-registered images is possible to calculate the mean amplitude image (see Fig. 4.13).

The following step consists in the interferograms generation which is achieved using all the co-registered images and the Digital Elevation Model (DEM).

The interferograms generation is constituted by two steps: in the first one, starting from two co-registered images (*master* and *slave*), a complex interferogram have been obtained; in the second step, a complex interferogram is simulated starting from the DEM. Using these two interferograms, is possible to achieve the *wrapped differential interferogram*.

After that, is possible to obtain the phase information through some selection criteria based on all the differential interferograms. Therefore, the phase information brings to the elaboration of mean deformation velocity map, cumulated displacements map and time series of deformation.

4.6.1. A-DInSAR applications

In the last twenty years many DInSAR applications have been developed, and the capability of the DInSAR has been extensively documented.

A great contribution to this success certainly comes from different fields of geosciences. Some of the most relevant DInSAR application fields are discussed below:

- *Seismology*: probably represents the field where the greatest number of scientific achievements have been obtained, including different types of coseismic studies, see e.g. (Massonnet et al., 1993; Peltzer and Rosen, 1995; Peltzer et al., 1999; Reilinger et al., 2000; Pedersen et al., 2001); post-seismic deformation studies (Peltzer et al., 1996; Massonnet et al., 1996), and inter-seismic tectonic events (Wright et al., 2001; Colesanti et al., 2003). As it is described later in this paper, such types of deformations can only be achieved by using advanced DInSAR processing and analysis tools.
- *Volcanology*: represents another relevant application field, with several studies of volcanic deflation and uplift, e.g. see (Massonnet et al., 1995; Lu et al., 2000; Salvi et al., 2004). Several examples of DInSAR applications to volcanology are described in Massonnet and Sigmundsson 2000.
- *Glaciology*: different researches have been led in this domain. They included InSAR ice topography measurements (Kwok and Fahnestock, 1996); ice velocity measurements (Goldstein et al., 1993; Joughin et al., 1996; Mohr et al., 1998); and other glaciological applications, like the determination of the discharge of glaciers (Rignot et al., 1997; Joughin et al., 1999).
- *Landslides*: with the A-DInSAR techniques for some types of landslide phenomena (slow and extremely slow movement) it has been possible to perform DInSAR deformation measurements. The most relevant results are described in Fruneau et al. 1996; Hilley et al. 2004; Delacourt et al. 2004; Colesanti & Wasowky 2006; Meisina et al., 2008; Herrera et al., 2009, Cascini et al., 2010.
- *Ground subsidence and uplifts*: several papers have analysed the case of vertical displacements, due to fluid pumping, construction works, geothermal activity, etc. Some examples can be found in Massonnet et al. 1997; Galloway et al. 1998; Amelung et al. 1999; Wicks et al. 2001; Crosetto et al. 2003; Lanari et al. 2004; Cascini et al., 2009, Tomàs et al., 2010, 2011, 2013. Most of the published results concern urban areas, over which DInSAR data remains coherent even with large observation periods.
- *Infrastructures*: deformations monitoring of man-made structures, such as dams, buildings and transport infrastructures, see e.g. Perissin et al., 2009; Proto et al., 2010; Stabile et al., 2012.

4.7. Coherent Pixels Technique

Among the different algorithms previously mentioned in this work, the algorithm implemented by Mora et al., 2003 - *Coherent Pixels Technique* (CPT) at the Remote Sensing Laboratory (RSLab) of the Universitat Politecnica de Catalunya (UPC) has been used.

CPT is able to extract from a stack of differential interferograms the deformation evolution over wide areas during large time spans (Di Martire, 2013).

The first step of the SAR images processing consists of the images co-registration. Co-registration represents the phase of overlapping, in the slant range geometry, of two or more SAR images that have the same orbit and acquisition mode. In fact, as introduced in paragraph 4.6, SAR images have to be co-registered in order to have all the other images with the same geometry. In particular, it represents a required step when multiple images cover the same region and need a spatial registration to correct relative translational shifts or rotational and scale differences or if the images have a different pixel size and need a resampling.

The registration process performed by CPT algorithm consists in:

→ *Coarse registration*: which align the cropped images with an accuracy of one pixel for the whole image. This step is performed through the amplitude correlation for a portion of both the images;

→ *Fine registration:* which align the cropped images with an accuracy of a fraction of pixel, processing each pixel separately. This step can be done also using the amplitude correlation of block divided images or through geocoding techniques that require an external DEM and the orbital information.

After the co-registration, the processing scheme is composed of three main steps:

A. *the generation of the best interferogram set among all the available images of the zone under study;*

B. *the selection of the pixels with reliable phase within the employed interferograms and,*

C. *the phase analysis to calculate, as the main result, the deformation time series within the observation period.*

- ***Interferograms set generation***

This phase allows to obtain, among all the possible interferograms achieving starting from the available SAR images, the best set, namely the minimum number of interferograms in the stack which have the maximum quality overall. The selection is made on the base of the spatial baseline (B_t), the temporal baseline (T_i) and the Doppler frequency difference (D_f) of all the available images. In order to estimate the perpendicular baseline values (B_n) a reference image is selected and, usually, it is the same image used as supermaster in the co-registering process.

Thereafter, through a *Delaunay triangulation*, all the available images are connected in the $\{B_n, B_t, D_f\}$ space; every arc connecting a pair of images represents an interferogram.

Only the interferograms having a Doppler frequency, and the spatial and temporal baselines under the minimum imposed thresholds are selected, in order to obtain a good phase quality information and to reduce the processing computational time.

- ***Pixel selection***

There are different criteria to the pixel selection; in particular it can be based on their coherence stability (Berardino et al., 2002) or considering their amplitude dispersion (Ferretti et al., 2001).

In fact, as described in paragraphs 4.3 and 4.6, because of de-correlation problems, the detection of the deformations is not possible in the whole area acquired by the SAR sensor, but only in those parts having enough phase quality during the acquisition period.

The pixel selection based on the coherence stability is based on the *spatial coherence estimator, γ* (Seymour et al., 1994).

It can be computed through the following expression:

$$\gamma = \frac{\sum_{n=1}^{ML} y_1^{(n)} y_2^{*(n)}}{\sum_{n=1}^{ML} y_1^{(n)2} \sum_{n=1}^{ML} y_2^{(n)2,}}, \tag{4.20}$$

where y_1 and y_2 represent respectively the master and the slave complex images.

The phase of this complex coherence is the multi-looked (or averaged, ML) interferometric phase while its magnitude is the phase quality estimator (Di Martire, 2013).

Therefore, CPT algorithm works at lower ground resolution, depending on the multilook set; typical ML values are 1x5, 3x15 or 4x20 pixels (range x azimuth), in the case of ERS and Envisat SAR data. The required coherence estimation window decrease the pixels spatial resolution and, in particular, a multilook of 5x1 achieves a pixel ground resolution of 20x20 m, while the 3x15 and 4x20,respectively a ground spatial resolution of 60x60 m and 80x80 m. However, with bigger multi-look windows, the quality of the estimation improves, and its inherent bias is reduced. In the coherence based methods, each pixel is selected if its mean coherence, (calculated on the base of its coherence in all the interferograms used in the processing) exceeds an imposed threshold value in a certain percentage of interferograms. The mean coherence, in fact, gives an estimation of the quality for the whole stack.

On the other hand, to the pixel coherence, for the used multilook, corresponds a standard deviation of the computed interferometric phase, σ_φ, (Hanssen, 2001), as shown in Fig. 4.16 (Blanco, 2009). According to this Fig., in order to increase the points density it could be possible to change the chosen multilook, (for example, preferring the multilook 1x5 which corresponds to a pixel ground resolution of 20 m x 20 m to the 3x15, having a pixel ground resolution of 60 m x 60 m). However, taking into account the chart proposed by Blanco, 2009 (Fig.4.16), in order to obtain 20° phase standard deviation value (which corresponds to a displacement standard deviation of about 1,5 mm), by means of a 1x5 multilook, an higher coherence threshold has to be fixed. Such threshold could also bring to a lower number of selected pixels.

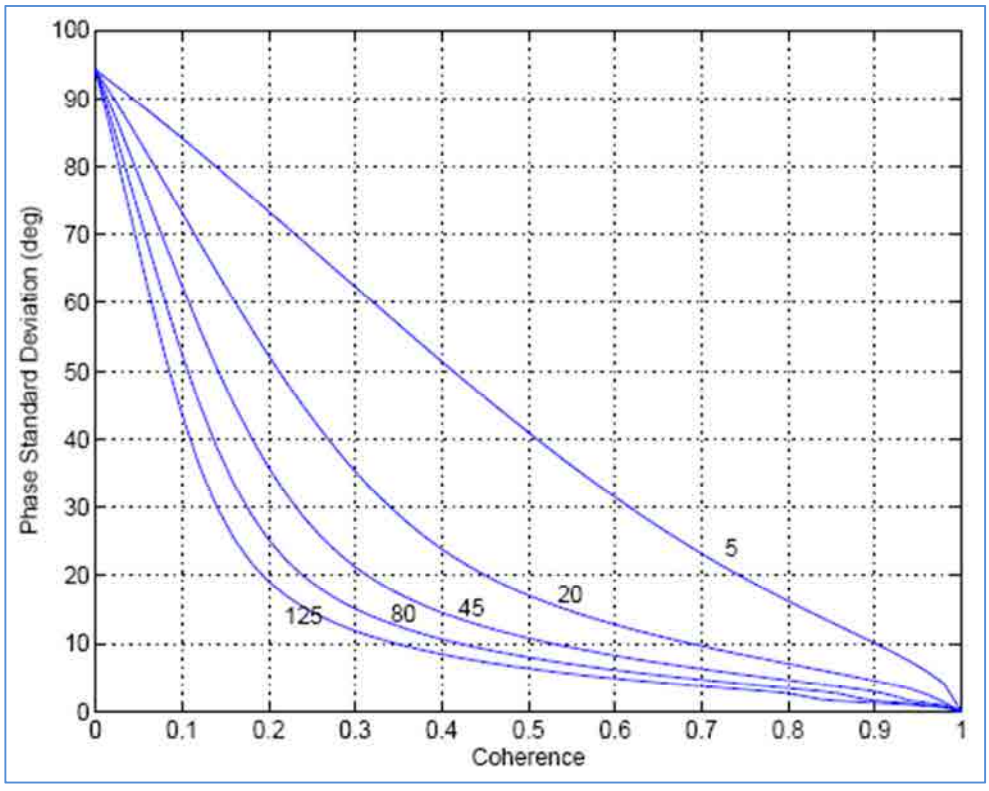

Fig. 4.16. Phase standard deviation vs coherence for different number of multilook (Blanco, 2009).

- ***Phase analysis***

In this step, the linear deformation time series within the observation period have been calculated.

Each interferogram is affected by a different global phase offset. In order to overcome this problem, nevertheless to work with an absolute phases (related to a pixel), we have to work with relative phases (related to links between pixels).

Another advantage of this criterion, is that is possible to minimize the atmospheric effects using close pixels (whose location is represented by the couple of coordinates in azimuth, range: x_m, y_m and x_n, y_n).

The strategy in order to obtain the relative phases is to consider the phase difference between neighboring pixels. The connection mesh is done using a *Delaunay triangulation* (Mora, 2004).

Therefore, the phase analysis is done over the links of the triangulation, which contain the relative phase information $\Delta\psi_{dif}$, instead of the pixels themselves, containing the absolute phase.

The phase analysis consists in adjusting a phase model to the relative phase information of each link. The model is described in equation (4.21):

$$\begin{aligned}\Delta\varphi_{\mathrm{mod}\,el}(x_m, y_m, x_n, y_n, T_i) = \frac{4\pi}{\lambda}\cdot T_i\cdot\left[v_{\mathrm{mod}\,el}(x_m, y_m) - v_{\mathrm{mod}\,el}(x_n, y_n)\right] + \\ \frac{4\pi}{\lambda}\cdot\frac{B_n(T_i)}{r_0(T_i)\cdot\sin\theta(T_i)}T_i\cdot\left[\varepsilon_{\mathrm{mod}\,el}(x_m, y_m) - \varepsilon_{\mathrm{mod}\,el}(x_n, y_n)\right]\end{aligned} \tag{4.21}$$

where λ is the wavelength, T_i and B_n are the temporal and the spatial baseline respectively, r_0 is the satellite to target distance, θ is the incidence angle, v is the displacement rate and ε is the topographic error.

In order to calculate v and the topographic error ε, the "model adjustment function" for all the pixel relations obtained with the Delaunay triangulation, reported in the equation 4.22, have to be optimized.

$$\Gamma(x_m, y_m, x_n, y_n) = \sum_{i=0}^{N}\left|\exp\left[j\cdot\Delta\psi_{dif}(x_m, y_m, x_n, y_n, T_i)\right] - \exp\left[j\cdot\Delta\psi_{\mathrm{mod}\,el}(x_m, y_m, x_n, y_n, T_i)\right]\right|^2 \tag{4.22}$$

where N is the number of interferograms.

In order to estimate the quality of the model adjustment, Mora (2004) proposed the function of the model coherence:

$$\Omega(x_m, y_m, x_n, y_n) = \frac{1}{N}\left|\sum_{i=0}^{N} \exp\left[j \cdot \Delta\psi_{dif}(x_m, y_m, x_n, y_n, T_i)\right] - \exp\left[j \cdot \Delta\psi_{model}(x_m, y_m, x_n, y_n, T_i)\right]\right| \quad (4.23)$$

where Ω is equal to 1 when the model adjusts perfectly to the data and tend to zero when there is a total data decorrelation. The Ω value is used to reject links where the data does not fit the model.

The minimization of function 4.22 leads to obtain the deformation rate and the topographic error increments related to each links between pixels in the Delaunay triangulation.

$$\Delta v_{est}(x_m, y_m, x_n, y_n) = \left[v_{model}(x_m, y_m) - v_{model}(x_n, y_n)\right]_{\Gamma\_minimized} \quad (4.24)$$

$$\Delta\varepsilon_{est}(x_m, y_m, x_n, y_n) = \left[\varepsilon_{model}(x_m, y_m) - v_{model}(x_n, y_n)\right]_{\Gamma\_minimized} \quad (4.25)$$

The absolute values of the deformation rate and of the topographic error of each pixel have to be computed, starting from the increments found in the previous step (eqs. 4.24 and 4.25).

To this aim, one or more control points (named seeds) are required (Carrasco, 1998). They have to be characterized by well-known linear velocity and height. Usually a stable point (or at least a point which has resulted stable during the processing temporal window), is considered. However it depends on the area extent and on the in situ available information.

$$v_{est}(x, y) = \frac{1}{\sum_i \Omega(x, y, x_i, y_i)} \cdot \sum_i \left[v_{est}(x_i, y_i) + \Delta v_{est}(x, y, x_i, y_i)\right] \cdot \Omega(x, y, x_i, y_i) \quad (4.26)$$

$$\varepsilon_{est}(x, y) = \frac{1}{\sum_i \Omega(x, y, x_i, y_i)} \cdot \sum_i \left[\varepsilon_{est}(x_i, y_i) + \Delta\varepsilon_{est}(x, y, x_i, y_i)\right] \cdot \Omega(x, y, x_i, y_i) \quad (4.27)$$

where i corresponds to the close pixels connected to that has been integrated. The integration process is shown in Fig. 4.18.

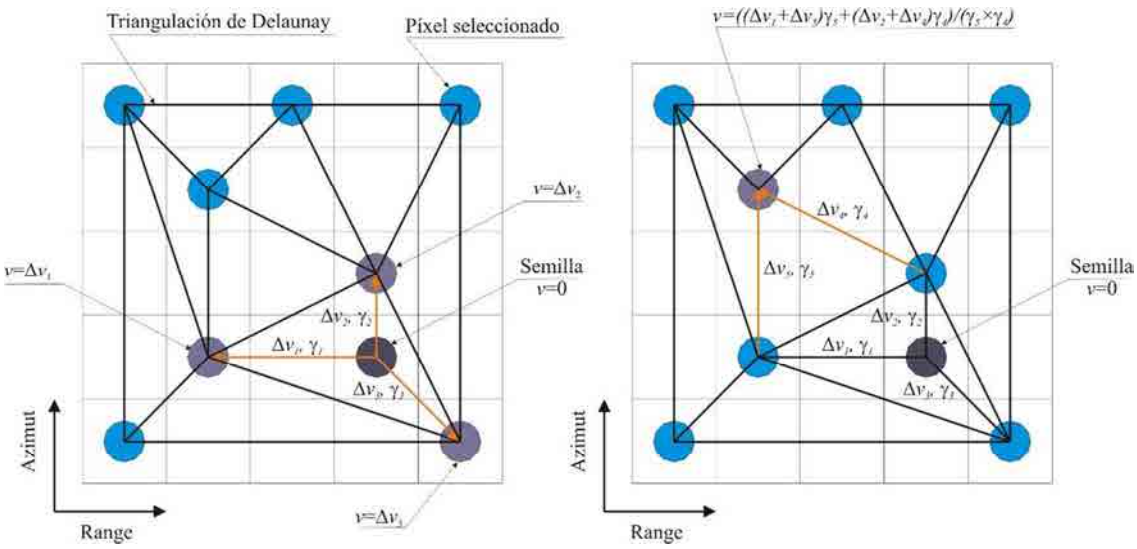

Fig. 4.18: Interactions to the absolute lineal velocity of coherent pixels (extracted from Tomàs, 2009)

A good distribution of control points is necessary, at least one for each isolated cluster of pixels. For pixels connected with bad links, wrong velocity values estimation can be achieved after the integration process. For this reason the pixels have to be divided into different layers on the base of the quality of their links.

In particular, starting from the layer corresponding to the best link quality, an iteration process brings to the addition of the other layers, considering the absolute values of each successive layer, as seeds for the next iteration. The criterion is the same for the following iterations.

In this way, the results corresponding to the high quality layers are preserved and the estimation of the low quality layers improves. This method is called "*multi-layer processing*" and allows to improve linear results and increase the pixel density, providing a quality label for each of them (Blanco et al., 2006).

After the calculation of the linear part of the deformation, the algorithm estimates the no-lineal component. The phase residues $\varphi_{residual}$ are obtained by subtracting, only for the selected pixels, the absolute linear phase model φ_{model} from the original interferometric phases φ_{dif} (eq. 4.18):

$$\varphi_{residual}(x,y,T_i) = \varphi_{dif}(x,y,T_i) - \varphi_{model}(x,y,T_i) \tag{4.28}$$

Specifically, φ_{model} represents the phase obtained from the lineal model for a coherent pixel (*x,y*) where the deformation rate and the topographic error are calculated according to the following expression:

$$\Delta\varphi_{model}(T_i) = \frac{4\pi}{\lambda}\cdot T_i \cdot \nu_{est} + \frac{4\pi}{\lambda}\cdot \frac{B_n(T_i)}{r_0(T_i)\cdot \sin\theta(T_i)}\varepsilon_{est} \tag{4.29}$$

The new computed phase residual contains the unknown components:

- *Atmospheric perturbations*: which can be considered as a low spatial frequency signal in each image due to its correlation distance (which is approximately of 1 km). However in each acquisition date the atmospheric conditions are variable.

- *No-Lineal deformation:* which can be assumed to present a narrower correlation window in space and a low pass behaviour in time.

- *Noises:* which account for all the other decorrelation sources.

$$\Delta\varphi_{residual}(T_i) = \Delta\varphi_{no-lineal}(T_i) + \Delta\varphi_{atm}(T_i) + \Delta\varphi_{noises}(T_i) \quad (4.30)$$

In order to separate the no-lineal deformation and the atmospheric phase, it is not applied a model, but a filter in both spatial and temporal domains (Blanco et al., 2008).

The addition of the so achieved non-lineal deformation map and of the linear one, will bring to the total deformation map of the study area.

CHAPTER V

Subsidence modelling

CHAPTER V: Subsidence modelling

5.1. Geotechnical overview

Soils are multiphase materials constituted by a solid particles skeleton which give rise to voids filled with water or gas. For this reason, the mechanical behaviour of a soil element is governed by laws which regulate the interactions between the solid and fluid phases.

In particular, the normal stresses are in part adsorbed by the fluid contained in the inter-granular voids in part by the solid skeleton; the last one, is the only responsible of the soil element deformations and of its strain strength. On the contrary, the strain stresses are completely hold up by the solid skeleton.

Therefore, the law which express the internal distribution of the stress applied on a generic soil element between the various phases is represented by the *Effective Stress Principle* (eq. 5.1), (Terzaghi,1923). According to this relation, the total stress acting in a point is constitute by two rates: the *pore water pressure u* and the *effective stress σ'.* Differently from the effective stress, to a change of the pore water pressure, which acts on the water and on the grains having the same intensity for all the directions, does not correspond a change in the soil element volume.

$$\sigma' = \sigma - u \tag{5.1}$$

In particular, the total vertical stress acted on a soil element at a depth z, under the ground surface is equal to:

$$\sigma_{v0} = (1 - n) \cdot \gamma_s \cdot z + n \cdot \gamma_w \cdot z \tag{5.2}$$

where:

n is the *porosity* of the soil element and is defined as the ratio of the volume of voids to the total volume;

γ_s is the specific solid weight and is defined as the dry weight of soil grains in a mass of soil;

γ_w is the water specific weight

The soil response to a boundary condition change could correspond to a deformation, which is defined as a relative displacement between two points in a continuous medium. The mechanisms which rule the temporal development of the deformations depends on the effective stress variations; these can be produced by several causes. Therefore these mechanisms can be divided essentially in two categories: the firsts which are related to the interstitial water diffusion ("*consolidation*" and "*swelling*" phenomena) and the seconds where effective stresses and pore water pressure are constants (called "*creep*" phenomena),

due to the structural viscosity. In the consolidation process, the temporal evolution of the deformations depends on the porous soil properties and on the system geometry, namely on the drainage water path and on the boundary conditions.

In particular, the application of a load on the soil corresponds to an increase of the total stresses which, as said before, are in part adsorbed by the solid skeleton and in part by the interstitial water. The pore water overpressure dissipation brings to a change in the void ratio (corresponded to the soil consolidation). The consolidation time is function of the soil permeability and deformability. According to the eq. 5.1, a decrease in the underground water level produce a decrease of the pore water pressure too, and, increasing the effective stress, a consolidation process.

At the end of the consolidation process, the pore water overpressure *Δu* turn to be null.

Depending on the relationships (*constitutive equations*) between the deformation tensor and the stress one, cause of the occurred perturbation, the soil behaviour, (as same as that of every material), can be considered *elastic* (*linear* and *non-linear; isotropic* and *an-isotropic*) or *elastic-plastic*. This is considered elastic if, for each loading phase (increasing or decreasing), a bi-univocal correspondence between the stress and the deformation components exists. That is to say that, the energy used for the deformation is completely returned if the perturbed load is removed and the deformation is reversible. In particular, in the linear, elastic and isotropic soil case, the deformations are proportional to the applied loads (*linear*) and independent to the loading direction (isotropic).

In 1676, Robert Hooke formulated the linear relation (the so called *Hooke's law*) analysing this class of solid materials (also called *Hookean*) through the test of a uniaxial body with a force (stress) applied only in one direction and measuring the corresponding elongation (strain). To explain his law, he used the anagram: "*Ut tensio sic vis*" which is Latin meaning "as the tension so the displacement".

In an isotropic medium, the normal stresses (σ'_z), acting on a cube of material, do not generate angular distortions, but only deformations $(\epsilon_x, \epsilon_y, \epsilon_z)$ in the stress direction and in its orthogonal ones, which are function of the so called "*Young elastic modulus*" *E'* (see eq. 5.5; Young, 1807).

The elastic modulus was introduced to define the stiffness of a material by *Thomas Young* in 1807 which said:

"we may express the elasticity of any substance by the weight of a certain column of the same substance, which may be denominated the modulus of its elasticity, and of which the weight is such, that any addition to it would increase it in the same proportion as the weight added would shorten, by its pressure, a portion of the substance of equal diameter".

Considering a cube element loaded by a normal stress in the z-axis direction, σ'_z, the produced longitudinal deformation, ϵ_z, is equal to:

$$\epsilon_z = \frac{\sigma'_z}{E'} \tag{5.3}$$

Young's modulus is defined as the ratio between the longitudinal stress and the strain referred to the same direction (within the elastic region of the stress strain curve). In the same way, is possible to define other two important elastic coefficients, respectively if the loads are represented by tangential stresses (which generate angular distortions) or by an uniform pressure (which have as consequence a volume decrease). In the first case, the ratio between stress and strain is called "*tangential elastic modulus" G* (eq. 5.6) and in the second case, *Bulk modulus* (eq. 5.7). The terms "*modulus*" indicates an inherent material property; this means that it depends only on the material and not on its geometry.

The stress applied in the z direction provokes also deformations in the orthogonal directions ϵ_x, ϵ_y which are proportional to the z-deformation (eq. 5.4); the proportionality coefficient between the longitudinal and the orthogonal deformation components, is called *Poisson's ratio* (1828) and results:

$$\epsilon_x = \epsilon_y = -\nu \cdot \epsilon_z = -\nu \cdot \frac{\sigma'_z}{E'} \tag{5.4}$$

Therefore, the longitudinal deformations components in the presence of the three normal stress components are equal to:

$$\begin{aligned} \epsilon_x &= \frac{1}{E'}\left[\sigma'_x - \nu \cdot \left(\sigma'_z + \sigma'_y\right)\right] \\ \epsilon_y &= \frac{1}{E'}\left[\sigma'_y - \nu \cdot (\sigma'_x + \sigma'_z)\right] \\ \epsilon_z &= \frac{1}{E'}\left[\sigma'_z - \nu \cdot \left(\sigma'_x + \sigma'_y\right)\right] \end{aligned} \tag{5.5}$$

If the load applied on the cubic soil element is a tangential stress $(\tau_{xy}, \tau_{yz}, \tau_{xz})$, the correspondent angular distortions $(\gamma_{xy}, \gamma_{yz}, \gamma_{xz})$ are equal to:

$$\gamma_{xy} = \frac{\tau_{xy}}{G};\ \gamma_{yz} = \frac{\tau_{yz}}{G};\ \gamma_{xz} = \frac{\tau_{xz}}{G} \tag{5.6}$$

At last, if the load is represented by an uniform pressure $p' = \frac{1}{3}(\sigma'_1 + \sigma'_2 + \sigma'_3)$, the consequent deformation generate a volume variation $\epsilon_V = \epsilon_1 + \epsilon_2 + \epsilon_3$ related to p' through the cubic deformation modulus K', (i.e. "*Bulk modulus*").

$$K' = \frac{p'}{\epsilon_V} \tag{5.7}$$

In case of isotropic medium, where the elastic properties have to be equal respect to every coordinate Cartesians axis, only two of the constants to characterize the stress-deformation relationships (μ, λ) are independent; they are called *Lamè constants* (1859) and are related to $\mathrm{E}', \mathrm{G}, \nu, \mathrm{K}'$ with the following equations:

$$\mu = G = \frac{E'}{2(1+\nu)} \tag{5.8}$$

$$\lambda = \frac{\nu \cdot E'}{(1+\nu)(1-2\nu)} \tag{5.9}$$

$$K' = \frac{1}{3}(3\lambda + 2\mu) = \frac{E'}{3(1-2\nu)} \tag{5.10}$$

In summary, in the case of elastic-linear-isotropic medium, is possible to represent the constitutive relation through the system 5.11, called "*generalized Hook's equations*", where the independent elastic constant are the two Lamè's constants.

$$\begin{bmatrix} \varepsilon_x \\ \varepsilon_y \\ \varepsilon_z \\ \gamma_{xy} \\ \gamma_{xz} \\ \gamma_{yz} \end{bmatrix} = \begin{bmatrix} 1 & -\nu & -\nu & 0 & 0 & 0 \\ -\nu & 1 & -\nu & 0 & 0 & 0 \\ -\nu & -\nu & 1 & 0 & 0 & 0 \\ 0 & 0 & 0 & 2(1+\nu) & 0 & 0 \\ 0 & 0 & 0 & 0 & 2(1+\nu) & 0 \\ 0 & 0 & 0 & 0 & 0 & 2(1+\nu) \end{bmatrix} \cdot \begin{bmatrix} \sigma_x \\ \sigma_y \\ \sigma_z \\ \tau_{xy} \\ \tau_{xz} \\ \tau_{yz} \end{bmatrix} \tag{5.11}$$

5.1.2. Over-consolidation stress

The soil behaviour is not characterized only by reversible deformations, but, more reliability, also by irreversible ones. In fact, is an-elastic and an-isotope, its deformations are non-linear, irreversible, dependent to its loading and geological history, as same as to a series of parameters such as saturation index, loading velocity and so on. For this reason, soil deformations could be considered as the sum of two rates, one elastic (computed as described above) and one an-elastic which occurs when a stress threshold is overcome (Fig. 5.1).

The limit between the recoverable deformations and the non-recoverable deformations is represented by the so called "*pre-consolidation pressure*" (σ'_p). It represents the highest pressure suffered by the soil along its life. When the vertical stress affected a soil is the maximum which has ever affected it, the soil is called

"*normal-consolidated*". In this case, the maximum vertical stress coincides with that due to its stratigraphic column weight (σ'_0). If the soil was affected in the past by an higher stress (σ'_p) respect the actual one (σ'_0), it is called "*over-consolidated*".

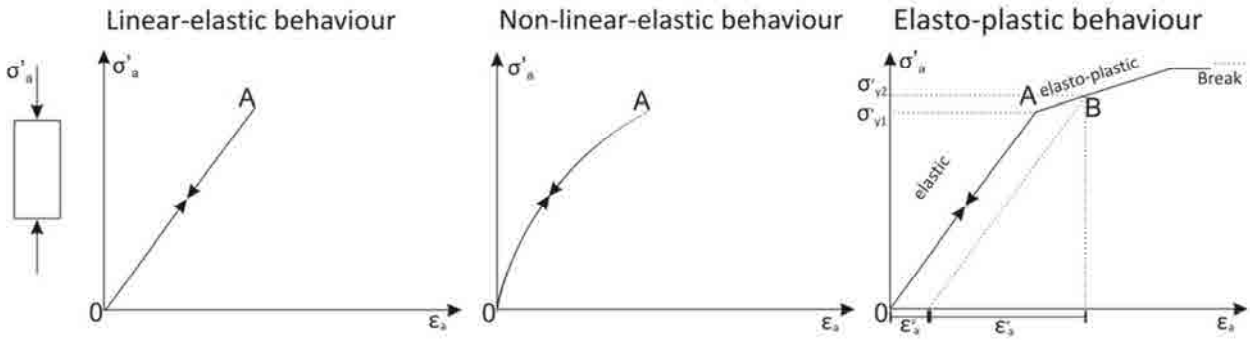

Figure 5.1: deformation-stress curves (modified from Lancellotta, 1993)

The pre-consolidation pressure overcoming, marks an increasing in the soil deformability and, consequently, in the occurred settlements and, for this reason, its determination is very important to the prevision of soil deformations. It can be determined through the mono-dimensional consolidation tests (UNE, 1994) using the oedometer cell (fig.5.2).

5.1.3. Oedometer test

The oedometer test, first proposed by *Terzaghi*, consists in the application of a sequence of different loads to a soil sample laterally confined where the water flow is allowed only in the vertical direction. In this way, it reproduces the one-dimensional consolidation conditions (namely, deformation and drainage conditions) that soils experience in situ. In fact, measuring the sample deformation response, (allowing the water movement out of the soil), the test permits to know how a soil in situ deforms in response to a change in effective stresses.

It is composed of rigid confining rings (which contain the soil sample) and of porous stones placed on the top and bottom (Fig.5.2). A rigid loading cap is then placed on the top of the upper porous stone.

The rings avoid the sample lateral displacement and the porous stones allow the drainage in the vertical direction.

At first, observing the deflection value over time data, it can be determined when the sample has reached the end of primary consolidation. Then, the load vertical increments ($\Delta\sigma'_v$) are applied using a geometric progression ($\Delta\sigma'_v = 25; 50; 100; 200; 400; 800; 1600\ kN/m^2$), starting from the condition $\Delta\sigma'_v/\sigma'_p = 1$.

After this phase, the sample is discharged using the half of the loading intervals introduced above ($\Delta\sigma'_v$=25; 100; 400; 1600 KN/m^2). The system of sample-rigid rings-porous stones is contained in a receptacle of water to prevent the soil drying and to give it water in this discharge phase.

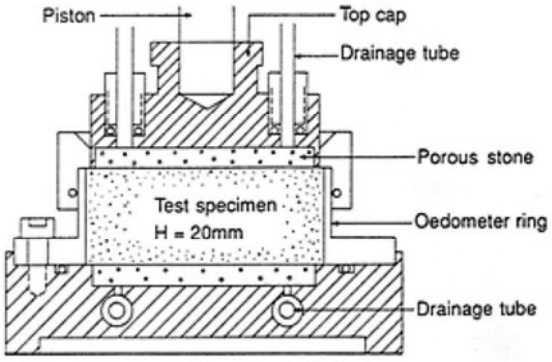

Figure 5.2: oedometer cell (http://www.ngi.no/)

To each loading step, corresponds a vertical change in the sample height (ΔH) related to the change of the void ratio (*e*). The void ratio is defined as the ratio of the volume of voids to that of solids (soil grains). Considering that the oedometer test is carried out impeding the lateral deformations, the following relation between the vertical deformation ("*axial strain*",ϵ_v) and the void ratio exists:

$$\epsilon_v = \frac{\Delta H}{H_0} = \frac{e_0 - e}{1 + e_0} \tag{5.12}$$

where H_0 and e_0 are respectively the initial sample's height and the void ratio.

The results of the test, can be reported in a *stress-deformation curve* represented in Figs.5.3 and 5.4. These allow to know the stiffness properties of the soil in normal-consolidated and over-consolidated condition and to determine the *coefficient of volume compressibility* (m_v) and the *coefficient of consolidation* (c_v).

The typical representation of the results is obtained reporting effective stress against the void ratio in a semi-logarithmic diagram (called "*oedometer curve*") and represented in fig.5.3. It presents two branches: the first is the elastic branch, correspondent to low recoverable deformations and the second is the load branch and occurs when the soil is affected by higher stresses, generating plastic non-recoverable deformations.

In the first part of the curve (AB), called "*recompression curve*", the soil has a non-linear elastic behaviour characterized by a low deformability, function of the vertical effective stress σ'_v. When this stress overcomes the pre-consolidation pressure (B), the soil deformability increases; in the BC part of the curve

(called "*compression curve*"), the deformations are both elastic and plastic. A soil which is currently experiencing its highest stress is said to be normally consolidated (NC) and has an *over consolidation ratio* (OCR, defined as the ratio between the highest stress experienced and the current stress) equal to one. If the soil is in a normal-consolidated state, the void ratio is a linear function of the logarithm of the effective stress. This means that, in the semi-logarithmic diagram in fig.5.3, the NC compression curve is represented by a straight line, having a slope called *compression index*. It represents a measure for the sediment compressibility in the NC state and is equal to:

$$C_c = \frac{\Delta e}{\Delta ln(\sigma'_{v\,NC})} \tag{5.13}$$

When the specimen is discharged (CD), the elastic part of the deformation is recovered, the OCR is greater than one and the soil is defined over-consolidated (OC). The section CD is called *swelling curve* and, in the semi-logarithmic diagram in fig.5.3, is represented by a straight line with a slope of:

$$C_s = \frac{\Delta e}{\Delta ln(\sigma'_{v\,OC})} \tag{5.14}$$

where Cs is called *swelling index.*

If the soil is reloaded, it "remembers" the previous history, and follows the unloading curve consolidating again with a deformability defined by the swelling index Cs. This occurs until the point C which represents the maximum stress it has been affected during its loading history.

This stress, in the first cycle has been the responsible of the plastic deformations occurred and its new passing signs the change from the elastic soil behavior on the recompression curve DC and the elasto-plastic of the compression curve.

Furthermore, the soil is called under-consolidated immediately after the application of a new load, but before the excess pore water pressure has had time to dissipate (in this case OCR<1).

The oedometer curve allows the knowledge of the pre-compression pressure (which separate the two branches) and of the compression indexes Cc and Cs which can be used to predict the amount of consolidation.

Among various method proposed to the pre-consolidation pressure computation, the most diffusely used is that proposed by Casagrande in 1936. According to this method, in correspondence of the point of maximum curvature (M) of the oedometer curve in Fig.5.3, an horizontal line and the tangent to the curve have to be traced. The bisector of this two line intersects the extension of the linear part of the loading

branch of the oedometer curve, in a point (i) correspondent to the pre-consolidation pressure.

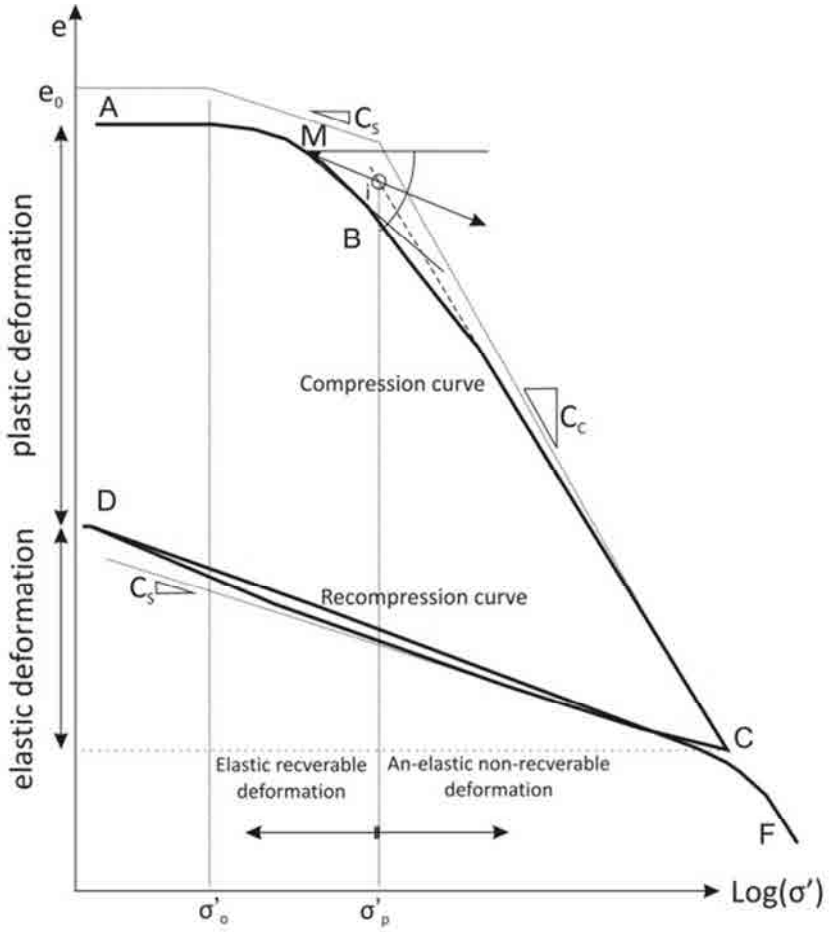

Figure 5.3: Oedometer curve (modified from Tomàs, 2009)

Through the oedometer test, is possible to introduce others three important parameters to define the soil deformability which are the compressibility coefficient m_v, and the compressibility index a_v (eq.5.15) and the oedometer modulus *M* (eq.5.16).

$$m_v = \frac{\Delta \epsilon_v}{\Delta \sigma'_v} a_v = \frac{\Delta e}{\Delta \sigma'_v} \tag{5.15}$$

$$M = \frac{1}{m_v} \tag{5.16}$$

The *Oedometer modulus* M is defined as the slope of the $\epsilon_v; \sigma'_v$ curve and represents the soil stiffness under geostatic conditions. In the case of NC soils, a linear relationship between modulus M and the effective stress σ'_v occurs. The three parameters depend on the stress level because in the $\epsilon_v - \sigma'_v$ and $e - \sigma'_v$ planes, the stress-deformation relationship are markedly non-linear (fig.5.4).

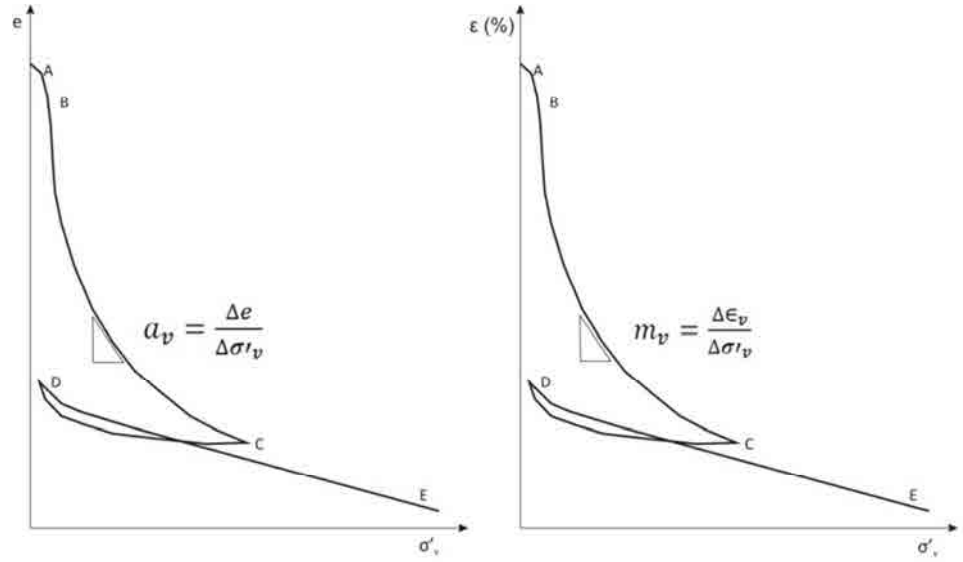

Figure 5.4: stress-deformation graphs (modified from Lancellotta, 1993)

Considering the equations 5.12, 5.13 and 5.15, is then possible to relate the compressibility coefficient to the compression index (eq. 5.18).

$$m_v = \frac{\Delta e}{\Delta \sigma'_v \cdot (1+e_0)} \cdot \frac{0.435 \cdot \Delta log(\sigma'_v)}{\Delta ln(\sigma'_v)} = \frac{0.435 \cdot C_c}{(1+e_0)} \cdot \frac{\Delta \sigma'_v}{\sigma'_v} \cdot \frac{1}{\Delta \sigma'_v} \quad (5.17)$$

$$m_v = \frac{0.435 \cdot C_c}{\sigma'_v \cdot (1+e_0)} \quad (5.18)$$

5.1.4. The consolidation process

According to Terzaghi (1923): *"… consolidation is any process which involves decrease in water content of a saturated soil without replacement of water by air"*.

Therefore, consolidation represents the phenomenon that implies the settlement of soils caused by a load application. This deformation is not instantaneous, because is due to the gradual adaptation of the solid grains and of the interstitial water to the force changes. As introduced above, the mechanisms which govern the time development of the deformations depend on the effective stress variations; these are function of the temporal dissipation of the water over-pressure which depends on the soil deformability, but mainly on its permeability K.

For the importance of this parameter, soils are divided in *coarse-grained* (having a great permeability: $K>10^{-6}$ m/s) and *fine-grained*. The first ones are like an open system, where the flow is free to occur and the interstitial water over-pressure is dissolved in a very short time. In this case, the soil behaviour can be

analysed in drained conditions, considering the hydrostatic water condition or that of stationary flow. For the fine-grained soils, is not possible to analyse the consolidation process without to consider the water transient flow which is necessary to the pore over-pressure dissipations. During this flow (consolidation process), there is a change in the soil deformability, strength and effective stresses. At the end of this process, the soil will be in drained conditions.

Usually time displacement development results, as confirmed by a lot of literature cases, more rapid than that obtained through the consolidation theory of Terzaghi (par. 4.1.4.1) because of its simplified hypothesis. In most cases, it is due to the geometry conditions which does not correspond to a mono-dimensional case (Lancellotta, 1993); in fact, the horizontal flow contributes to accelerate the water over-pressure dissipation.

For this reason, bi-dimensional or three-dimensional theories often results more appropriate to the modelling reliability. In the following (par. 4.1.4.2), the *Biot's poro-elasticity theory*, used in the present thesis, will be introduced.

To completely describe the water flow in a porous system, the following laws have been considered:

1. *Terzaghi law*, which represents the fundament of coupling between hydraulic and mechanical processes in geological media and which defines the effective stress (responsible of the soil deformations) as the total stress less the pore pressure (eq. 5.1);
2. *Continuity law*, for which the mass in a system remains constant in the time (eq. 5.19);
3. *Equation of state*, which represents a thermodynamic relation between the state variables of pressure, density and temperature (eq. 5.20);
4. *Equation of dynamic equilibrium*, equivalent to the Newton's law.

About items 2, 3 and 4, we can observe the following:

***Continuity law*:**

Considering a water flow in a cubic element of soil, having a volume of $dx \cdot dy \cdot dz$, where $v_x \cdot v_y \cdot v_z$ are the velocity components in the x, y, z directions, the difference between the entered and the exiting mass have to be equal to the mass variation of the soil element in the same time interval:

$$-\left[\frac{\partial}{\partial x}(\rho_w \cdot v_x)+\frac{\partial}{\partial y}(\rho_w \cdot v_y)+\frac{\partial}{\partial z}(\rho_w \cdot v_z)\right]\cdot dx\cdot dy\cdot dz=\frac{\partial}{\partial t}\left(\rho_w \frac{S\cdot e}{1+e}\cdot dx\cdot dy\cdot dz\right) \qquad (5.19)$$

where *S* and *e* are respectively the grade of saturation and the void ratio of the porous medium and ρ_w is the water density.

***State equation*:**

Considering the water density at the atmospheric pressure ρ_0 and the liquid compressibility β, the state equation is expressed as the following:

$$\rho_w = \rho_0 \cdot (1 + \beta \cdot u) \tag{5.20}$$

Through the combination of the equations 5.19 and 5.20, the following equation is obtained:

$$-\left[\frac{\partial v_x}{\partial x} + \frac{\partial v_y}{\partial y} + \frac{\partial v_z}{\partial z}\right] = \frac{3(1-2\nu)}{E'} \cdot \left(\frac{\partial u}{\partial t} - \frac{\partial p}{\partial t}\right) \tag{5.21}$$

Where $p = (\sigma_x + \sigma_y + \sigma_z)/3$

Equation of dynamic equilibrium

This equation represents the relation between the flow movement components and their causes; in particular, the flows accelerations in the x, y, z directions can be related to the pressure and gravity loads and to the viscous resistances. The equation 5.21 and the three equations of dynamic equilibrium represent the system of equation of *Navier-Stokes.*

This equations are solvable only in few cases with very simples boundary conditions. For this reason, to carried out fluid motion equations, the *Dancy's laws* (eq. 5.23) have been used.

$$v_x = -k_x \frac{\partial h}{\partial x}; v_y = -k_y \frac{\partial h}{\partial y}; v_z = -k_z \frac{\partial h}{\partial z} \tag{5.22}$$

Through the equations 5.21 and 5.22, the fundamentalfluid motion equation is achieved:

$$k_x \frac{\partial^2 h}{\partial x^2} + k_y \frac{\partial^2 h}{\partial y^2} + k_z \frac{\partial^2 h}{\partial z^2} = \frac{3(1-2\nu)}{E'} \cdot \left(\frac{\partial u}{\partial t} - \frac{\partial p}{\partial t}\right) \tag{5.23}$$

5.1.4.1. Terzaghi's equations

The *unidimensional Terzaghi's consolidation theory* allows the interpretation of the oedometer tests and an approximate analysis of the temporal soil settlements. In fact, the first limiting hypothesis of "mono-dimensional" consolidation conditions entail that both deformations and flows occurred in only one direction. The hypothesis of this theory can be resumed as the following:

- → The soil is homogenous and fully saturated;
- → The solid particles and water are incompressible;
- → The compression and flow are one-dimensional (vertical);
- → Strains are small;
- → Darcy's law is valid at all hydraulic gradients;
- → The coefficients of permeability (k) and of volume compressibility (m_v) remain constants throughout the process;
- → There is an unique relationship, independent of time, between void ratio and effective stress.

Starting from the continuity equation (eq. 5.19), it is possible to note that the ratio $dx \cdot dy \cdot dz/(1+e)$ represents the solid volume; for as much as it is constant in the time, and as the flow is produced only by a pore pressure variation, the 5.19 can be simplified as reported in the eq. 5.25

$$\frac{K}{\gamma_w} \cdot \frac{\partial^2 u}{\partial z^2} = \frac{1}{1+e} \cdot \frac{\partial e}{\partial t} \tag{5.24}$$

Assuming that the consolidation process does not change in the time (that is to say that $\partial \sigma'_v / \partial t = -\partial u / \partial t$), the 5.20 becomes:

$$c_v \cdot \frac{\partial^2 u}{\partial z^2} = \frac{\partial u}{\partial t} \tag{5.25}$$

which describes the spatial-temporal variation of pore pressures (u) through the primary consolidation coefficient c_v dependent upon the permeability K, the volume weight of water γ_w and the compressibility ratio m_v

$$c_v = \frac{K}{\gamma_w \cdot m_v} \tag{5.26}$$

The 5.25 governs the filtration in a transition regime. Its solution depends on the initial distribution of the interstitial water over-pressure and on the drainage boundary conditions. Considering the simple case represented in figure 5.5, where the pore water over-pressure is constant with depth and the clay layer is

between two draining layers, (namely the same conditions occurring in the oedometer test), the following solution of the Terzaghi's equation 5.25 is achieved.

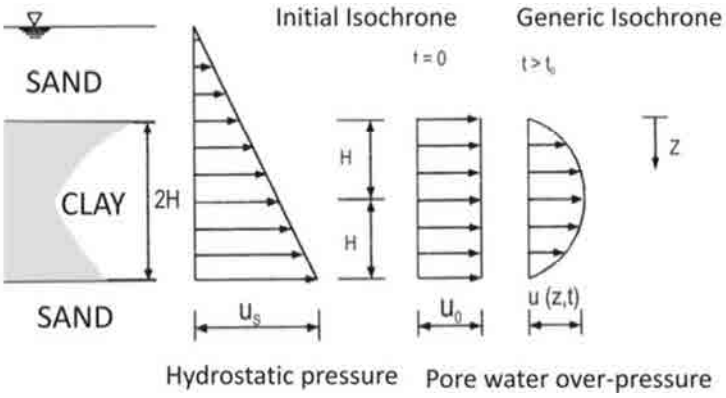

Figure 5.5: Initial isochrones, constant with depth (modified from Lancellotta, 1993)

Using the a-dimensional variables:

$$T_v = \frac{c_v \cdot t}{H^2} \quad \text{and} \quad Z = \frac{z}{H} \tag{5.26}$$

where H represent the maximum flow path of the water particle, the 5.25 becomes:

$$\frac{\partial^2 u}{\partial Z^2} = \frac{\partial u}{\partial T_v} \tag{5.26}$$

The analytic solution of the equation 5.26 was proposed by *Taylor* in 1948 and allows to calculate, if c_v is known, the water pore over-pressure value *u(z, t)* at a depth z and in an instant t.

$$u(z,t) = \sum_{m=0}^{\infty} \frac{2u_0}{M} (\sin MZ) \cdot e^{-M \cdot T_v} \tag{5.27}$$

where $M = \frac{\pi}{2}(2m+1)$ and u_0 is the initial pore over-pressure

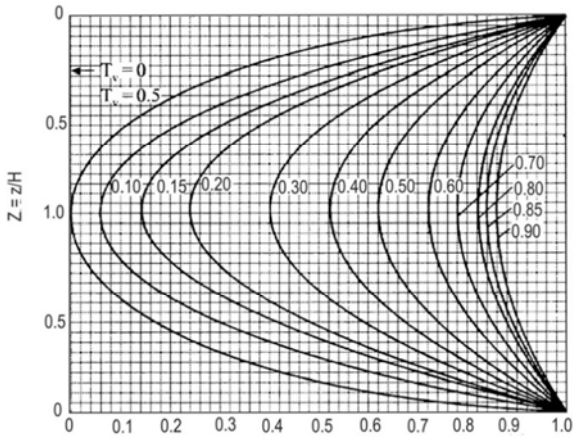

Figure 5.6: Consolidation grade Uz for various isochrones (drainage allowed in the two directions)

The equation solutions are often represented in function of the T_v (a-dimensional time) and of the consolidation grade U_z, defined as the ratio between the dissipated over-pressure and the initial one (eq. 5.28).

$$U_z = \frac{u_0 - u(z,t)}{u_0} \tag{5.28}$$

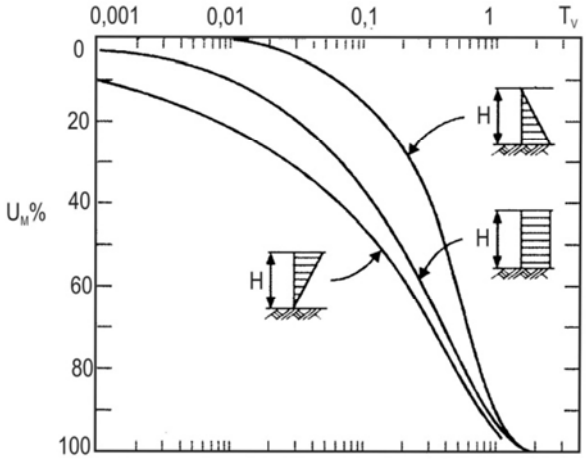

Figure 5.7 Average consolidation grade for various initial isochrones (Janbu et al., 1956)

In the simplified case of figure 5.5, the solution of the equation 5.26 is reported in table 5.1

U	0	5	10	15	20	25	30	35	40	45	50	55	60	65	70	75	80	85	90	95	100
Tv	0	0	0.01	0	0	0.05	0.07	0.1	0.13	0.16	0.2	0.24	0.29	0.34	0.4	0.48	0.57	0.68	0.85	0.13	∞

Table 5.1: U-Tv values in the case of isochrones constant with depth

The consolidation coefficient c_v can be determined through the oedometer test results. In fact, these can be reported in a deformation-time diagram (t, U_z).

Plotting the deformation of the specimen versus the time for a given loading increment, (Fig. 5.8), three distinct stages are obtained, which may be divided in:

1. ***Instantaneous initial deformations:*** plastic deformations due to the presence of bubbles in the sample and takes place in a consolidation test between the instant of application of the load and the beginning of the primary consolidation phase.
2. ***Primary consolidation***: The sample deformations in this phase are due to the water drainage and pore pressure dissipation.
3. ***Secondary consolidation:*** In this phase the viscous deformations occur.

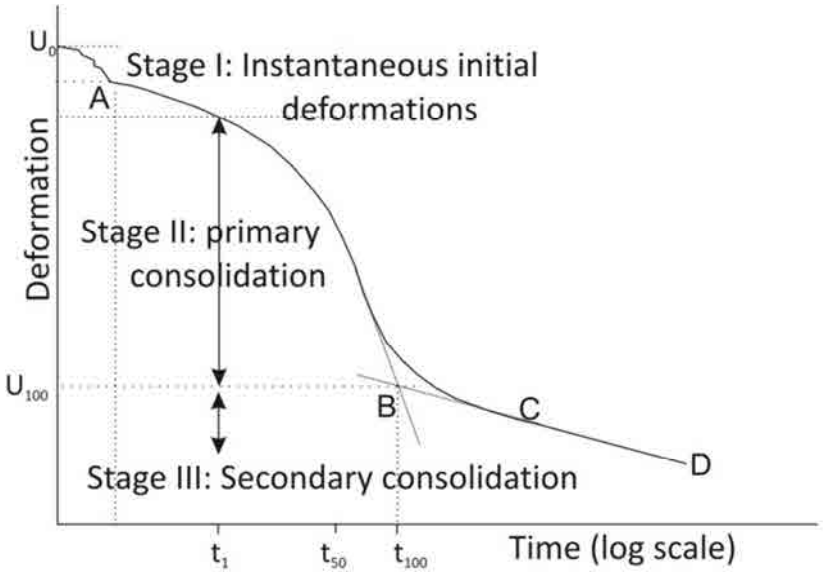

Figure 5.8. oedometer test time-deformation curve (modified from Lancellotta, 1993)

Only the deformations obtained between the point A and B in fig.5.8 allow to achieve the oedometric curve (log σ'_v– e) previously described in figure 5.3. This geometric construction was proposed by *Casagrande,* (1936) and allows to separate the primary to the secondary consolidation displacements. The tangent in the point of maximum inflection of the deformation-time curve intersects the extension of the final straight part of the graph, identifying the limit of the primary consolidation phase (which, on the time axis corresponds to t_{100}). The geotechnical parameters obtained from the oedometer tests are function of the deformations corresponding to a fraction of the t_{100}.

In particular, c_v can be achieved through two methods of Casagrande (1936) and Taylor (1948)

- *Casagrande's method*

According to this method, c_v is achieved considering the time to obtain a drop of the specimen in the 50% respect to its initial high.In this case, results $T_v = 0.197; U = 50$ (Tab. 5.1).

$$c_v = \frac{H^2 \cdot 0.197}{t_{50}} \quad \text{per } \Delta H_{50} = \frac{\Delta H_{100}}{2} \tag{5.29}$$

- *Taylor's method*

Plotting the displacements against $\sqrt{t}$, the obtained curve can be interpolated as a straight line and by trial, have to result $X_{AC} > 0.15 X_{AB}$ (fig.5.9). Intersecting AB with the curve,t_{90} is obtained (T_v=0.848 from table 1) and c_v results equal to:

$$c_v = \frac{H^2 \cdot 0.848}{t_{90}} \quad \text{per} \quad \Delta H_{100} = \frac{10}{9} \Delta H_{90} \tag{5.30}$$

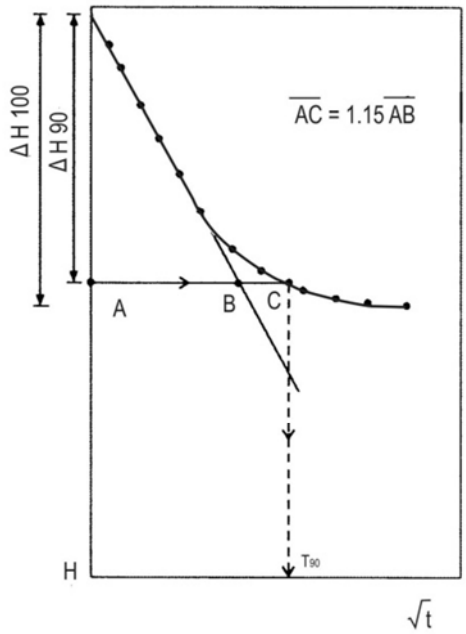

Figure 5.9: Taylor method (extract from Lancellotta, 1993)

5.1.4.2. Biot's elastic theory

In 1941, Biot formalized the three dimensional consolidation for an elastic porous medium writing the *pore-elasticity theory*.

In case of porous, elastic and isotropous medium, the general move equation 5.23, (obtained taking into account the flow continuity condition, state equation and dynamic equilibrium of the pore pressure), can be written as the following:

$$\frac{K \cdot E'}{3\gamma_w(1-2\nu)} \cdot \left[\frac{\partial^2 u}{\partial x^2} + \frac{\partial^2 u}{\partial y^2} + \frac{\partial^2 u}{\partial z^2} \right] = \frac{\partial u}{\partial t} - \frac{\partial p}{\partial t} \tag{5.31}$$

That, in the three-dimensional case, can be express as:

$$c_3 \cdot \nabla^2 u = \frac{\partial u}{\partial t} - \frac{\partial p}{\partial t} \tag{5.32}$$

$$c_3 = \frac{K \cdot E'}{3\gamma_w(1-2\nu)} \tag{5.33}$$

furthermore in the bi-dimensional case:

$$c_2 \left[\frac{\partial^2 u}{\partial x^2} + \frac{\partial^2 u}{\partial z^2} \right] = \frac{\partial u}{\partial t} - \frac{1}{2} \frac{\partial}{\partial t} (\sigma_x + \sigma_z) \tag{5.34}$$

$$c_2 = \frac{K \cdot E'}{2\gamma_w (1-2\nu)(1+\nu)} \tag{5.35}$$

And in the unidimensional case:

$$c_1 \frac{\partial^2 u}{\partial z^2} = \frac{\partial u}{\partial t} - \frac{\partial \sigma_z}{\partial t} \tag{5.36}$$

$$c_1 = \frac{K \cdot E' \cdot (1-\nu)}{\gamma_w (1-2\nu)(1+\nu)} \tag{5.37}$$

where c_3, c_2 and c_1 are respectively the three-dimensional, bi-dimensional and mono-dimensional consolidation coefficients, and depend to the soil permeability K.

In the three-dimensional case, the equation 5.32 have to be solved coupled with equation of *Navier* to obtain the system of 4 equations and 4 variables (u and three displacement components $\varrho_x, \varrho_y, \varrho_z$), showed in the eqs. 5.38- 5.41.

$$G \cdot \nabla^2 \varrho_x + \frac{G}{1-2\nu} \cdot \frac{\vartheta \epsilon_v}{\vartheta x} - \frac{\vartheta u}{\vartheta x} = 0 \tag{5.38}$$

$$G \cdot \nabla^2 \varrho_y + \frac{G}{1-2\nu} \cdot \frac{\vartheta \epsilon_v}{\vartheta y} - \frac{\vartheta u}{\vartheta y} = 0 \tag{5.39}$$

$$G \cdot \nabla^2 \varrho_z + \frac{G}{1-2\nu} \cdot \frac{\vartheta \epsilon_v}{\vartheta z} - \frac{\vartheta u}{\vartheta z} = 0 \tag{5.40}$$

$$\frac{K}{\gamma_w} \cdot \nabla^2 u - \frac{\vartheta \epsilon_v}{\vartheta t} = 0 \tag{5.41}$$

Where:

$$\epsilon_{v=} \frac{\vartheta \varrho_x}{\vartheta x} + \frac{\vartheta \varrho_y}{\vartheta y} + \frac{\vartheta \varrho_z}{\vartheta z} \tag{5.42}$$

The system of equations 5.32, 5.38, 5.39, 5.40, 5.41 represents the three-dimensional consolidation theory of Biot (1935, 1941) which expresses the time dependent coupling behavior between the solid matrix and the interstitial fluids.

5.1.4.3. Subsidence due to water exploitation

5.1.4.3.1 Cause-effect hydrogeological mechanism

An aquifer is an underground layer of water-bearing permeable rock or unconsolidated materials from which groundwater can be extracted using a water well. Typical aquifers are gravel, sand, sandstone, limestone, and fractured igneous and metamorphic rock. If the aquifer is confined by low-permeability layers (*aquitard*), the reduced water pressure causes slow drainage of water from the adjoining confining layers.

If these aquitard layers are composed of compressible silt or clay, the loss of water to the aquifer reduces its pore pressure, causing it to compress by the effective overpressure of overlying geologic materials. In severe cases, this compression can be observed on the ground surface as subsidence.

In the hydrogeological simplified scheme in figure 5.10, a gravel and a clay layers, which respectively constitute the aquifer and the aquitard, have been reported.

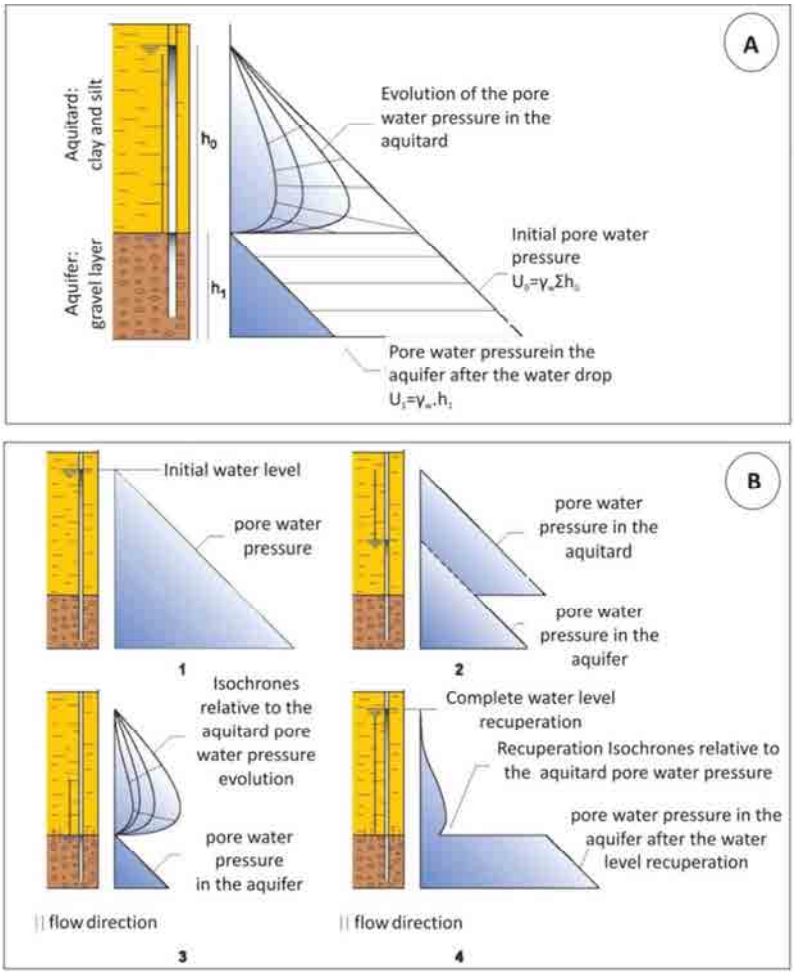

Figure 5.10: Simplified hydrogeological scheme (A); Pore water pressure evolution due to the underground water exploitation (B) (modify from Mulas et al., 2010)

Before the exploitation, the soil is considered saturated and in an hydrostatical equilibrium state. The water exploitation in the gravel layer provokes a sudden decrease of the pore water pressure in the deep permeable aquifer.

In a first phase, the water exploitation only decrease the aquitard recharge where an hydrostatical pore water pressure distribution continues to persist (Fig. 5.10b). In a second phase it annuls the aquitard recharge and starts to take water from it, decreasing the pore water pressure according to the isochrones in figure 5.10b (3).The vertical flow established between aquifer and aquitard is due to a gradient of the pore water pressure; the different permeability of the two layers governs the velocity of the pore water overpressure dissipation (and the different evolution in their distribution).Therefore, the consolidation process established in the aquitard is not instantaneous because of the low permeability of its soils which does not allow an immediate pore over pressure dissipation. A further water up-lift causes a flow in the opposite direction; in this case, the isochrones evolution has to reach the original equilibrium state.

Usually real aquifers are not elastic because the consolidation process changes the grains distribution which cannot come back completely to the original configuration (Fig. 5.11). For this reason, a part of the produced subsidence cannot be recovered and the compressed aquifer suffers a permanently reduced capacity to hold water.

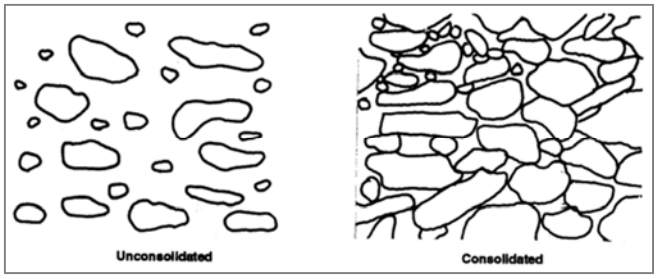

Figure 5.11: Effects of consolidation on porosity and permeability (http://www.globalsecurity.org/)

Considering the figure 5.10b (3 and 4) and supposing h_1 as the water level historical minimum, the water up-lift phase provokes the soils overconsolidation. As explained in the previous paragraphs, the OCR is defined as the ratio of maximum past pressure (pre-consolidation pressure) to the current effective stress (eq.5.43). In the case of figure 5.10b (4), soils should have an overconsolidation ratio equal to:

$$OCR = \frac{\sigma'_1}{\sigma'_0} = \frac{\sigma'_0 + \Delta\sigma}{\sigma'_0} = 1 + \frac{(h_0 - h_1)\cdot\gamma_w - (h_0 - h_1)\cdot(\gamma_{sat} - \gamma)}{\sigma'_0} \tag{5.43}$$

However, in this case, because of the delay between the piezometric head changes and the aquitard consolidation, this expression overestimate the OCR (Tomás, 2009).

This has been observed in several aquifers where, to a great piezometric head decrease, corresponded a fewer pre-consolidation pressure in the aquitard layers.

For this reason, the characteristics of the deformations affected an aquifer, results of great interests to well understand the subsidence cause-effect mechanism and to implement the predictive models. Therefore, as referred by Tomás, 2009, several studies have been carried out to compare the real measured deformations occurred in the aquitard and the piezometric level variations in the aquifer (Riley, 1969; Poland et al., 1975; Helm, 1976; Holzer, 1981; Ireland et al., 1984; Riley, 1984; Burbey, 2001; Zhang et al., Burbey, 2003; 2007a; Zhang et al., 2007b; Shi et al., 2007, Tomás et al, 2009, 2010, 2011).

Among these, in the case of Murcia city (Tomás et al., 2010), permeability laboratory tests taken under five undisturbed silty and clayey samples have shown a very low and variable permeability values (from 8.20×10^{-11} to 6.24×10^{-8} m/s) which have to correspond to a slow consolidation process. From the analysis of the piezometric level comparison of two cells piezometers installed in aquitard and aquifer level in Murcia City by the Confederación Hidrográfica del Segura (CHS, 2007) in (Fig. 5.12), a very similar response has been manifested. This has been probably due to the presence of several sand layers intercalated immediately over the aquifer gravels layer (fig. 5.10) which have favoured water drainage.

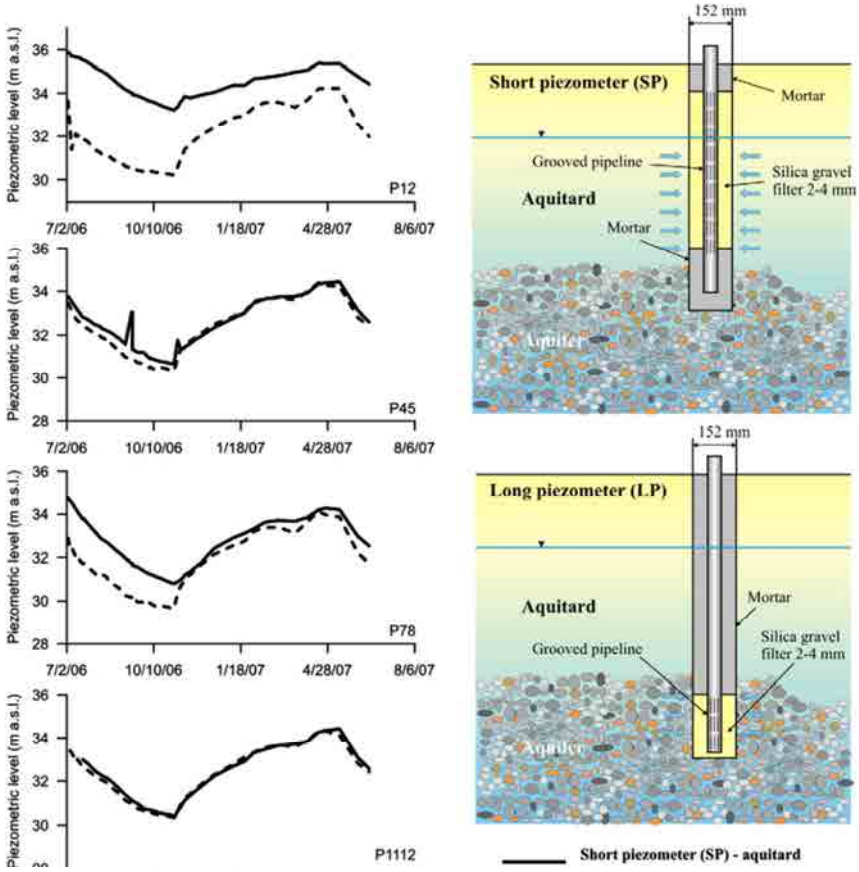

Figure 5.12: Temporal evolution of piezometric level and installation scheme of multilevel piezometers of the city of Murcia (Tomás et al., 2011).

5.1.4.3.2. Subsidence models of soil response to the water exploitation

The case of subsidence caused by underground water exploitation has been studied by several authors (Janbu, 1987; De Simone and Viggiani, 1978; Rivera et al., 1991;De Justo and Vázquez, 1999; Vázquez, 2001; Vázquez and De Justo, 2002a; Vázquez and De Justo, 2002b; De Justo and Vázquez, 2003).

According to De Justo and Vázquez, 1999, the unidimensional consolidation equation can be expressed as the following:

$$k_v \frac{\partial^2 u}{\partial z^2} + \gamma_w m_v \frac{\partial \sigma}{\partial t} \gamma_w (m_v + n\beta) \tag{5.44}$$

and relate to a coefficient, i.e. "*specific storage coefficient*" S_{sk} (eq. 5.45); it is defined as the volume of water released from storage from a unit volume of aquifer per unit decline in hydraulic head.

$$S_{sk} = \gamma_w (m_v + n\beta) \tag{5.45}$$

where β represents the water compressibility, almost negligible.

The specific storage coefficient represents, in other words, the aquitard deformability. As described above, in the case of water overexploitation, when the pre-consolidation pressure (namely the highest pressure suffered by the soil along its life) is overcome, a part of the produced deformation is not recoverable; in this case, the water released from storage derives from an inelastic compaction of the aquitard. Fine-grained sediments that constitute the confining and interbedded aquitards may deform both elastically and an-elastically. To define the capacity of the whole aquifer system to release groundwater, the skeletal storage coefficients S_k can be introduced. It is function of the thickness of the aquifer system *b* and of the skeletal specific storage S_{sk} (eq. 5.46) and varies with the stress state; so can be defined for the elastic and inelastic ranges of stress.

$$S_k = S_{sk} \cdot b \tag{5.46}$$

The aquifer skeletal storage S_k can be calculated (Riley, 1969) as:

$$S_k = \frac{\Delta b}{\Delta h} \tag{5.47}$$

where Δb represents the change in the aquifer thickness (by means the subsidence) and Δh the water level variation. Riley proposed a graphical methodology to the skeletal storage computation, consisting in the determination of the slope of the branch of the stress–strain curve (elastic or anelastic).

This methodology has been used also by Hoffman, (2003); Hoffmann et al., (2003); Schmidt and Bürgmann, (2003); Galloway and Hoffmann, (2007).

CHAPTER VI

Case studies

CHAPTER VI. Case studies

6.1. Murcia case study: introduction and phenomenon description

Murcia city is located in the in the flood plain of the Segura River Valley (SE Spain) called "*the Vega Media*"; it represents the first reported case of ground subsidence induced by water withdrawal in Spain (Mulas et al., 2003). In particular, in the metropolitan area of Murcia City, this phenomenon caused damage to structures and infrastructures (Martínez et al., 2004; Rodríguez Ortiz and Mulas, 2002; Mulas et al., 2003) with an estimated cost of more than 50 million euros in the years '90s. Consequently, a monitoring network of extensometers and piezometers was installed in order to understand the cause-effect mechanisms of this phenomenon to better plan the subsequent water resources exploitation and the land use management. In particular, the temporal evolution of the subsidence in Murcia city has been monitored by an extensometer network since 2001 (Mulas et al., 2001, 2005; Peral et al., 2002). Additionally, groundwater table has been measured since 1974 (Aragón et al., 2004) through a spatially dense piezometric network. The observed historical piezometric drawdown, occurred in the periods 1980–1983, 1993–1995 and 2006–2008, presents a maximum fall of 13 m of the groundwater level, which is resulted to be correlated with the temporal evolution of ground surface displacement estimates. Since 2008 the recuperation of the aquifer has led to an uplift of the ground.

Thus, in the past 20 years, a great amount of studies have been carried out to understand the cause-effect mechanism of the phenomena, which have been reported in the following paragraph.

6.1.1. Previous studies

Subsidence case of Murcia City has been studied since the '90, when severe structural fractures affected the buildings of the metropolitan area (Fig. 6.1). For this reason, since 1996, several scientific studies have been published.

The firsts scientific works were two master thesis; one, carried out at the Department of Engineering Geology of the University of Madrid, entitled*: "Evolución piezométrica de Murcia. Consecuencias geotécnicas"* (Andrés Puche, 1996); the second, carried at the University of Alicante concerned some real cases of underpinning adopted in Murcia city have been described.

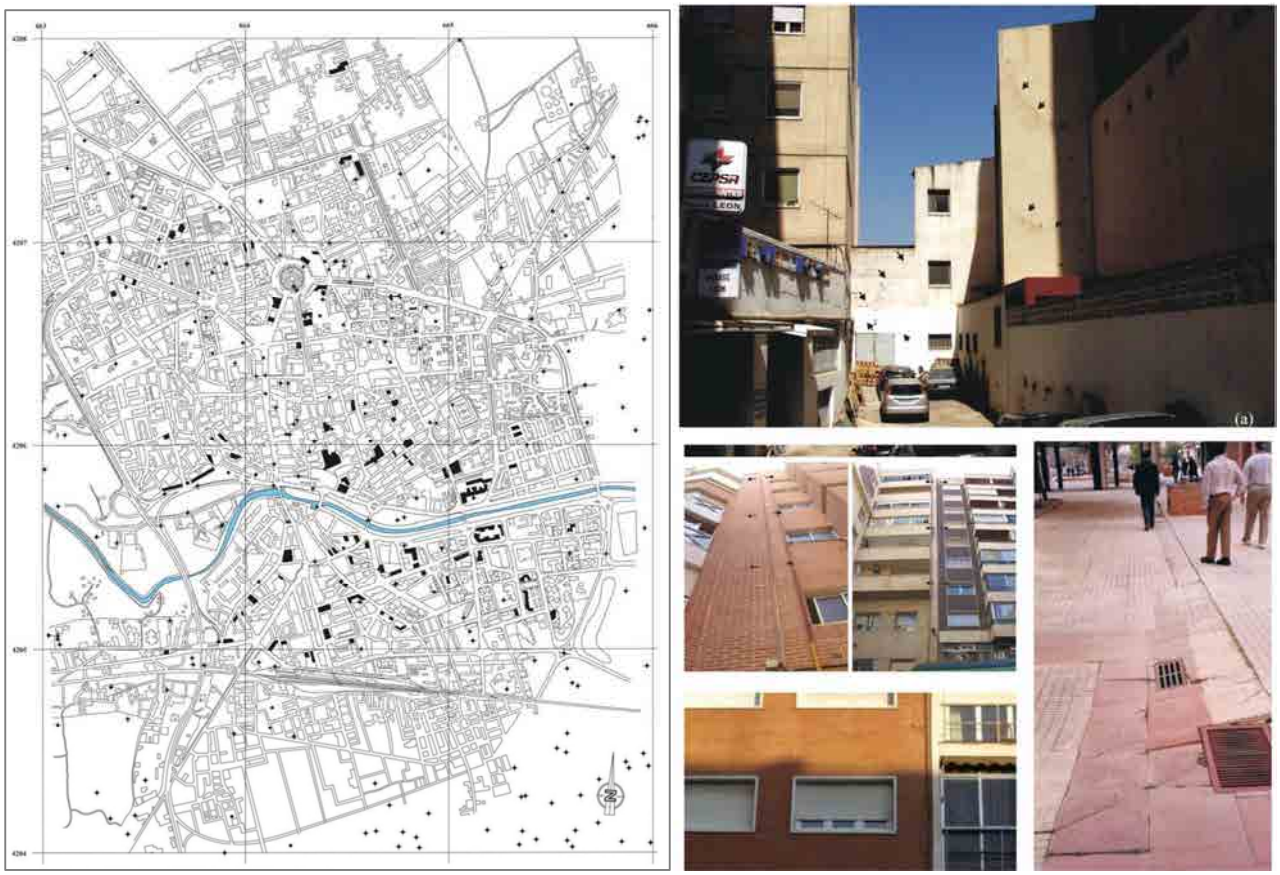

Figure 6.1: Damaged buildings map of Murcia city (extracted from Tomás, 2009; based on Mulas et al., 2003 and Vàzquez & De Justo, 2002a); some damaged buildings of the metropolitan area (on the right), (extracted from Tomás, 2009 and Mulas 2007).

Because of the intensity and the extension of the phenomenon, local authorities requested detailed studies about the subsidence cause-effect mechanism.

Among them, principal research works which gave a great contribution to the phenomenon analysis were carried out by the IGME (*Instituto Geológico y Minero de España*) on request of the *"Consejería de Obras Públicas y Ordenación del Territorio de la Región de Murcia"*.

In partitular, the following studies are cited:

- *Estudio geotécnico para el análisis, prevención y corrección de la patología constructiva derivada del cambio en las condiciones del subsuelo en la ciudad de Murcia (IGME, 2000a);*
- *Estudio geotécnico del Subsuelo del Área Metropolitana de Murcia (IGME, 2000b);*
- *Seguimiento y control instrumental de asentamientos del terreno en el área metropolitana de Murcia (IGME, 2001a);*

- *Estudio hidrogeológico del acuífero de las Vegas Media y Baja del Segura y su relación con los cauces naturales y artificiales de su territorio (IGME, 2001b);*
- *Geotechnical and hydrological analysis of land subsidence in Murcia (Spain), (Mulas et al., 2003);*
- *Proyectos de Seguimiento y Control Instrumental en un sector del Área Metropolitana de Murcia: Fase I (2001); Fase II (2005) Fase III (2009);*
- *Proyectos Terrafirma Pan European Ground Information Service: Phase I (2003-2006); Phase II (2006-2008) and Phase III (2008-20011);*
- *La subsidencia del terreno en la ciudad y área metropolitana de Murcia: Modelización, seguimiento y control (Mulas et al., 2010).*

Another important contribution to the phenomenon analysis was brought by several doctoral thesis, like *"Cálculo de la subsidencia unidimensional debido a los descensos de nivel piezométrico. Aplicación al casco urbano de Murcia y los efectos sobre los edificios",* (carried out by Narciso Jesús Vázquez in 2001, whose results were published in 2002 by Vázquez and De Justo) and "*Estudio de la subsidencia de la ciudad de Murcia mediante interferometría SAR diferencial avanzada*" carried out by Roberto Tomás in 2009, concerning the study of the soil consolidation due to the piezometric regime and an application of the DInSAR to study the Murcia city subsidence. The last mentioned PhD thesis was followed by several publications about the application of DInSAR techniques to the subsidence monitoring (Tomás et al., 2005, 2006, 2009, 2010a, b, 2011, 2012, 2013).

Therefore, about 20 years of proceedings, publications, thesis and reports have been produced which have done of Murcia a case study suitable to a multidisciplinary approach, thanks to the great amount of in situ data and validated models. In particular: De Justo and Vázquez, 1999; Rodríguez et al., 2000, 2002; Vázquez, 2001, 2002a, b; Mulas et al., 2001, 2002, 2003, 2004, 2005, 2010; Rodríguez, 2000, 2002; De Justo et al., 2003; García et al., 2003; Aragón, 2004; Martínez, 2004; Tomás et al., 2005, 2006, 2009, 2010a, b, 2011, 2013; Pardo, 2007, 2013; Herrera et al., 2008, 2009a,b, 2010; Bru, 2010, 2013; Tessitore et al., 2013).

Thanks to the technical documentations, geological, hydrogeological and geotechnical characterizations, subsidence models and DInSAR processing validated results (see par. 6.1.2), a great amount of information were available to the implementation of the work proposed in the present thesis.

The principal obtained information about the study area settings are resumed in the following.

6.1.2. Study area settings

The metropolitan area of Murcia city is located in the flood plain of the Segura River Valley (SE Spain) known as the Vega Media (VMSR). The majority of the plain (having a total surface of 206 km^2) is destined for cultivated land (Gumiel et al., 2001) and Murcia is the most populated city of the basin, registering in the '90 more than 1.000.000 inhabitants (which became about 1.400.000 in 2012).

For this reason, here the subsidence consequences were particular heavy, causing cracks in several buildings and sidewalks of the urban area (Fig. 6.1) since the 1991. Vázquez y De Justo (2002) individuated more than 100 damaged buildings well distributed in the whole urban area (Fig. 6.1).

Rodríguez Ortiz and Mulas (2002), Mulas et al., (2003) and Martínez et al., (2004) estimated the costs of 150 damaged buildings for a total amount of more than 50 million euros.

6.1.2.1. Geological settings

From a geological point of view, the study area is located in the eastern sector of the Betic Cordillera. A compressive stress field has acted since the Upper Miocene in this sector and has led to the development of a basin bounded by active faults, the Lorca – Alhama fault, to the north, and the Carrascoy - Bajo Segura fault, to the south (Montenat et al., 1990). The sedimentary record of the basin has been deformed simultaneously to its deposition, creating a broad syncline in which progressively younger sediments have been deposited.

The basement is made up by old (Permian and Triassic), deformed materials corresponding to the Internal Zones of the Betic Cordillera. These materials also crop out along the border of the Segura River Valley. The basin fill comprises Upper Miocene to Quaternary sediments that can be divided into three units.

Older materials (Upper Miocene) composed mainly by a thick sequence (more than 600 m) of marls (Cerón & Pulido-Bosch, 1996; Mulas et al., 2003). Above them, Pliocene-Quaternary rocks comprise marls and clays interbedded with several levels of gravels and sands, deposited in a continental environment that can reach 250 m at some places (Aragón et al., 2004). At the ground surface, recent continental (meander, channel, oxbow lakes, flood plain, alluvial fans, etc.) sediments are found. Silts and clays are abundant in flood plain and oxbow deposits, while sand is common in channel areas and in the alluvial fans formed in the reliefs that surround the valley (Fig. 6.2). Thickness of recent sediments varies between 3 and 30 m (Rodríguez-Jurado et al., 2000). Additionally, at some places anthropic deposits can be found on top.

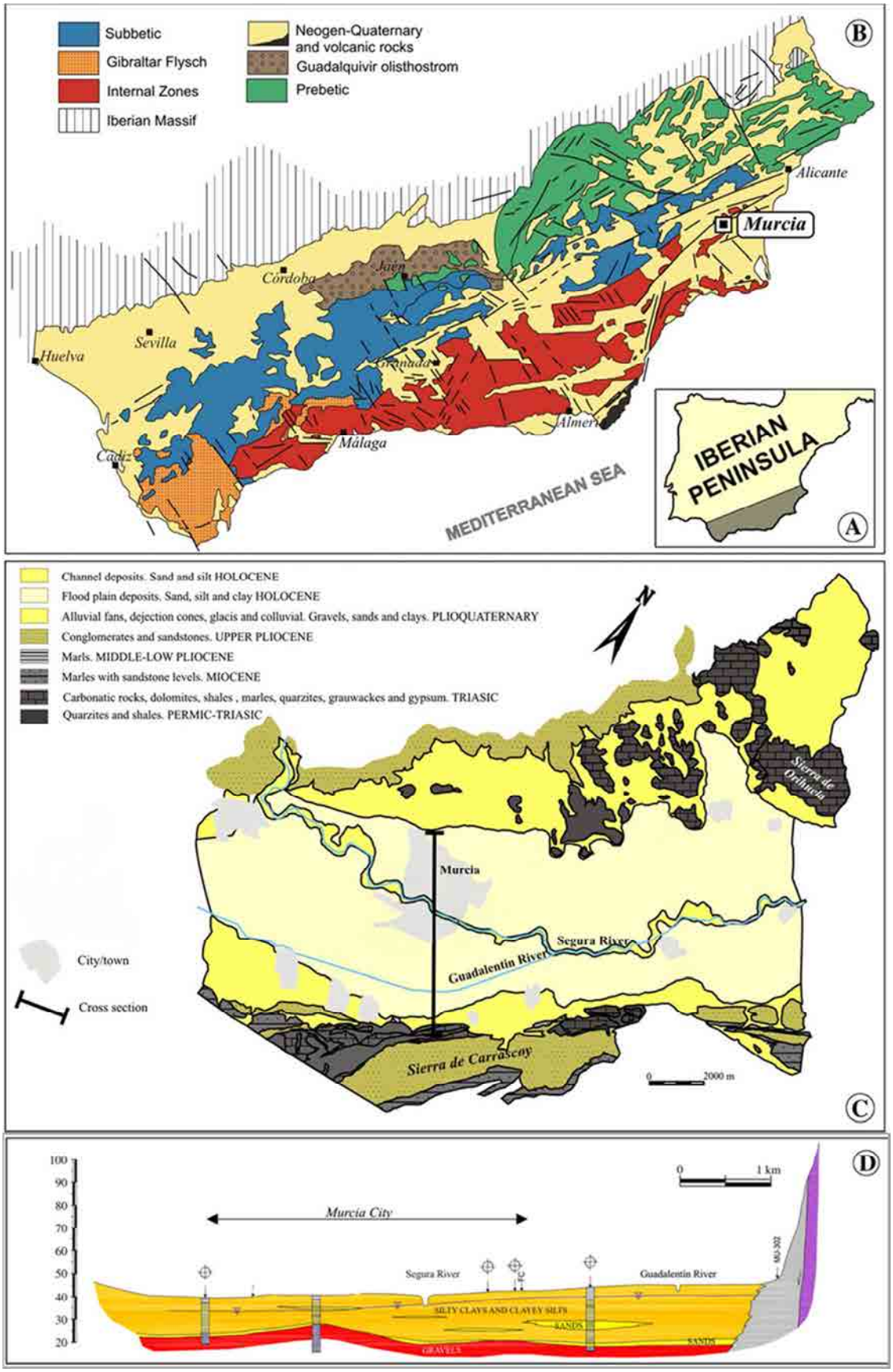

Figure 6.2: Geological setting of the study area (based on Montenat, 1977 and Aragón et al., 2004; extracted from Mulàs et al., 2003).

6.1.2.2. Hydrogeological and geotechnical settings

The materials which constitute the aquifer of the Vega Media correspond to a detritic layer which reaches a thickness of 250 m, dated between Pleistocene and the present in age (IGME 2002). In particular, the aquifer system is constituted by two units, a superficial aquifer and a deep one (Cerón & Pulido-Bosch, 1996; Aragón et al., 2004). The superficial aquifer comprises the first 5 to 30 m of recent clay, silt and sands facies (Fig. 6.2d), which represent the most compressible materials of the stratigraphic column and are susceptible to suffer consolidation due to variations (increase) of effective stresses acting on them.

The deep aquifer system, scarcely studied and located under the previous, is composed of a sequence of gravels and sands alternating with marls, clay and silts (Pleistocene to Pliocene in age).

In the upper part of the deep aquifer there is a gravel layer, 10 to 30 m thick, that has been intensively exploited since the '90s as an important water resource.

From a geotechnical point of view, this surficial gravel layer constitutes the plain substratum. These materials, in fact, are more rigid and are used as the support level for deep foundations; they can be found in the whole metropolitan area, with a thickness also higher than 10 m. The gravel layer can be interbedded by sandy clay layers with a power of 1-3 m (Mulàs et al., 2010). Sandy clay layers usually are found up to the gravel layer: from an hydrogeological point of view, they can be considered comparable to the sand layer. Locally, also clay intercalations can be found at a depth variable between 9 and 32 m. The minimum thickness of clay layers is in correspondence of the city centre. According to Tomás, 2009, sandy layers are not found in all the metropolitan area underground and their power (namely the total amount of the thickness of sand layers above the surficial gravel layer) results of 2.3±2.8 m (computed taking into account the available boreholes for the VMSR), with a maximum of 14 m. Above the sandy layers, a silty clay layer having a power varying between 11.8±5.9 m, with a maximum of 31.8 m is found. Its top is at a depth of 2.2±1.3 m from the ground surface and the bottom at 14.2 ± 5.5 m.

In 2004, other pumping wells have been drilled (CHS, 2007) extracting water from the lower gravel too. The piezometric level of the deep aquifer, located in the upper gravel, coincides with the one of the shallow unit in an undisturbed state (without pumping) (Tomas et al., 2011).

The water extraction triggers a gradient between the two aquifers that implies a water flow from the shallow unit to the upper gravels of the deep aquifer. This provokes a pore pressure declines in the superficial aquifer and consolidation process, affecting the medium to soft compressible materials of the surficial aquifer.

A geotechnical and hydrogeological characterization for the VMSR materials has been performed by Mulas et al., (2010) and used in the present thesis.

The parameters found in this study, were obtained from hydrogeological tests, in situ (SPT, CPT-CPTU) and laboratory tests (oedometers) and the stratigraphic records (ITGE and CPTOP, 2000).

Here, the VMSR has been divided into five sectors on the basis of a statistical regionalization (Fig.6.3).

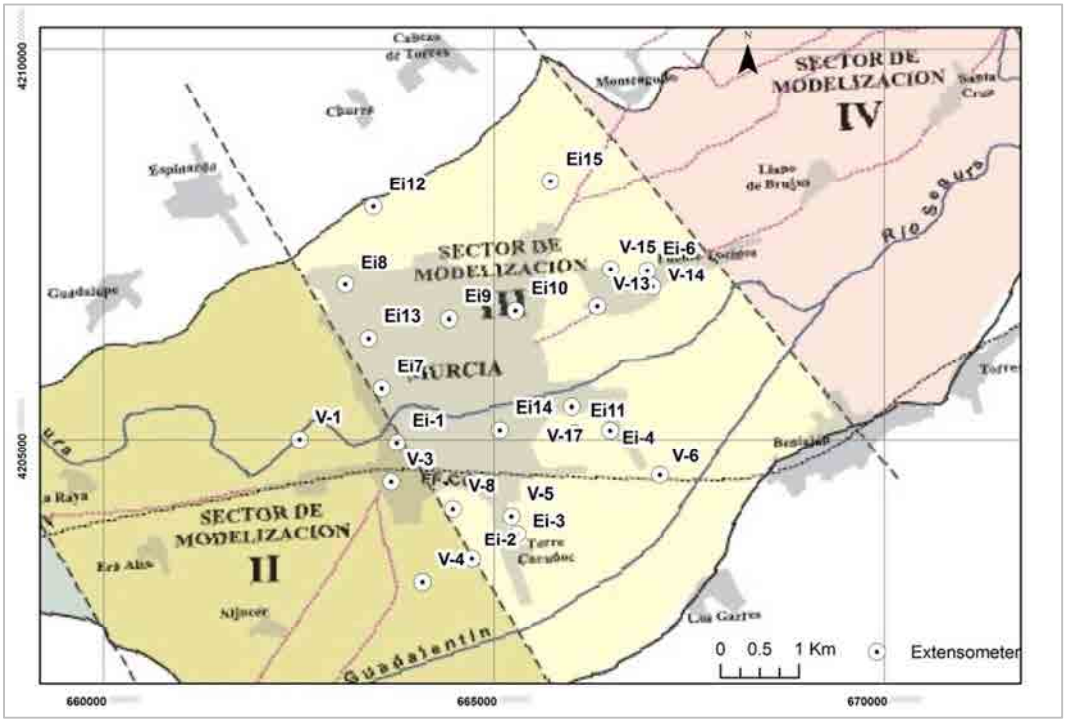

Figure 6.3: Murcia area subdivision on the basis of the geotechnical characterization (modified from Mulas et al., 2010)

According to this study, Murcia city metropolitan area is included between sectors II, III and "city center" whose permeability and rigidity found values, reported in table 6.1, result to be very different.

	City center				Sector II				Sector III			
	E (KN/m²)	γ_{sat} (KN/m³)	K_y (m/s)	ν	E (KN/m²)	γ_{sat} (KN/m³)	K_y (m/s)	ν	E (KN/m²)	γ_{sat} (KN/m³)	K_y (m/s)	ν
Clay	7500	20-20.3	$0.7\text{-}5.6\times10^{-10}$	0.35	10000	20	6.5×10^{-9}	0.35	13000	20	3.87×10^{-9}	0.35
Sand	15000-20000	20-20.8	$2.8\text{-}28\times10^{-9}$	0.3-0.35	15000-20000	20-20.8	$2.8\text{-}28\times10^{-9}$	0.3-0.35	15000-20000	20-20.8	$2.8\text{-}28\times10^{-9}$	0.3-0.35
Gravel	80000	21	2.8×10^{-6}	0.3	80000	21	2.8×10^{-6}	0.3	80000	21	2.8×10^{-6}	0.3

Table 6.1: Geotechnical properties of the metropolitan area of Murcia city (extract from Mulas et al., 2010). γ_{sat}: specific saturated weight; k_y: vertical permeability; E: Young's modulus; ν: Poisson's coefficient.

In the past 20 years, because of the intensity and the wideness of the consolidation process, manifested during the drought periods, the local authorities requested a detailed study of the aquifer system including a considerable number of boreholes (Fig. 6.4 b) and laboratory and "in situ" tests (Mulas et al., 2003).

6.2. Monitoring data

In this section all the available in situ (6.2.1) and radar data (6.2.2) are presented. Then, in the later section (6.2.3), SAR based estimations of deformation have been compared with the ground based measurements and piezometric data.

6.2.1. In situ monitoring

In the study area, a monitoring network of extensometers and piezometers has been installed and implemented during the years. It consists of overall 31 extensometers and 85 piezometers in the area reported in Fig. 6.4. (The ground data's references are reported in the acknowledgement's subsection).

6.2.1.1. Piezometers data analysis

The piezometer network of the VMSR was installed in 1974, and extended in different epochs (1994, 1998, 2000, 2008 see Fig. 6.5). Before 1994, only three piezometers were placed around the city of Murcia and P-1, located several kilometres from the city, was the closest and more representative for the urban area (Figure 6.4d). After this period overall 64 new piezometers were installed (34 between 1994 and 1995) and 7 piezometers are currently available in the urban area of Murcia.

The analysis of complete groundwater piezometric series shows that three important ground water level declines due to the water overexploitation and associated with important and prolonged drought periods affected the VMSR during 1982–1984, 1993–1995 and 2005–2008. The firsts drought periods derived respectively in a piezometric fall of 3.4 m (in the period 1982-84) and of 8.3 m in the 90's.

The piezometric level recuperated 85% until 1998 and remained almost constant, showing small seasonal fluctuations and a general descending trend 1.6 m until 2005 (0.3 mm/yr). Aragón et al. (2004) established a flow model for the surficial aquifer for the whole VMSR in the 1994-2001 period. The results of this model reveals in 1994 a variation of the water table between 31 and 35 m a.s.l within the urban area of Murcia city. According to this model, the flow direction of the surficial aquifer follows the topographical gradient of the basin. Groundwater flows from the peripheral areas towards the centre following the north east direction of Segura river.

Therefore the highest piezometric heights are found in the outskirts of the city and the lowest in the north of the city, immediately above Segura river. This is in agreement with the measurements of the piezometric boreholes drilled since 1994 (Fig. 6.5).

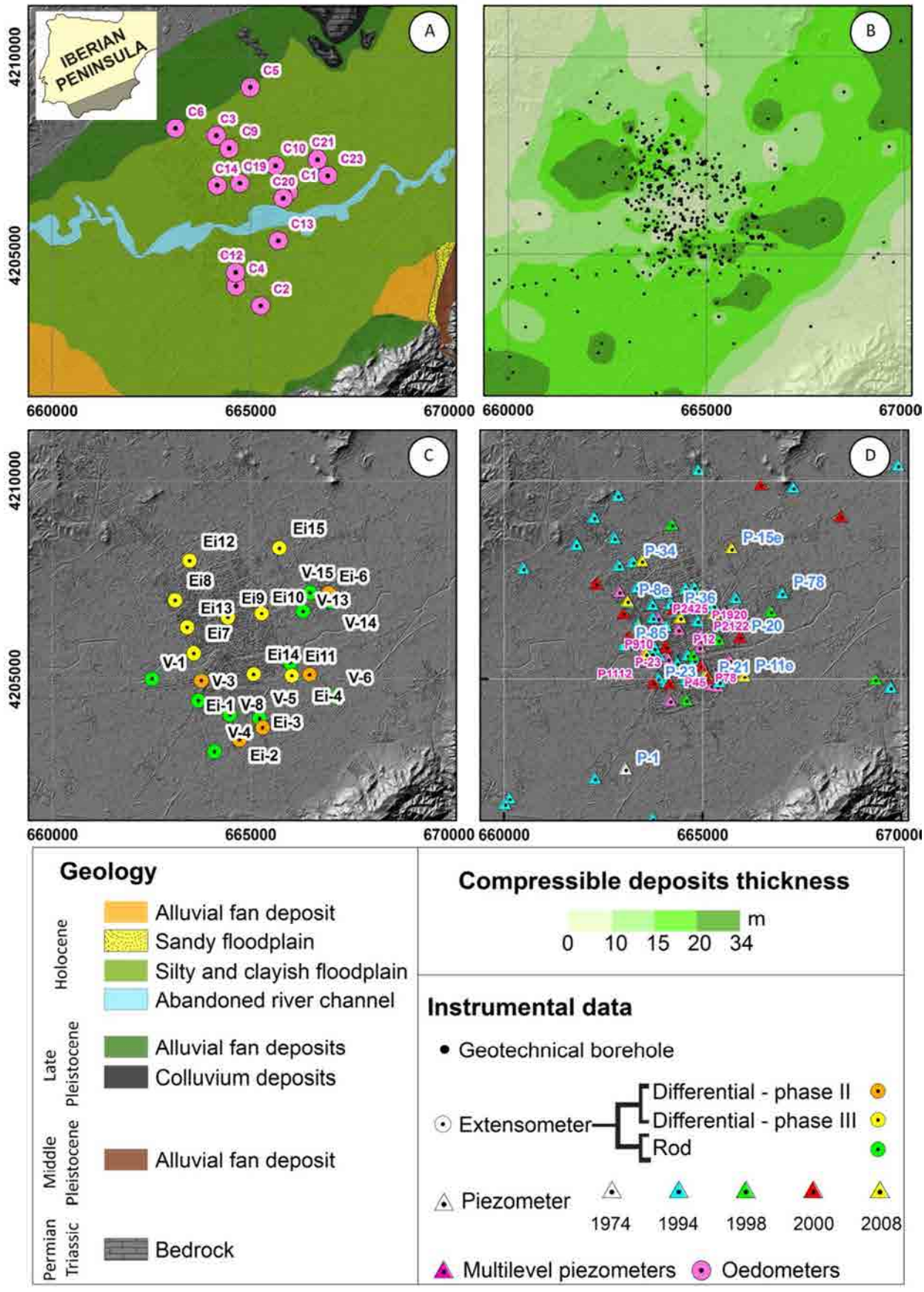

Figure 6.4: Geological Map (a), map of compressible deposits thickness (b), extensometers (c) and piezometric (d) networks.

For instance, after the second drought (1998-2005), the water table varied between 35 and 39 m a.s.l, presenting the lowest values at north from the river and the highest towards the south (P-21, P-23 and P-1 in the Fig. 6.5).

The water table drop was larger than in the previous drought, reaching 10 m in the southern side of the river, and between 2 and 7 m in the northern side (Figs. 6.5). The last groundwater piezometric level fall period started before March 2005 for the southern part of the city, and after November 2005 for the northern part. The minimum piezometric level was registered for the majority of the piezometers in September 2008. As it can be seen in Figure 6.5, most of the piezometric decline occurred in the first year of drought, and most of the recuperation (79% on average) were achieved in March 2010, whereas in February 2012 the average recuperation reached 92%. Note that piezometer P-1, registered a maximum cumulated water level drop of 12 m in the period 1982-2009, which had almost completely recuperated in November 2012 (-0.6 m difference).

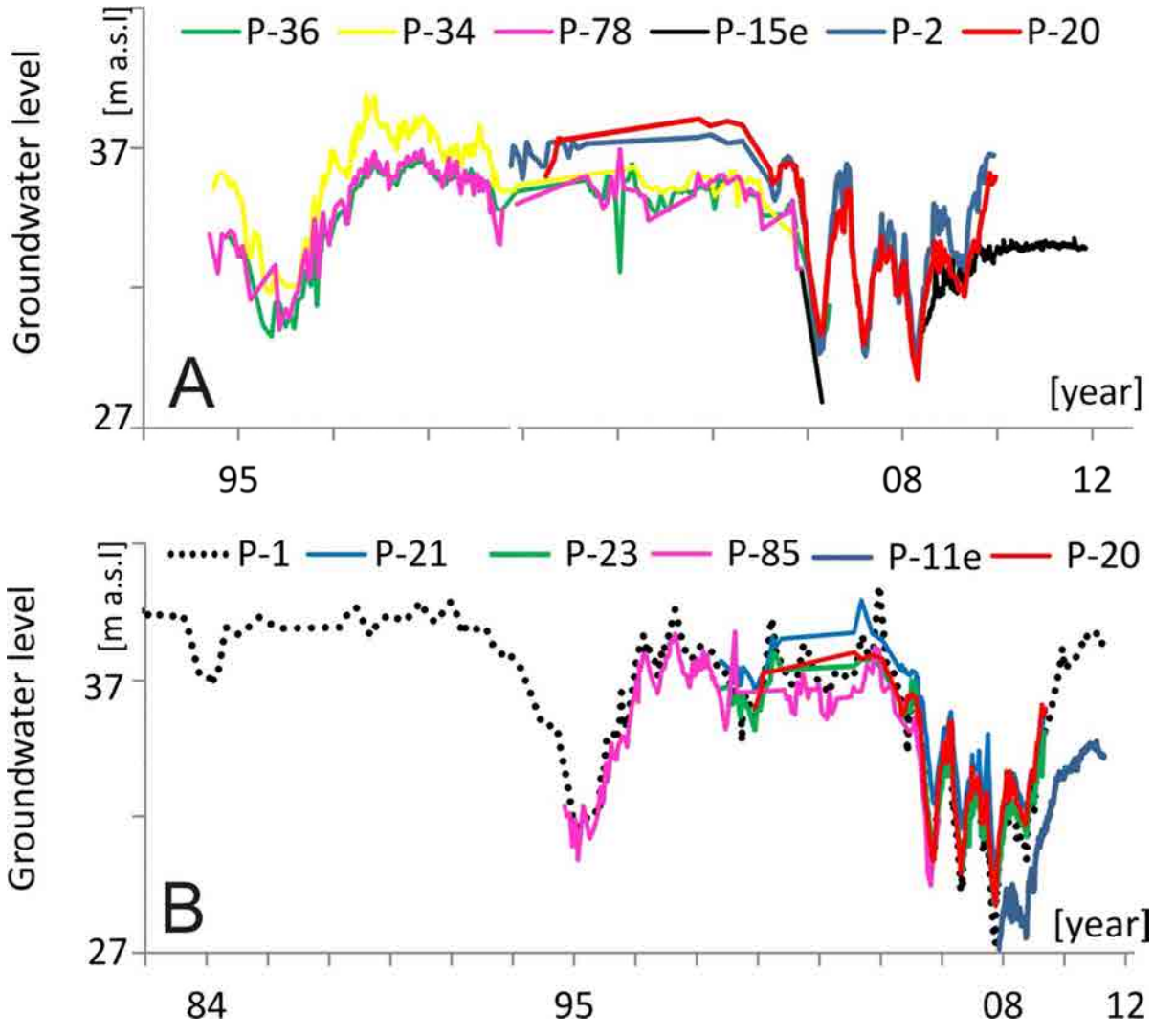

Figura 6.5. Piezometric time series. See piezometers location in Figure 6.4d.

In the metropolitan area of Murcia city, also several multipiezometers have been installed (for the most part by the "*Confederación Hidrográfica del Segura*" [CHS, 2007] and some others by the IGME) in order to measure both the aquitard and aquifer piezometric level (Fig. 6.4d). From their comparison, is possible to understand the grade of the hydrological connexion existent between the silt and the gravel layer. To this connection, depend:

→ *the delay between the deformations occurred in the surficial fine-grain layers and the piezometric variation measured in the gravel layer;*

→ *the magnitude of the deformations occurred in the surficial layers (function of the pore water overpressure dissipation mechanism; (see paragraph 5.1.4.3.).*

Figure 6.6 shows some multipiezometers data comparison (see also their ubication in Fig 6.4d). The aquitard and aquifer layers have a very similar response related to the existence of several sand layers intercalated or immediately over the gravels which favour water drainage (Tomás et al., 2010). In several cases near to the river (P2122, P78, P12, P910) some differences between the piezometric time series occur (Fig. 6.6).

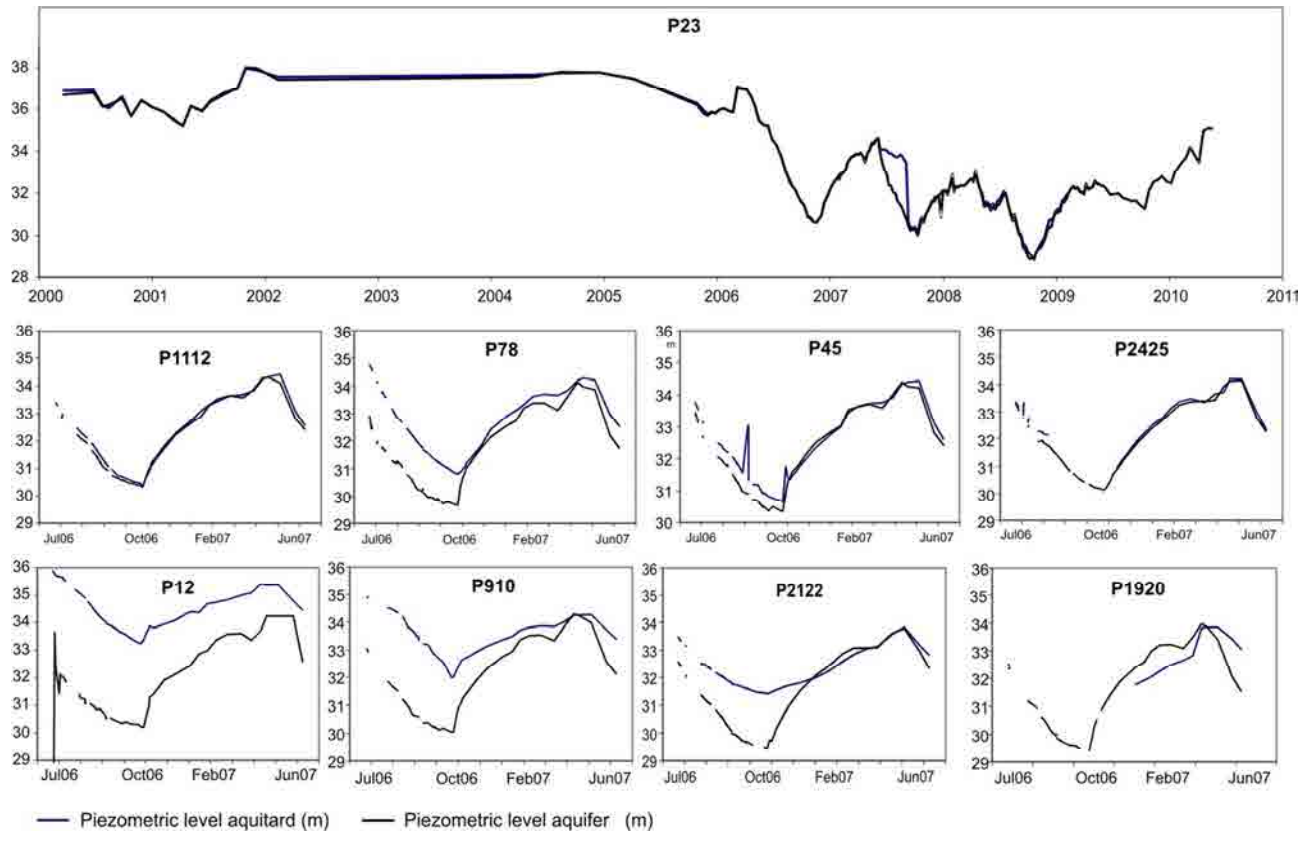

Figure 6.6: Temporal evolution of multilevel piezometers time series of the city of Murcia.

6.2.1.2. Extensometers

In Murcia city, a subsidence monitoring system was installed in February 2001 (phases 1 and 2) and extended in July 2008 (phase 3). In the first two phases 22 extensometers were installed, 16 incremental and 6 rod extensometers. In the 3rd phase, 9 additional incremental extensometric were placed in new drilled boreholes including a piezometric sensor for each of them. The incremental extensometers provide accumulated deformation measurements every meter along the first 10 to 20 m below the surface, while the rod extensometers measure the deformation of the first 10 to 15 m, using two or three rods of different lengths. According to Mulas et al., (2010) both types of extensometers provide measurements with 0.1 mm accuracy. The acquisition of measurements was performed approximately two or three times a year, being 194 days the average separation between extensometer measurements. From the total amount of installed extensometers (31) only 17 of them were operational in 2012. Urban changes in the city, such as streets re-pavement, installation of electrical equipments, communication devices, playgrounds and vandalism are responsible for the loss of 14 extensometric boreholes.

Figure 6.7 shows the extensometers time series between 2001 and 2012. Measured displacement range from -51 mm to +31 mm. Since January 2006 to the end of the recuperation phase, the highest subsidence rate has been registered by V-13 in the north-eastern part of the city. Coinciding with the start of the second drought, an acceleration of the subsidence rate is observed, increasing from 1.5 mm/yr, in 2004-2005, to 4 mm/yr in November 2008, when the cumulated average displacement reached -31 mm for all the extensometers. At the start of this drought period a dissimilar behavior (uplift) was only observed for V-4 and Ei-2 (Figs. 6.7 and 6.8).

The recuperation of the piezometric water level triggered an uplift (18 mm on average) until September 2010 for most of them, except for V-8, V-17, V-13, V14 and V-1 which showed a rather stable behavior (Figs. 6.7 and 6.8). From this date until November 2012 only four extensometers (V-8, V-17, V-4 and Ei-14) showed an uplift (three of them exhibited an incipient subsidence trend (Ei-10, Ei-15, V-14) and the rest an stabilized situation (Figs. 6.7 and 6.8).

An interpolation of the extensometric data through the IDW (Inverse Distance Weighted) method has been performed in order to understand the spatial evolution of the phenomena (Fig. 6.8). The interpolation involves all the extensometers of the phase I and II until July 2008 and also that of the phase III between July 2008 and November 2012 (Fig. 6.4a).

The IDW method has been chosen because of the limited number of available data for the interpolation.

The used interpolation technique has been described in paragraph 6.4.1.

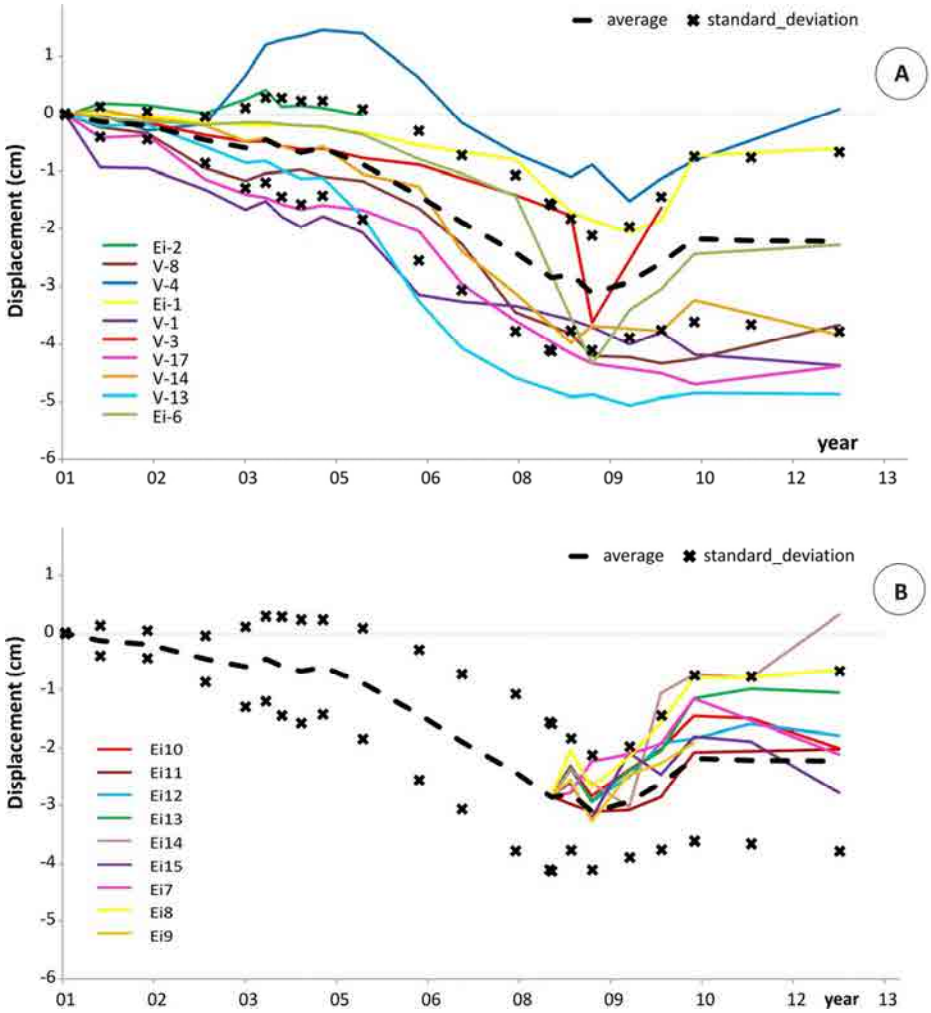

Figure 6.7: Extensometers data from phase I-II (a) and phase III (b). See extensometers location in Fig. 6.4c.

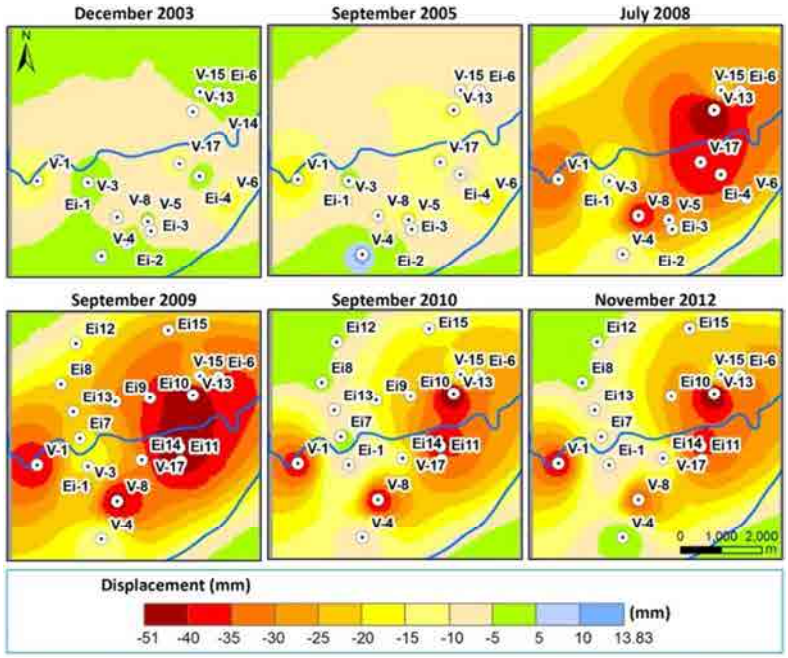

Figure 6.8: Extensometers data interpolation.

The interpolation pixel resolution is of 50 m and the boundary applied to the extensometers considers that no deformation is produced in the ranges that limit the VMSR and the power of the interpolation has been performed in order to obtain the minimum error related to the interpolation estimation.

Subsidence appears with an higher intensity in the eastern and southern part of the city, in according to the piezometric water level drop of the period 2001-2008. The maximum ground up-lift occurs in the city center (Fig. 6.8).

6.2.1.3. Comparisons between extensometric data and water level variations

In-situ monitoring data (i.e. those provided by the extensometers and the piezometers) have been compared to identify ground surface displacements related with water level changes. In figure 6.9 it is observed that changes in the water level produce a rapid response on the aquitard deformation.

As introduced above (Par. 6.2.1.1.) this is to relate to the hydrogeological connection between aquifer and aquitard in correspondence of the extensometer boreholes.

Figure 6.9 shows that most of the extensometers have a quick response related with piezometric level changes. This means that the piezometric level in the gravels (where water level changes are measured) results almost the same than that in the silty layer (where deformations are measured). In fact, as showed in figure 6.6, in the metropolitan area of Murcia, usually aquifer and aquitard result well connected from a hydrological point of view (Tomás, 2010).

For several extensometers an higher uncertainness of the piezometric data, (due to the high distance, *"d"* in Fig. 6.9, between piezometer and extensometer), does not allow the considerations about the delay between the deformations and the water level variations; nevertheless, for the extensometers of phase III, these analysis are not affected by uncertainness related to the piezometer's distance.

The comparison between piezometers and extensometer measurements also allows to obtain information about the change in the deformability of the aquitard layers related to the stress level.

In fact, during the third drought period, (the only one for which we have extensometric measurements), an acceleration of the subsidence rate is produced in August 2006. Around this date the displacement rate increased 3 times (on average) with respect to previously measured velocity (2001-2006).

This acceleration trend can be related with the water level drop (Figure 6.9) which overpass its historical minimum; in consequence the effective stresses probably overcome the "pre-consolidation pressure", i.e.

the highest stress suffered by the soil deposit along its life. The overcoming of this stress marks an increasing in the soil deformability and, consequently, of the occurred settlements. In the case of a good hydrogeological connection between aquifer and aquitard, the overcoming of the preconsolidation pressure in the clay layers occurs almost at the same time of the water level historical minimum overpassing.

As described in paragraph 5.1.4.3, the different permeability between aquifer and aquitard layers governs the velocity in the pore water overpressure dissipation (and the different evolution in their distribution). Therefore, the consolidation process established in the aquitard, in the case of an absence of hydrogeological connection with the upper aquifer, will be not instantaneous; thus, the overcoming of the preconsolidation pressure will be later than that of the water level minimum registered in the aquifer (Fig. 5.10b). Also a water level up-lift, in this case, will be felt by the surficial layers with a delay, function of the permeability.

Underlining that the preconsolidation pressure separates high non recoverable deformation from lower ones (recoverable), it is clear the importance of the previous considerations.

In the period 2008-2012 the water level was completely recuperated for the whole study area.

Figure 6.9 allows the recognition of different soil responses against groundwater level rise. In fact, a little or no uplift has been registered for 5 extensometers (less than 13% of the previously measured subsidence) and more than 47% for the other 4 extensometers. Therefore, it can be deduced that certain plastic deformation occurred in the surficial aquifer (aquitard).

The other 9 extensometers did not provide measurements in the 2005-2008 drought periods, and therefore the displacement percentage recuperation cannot be evaluated. However a marked uplift (13.3 mm on average) was observed in all of them, having a perfect correspondence with the ground water level recuperation (8 m on average).

From a spatial point of view, the greatest recuperation and uplift was produced in the Northern part of the city, where the thickness of compressible materials and the magnitude of the water level decrease were lower (Fig. 6.5).

Note that for the extensometers placed in the North-Western part of the city (Ei8, Ei13, Ei12, Ei10, Ei7) and in the southern of the river (E1, Ei14) the water level minimum reached in 2008 is almost equal to that of 1996 (Figure 6.9). Thus, the plastic deformations for the overpassing of the preconsolidation pressure (which, because of the good connection between aquifer and aquitard can be reached with a little delay respect to the historical water level minimum overpassing) have not occurred or are little.

On the other hand, when the water table fall was more intense (e.g. V13, V14, V15, V17, Ei-6, V8) the plastic not-recuperated part of the deformation is evident.

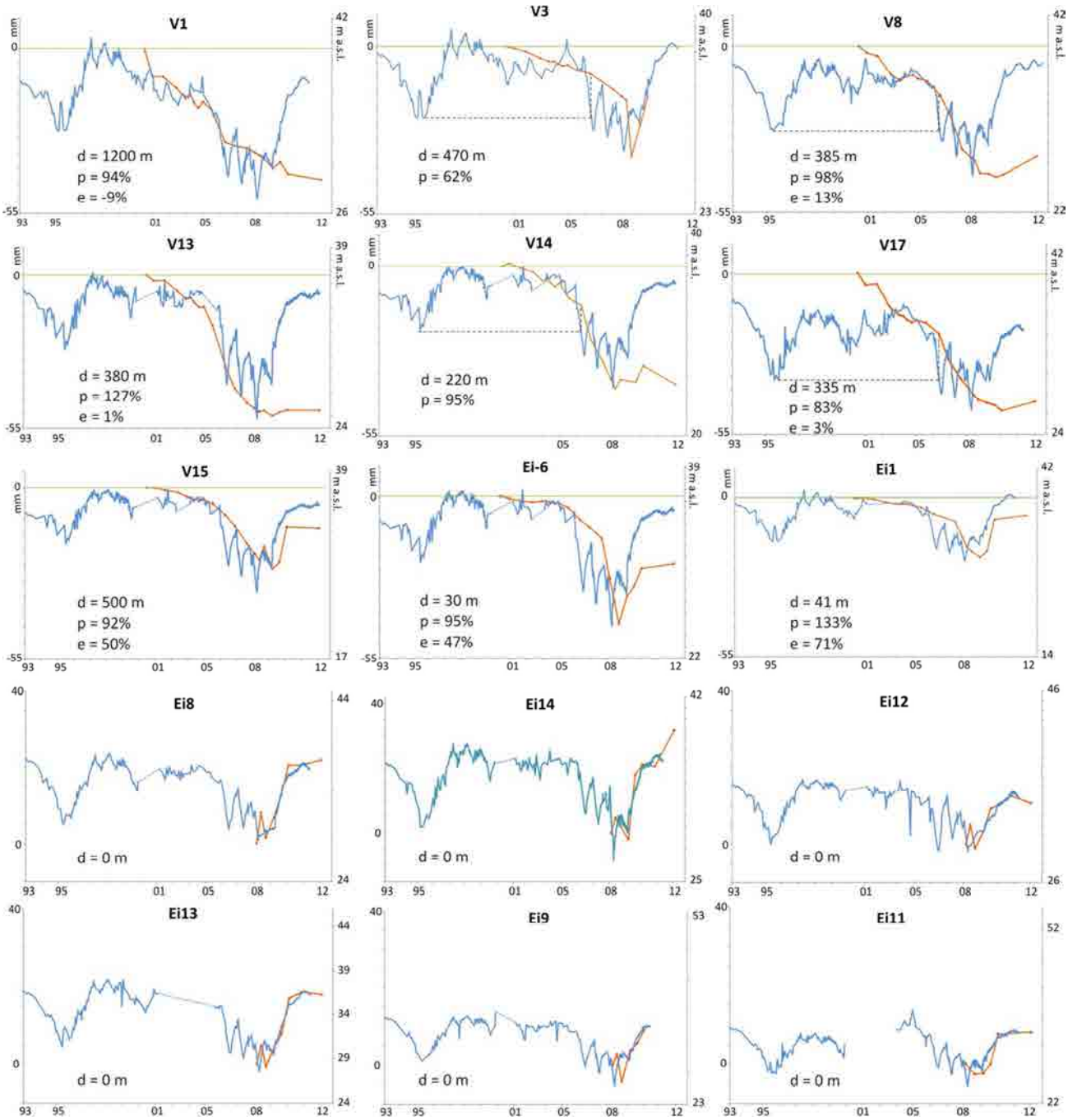

Figure 6.9: Comparisons between piezometric and extensometric data (d: distance between the nearest piezometer to each extensometer; p: percentage of water level recuperation in the last drought period; e: percentage of the recuperated deformation measured by the extensometer in the last drought period).

6.2.2. A-DInSAR monitoring

Murcia case study has been analyzed through A-DInSAR techniques in many works (Herrera et al., 2008, 2009; Tomás et al., 2005, 2010, 2011). In the present thesis, the already available radar data have been used to the validation of the processing results, obtained through *Coherent Pixel technique* (CPT).

In particular, SPN radar data, published by Herrera et al. (2009), achieving an accuracy of ± 5 mm in their comparison with the extensometer measurements in the period 2001-2007 have been used.

6.2.2.1. CPT processing

In the present work, the SBAS "*Coherent Pixels Technique*" (CPT) algorithm, implemented by Mora et al., 2003 has been used to process all the SAR images available in the study area. Here, 151 C-band images between 1995 and 2010 and 117 X-band images in the period 2008-2013 have been processed. Both the processings have been centered on the metropolitan area of Murcia city (respectively considering a processing window of 12 x 14 Km for the C-band images and 5.5 x 6.5 for the X-band ones).

X-band images have an higher pixel resolution (about 2x3 m - azimuth-range) against the 5x20 m of C-band images; this allows to obtain a very high spatial and temporal density of measured displacements.

CPT processing scheme (as described in paragraph 4.7) is composed of three main steps:

A. *The generation of the best interferogram set among all the images available in the study area;*
B. *The selection of the pixels with reliable phase within the employed interferograms;*
C. *Their phase analysis to calculate, mainly, the deformation time series within the observation period.*

CPT processing is achieved through the software SUBSIDENCE, implemented at the *Remote Sensing Laboratory (RSLab)* of the *Universitat Politècnica de Catalunya (UPC)*, which consists of two sections:

→ *software Prisar:* which allows the SLC images crop, their co-registration, the differential interferograms and the coherence maps generation;

→ *software Subsoft:* which allows the solution of the CPT algorithm, (described in the chapter IV), namely the decomposition of the differential phase in DEM error and estimated deformations.

A. CPT is a *Small BAseline Subset (SBAS)* technique and, uses pairs of images characterized by small spatial and temporal baseline to minimize the error induced by temporal and spatial decorrelation (see chapter IV). Interferograms have to be computed using images acquired by the same satellite sensor (ERS1-2 and ENVISAT), but all the achieved interferograms are combined together in the processing.

The temporal distribution of the interferometric pairs of the ERS-ENVISAT images used in the processing is shown in Fig. 6.10. In order to choose the best interferogram set, the images three-dimensional *Delaunay triangulation* (using their spatial baseline, temporal baseline and *Doppler* difference) have been used.

The lists of the used images and of the filtered interferograms (with their spatial and temporal baselines) are reported in the Annex I.

Tanks to this triangulation, it is possible to know the interferograms relationships and to select the best set through an algorithm proposed by Blanco et al., (2006); consequently, redundant calculations can be avoided, minimizing the time for the processing and increasing the coherence.

In the C-band processing, using a maximum spatial baseline of 250 m, a maximum temporal baseline of 1000 days and a maximum Doppler difference of 800 Hz, 405 interferograms have been selected. In the X-band processing, using a maximum spatial baseline of 200 m, a maximum temporal baseline of 250 days and 308 interferograms have been selected (Annex I).

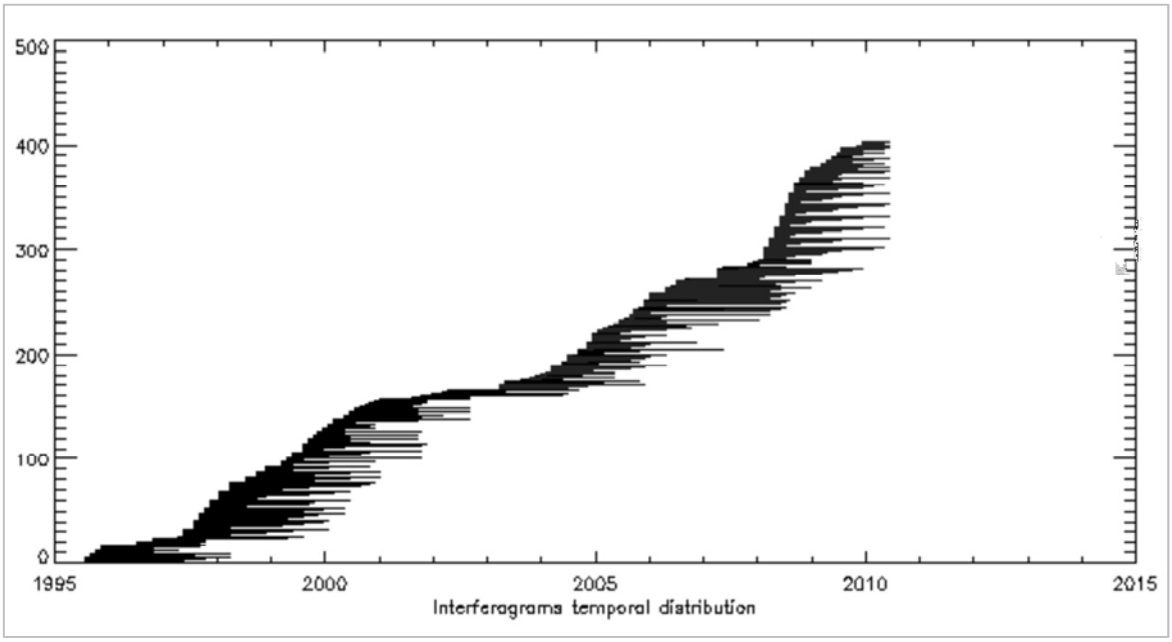

Figure 6.10: temporal distribution of the interferometric pairs of the ERS-ENVISAT images processing.

B. The pixels selection is achieved on the base of their coherence in the interferogram set. In C-band images processing, all the pixels having a coherence (γ) higher than 0,6 in the 40% of the interferograms have been selected. Because of the few number of selected pixels, due to the bad resolution of the C-band images, two coherence thresholds have been considered (γ=0,6 and γ=0,4).

After this phase, the software generate a Delaunay triangulation (Fig. 6.12) between selected coherent pixels (Fig. 6.11d), having a maximum distance of 1000 m (to consider reliable the hypothesis of invariable atmospheric conditions).

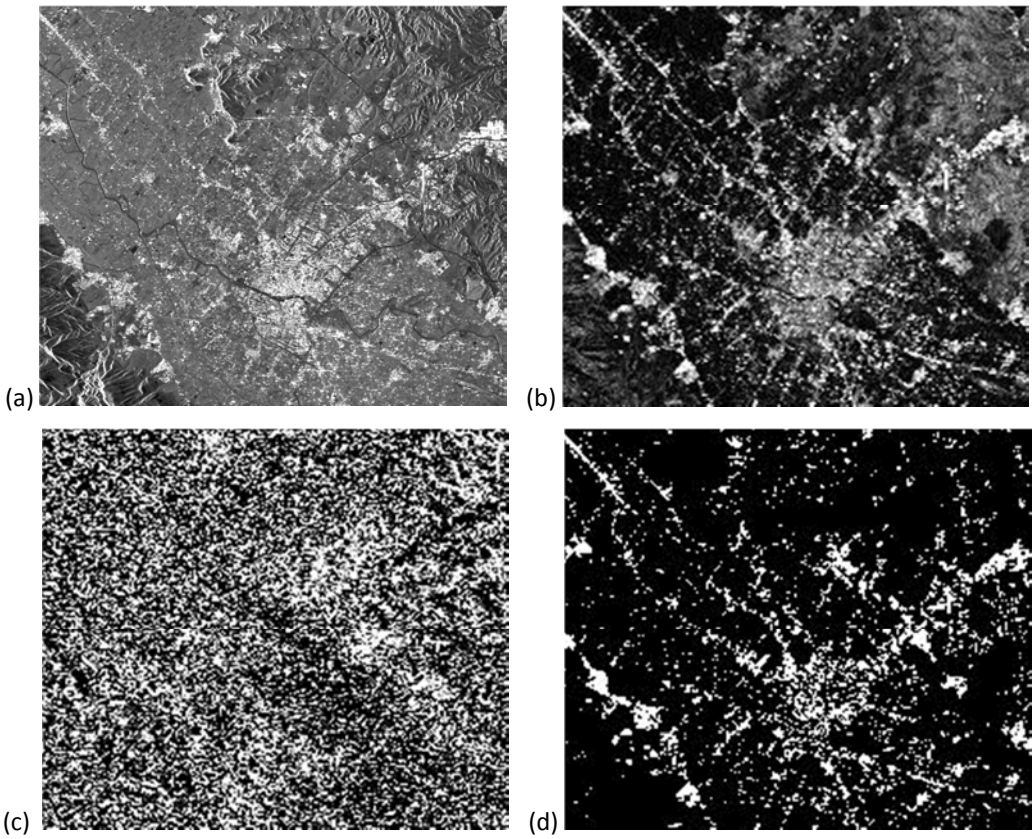

Figure 6.11: a) Amplitude high resolution image obtained using the available C-band images of Murcia; b) Differential coherence (scale colour: black=incoherent; white=coherent); c) Interferometric cleaned phase relative to the images 07/12/06 and 01/07/08 (between +π and - π radians); d) Selected pixels.

C. The last step consists in phase analysis to calculate their linear deformation time series within the observation period. The phase of each pixel is difficult to evaluate due to the occurrence of an offset among the different interferograms. In order to overcome these constraints, CPT algorithm uses a model coherence (Ω) to refine the results. In this case the considered thresholds value is 0.35 and brings to the definitive coherent pixels selection which will constitute the processing results. In particular, it relates the neighbouring selected pixels by means of a *Delaunay triangulation* (Fig. 6.12). Each link between the coherent pixels corresponds to a quality function of

the selection level of its extremities. Figure 6.12 shows the link qualities in function of Ω; in particular the green links represent 0.5125>Ω>0.35; the blue ones: 0.675>Ω>0.5125; the red ones: 0.8375>Ω>0.675; and the black ones: 1>Ω>0.8375.

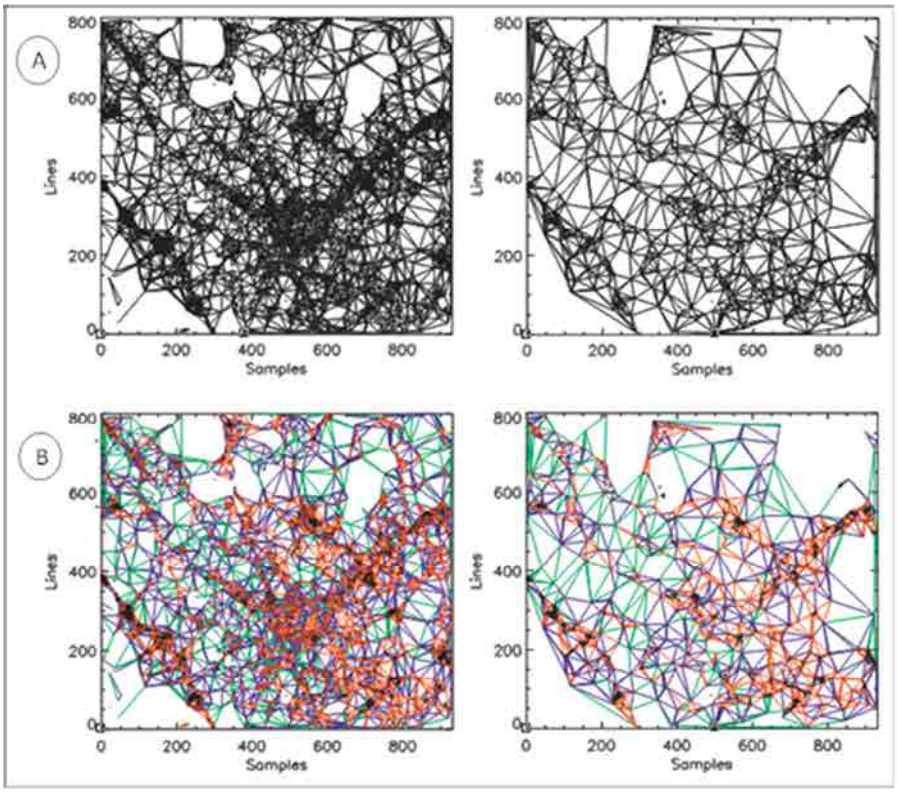

Figura 6.12: Delaunay triangulations of Murcia processing: (A) initial; (B) after the selection in function of the model coherence. From left to right: coherence threshold 0.6; coherence thresholds 0.4.

This kind of triangulation allows to connect neighbouring pixels with non-overlapped triangles. The selected pixels are the nodes of the mesh and the connections among the pixels represent the links. After this step, the phase component due to the linear displacement (and the linear velocity map in Fig. 6.13 a) and that due to the error DEM (and the error DEM map, Fig. 6.13 b) are known.

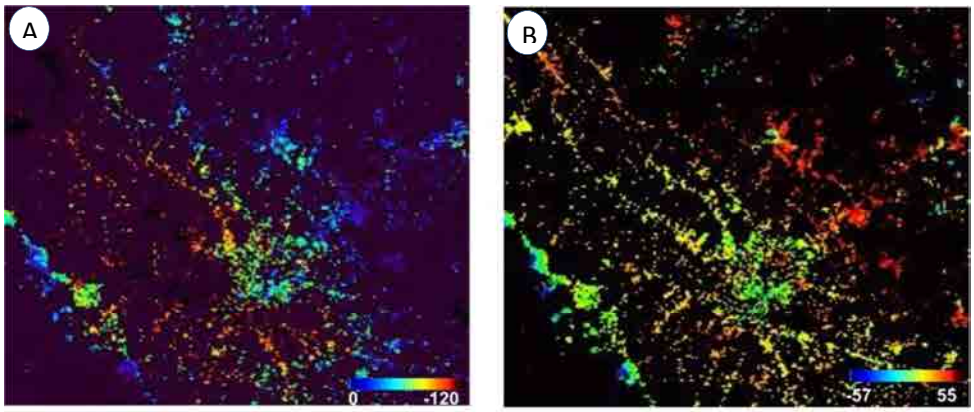

Figura 6.13: Velocity map (A) and error DEM map (B).

In an hypothetical theoretical case, if the A-DInSAR processing would be done only using interferograms having null spatial baseline, the achieved output would simply consists of deformations and not also of a DEM error.

D. After that, to achieve the differential phase component due to the displacement, is necessary to determine the components due to the atmosphere ($\Delta\varphi_{atm}$). To find the non-linear deformation, a filtering process in both spatial and temporal domains is applied in order to obtain the time-series of the deformation, as in detail described in Blanco et al., 2008. Therefore, the total vertical displacement, (sum of the linear and non-linear components) is achieved.. To obtain the time series, another filter is applied to reduce the time series standard deviation. In this way is possible to obtain a general trend of the displacement without time series noises.

6.2.2.1.1. Sensibility analysis of the parameters influencing the displacement time series

The error related to the A-DInSAR processing is a key topic of current research projects. The correct use of radar data results depends on their evaluation.

The *Coherence based* methods lead up to a mean coherence map which takes into account all the interferogram set. Therefore, also if a pixel has a high mean coherence (and, consequently, as explained in chapter IV, a lower displacement standard deviation), all the interferograms have given their contribution to the computation of its displacements time series. Several used interferograms derive from very noisy images and bring incorrect displacement information. In particular C-band ERS and ENVISAT images, differently from Terrasar-X ones, are characterized by a low resolution and high noises which affect the goodness of the results.

Each noisy image is contained in one or more interferograms and that causes the mean coherence decrease of all the pixels. Several of them, therefore, are excluded from the pixels selection because their mean coherence do not reach the imposed threshold values; this decreases the number of pixels obtained in the processing results. At the same time, one noisy image can be contained in more than one interferogram, but not necessarily all the interferograms which contain this image can decrease the mean coherence.

Taking this into account, the time series, resulting from CPT processing of all the interferogram set can be characterized by a high variability. Therefore, CPT algorithm, hold a final part regarding a time series filtering to obtain the global trend of the computed displacements not taking into account measures which are very different from the global trend (*outliers*) in a fixed time period (in C-band images case, for example, is possible to vary the filtering parameter starting from 35/365=0.095 years).

To understand how this filter reduces the time series standard deviation, the following processing tests, carried out for Murcia case study, are presented (Fig. 6.14). In particular three time series have been obtained for three different filter values (Fig. 6.14): the black line corresponds to a null filter, the green one to a filter on half of year and the red one to a filter of one year and half. All the three curves present the same global trends which can be compared with that of in situ measurements or piezometer time series.

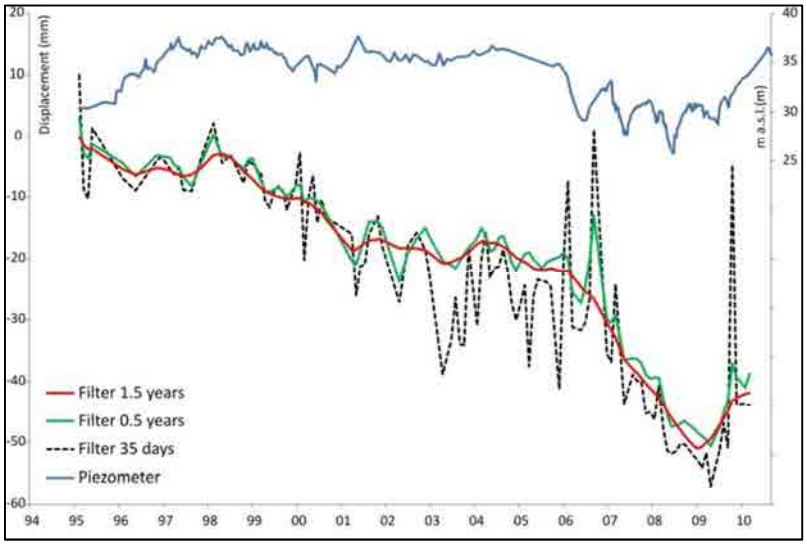

Figure 6.14: Example of different time series filtering results

Another important consideration to do, is that all the anomalous peaks, mainly of the black line, could be due to noisy images which have affected not only the time series trends, but also the number of selected pixels and, therefore, the output points density. Thus, from figure 6.14 is possible to identify them to their elimination from the processing. Figure 6.15 shows the time series (without filters) obtained eliminating six images (09/08/03; 09/07/05; 11/03/06; 20/05/06; 16/12/06; 09/01/10) which correspond to the main peaks of the black line of figure 6.14.

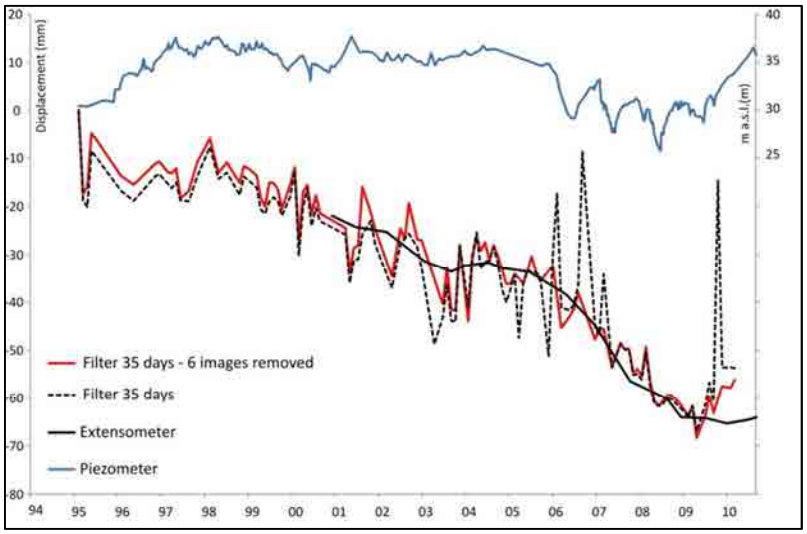

Figure 6.15: Example of outlier elimination

However, analyzing the coherence of the interferograms which contain the eliminated images, that of several of them has resulted to be very high and, among them, only that having an high *Doppler difference* have been excluded. High Doppler differences make the azimuth spectra of the teo images to do not overlap; i.e. see figure 6.16. It is similar in range if we are using spatial baselines larger than the critical one.

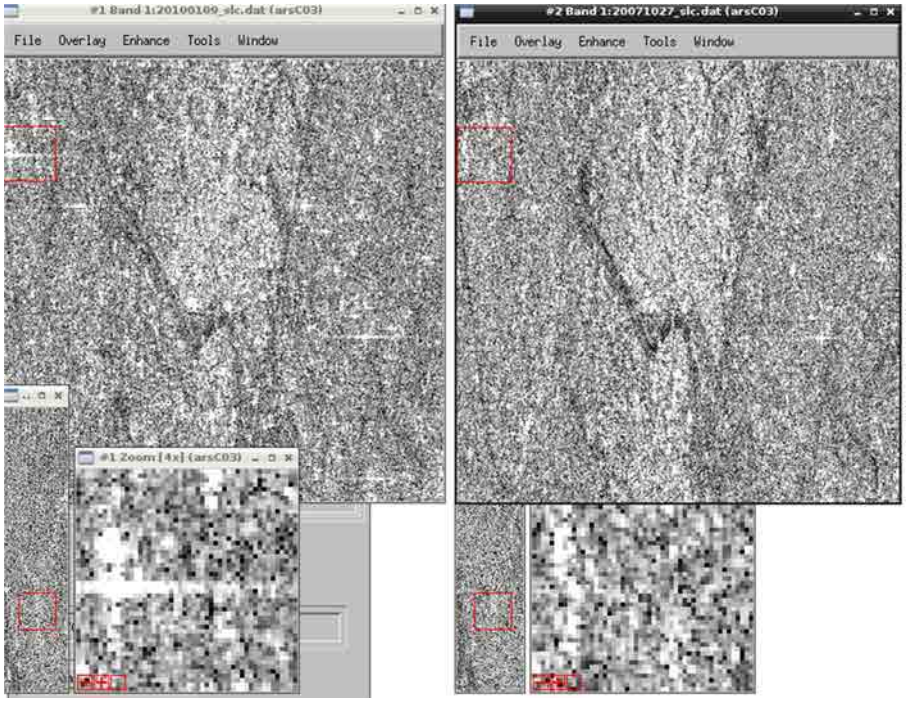

Figure 6.16: Example of images having high Doppler difference

Finally, only 2 images and 5 interferograms (Table 6.2) have been eliminated from the processing, achieving an increasing of the mean coherence and of the pixels number of 1%, (for a total amount of 5651 pixels). Of course, the processing could be further bettered and, in a more extended area than that considered in this thesis (12x14 Km), a percentage increase of 1% or 2% can corresponds to thousands pixels more.

I image	09-01-2010	16-12-2006	20-05-2006		11-03-2006			09-07-2005			09-08-2003
II image	27-10-2007	31-12-2005	09-06-2007	24-05-2008	31-01-2004	24-07-2004	09-07-2005	31-01-2004	24-07-2004	11-03-2006	31-01-2004
coher dif	0.17	0.31	0.19	**0.77**	0.33	0.17	**0.53**	0.29	0.09	**0.53**	**0.77**

Table 6.2: differential coherence of the pixel (116,172) in the different interferograms

Taking into account the previous considerations, the results achieved removing 2 images and 5 interferograms have been used and analyzed in the following paragraphs.

In any case, is important to remember that the time series computation with the coherence based method is affected by errors which have influence in the magnitude of the cumulated deformation; these are related to the coherence of every used interferogram and it is very difficult to individuate the images whose interferograms reduce the average coherence, incrementing or reducing the noises and the errors in

the computed final displacement.

However, all the proposed comparisons show that CPT represents a very stable algorithm because the global trend of the time series as same as the spatial distribution dos not vary, except for variations of the same order of magnitude of the phase noise. Figure 6.17 shows different filtering possibilities of the so obtained time series. In particular, the red line corresponds to a "*variable filter*": it consists in a fixed filter (in this case of 35 days, namely the null filter) that is considered only if, in this time interval, at least one interferogram exists; otherwise, the algorithm considers multiples of the filter interval (in this case of three time).

The filter choice only depends to the phenomenon characteristics which is possible to observe and to how it can be well represented. In this case, the results obtained with a filter of 1 year seem to well correspond to the piezometric water level variations; for this reason, it has been applied to the time series representation. However, the absolute difference between the two curves of Fig. 6.17 (filter=1 and 0) is of 3.2±3.0 mm and both of them represent DInSAR results which can be compared to in situ data. As it is possible to note in the figure, in both cases, their comparison with the extensometer measured displacement time series is good, but to the quantification of this comparison with in situ data, the orange curve will correspond to a lower absolute error. Therefore it is important to underline that displacement time series give (independently to the used filter) information about the global trend of the deformations which can be more clear through the application of a filter which reduce the time series standard deviation.

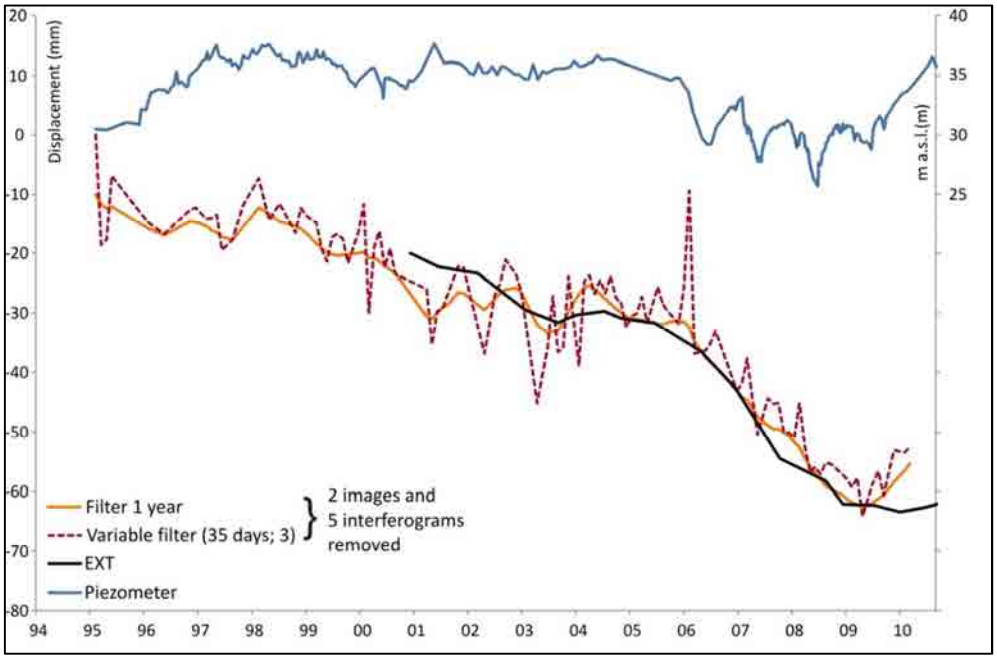

Figure 6.17: processing results achieved removing 2 images and 5 interferograms, represented with two different filtration criteria: variable filter (red line) and fixed filter (orange line).

Another choice to make to the results improvement regards the processing temporal windows. If the deformation in the study area is not characterized by accelerations or trend changes, the linear velocity estimated by the algorithm allows a good evaluation of the non-linear deformation component. Nevertheless, if, like in the examples proposed in the previous, this acceleration occurs, is more advisable to divide the processing in different periods ("temporal windows"). In this case the two different processing would be referred to the periods: 1995-2005; 2005-2010. Figure 6.18 shows the comparisons between the processing reported in figure 6.14 and the correspondent obtained dividing the computations.

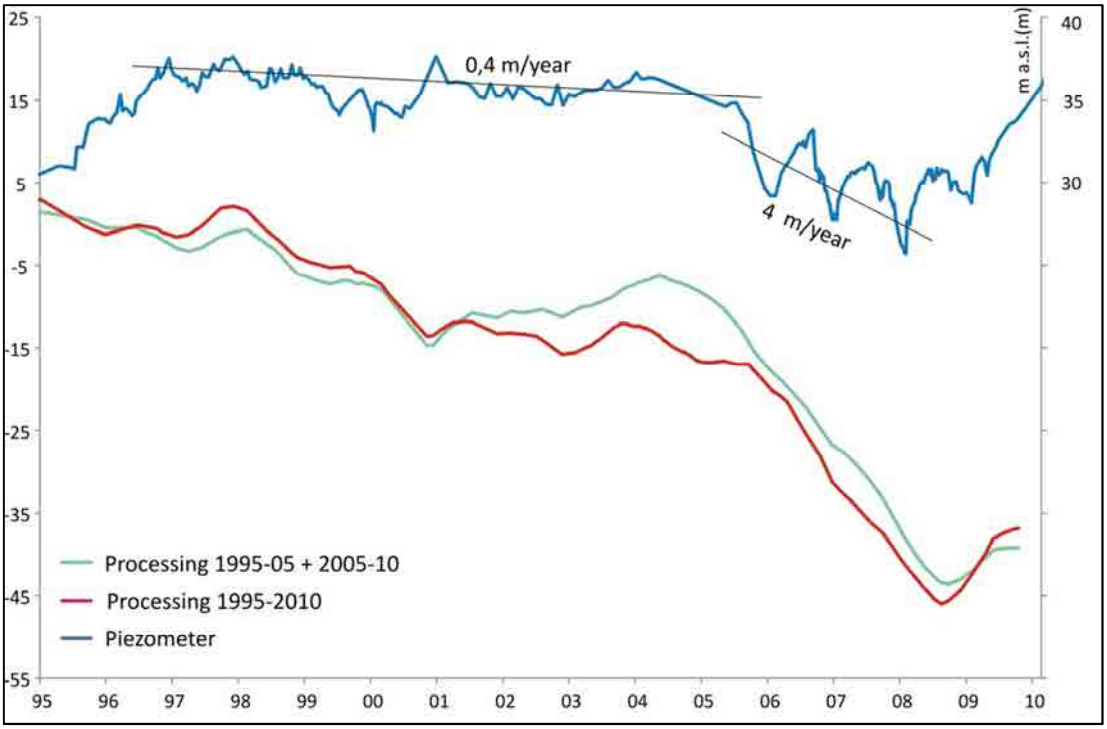

Figure 6.18: example of processing achieved dividing it in two branches

As shown in figure 6.18, the processing carried out using all the images between 1995 and 2010, does not perfectly appreciate the strong change of velocity occurred in 2005. However, the difference between the two curves is not so relevant and a processing obtained for the whole period 1995 and 2010 has been preferred; in fact, to a better estimation of the trend changes corresponds a different tally of selected pixels. In other words, a pixel which is selected using images of the period 1995 and 2005 can result incoherent in the processing referred to the second period and the comparisons with in situ data can be more difficult and affected by other kinds of errors.

Thus, among the various obtained results, that shown and commented in figure 6.17, have been chosen and the achieved cumulated displacement and velocity maps, as same as the time series have been reported and analyzed in the following paragraphs.

6.2.2.1.2. CPT processing results

CPT technique results consist of vertical displacements, chiefly the velocity map and the displacements time series for the whole observation period. These allow assessments about the phenomenon spatial extension and its different rate distribution.

Figure 6.19 shows the cumulative vertical displacement map between July 1995- July 2009, July 2009 - May 2010 (obtained from the C-band ERS and ENVISAT images processing) and between May 2010 and December 2013 (carried out from TSX images processing).

In the period 1995-2009, according to Fig. 6.19a, subsidence is observed mainly in the central part of the valley and results more intense in the North-Eastern part and where the compressible sediments thickness is higher; this is in according with the evaluations achieved by Herrera et al. (2009b), obtained using SPN radar data for the period 1995-2007. Displacements measured through CPT technique in the period 1995-09 are of -4±3 cm on average in the valley and of -5±2 cm in the area covered by the extensometers around the urban area of Murcia.

In the period 2009-10 a general ground up-lift is observed in the central part of the VMSR (detected by both ERS, ENVISAT satellites); the ground up-lift results more intense in the southern part of the valley. Nevertheless, a little subsidence (of 5±2 mm on average) is detected in the northern part of the valley (Fig. 6.19b) and an almost stable behavior is observed in some zones of the urban area, in particular, around V1 and V17 (at South of the river).

The Terrasar-X image processing results show a general ground uplift after May 2010 which turns out to be more intense in the Southern part of the valley (Figs. 6.19c and 6.20). Moreover, the results achieved for the whole period 2008-2013 (Fig. 6.20) show that the area at South of the river is characterized by a stable behavior (or at least by a little and localized subsidence). These results are in according with that achieved from the C-band images processing, shown in Fig. 6.19b, for the period 2009-2010.

The spatial distribution of the TSX measured displacements in the period 2008-2013 (Fig. 6.20), in particular, is in agreement with the considerations achieved through the extensometric data analysis (Par. 6.2.1.2). The in situ data, in fact, have showed a general uplift in the urban area, except for V-8, V-17, V-13, V-14 and V-1 which have showed a rather stable behavior.

Through the comparison between Figs. 6.19b and c, is possible to note some differences referred to the central part of the urban area (at North of the river). Between July 2009 and May 2010, (when the extensometers register a higher ground up-lift respect to the later period, as shown in Fig. 6.7), in the central part of the urban area the ground up-lift turns out to be more intense than in the northern part.

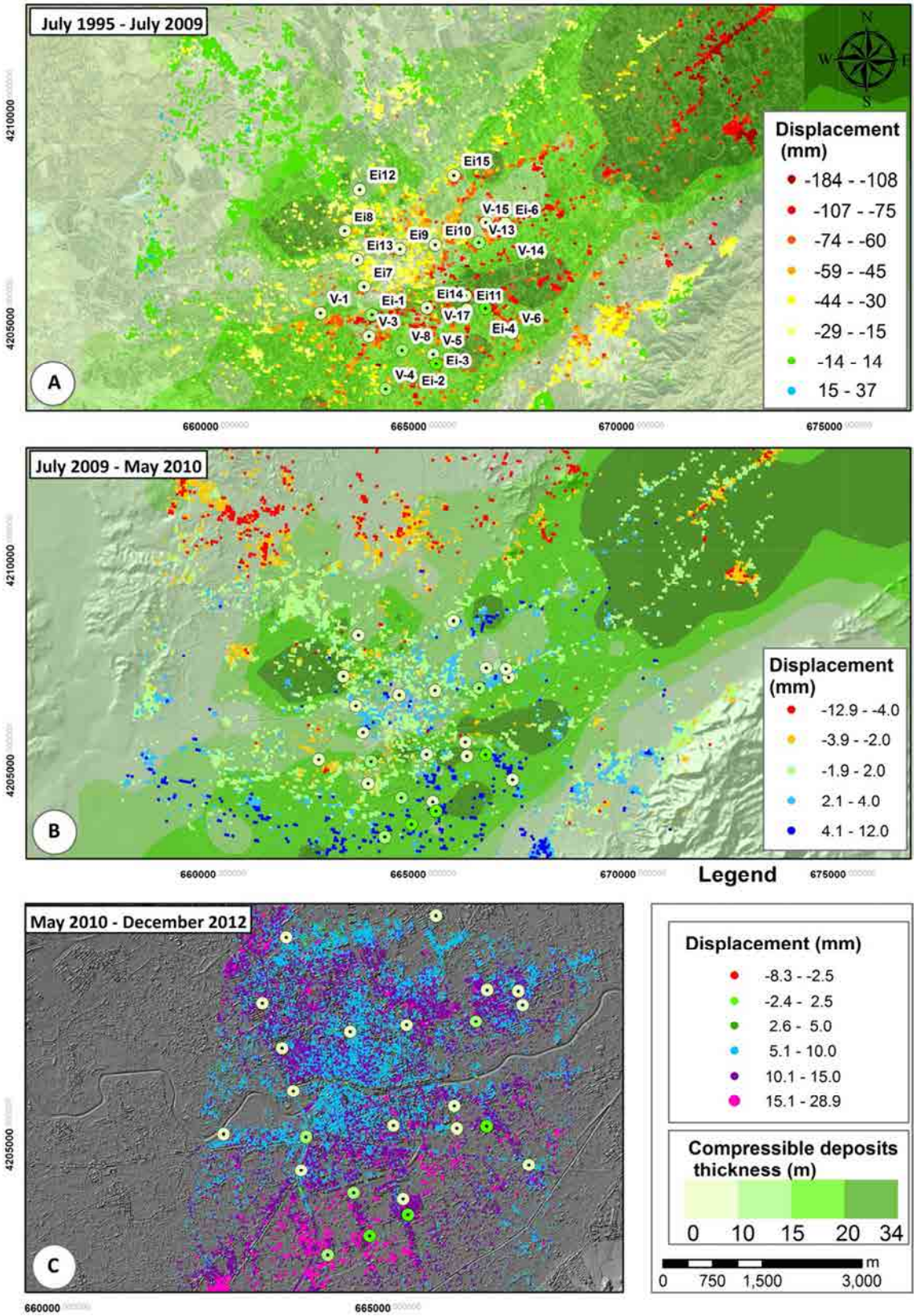

Figure 6.19: (a) Measured vertical displacement between 1995 and 2009 and (b) between 2009 and 2010 (C-band images processing), superposed over the thickness map of compressible deposits (modified from Mulas et al., 2000; Herrera et al., 2009); (c) Measured vertical displacement between 2010 and 2013 (TSX images processing). Labels have been placed in those extensometers that have been introduced in the previous section, symbolized in function of their different acquisition depth.

This is probably related to the lower depth of the gravel layer which causes a higher rapidity of the surficial layers deformations related to the water level variations. Nevertheless, after May 2010, the central part of the city seems to be characterized by lower deformations respect to northern part of the metropolitan area. Probably this is due to the geological and hydrogeological local differences, (i.e. to the stratigraphy's differences, to the higher thickness of compressible materials, to the depth of the gravel layer) respect to that in the city center. These can, in fact, justify a greater ground up-lift magnitude as same as a delay between the water level recuperation and the consequent ground uplift.

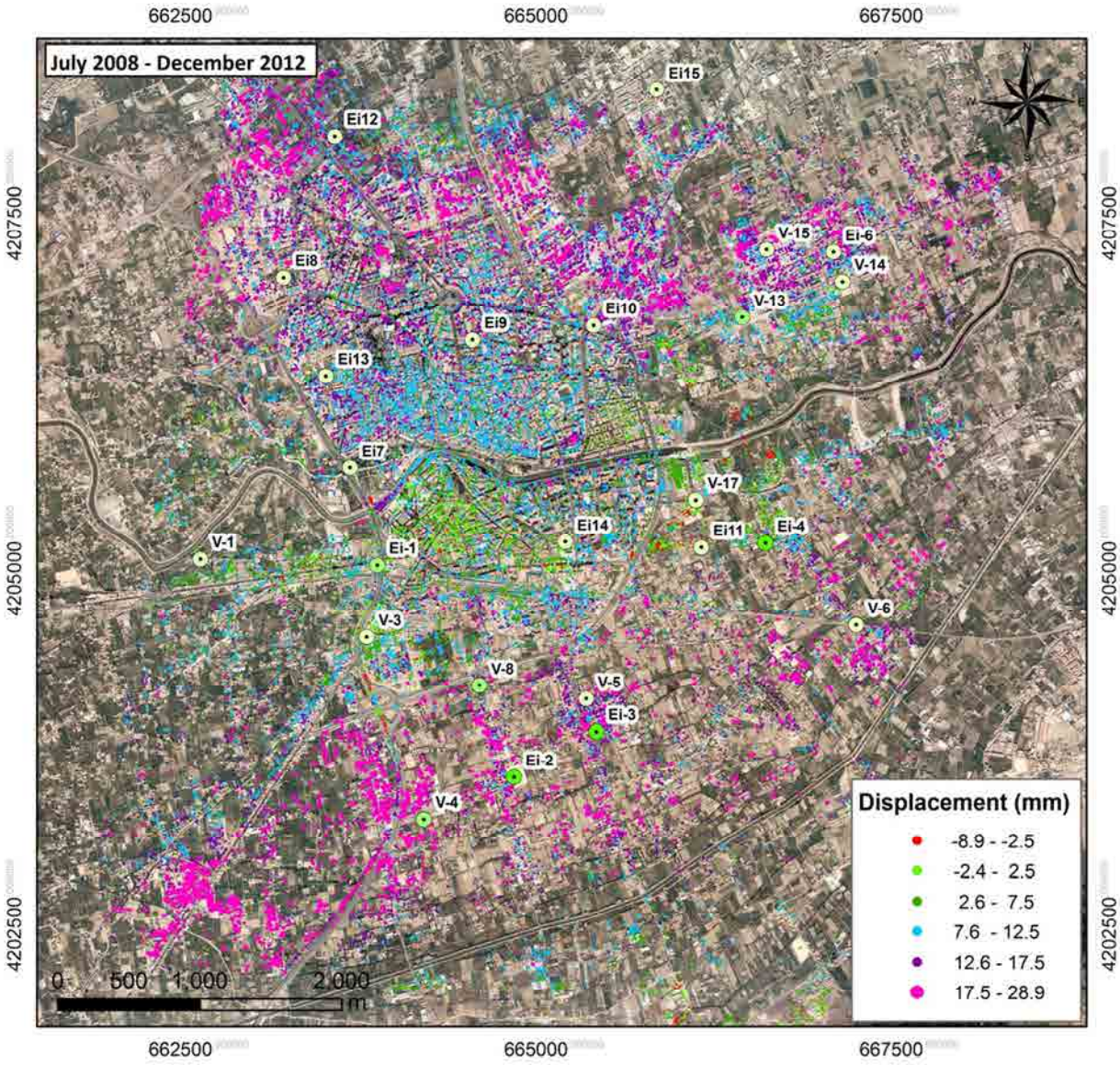

Figure 6.20: Measured vertical displacements between 2008 and 2013 (CPT processing of Terrasar-X images).

CPT's results (period 1995-2010) have been cross-validated through the comparison with available SPN's data (1995-2009). Furthermore, according to the procedure described in Herrera et al. (2009), the results validation and interpretation of both the C-band and X-band images processing results have been carried out also through the comparison with available in situ data.

6.2.2.2. SPN data

Whitin *Terrafirmae Project* (2008), 129 *Single Look Complex* (SLC) SAR images acquired from descending orbits by the *European Space Agency* (ESA) ERS-1/2 and Envisat ASAR sensors (covering two periods, July 1995-December 2005 and January 2004-December 2008 respectively) were processed by Altamira and IGME. A similar crop of about 9 km x 9 km was selected from the 100 km x 100 km acquired SAR images, corresponding to Murcia urban area (Fig. 6.21a). The DEM of the Shuttle Radar Topography Mission (SRTM) was used.

In the processing, each interferometric pair was selected with:

- a perpendicular spatial baseline smaller than 800 m;
- a temporal baseline shorter than 6 years, in the case of 1995-2005;
  and 3 years in the case of 2004-2009;
- a relative Doppler centroid difference below 400 Hz.

The pixel selection to the displacements estimation was based on a combination of several quality parameters including low amplitude, standard deviation and high model coherence.

In particular, the PS selection methods, based on amplitude criteria, work at *"full resolution*", (namely it allow keeping the original resolution of the SAR image), differently from the coherence based methods. The latters, in fact, as described in Chapter IV, work at lower ground resolution depending on the multilook set. This means that the pixel selection involves an averaging of adjacent pixels of the original image with the consequent degradation in spatial resolution (Tomàs et al., 2013).

As referred by, Herrera et al., (2012), if the subsidence phenomenon to observe is localized in an area of few Kilometres, the Coherence based methods bring to an appropriate compromise between resolution and electromagnetic response stability.

To have more information about the SPN technique and the parameters used in the processing is possible to refer to Arnaud et al., (2003) and Herrera et al., (2008).

In Paragraph 6.2.3.1 SPN data have been used to the CPT results cross-validation.

In order to provide a measurement of the displacement along the period 2001-2009 (the last date is 22 December 2008) which coincides with the third drought and a whole period monitored by the extensometer network, both 1995-2005 and 2004-09 SPN datasets have been integrated (Fig. 6.21a).

6.2.3. Comparisons

6.2.3.1. Comparisons between CPT and SPN radar data

6.2.3.1.1. Spatial analysis

From a spatial point of view, the comparison of the results achieved through CPT and SPN data shows a very good correspondence.

Figure 6.21 shows a different point density due to the used processing algorithms: the area of interest (9 Km x 9 Km) includes 9620 and 3588 points, respectively identified by SPN and CPT algorithms.

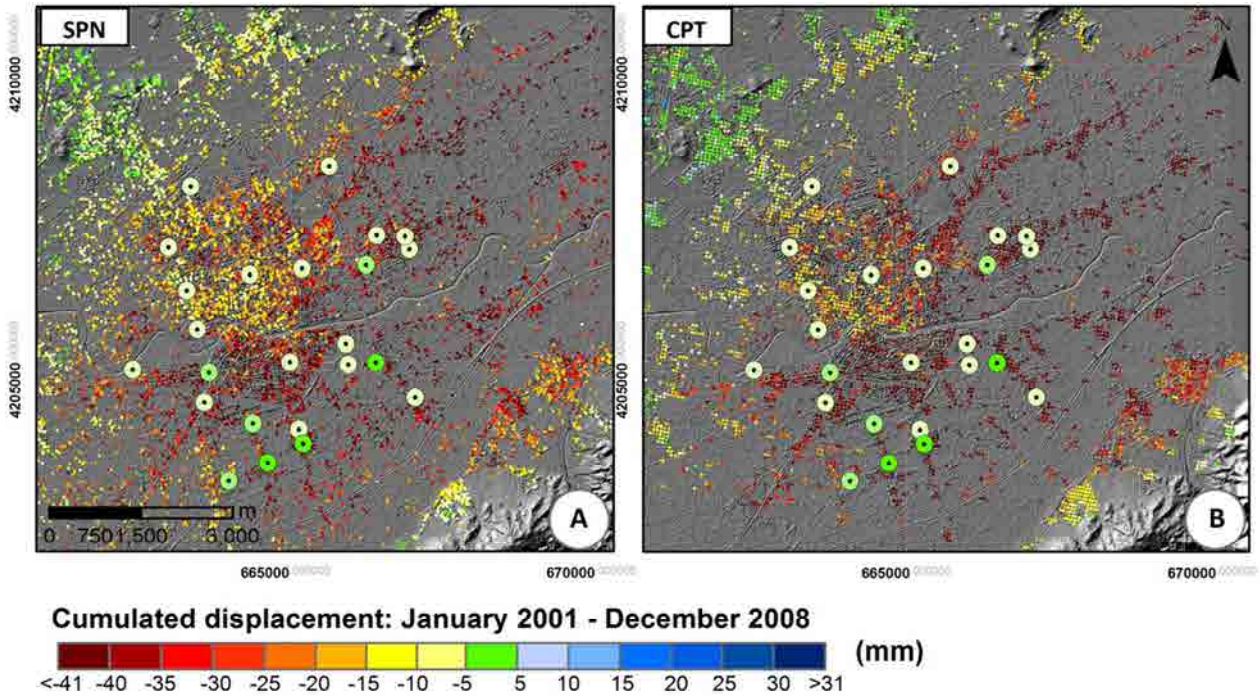

Figure 6.21: SPN-CPT spatial comparison; Labels have been placed in those extensometers whose comparisons are analysed in the next sections (see also fig. 6.4c).

As described in chapter IV, SPN is a PSI technique which works at full resolution, selecting all the targets having a stable reflectivity along time. On the other hand, CPT algorithm is a SBAS method which works at lower ground resolution depending on the multilook set.

A multilook of 15x3 has been used, achieving a pixel ground resolution of 60 m x 60 m.

In order to increase the points density it could be possible to choose a different multilook, such as 5x1 which corresponds to a pixel ground resolution of 20 m x 20 m.

However, taking into account the chart proposed by Blanco, (2009) (Fig. 4.15, chapter IV), in order to obtain 20° phase standard deviation value (which corresponds to a displacement standard deviation of about 1,5 mm), by means of a 5x1 multilook, an higher coherence threshold has to be fixed.

Such threshold could also bring to a lower number of selected pixels.

Therefore, a 15x3 multilook has been considered as an acceptable compromise.

At the same time, CPT technique allows areal analysis while SPN punctual ones. Inside a cell of 60x60 m, some persistent scatters can measure ground deformations and some others structural responses to the ground deformations (which very often are not representative of the subsidence phenomena because are function of the structural characteristics of the reflective target).

For this reason, following the approach proposed in Herrera et al. (2009), to the time series comparisons, only PS selected on the ground have been considered, avoiding PS located within building areas.

6.2.3.1.2. Time series analysis

CPT and SPN punctual comparisons have been carried out by overlapping SPN's time series on CPT ones in correspondence of an intermediate date between 1995 and 2010.

As shown in the time series (Fig. 6.18), the generalized subsidence affecting the VMSR go through an acceleration after 2005 (piezometric level remained almost constant between 1998 and 2005). For this reason, the 15/01/2005 (a common date to both the time series, preceding the third subsidence phase) has been chosen.

The temporal evolution of the displacements measured in points around each extensometer with the two techniques is plotted in Figs. 6.22 and 6.23. A general good agreement can be observed (see also the extensometer location in figure 6.4c).

Both time series present a stable behavior until the end of 2004 and January 2005 when a subsidence rate increase have been detected. This acceleration results more evident in the SPN's time series.

However, as said above, SPN's results were achieved processing the ERS and ENVISAT images (respectively covering the periods 1995-2005 and January 2004-2008) separately.

As described in the Par. 6.2.2.1.1., the chosen CPT results, analyzed in the present thesis, have been

performed processing all the available images (ERS1-2 and ENVISAT are processed together) for the whole period 1995-2010; this causes an estimation of the linear velocity by the algorithm which does not well appreciate the trend changes.

In fact, in the comparison shown in figure 6.18, the time series obtained separating the processing (in periods characterized by different mean velocities), this change rate is more evident.

However, as explained in paragraph 6.2.2.1.1, the processing achieved for the whole period 1995-2010 has been preferred to avoid other kinds of errors. In fact, in the output of the two different CPT processing (1995-2005; 2005-2010) there are different pixels. In other words, a pixel whose mean coherence results high in the first processing can be low in the second one.

Therefore, the use of the different processing achieved separating the images in two branches, causes uncertainness related to the pixel choice.

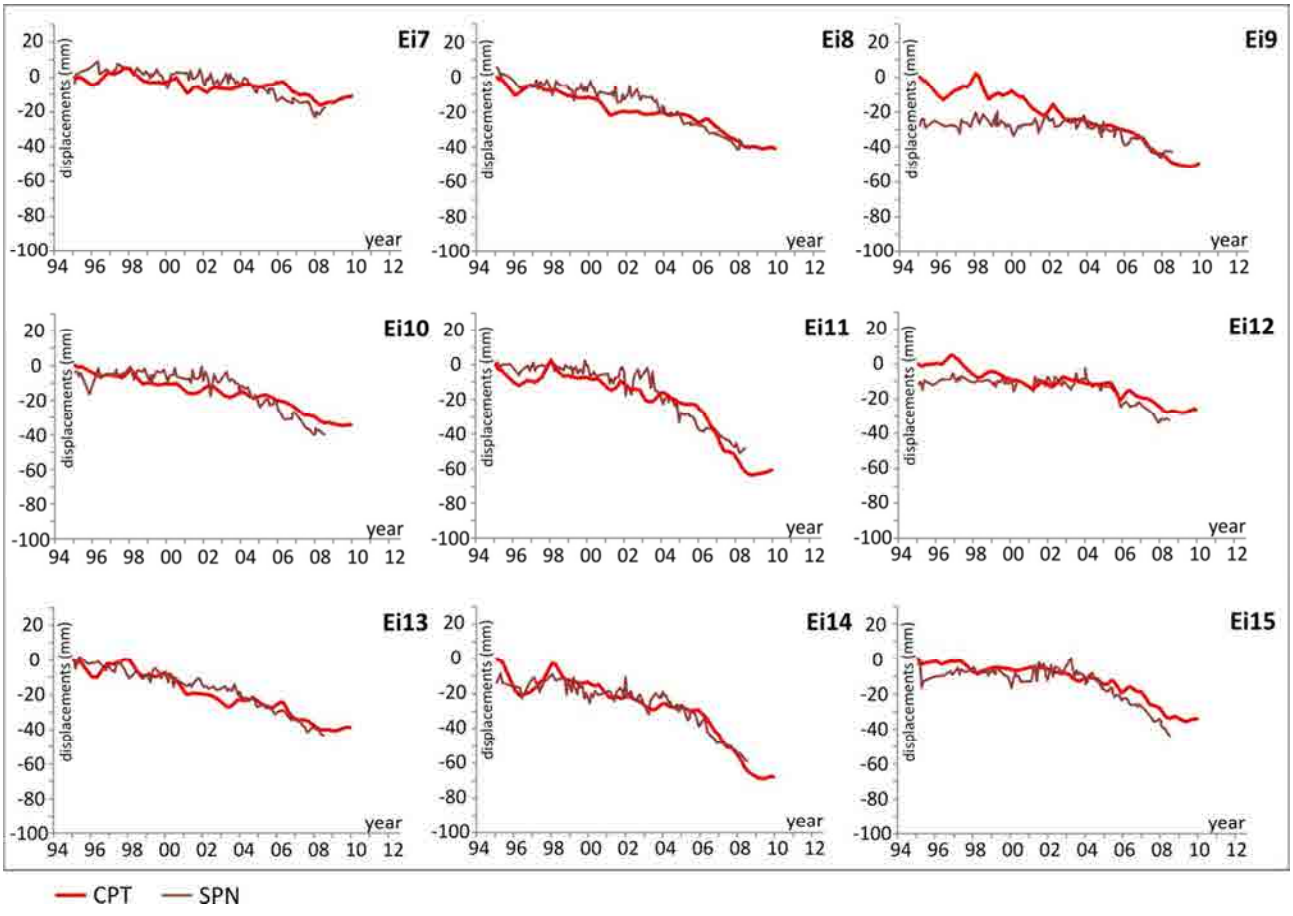

Figure 6.22: CPT-SPN's time series comparisons; (it has been achieved for points around the extensometers of phase III)

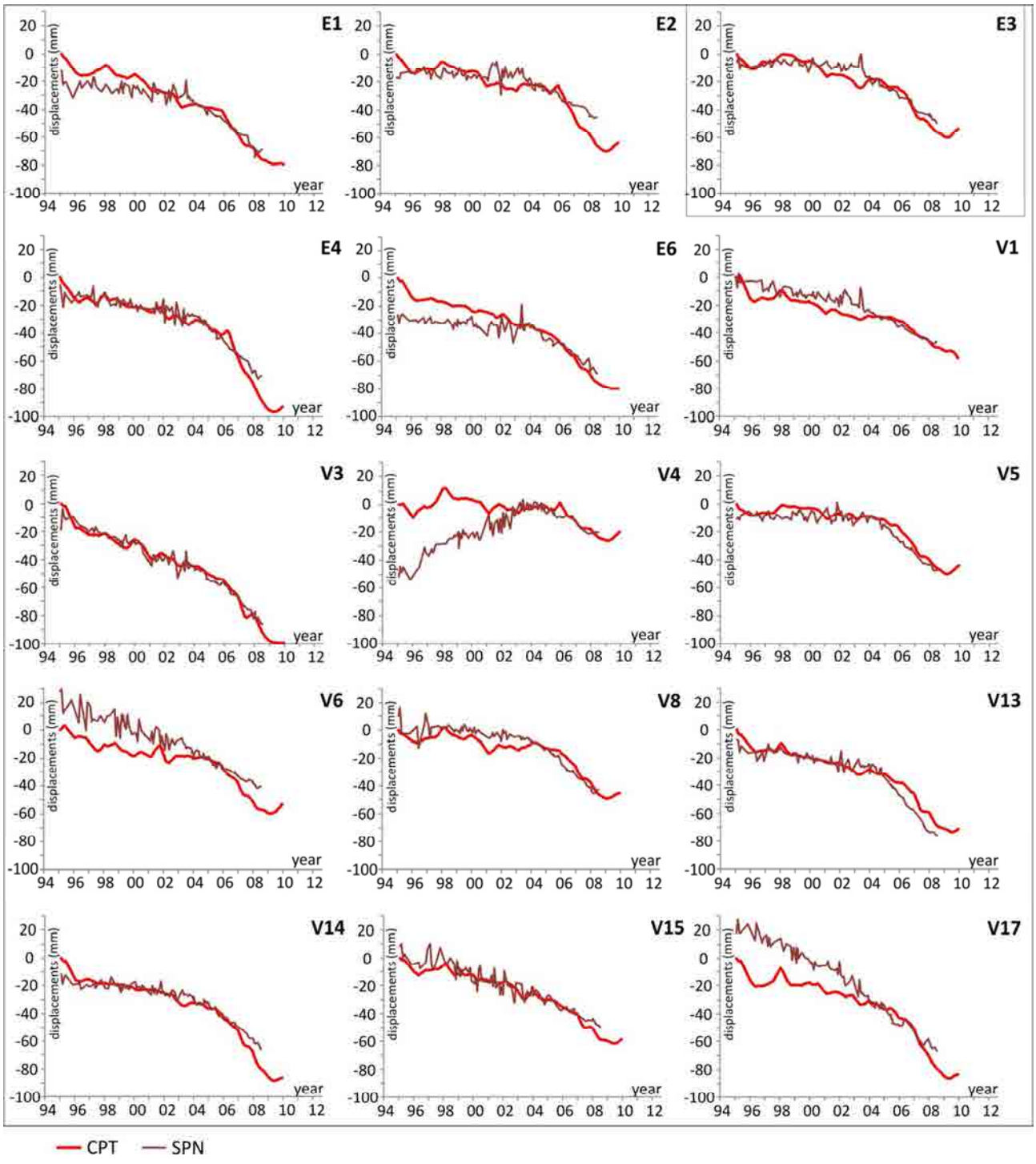

Figure 6.23: CPT-SPN's time series comparisons; (it has been achieved for points around the extensometers of phase I and II)

The differences of the CPT and SPN's punctual comparisons have been calculated and shown in table 6.3.

			Absolute difference (mm) |XCPT-XSPN|			Difference (mm) (XCPT-XSPN)		
Extensometer	**CPT point**	**SPN point**	**μ**	**σ**	**Max**	**μ**	**σ**	**Max**
Ei-2	5309	51171	6.1	5.4	18.7	-2.0	8.1	17.3
V-8	5043	49040	5.0	3.8	18.8	-2.5	5.8	9.0
V-4	5487	52225	14.2	14.6	51.8	13.4	15.4	51.8
V-5	5013	49018	4.3	2.9	10.7	3.7	3.7	10.7
Ei-3	5102	49522	4.2	4.0	24.8	-0.9	5.8	8.0
Ei-1	4675	46594	5.7	4.9	20.6	3.5	6.6	20.6
V-1	4755	47187	4.9	4.3	22.6	-3.5	5.5	7.1
V-3	4889	48405	3.1	2.6	19.0	0.4	4.0	19.0
V-6	4538	45875	10.8	8.1	28.8	-10.4	8.6	4.1
Ei-4	4243	43795	4.4	3.9	17.2	-1.5	5.7	16.6
V-17	4089	42874	12.7	9.8	35.8	-10.9	11.7	10.0
V-14	2855	35759	4.0	3.9	17.8	-1.5	5.4	17.8
V-13	3222	37787	4.4	4.0	14.1	2.5	5.4	14.1
V-15	2773	34932	4.1	3.7	19.3	-2.3	5.0	10.7
Ei-6	2702	34705	8.0	6.5	30.6	5.9	8.5	30.6
Ei10	3373	39046	5.0	3.0	13.3	-0.9	5.7	10.7
Ei11	4540	44394	5.4	3.6	16.9	-2.1	6.1	12.1
Ei12	2718	33759	4.3	3.4	13.5	3.4	4.3	13.5
Ei13	3914	41670	3.1	2.7	11.0	-0.2	4.1	10.8
Ei14	4432	44775	4.0	2.9	13.6	0.8	4.9	13.6
Ei15	2200	30616	4.3	3.0	13.8	3.3	4.1	13.8
Ei7	4253	43801	4.2	3.0	12.6	-0.6	5.2	10.6
Ei8	3475	39371	4.1	3.4	15.1	-2.1	4.9	7.5
Ei9	3531	40061	8.9	8.4	27.7	8.2	9.1	27.7
		μ	**5.8**	**4.8**	**20.3**	**0.1**	**6.4**	**15.3**

Table 6.3: Comparison between SPN's and CPT's vertical displacement time series (close to the extensometers in figure 6.4c).

Here, the mean (μ) and the standard deviation (σ) of the difference and of the absolute difference between the time series in Figs. 6.22 and 6.23 have been reported.

The average value of the absolute difference between the two time series for all the extensometers is **5.8±4.8** mm and their difference is **of 0.1±6.4** mm on average.

The maximum distance between the time series is registered for V4 which is located in a low coherence area; furthermore, in the CPT pixel of 60x60 m (relative to the V4 location), several SPN persistent scatters (belonged to a street and a parking) have been found and are characterized by a trend similar to that observed by the CPT's time series.

However a SPN persistent scatters found on the ground has been considered in order to report the most probable soil deformation behavior not affected by the effects of the presence of structures.

6.2.3.2. Comparisons between radar and in situ monitoring data

6.2.3.2.1. Comparisons with piezometric data

As described in paragraph 6.2.1.1, in the metropolitan area of Murcia city, piezometric time series show a similar behavior. In particular, three important ground water level declines have been registered in the periods 1982–1984, 1993–1995 and 2005–2008, correlated with the temporal evolution of ground surface displacement estimates.

Of course, subsidence magnitude and rapidity are not only a function of the effective stress increase due to the water level falls, but also of the deformability (function of the stress level) and of the thickness of the compressible soils (Terzaghi, 1923). For this reason, the comparisons between piezometric variations and measured settlements result to be useful to understand the phenomenon mechanism and to identify anomalies in the soil general behavior.

Differently from the comparisons between piezometer and extensometer time series, shown in figure 6.9, that ones carried out using DInSAR results are not affected by the uncertainness related to the piezometer distance from the extensometric columns and allow some interesting considerations.

In general, in most areas inside the VMSR, the temporal evolution of A-DInSAR measured ground deformations (available only after 1995) shows a good correlation with piezometric level changes measured in the surficial gravel layer. As introduced in par. 6.2.1.1, it depends to the goodness of the connection between aquifer (where pore pressures are measured) and aquitard (where the main deformation occurs). Fig. 6.25 shows several comparisons carried out in some emblematic cases whose location is reported in Fig. 6.24.

The first comparison regards the historical piezometer P-1 (located in the South-Western part of the study area) closest to the city center. It is evident that, in this case, advanced DInSAR measured displacements perfectly agree with piezometric water level changes and this can indicate that, here, there is a good connection between aquifer and aquitard.

The other significant considerations regard the comparisons of radar measured displacements and multilevel piezometric data. In particular, some of the piezometers where aquifer and aquitard results to be well connected, CPT vertical displacement time series have a good agreement with the water level variation (P-23; P-46; P-32; P-45; P-1415; P-19); on the other hand, if piezometric measurements are very different, CPT's time series, follow the water level variation detected by the surficial piezometer (P-21). The comparison referred to P-78 shows a little delay in according to the considerations of par. 6.2.1.1.

These comparisons are very interesting because they show that, when multilevel piezometers are not available, the connection between aquifer and aquitard could be analysed through the use of DInSAR data.

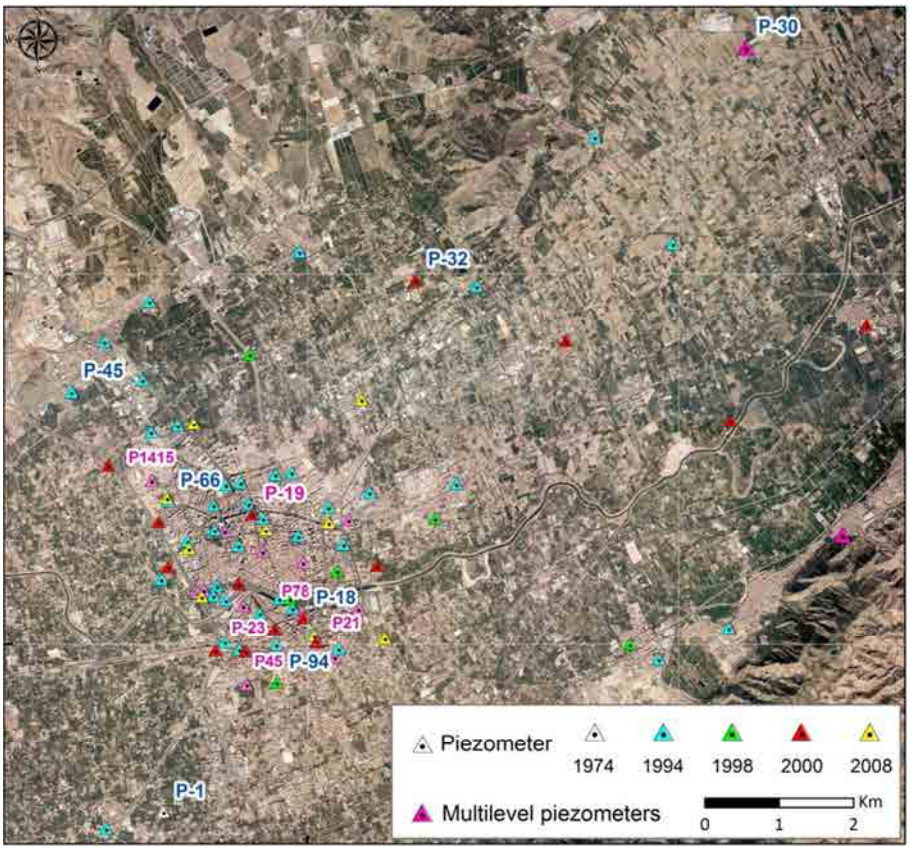

Figure 6.24: Location of the piezometers compared with CPT results

Moreover, most of the comparisons show the subsidence acceleration due to the overpassing of the pre-consolidation pressure (P-1; P-19; P-21; P-23; P-45; P-78) which, in the case of no-connection between aquitard and aquifer is not simultaneous for surficial and deep layers (P-21).

The preconsolidation pressure, as introduced above, marks the change in soil deformability and separates high non recoverable deformations from lower deformations (recoverable). In the study area, the first historical minimum was registered in 1984 and overpassed in 1995, but no in situ measurements are available to quantify the plastic part of deformation which has not been recovered. After the last two droughts, the piezometric level recuperated 85% until 1998 and more than 92% until February 2012. Thus, in previous studies (i.e. Tomás et al., 2010) the piezometric data have been used together with radar displacement measurements (available for the second draught occurred in 1993-95) to find the storage coefficients (physical properties that characterize the aquitard deformability and vary with the stress state). The ratio between the an-elastic (S_{kv}) and the elastic storage (S_{ke}) coefficient resulted to be of 15% on average and allows to achieve the non-recoverable part of the displacements cumulated in the draughts occurred in the study area when the pre-consolidation pressure was overpassed.

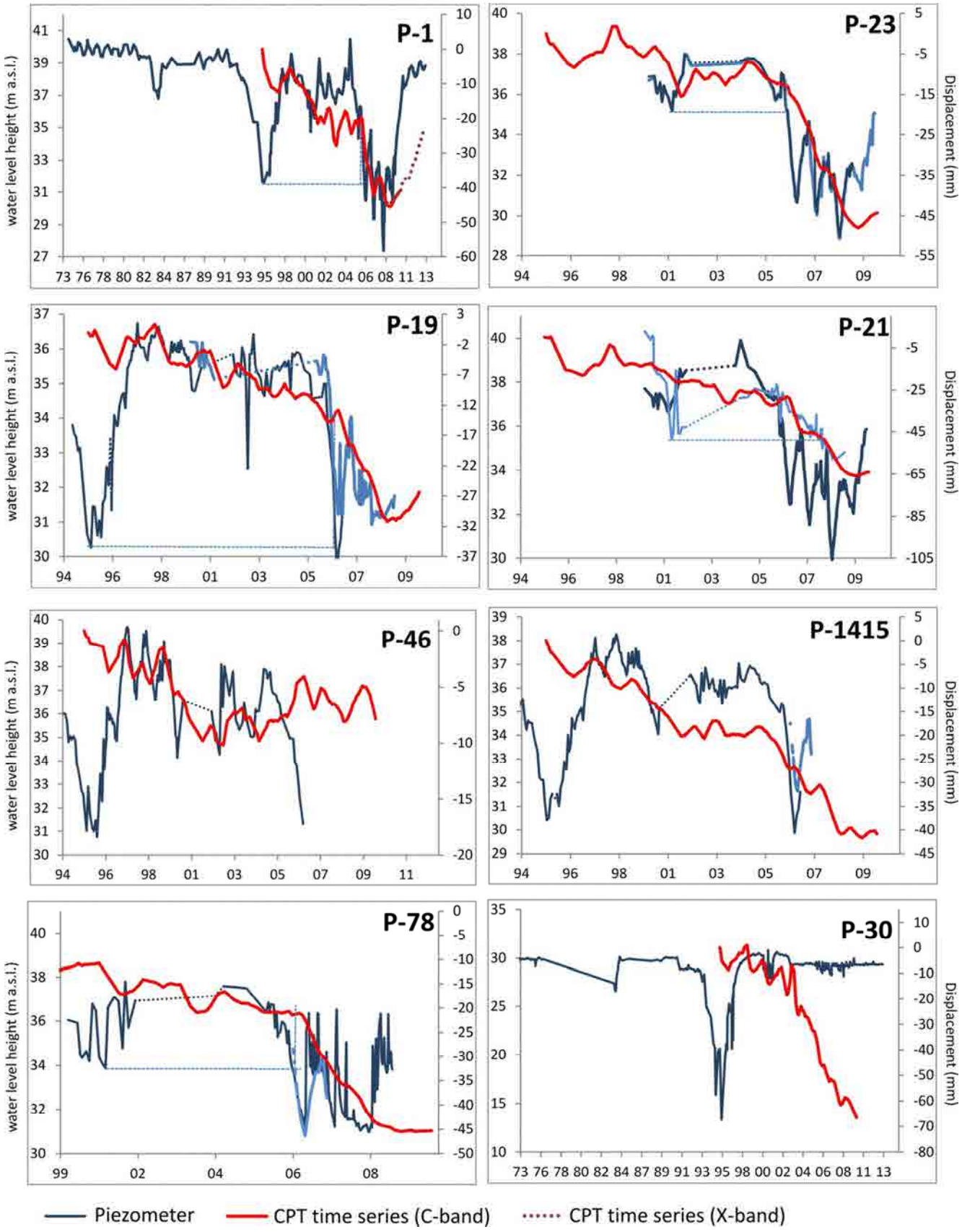

Figure 6.25 Comparisons between CPT's measured displacements and piezometric time series

An anomalous comparison is achieved for the piezometer P-30, located in the North-Eastern part of the VMSR. In this case, according to the comparison shown in Fig. 6.25, the maximum groundwater level fall of 15 m, measured in 1995, seems to have produced a consolidation process started in 2003; this, seems to have provoked a ground surface down-lift of 7 cm until May 2010.

This is in agreement with the general spatial analysis of par. 6.2.2.1.2. Here, the CPT results (Fig. 6.19) have shown that the recuperation of the aquifer occurred in the period 2008-13 has led to a general uplift of the ground surface; in particular, it has been detected from the SAR in the southern part of the valley and in the metropolitan area of Murcia city, while in the Northern part, a little subsidence (-1 cm on average) phenomenon (not detected before) has been registered between 2009 and 2010.

Therefore, subsidence detected by SAR for P-1 and P-30, could be due to two different mechanisms:
in P-1's case, a rapid consolidation process due to the hydrological connection between aquifer and aquitard generates a ground subsidence in 2008-09 related to the fall of the water level registered in 2008.
In P-30 case, the ground drop detected in 2008-09 seems related to the 1995 fall of the water level.

This is a key point for the later analysis because, for a spatial analysis and interpolations, only in situ and radar data belonging to the urban area can be used.

However, as should be noted, this result can also be due to the distance between P-30 and the *"seed"* used in the CPT processing, located on the Sierra.

In fact, pixels located too much far from the seed used in the processing, can have a low coherence of the links with the other pixels; this, using a SBAS technique, as explained in chapter IV, can affect the results.

In fact, considering all the available radar data in the valley (for the period 1995-2009), a trend is observed along the valley axis, which corresponds to a subsidence increase in S-E direction; however, to understand if the maximum deformations measured in 2009 in the whole valley is related to water level fall registered in 2008 (and not, like in P-30's case, to that of 1995) an in depth-analysis of the phenomenon must be carried out. In particular, the aquifer characteristics in the North-Eastern part of the valley, the wells' position and the comparisons of the CPT results (function of the used seed) with the PS ones have to be considered to understand if this anomaly is caused by the processing method.

However, independently from the cause of these anomalies, all the spatial analysis have been carried out at a local scale (Par. 6.4.2), considering the area of 36 Km^2 introduced in Fig. 6.20; here, in fact, as showed in Fig. 6.12, the pixels' links have a high coherence and no anomalies (both due to the processing or to the consolidation process characteristics) have been observed.

6.2.3.2.2. Comparisons with extensometric data

The temporal evolution of the displacements measured by the 24 available extensometers have been compared with that estimated through the CPT technique.

The extensometers' locations are reported in figure 6.26a, where their acquisition depths have been represented.

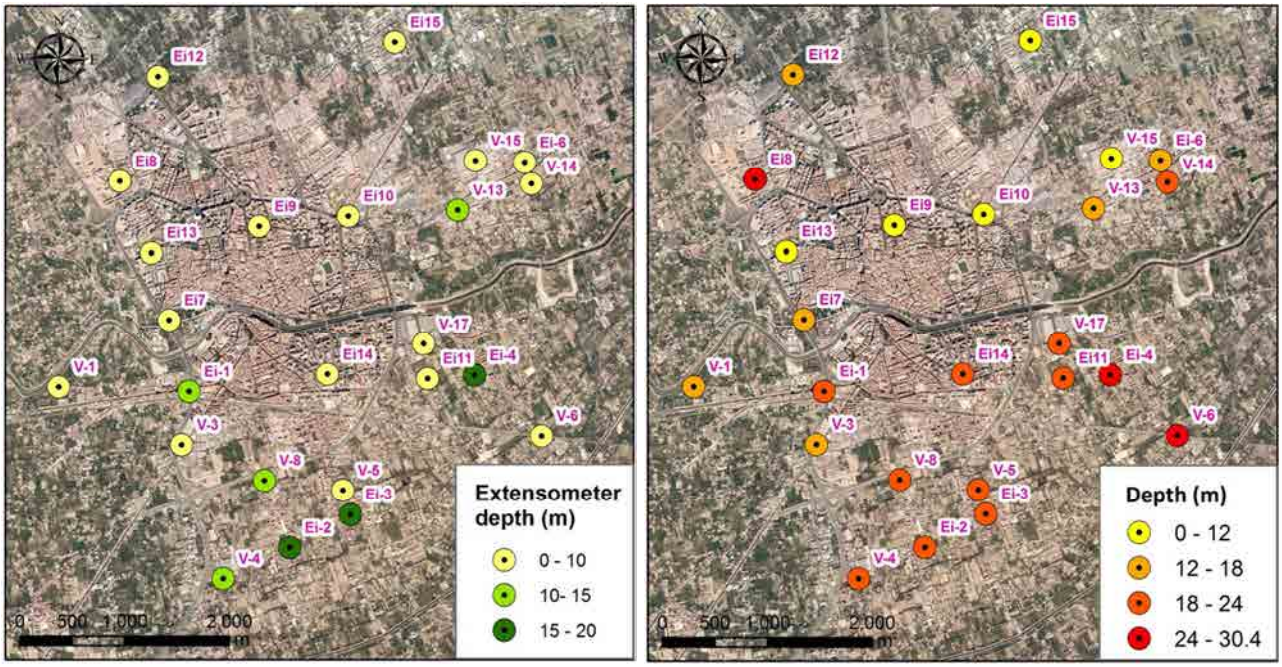

Figure 6.26: Extensometers depth (left); compressible material thickness (right)

It is possible to note that extensometers' network registers deformations occurred up to the depth of 10-20 m (Fig.6.26a), while radar measures the whole deformation of the entire stratigraphic column.

For this reason, is useful to refer to the parameter "Θ" (Fig. 6.27), defined as the difference between the gravel top and the extensometer's depth. Thus, it is an indicator of the part of soil not monitored by the extensometer but monitored by the radar. It is useful to better analyze the comparisons between extensometers and radar displacement's time series shown in Figs. 6.28 and 6.29. In particular, in Figs. 6.28 and 6.29, the CPT's data (1995-2010 and 2008-2013) and the SPN's data (1995-2009) have been reported.

A general good agreement can be observed between the ground based measurements and the SAR based estimations of deformation. This is probably due to the hydrological settings, as described in Par. 6.2.1.1.

Therefore, (according to the procedure described in Herrera et al. 2009), the mean and standard deviation respectively of the difference and of the absolute difference between CPT's coherent points and extensometer deformation's time series, have been calculated.

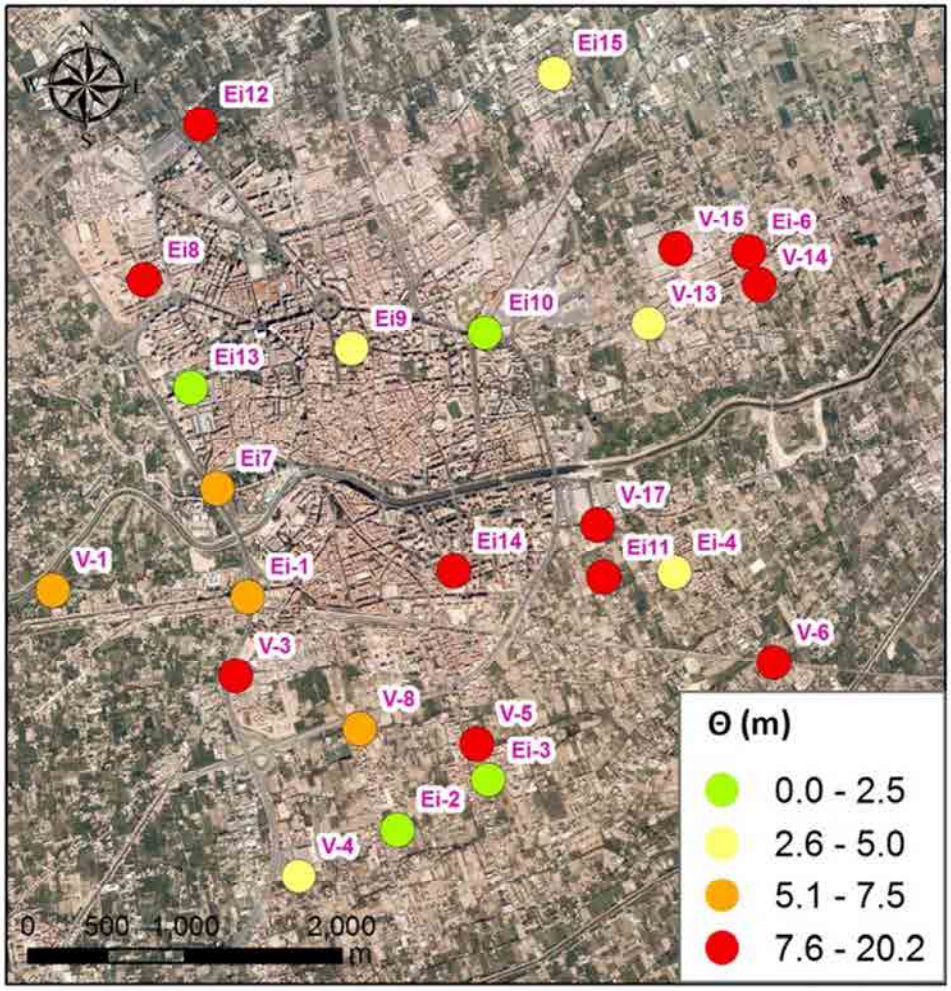

Figure 6.27: Difference between the gravel top and the extensometer's depth (Θ)

The two time series have been overlapped in correspondence of the 24/10/01, (first common date of the time series) to verify the distance between them at the end of the monitored period.

When $X_{EXT} - X_{CPT}$, in Tabs. 6.4 and 6.5 is positive, it means that radar displacement estimates a higher vertical deformations respect to the extensometers.

This has to be in agreement with others parameters, i.e. compressible material thickness, soil stiffness, OCR, and permeability values. In particular, radar detects a higher deformation respect to that measured by the extensometers for Ei1, Ei6, V3, V14, V17, (Fig. 6.28).

Specifically, in all these extensometers, Θ>5m and the compressible material thickness is between 12 and 24 m.

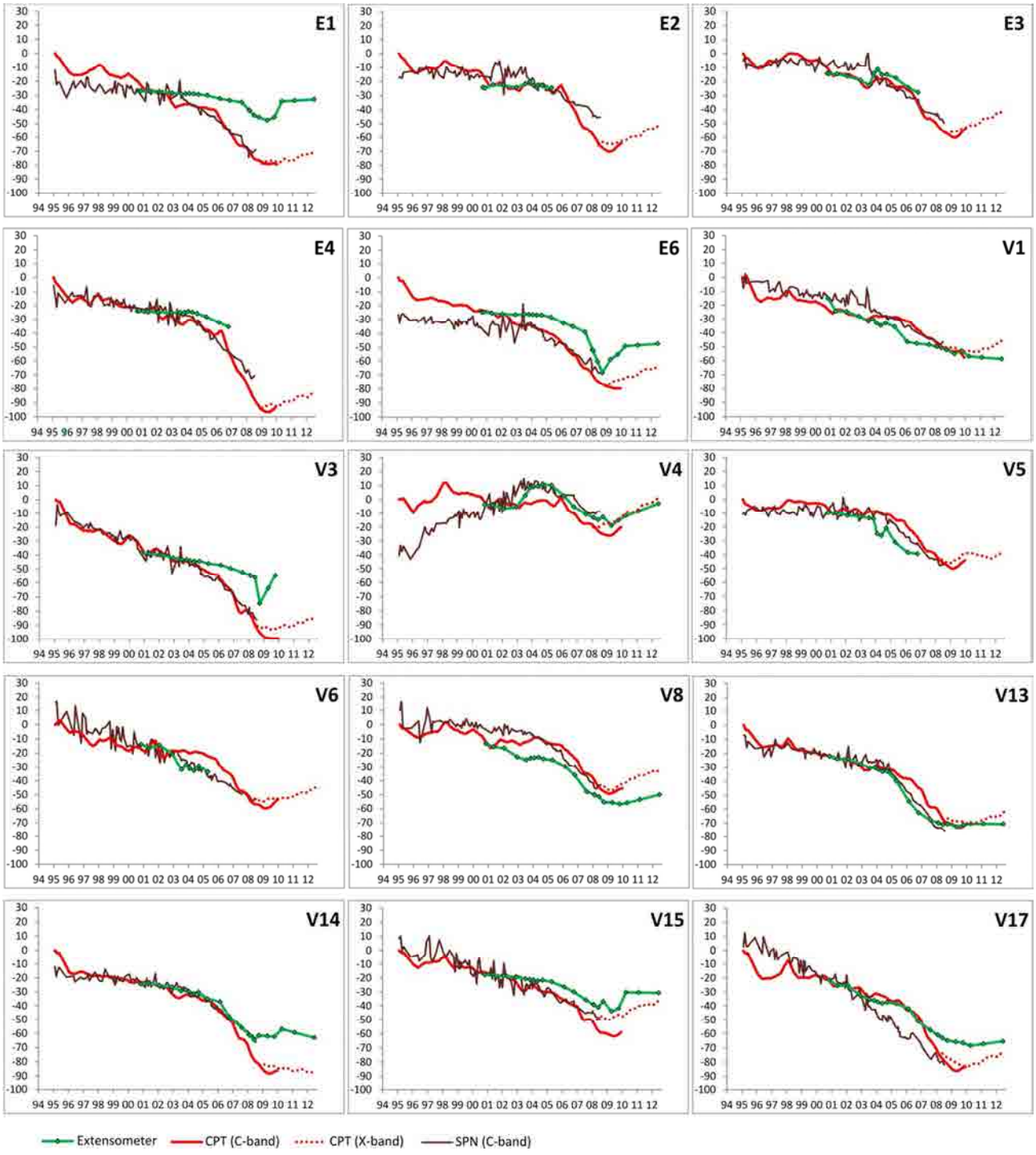

Figure 6.28: Comparisons between extensometers of phase I and II and DInSAR displacement time series (C-band images processing achieved through SPN algorithm for the period 1995-2009 and through CPT technique for the period 1995-2010 have been integrated with the X-band images processing results obtained through the CPT technique for the period 2008-2013).

Comparing the 15 extensometers of the phases I and II with the CPT's vertical displacement time series estimated by the C-band images' processing for the common monitoring period 2001-10, an error of **3±7** mm and an average absolute error of **8±6** mm have been achieved (Table 6.4).

	ERS_ENVISAT data 2001-2010	Absolute difference (mm) |Xext-XCPT|			Difference (mm) (Xext-XCPT)			
Extensometer	**CPT point**	**Θ (m)**	**μ**	**σ**	**Max**	**μ**	**σ**	**Max**
Ei-2	5309	2.5	2.1	2.8	0.0	-1.2	3.4	-8.5
V-8	5043	6.0	9.7	4.1	1.4	-9.7	4.1	-14.3
V-4	5487	4.0	7.2	3.8	1.2	6.2	5.3	-5.7
V-5	5013	12.5	9.0	6.5	2.4	-9.0	6.5	-18.1
Ei-3	5102	2.5	3.4	2.5	1.1	2.2	3.7	-3.9
Ei-1	4675	6.5	16.1	12.3	1.1	15.2	13.5	-5.6
V-1	4755	7.3	4.1	3.9	0.1	-2.9	4.9	-14.8
V-3	4889	8.3	14.1	14.6	0.8	13.4	15.3	-3.2
V-6	4538	15.1	8.0	4.8	2.4	-6.4	6.9	-13.7
Ei-4	4243	5.0	5.9	4.9	0.7	5.4	5.3	-1.6
V-17	4089	11.5	7.1	6.5	0.5	3.8	8.9	-5.7
V-14	2855	9.0	7.8	8.1	0.5	7.7	8.3	-1.5
V-13	3222	3.2	4.3	5.3	0.1	-3.8	5.7	-17.7
V-15	2773	10.0	9.5	6.5	1.1	9.2	6.9	-1.7
Ei-6	2702	10.0	11.6	7.9	0.5	11.4	8.2	-1.4
		μ	**8.0**	**6.3**	**0.9**	**2.8**	**7.1**	**-7.8**

Table 6.4: Comparison between CPT vertical displacements (C-band images processing) and extensometers time series for the common monitoring period 2001-10.

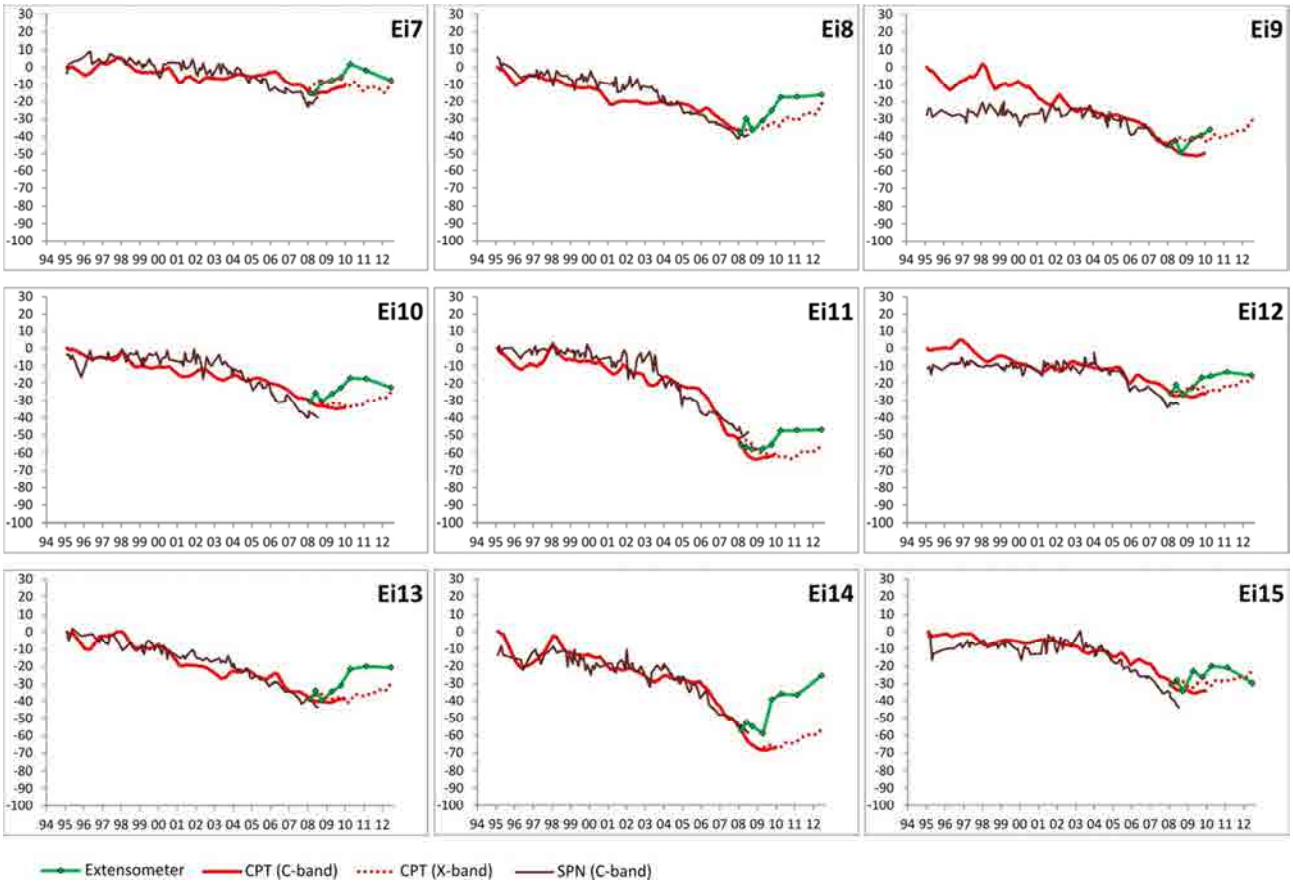

Figure 6.29: Comparisons between extensometers (phase III) and DInSAR displacement time series: SPN data 1995-2009; CPT data 1995-2010 (C-band) and 2008-2013 (X-band).

For the 18 extensometers having data after 2008, also the error and the absolute error of their comparison with Terrasar-X images' processing results, achieved through the CPT technique for the period 2008-2013, have been computed and shown in Tab. 6.5.

In the recuperation phase, a different behavior between extensometer and radar measurements can be appreciated: most of the extensometers show a marked uplift between 2009 and 2010 and a stable behavior after 2010; nevertheless, radar results, in general, do not register a change of trend in 2010 but a gradual ground up-lift (Fig. 6.29).

From these comparisons, an error of **1.5±5.8** mm and an average absolute error of **5.6±5.0** mm have been obtained (Table 6.5).

	Terrasar-X data 2008-2013	**Absolute difference (mm) |Xext-XCPT|**			**Difference (mm) (Xext-XCPT)**			
Extensometer	**CPT point**	**Θ (m)**	**μ**	**σ**	**Max**	**μ**	**σ**	**Max**
V-8	32810	6.0	4.7	4.0	9.5	-4.7	4.0	-9.5
V-4	36521	4.0	4.7	4.2	9.5	-4.7	4.2	-9.5
Ei-1	28679	6.5	4.2	2.6	7.0	-2.6	4.4	-7.0
V-1	29670	7.3	3.6	7.0	20.8	-2.7	7.5	-20.8
V-17	23196	11.5	2.2	2.7	8.1	-0.1	3.6	-8.1
V-14	8170	9.0	2.5	3.1	7.6	-0.2	4.1	-7.1
V-13	11982	3.2	1.1	0.9	2.3	-0.7	1.4	-2.3
V-15	6115	10.0	3.4	3.5	8.4	-2.7	4.2	-8.4
Ei-6	5796	10.0	8.3	6.8	21.2	-8.3	6.8	-21.2
Ei10	13862	2.5	11.9	9.2	24.4	11.9	9.2	0.0
Ei11	25926	10.7	3.1	2.7	7.3	-1.0	4.2	-5.8
Ei12	3151	16.1	5.5	4.4	11.8	4.7	5.4	-3.1
Ei13	19345	2.4	8.0	6.6	18.1	7.8	6.9	-0.8
Ei14	26615	10.5	10.7	9.8	22.6	10.7	9.8	0.0
Ei15	4	3.2	5.1	4.2	10.1	0.3	6.9	-8.8
Ei7	24369	7.3	4.6	4.3	12.6	2.4	6.1	-7.0
Ei8	13993	20.2	8.2	6.5	18.2	7.6	7.2	-2.3
Ei9	15745	3.3	8.7	8.2	19.8	8.5	8.5	-0.7
		μ	**5.6**	**5.0**	**13.3**	**1.5**	**5.8**	**-6.8**

Table 6.5: Comparison between CPT vertical displacements (X-band images processing) and extensometers time series for the common monitoring period July 2008 – November 2011.

As reported in Herrera et al., 2009, some recent validation experiments available in the scientific literature (Strozzi et al., 2001; Hanssen, 2003; Colesanti et al., 2003; Casu et al,, 2006; Crosetto et al., 2008; Herrera, 2008, 2009; Tomás 2009) have found that the error of the deformation time series, estimated with different A-DInSAR techniques, compared with "ground truth" measurements was within the ±6.9 mm interval.

These values are in accordance with those found in this analysis, but, in this case, the trend analysis has shown, in some comparisons (Ei1, V3, V17), a not very good correspondence, probably related to the different consolidation characteristics at different depths due to the aquifer features.

Moreover, according to the comparisons in figures 6.28 and 6.29, (referring to the subsidence phase), Ei2, Ei3 (Θ<2.5 m) and Ei4, V4, V13, Ei9 (2.5<Θ<5 m) register almost the same deformations detected by SAR; all the rest (Θ>5 m) a lowest or at least equal deformation respect to DInSAR measurements.

So, in the subsidence phase, an increase of the parameter Θ, corresponds to a higher radar measured deformations respect to the extensometer ones, or, at least, they can be equal, due to the increase of the stiffness with the depth. This has been quantified and reported in Figs. 6.30 and 6.31.

Fig. 6.30 shows the correlation between Θ values and the absolute error of the CPT-extensometer's comparison. In particular, the absolute difference between extensometers and CPT's measured displacements increase with Θ.

In the recuperation phase, other parameters, like the soil plasticization, the hydrogeological settings or the percentage of sand below the extensometer basis have a greater influence in the measured ground uplift than the compressible thickness; thus, the correlation with Θ parameter does not result significant.

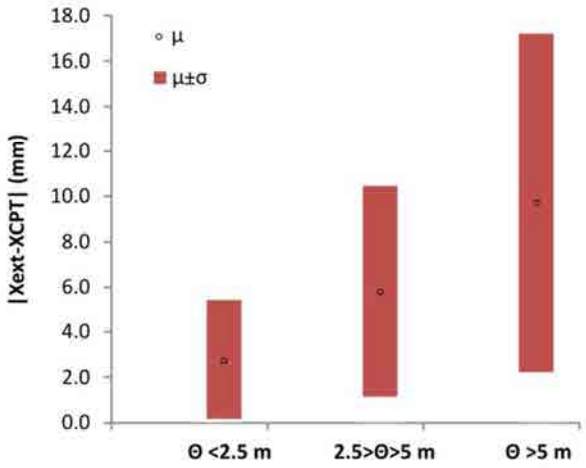

Figure 6.30: Error correlation with the parameter Θ

Figure 6.31 shows the comparison between the average of all the extensometers' measured deformations and the average of the CPT's displacement time series, plotted in figures 6.28 and 6.29.

As it can be seen, in general, CPT's and extensometer's time series present a similar deformation trend. In this case, as observed in the previous paragraphs, these deformations result to be rapid respect to water level variations; this is due to the presence of a high permeability layer of sandy-clay above the gravel layer.

It is evident that the two averages are equal until 2006-07; after CPT's measured displacements are greater than the extensometers ones.

However, all these evaluations and estimated errors cannot completely demonstrate if the whole extensometric network is representative of the observed phenomenon, but only that, in general, CPT's time series trends are in according to in situ measurements.

In fact, as described in paragraph 6.2.2.1.1, the time series computation with the coherence based method are affected by errors which have influence in the magnitude of the cumulated deformation; these are related to the coherence of every used interferogram and is very difficult to identify the images whose interferograms reduce the average coherence, increasing or reducing the noises and the errors in the computed final displacement. For this reason, a difference of an order of millimeters between the CPT's time series and the extensometers is not enough to be considered as an indication about when the in situ measurements could not be representative of the observed phenomenon. Only in some few cases (Ei1, V3, V17, Ei6, V14 and V15), the difference (during the subsidence phase) is of the order of the centimeter and the trends analysis confirms that is very probable that, in these cases, the extensometers are monitoring only a part of the deformations which affect the underground soils.

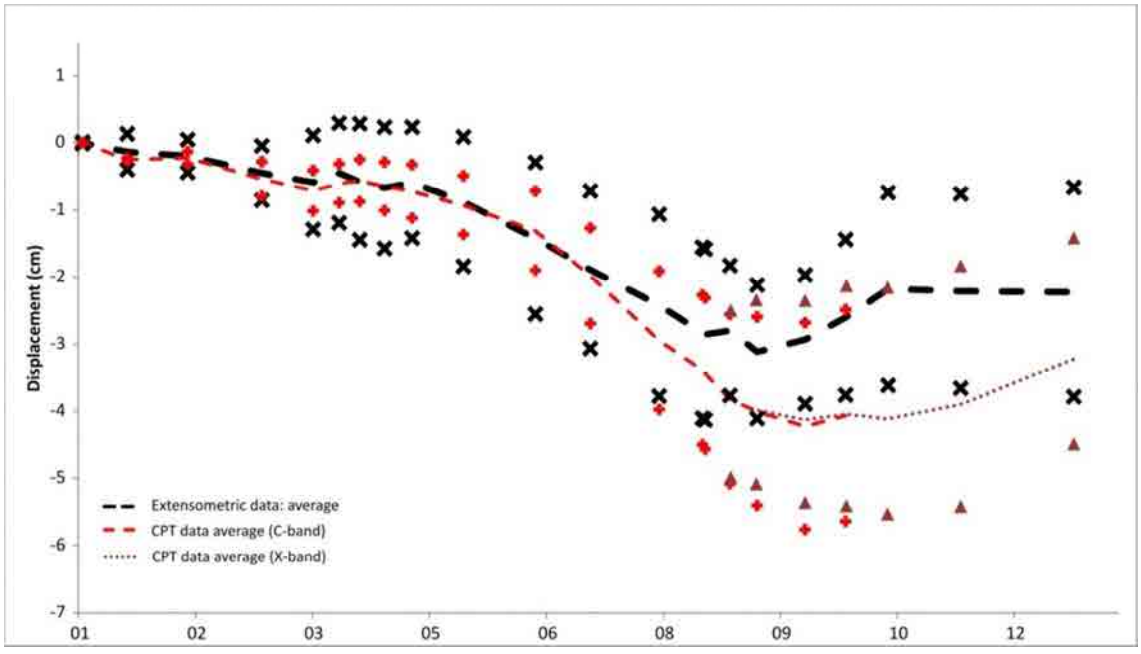

Figure 6.31: Comparison between the averages of extensometric and CPT's estimated deformations (1995-2010 and 2008-2012)

However these comparisons allow to understand that most of the deformations occurred in the firsts 10-20 m from the ground surface. In fact, considering Fig. 6.31, the average of the maximum cumulated displacement measured by the extensometers is about 75% of the CPT one.

In particular, it is possible to note that:

V-3 is registering deformations (in the first 10 m) which correspond to a very slow consolidation; it presents a rate increase, probably related to the overpassing of the pre-consolidation pressure of the surficial soils, in November 2008. Nevertheless, the radar registers a velocity increase in March 2006 (in correspondence of the overpassing of the historical minimum water level and probably, of the overpassing of the pre-consolidation pressure for the deepest soils). V3's stratigraphy presents the firsts 10 m (to the ground) of clay, then about 4 m of sands and, below, 4.5 m of clay up to the gravel layer; the water level variations occurs between 3.5 m and 13 m below the ground level. Thus, it is probable that the deepest clay layer is suffering deformations that the extensometer cannot monitor.

Ei-1 is located in correspondence of the multilevel piezometer P-23 (Fig. 6.6) which has shown a very good connection between aquifer and aquitard; the very little detailed stratigraphic column description reports 0-14 m of clay or sandy clay; 14-21.5 m of sandy clay, 21.5-25 m of gravel. Nevertheless, while radar data are in perfect agreement with piezometric time series (Fig. 6.25), Ei-1 registers little deformations, only having a velocity increase in correspondence of the pre-consolidation pressure overcome. Radar data seems to measure a higher deformation with a trend change before that registered by the extensometer and this could mean that it is measuring deepest soils deformations. However, here, are not available geotechnical tests to the aquitard characterization except for some permeability laboratory and Lefranc's tests. According to the laboratory test, aquitard permeability is of 3.37×10^{-7} m/s, while for the Lefranc tests is 9.37×10^{-6} m/s. In both cases, as will be demonstrated in the paragraph 6.3.3, this values guarantee rapid deformation response to water level changes.

Ei-6, V-14, V-15 are very close and differs only for the sand percentage respect to the total compressible materials thickness of the stratigraphic column.

Ei-7, Ei-8, Ei-9, Ei-10, Ei-11, Ei-12, Ei-13, Ei-14, Ei-15 have data only after August 2008 which present a perfect correspondence with the water level recuperation. For some of them (**Ei-7, Ei-12, Ei-15**), a quite good correspondence with CPT's time series (obtained from the TSX images' processing) has been observed, while in the other cases, they do not appreciate the strong trend change registered by the extensometers after 2010. Among them, in some cases (**Ei-7, Ei-8; Ei-9, Ei-13**), radar data do not show the marked bi-linear deformation behavior observed in the period 1997-2009 for all the others. In particular, they are located in the North-Western part of the city where the fine-grained soils have suffered a pre-consolidation due to the presence of the ancient city walls and, in general, present a higher stiffness. This can justify the deformations detected both through CPT's and SPN's algorithms which are characterized by an almost constant linear velocity, without marked trend changes.

6.2.3.2.3. Spatial evolution

In order to perform a spatial comparison between the different monitoring data, both the extensometers and the groundwater level changes (obtained from the data introduced in Pars. 6.2.1.1 and 6.2.1.2) have been interpolated using the IDW method (Fig. 6.30). This method has been chosen due to the limited number of data available for the interpolation, considering that no deformation is produced in the ranges that limit the VMSR. To the interpolation technique description, see Par. 6.4.

Concerning the groundwater level variation's interpolation, all the VMSR piezometric data available for the periods 2001-2009 and 2009-2012 have been used. The error introduced by the interpolation is significant, especially in those areas where in situ data are not available. However, the generation of these maps is useful to enhance the spatial analysis of the results. This analysis is partially supported by the radar displacement data that are more densely populated.

From the so obtained 2D maps is possible to make some considerations.

The water level drop occurred in the period 2001-2008 is more intense in the South-Eastern and North-Western areas (6-8 m) than in the city centre (2-4 m), coinciding with the magnitude of the displacement measured with both the extensometers and the radar data (c and e in Fig. 6.32).

On the other hand, during the period 2008-2012, it is observed that the ground water level recuperation is intense and uniform (11-7 m), showing a decreasing gradient towards the North where the recuperation is smaller (Fig. 6.32).

In this period, as previously noted, also from the time series comparisons in figure 6.9, the extensometers show a generalized uplift, that is especially more significant in the city center. Note that in this area, the gravel layer is surficial (about 10 m deep with sand layers up to its top); the water level drop turns out to be less than 4 m and the recuperation passed 7 m, favoring the measured terrain uplift. TSX data (Fig. 6.32 f) show a generalized uplift which is more intense in correspondence of V4, Ei8 and Ei12. There is a good correspondence of the more stable areas detected by SAR, in particular near V1, V17, V13 where extensometers do not show a marked uplift (see also Figs. 6.28 and 6.29). However, in general TSX data registers a lower ground uplift than the extensometers.

Obviously, the greatest disagreement between the monitoring data occurs where in situ data are not available and the interpolation error is greater (i.e. northern part of the city where extensometers data started to be acquired in 2008).

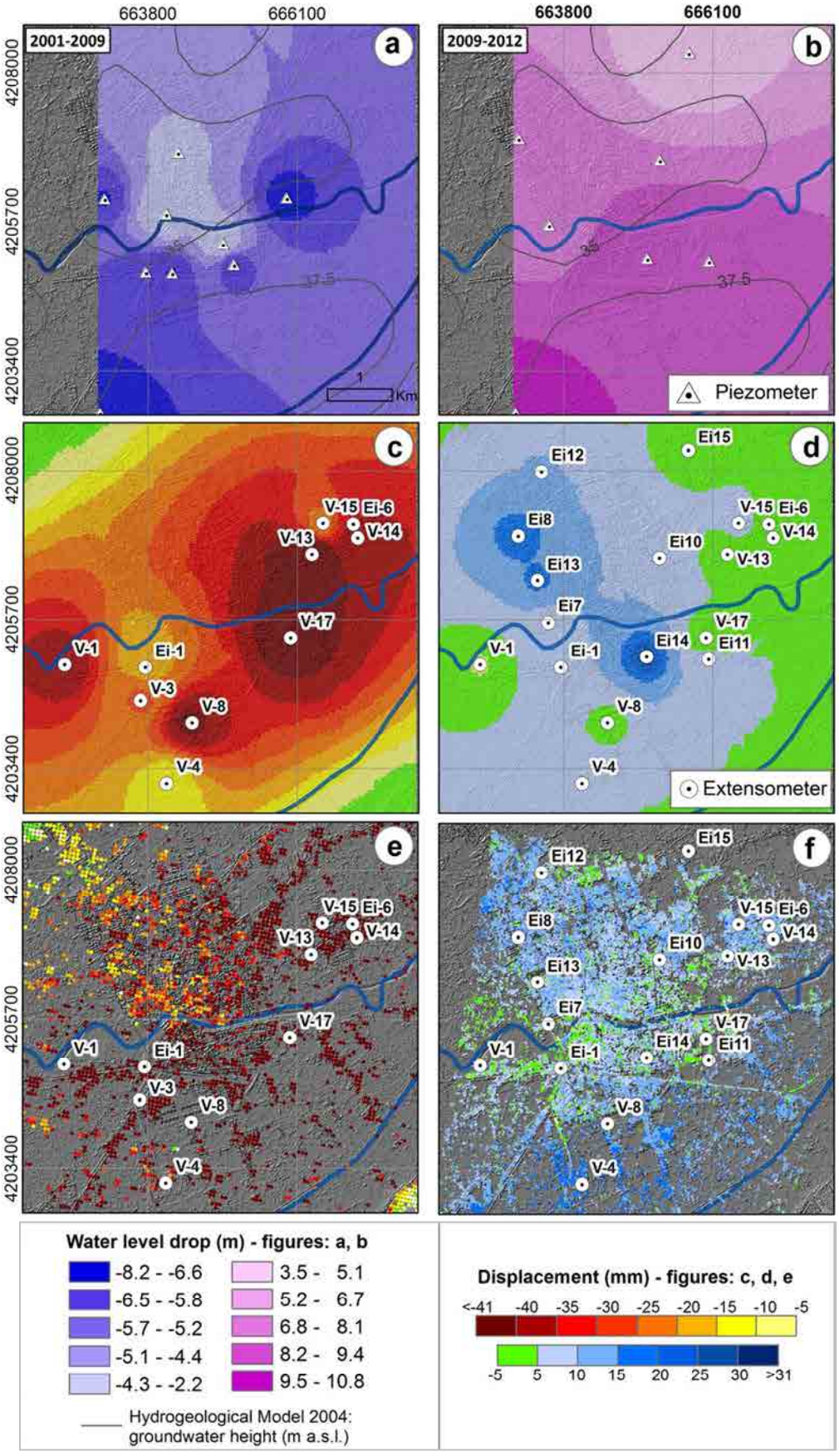

Figure 6.32: Interpolation of the piezometric differences between 2001-09 (a) and 2009-12 (b) related to interpolated extensometric data (c, d) and to the ground level displacements measured by SAR (e, f).

6.3. Subsidence modeling

6.3.1. Model description

Soil consolidation is a process which entails the gradual soil volume decrease. According to Karl von Terzaghi (1923):

"C*onsolidation is any process which involves decrease in water content of a saturated soil without replacement of water by air*."

In general it is the process in which reduction in volume takes place by expulsion of water under long term static loads.

In the present thesis, in which the deformations are due to the dissipation of the excess pore pressure caused by the groundwater table variations in the compressible materials of the surficial aquifer, has been computed.

Herrera et al., (2009) found that the consolidation process resulted the most important phenomenon to be simulated for the study area.

Therefore, the elastic constitutive relation proposed by Biot (1941), (described in Par. 5.1.4.2), has been chosen to model the soil behavior and the possible occurrence of plastic deformations has not been taken into account. This hypothesis could be considered acceptable on the bases of the comparisons between extensometers and piezometers (Fig. 6.9), introduced in the previous section. They have shown that, in most of the modelled columns, the upper material is heavy over-consolidated and, for this reason, its stress-strain behaviour can be considered linear.

As described in the previous, for some of the extensometers (V13, V14, V15, V17, Ei-6, V8) the overpassing of the pre-consolidation pressure has probably provoked the occurrence of certain plastic deformations in the last uplift period; however they cannot be taken into account in the model computation for the few available laboratory tests to define a constitutive relationship. This hypothesis is also supported by the statement that Mohr-Coulomb criteria does not permit to compute plastic deformations for recorded water table variations nor for residual values of cohesion and friction angle (c=0 kPa, Ø=28º).

The Biot's equation, which states a time dependent coupling behaviour between the solid matrix and the interstitial fluids of soils, has been solved using a finite element method. In particular, the finite element code ***GEHOMADRID***, developed by the M_{2i} group (*Mathematical Models in Engineering*) belonging to the Civil Engineering School of Madrid (*Universidad Politécnica de Madrid*) has been used.

In the present thesis, two models have been carried out: one up to the end of the gravel layer (called ***"deep"***) and one up to the extensometers' base (called ***"shallow"***).

In the first part of the study (Par. 6.3.3.1), the deep models for all the extensometric boreholes have been implemented following the approach and the geotechnical characterization proposed in Herrera el al. (2009).

Therefore, in this step, the results achieved in the cited work have been updated (extending the extensometric observation period [2001-2007] until November 2012 and DInSAR and elastic model processing until December 2012).

Furthermore, 10 new modelled columns have been introduced to complete the coverage of the modelled urban area. These columns correspond to the extensometers of phase III which was installed in 2008 to monitor the North-Western part of the city which had no coverage in the network.

The comparisons between the achieved deformation's maps and DInSAR data have showed that the model results are not representative of the North-Western part of the city where, plausibly, the soils have suffered a pre-consolidation (due to the presence of the city walls) and have a higher stiffness.

Therefore, in this part of the city, new models (increasing the clay stiffness) have been proposed (Par. 6.3.3.1.2), supported by the available oedometric tests.

From the obtained deep models, the deformations occurred in the first 10-20 m have been computed. However, the so obtained shallow models have not turned out to be representative of the observed phenomenon.

An in-depth analysis of the stratigraphy, oedometric tests, in situ and laboratory permeability tests has showed the presence of an high-permeability sandy-clay layer up to the gravel top, responsible for the good connection between aquifer and aquitard.

Taking this into account, new models have been proposed and validated through in situ extensometric measurements (Par. 6.3.3.2).

6.3.1.1. Input data:

6.3.1.1.1. stratigraphic columns

The 24 extensometric boreholes shown in Fig. 6.33, have been modelled and discretized using a mesh of eight node quadrilateral element with four gauss point reduced integration that permits to simulate the coupling between the solid skeleton and the interstitial water. In particular, the Q8P4 mesh element has been used; it is a mixed element where the vertical and horizontal unknown displacements are associated to the eight nodes and the unknown pore pressures are associated to the four corners of the element.

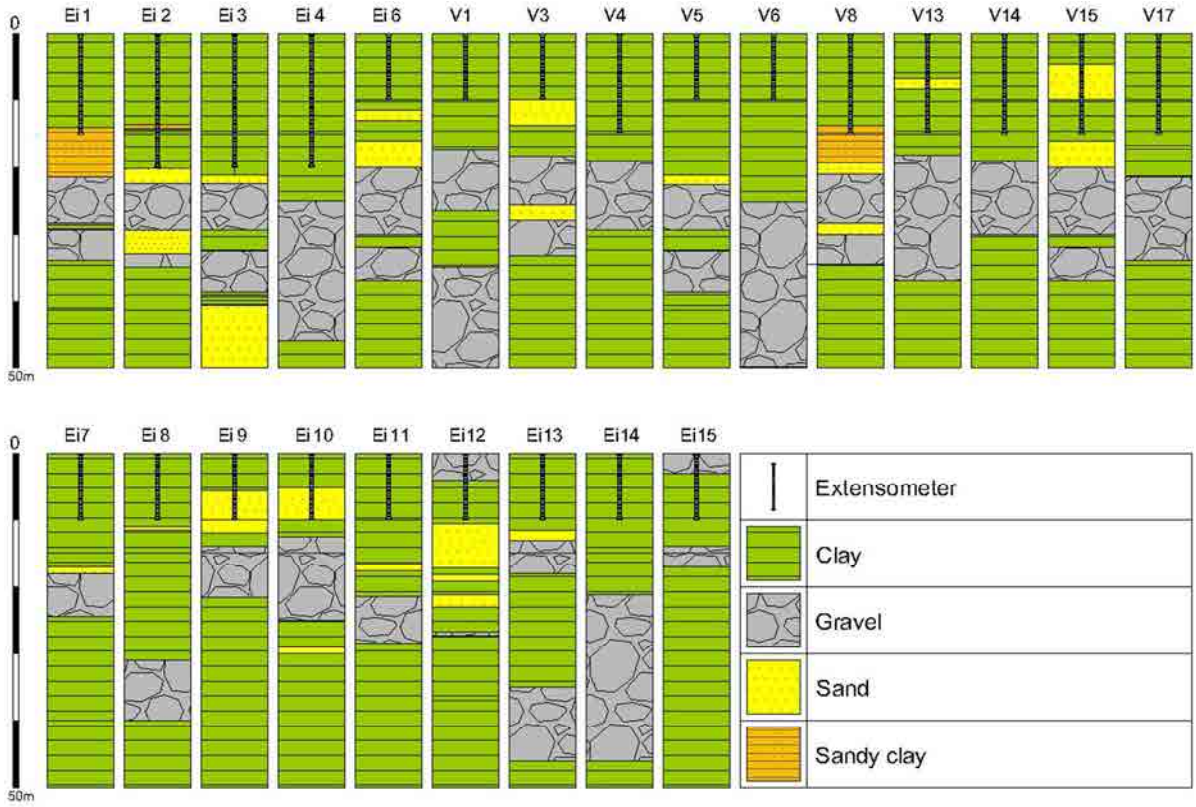

Figure 6.33: Stratigraphy of the modelled boreholes

The subsoil columns modelled in the present work are composed by 13 - 35 m of surficial cohesive soft sediments (clays and silts) of medium-low plasticity, soft consistency and half-high water contents with interlayers of silts and sands. Below of them, materials characterized by a lower compressibility are found. In particular, after a layer constituted by gravels and sands, there are hard clays and marls which have been considered as the incompressible and impervious bedrock for the displacement calculation. Therefore, three main materials have been considered to model the aquitard deformation. In the models the horizontal displacement is assumed equal to zero and the base is fixed to compute only the displacement occurred one up to the base of the surficial gravel layer. An extrapolation of the one dimensional results will be performed to elaborate the 2D subsidence maps in Par. 6.4.

6.3.1.1.2. Piezometers:

For the numerical simulation, the closest piezometer to every extensometer borehole has been chosen.

The piezometric time series started in 1994 and, to obtain the groundwater table height for the period 1975-1994, piezometer P-1 has been used since it is the only available data source for this period. In order to control the translation of the P-1 curve on the time series available after 1994, the flow model for the surficial aquifer for the whole VMSR in the 1994-2001 period (Aragon et al., 2004) has been used (Fig. 6.32).

Then, as described is paragraph 6.2, it is possible to note that the extensometers installed in the phase III to monitor the Northern part of the city (that was not covered until 2008 by in situ measurement) are equipped with a piezometer; this grant the goodness of the pore pressure computation to model the last recuperation phase.

The model relative to the other available extensometers (phases I and II) was affected by the uncertainness of the piezometric data; so the distance to the closest piezometer was reported in the Figure 6.9.

A first static analysis has been computed for each case in order to obtain an initial effective stress state and an initial pore pressure distribution. These correspond to the geostatic and hydrostatic equilibrium states for the given water table height in the date 05/07/1974 (first available record of the water table height).

Then, the slow consolidation process is modeled using a time dependent analysis without considering inertia effects. The time dependent analysis is numerically solved using a Newmark scheme with a time step equal to 8 hours (minimum time step of the piezometric measurement).

Concerning the hydraulic boundary conditions, fluctuations of water table height measured by the piezometers have been imposed prescribing the pore pressure in the base of the surficial gravel layer of the deep aquifer.

Below of it, in fact, is realistic to consider impervious the hard clays and marls.

6.3.1.1.3. Geotechnical and hydrogeological properties:

In the aquitard deformation models, the permeability, the Young's modulus and the degree of saturation have been considered constant.

The geotechnical and hydrogeological characterization performed by Mulas et al. (2010) has been adopted in the present thesis.

As introduced in paragraph 6.1.2.2, the metropolitan area of Murcia is included in the three sectors II, III and "*city center*" (see Fig. 6.3). According to the results obtained by Mulas et al. (2010), the following values, reported in Tab. 6.6, (average between the maximum and minimum of the range of values reported in Tab. 6.1 for the sectors "*city center*", II and III), have been considered:

	City Center	Sector II	Sector III	
E	7500	10000	13000	KN/m^2
K_y	$3.14x10^{-10}$	$6.46x10^{-9}$	$3.87x10^{-9}$	m/s

Table 6.6: Geotechnical parameters of the Murcia sectors (extract from Mulas et al., 2010)

The permeability and stiffness values found for each sector results to be very different and, for a first general computation, the one corresponding to the so-called "*city center*" area has been used. The same parameters have also been tested in previous studies concerning the Murcia subsidence modelling (e.g. Herrera et al. 2009).

The ranges of horizontal and vertical hydraulic conductivity obtained for each of the two aquifer sections, have been estimated from the available in situ tests (laboratory tests and Lefranc's tests) and from numerical flow model of the 1994-2001 period (Aragon et al., 2004).

According to this model, the horizontal conductivity varies between 0.5 and 5.0 m/day for the surficial layers and 100 m/day for the deepest section. These values are in agreement with Lefranc's tests results which estimates the aquitard permeability between 9 and 13 m deep.

However, more surficial layers (up to 9 m) are characterized by a lower permeability which, according to Mulas et al. (2010), are of the order of magnitude of $3.14x10^{-10}$ -$3.87x10^{-9}$ m/s.

Unfortunately, all the available Lefranc's tests are located below the river where sandy intercalations increase the vertical permeability, while no one has been found in the northern part. The only available permeability values in the northern part of the river are $7x10^{-9}$ m/s in the city center and $1.55x10^{-10}$ m/s in correspondence of V-13, obtained from laboratory tests.

The soil response to the boundary condition changes depends on its physical characteristic (compression and tensile strength, elastic modulus, void ratio, specific unit weight, degree of saturation, etc.) and on the historical evolution of the stress states. As it is well known, all this parameters, and mainly vertical conductivity, have a great influence on the results. The permeability, for the proposed coupled-elastic model and mono-dimensional case, not only influences the delay in the soil response to the pore pressure variations, but also the magnitude of the deformation.

For the modelled columns, a detailed borehole stratigraphy description is often not available. For this reason, only the three main materials (**clay, sand, gravel**), for which the geotechnical and hydrological characterization is available, have been considered. However, in several cases, a sandy-clay layer is present above the gravel and it enhances the good-connection between aquitard and aquifer. This has a great influence on the results, as described in par. 6.3.3.

Therefore, a sensibility analysis of the parameters' influence on the model results have been carried out in the paragraph 6.3.2 (i.e. the degree of saturation and Young's modulus E and vertical permeability K_y). This analysis has been useful to verify the simplified hypothesis made to the model implementation and to introduce the main differences between deep and shallow models, as same as, the different response obtained when the higher permeability sandy-clay layer is considered in the deepest aquitard.

Having very few data to understand the occurrence of vertical permeability changes, for the shallow model, two different computations have been achieved: the first, considering the vertical permeability constant for the clay layer (up to the gravel layer top) and one which takes into account the presence on a higher permeability layer up to the top of the gravel layer (on the basis of the available information about the aquitard-aquifer connection, par. 6.2.1.1).

6.3.1.1.3.1. Local geotechnical characterization: oedometers

To complete the available geotechnical information and to the model results analysis, several oedometric data have been considered (Fig. 6.34). These have resulted too few to characterize each column; so, the parameters reported in table 6.6 (based on a great number of in situ data and geological boreholes) have been used for the model implementation and the following data have been considered to its interpretation.

In the metropolitan area of Murcia city, several oedometer tests, (IGME, 2000) are available (Figs. 6.34 and 6.35). From their analysis, the compression index C_c has resulted to be of 0.134 ± 0.04 on average (almost 6 times the expansion index C_s).

Fig. 6.34 shows the study area divided into four zones, to analyse possible spatial changes, comparing some representative oedometer curves, taken more or less at the same reference depth (reported on the graphs).

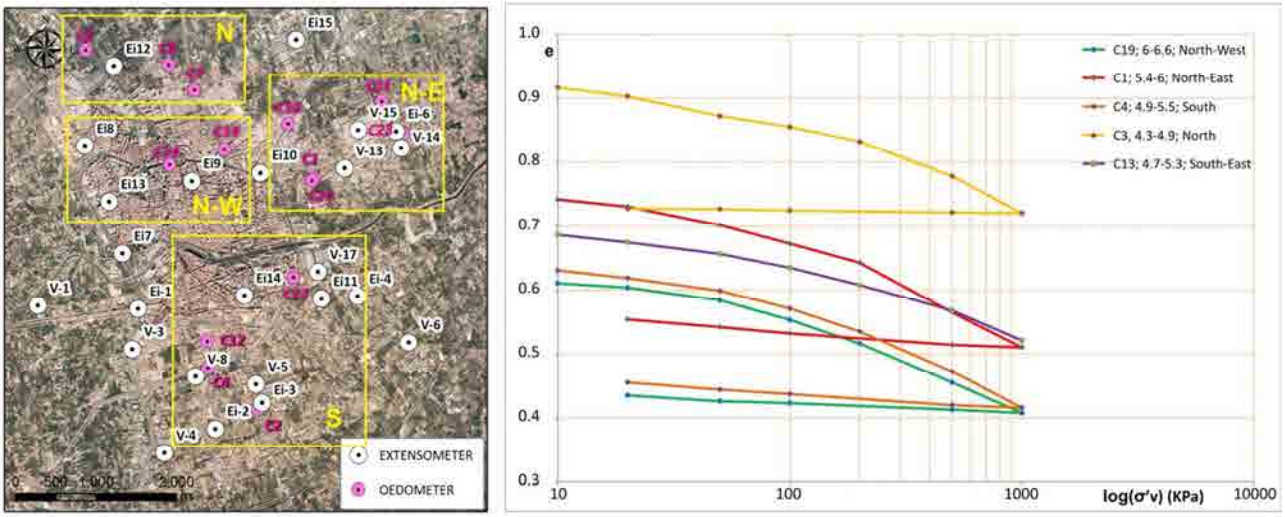

Figure 6.34: Oedometer tests available in Murcia city and areal subdivision

As it possible to note, some oedometers presents a different stiffness and initial void ratio; this is related to the presence of sands in the clay layer; i.e. C14 (between 4-12 m includes clay) and C19 (at the depth of 6 m includes sands). Furthermore, figure 6.35 shows the available oedometric curves (of specimens taken at different depths) divided into the mentioned four areas.

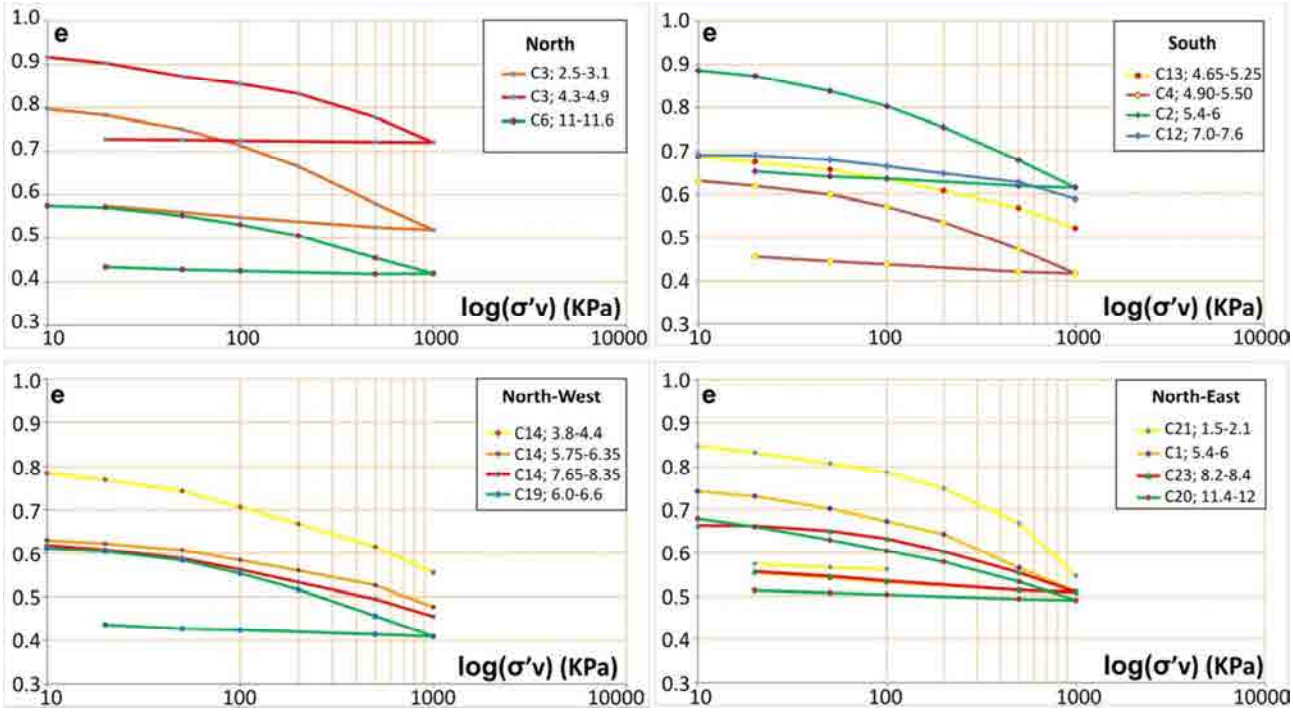

Figure 6.35: Oedometer data at different depths (m)

Considering the subdivision in figure 6.34, the oedometric modulus "E_{ed}", (in the case of dry soils) have been computed.

Through the oedometer curves analysis it is possible to assert that:

- ⟶ Soils of the South-Western part of the river (between 5 and 7 m depth) are characterized by E_{ed} varying between 6900 KN/m^2 and 10500 KN/m^2.
- ⟶ In the Northern part, only few data are available and show an higher stiffness of surficial soils (E_{ed}= 24000 KN/m^2 on average).
- ⟶ In the North-Eastern part, at the same depth corresponds an E_{ed} varying between 6700 and 27000 KN/m^2 due to the presence of sand clay surficial layers.
- ⟶ At North-West, below a filling layer (at 4 m depth) having an E_{ed}=4500 KN/m^2, there is a clay layer with E_{ed}=8000-14000 KN/m^2. The few available oedometer curves show a lowest initial void ratio (0.6) and an homogeneous higher stiffness for all the specimens below a depth of 4 m (values comparable to that found for specimens from other parts of the city at a depth of 11 m. Here, in fact, the fine-grained soils have suffered a pre-consolidation due to the presence of the ancient city walls and, in general, present an higher stiffness also due to the great percentage of interbidded sands layers.

The found values are in agreement with the geotechnical characterization performed by Mulas et al., (2010) where E_{ed} resulted to vary between 7500 and 13000 KN/m^2 for the clay layers and 15000 and 20000 for the sand ones.

In the model hypothesis, E_{ed} has been considered constant with depth. As it possible to note, when more than one specimen at different depths (referred to the same vertical) is available, is possible to analyse E_{ed} vertical changes and this could allow to improve the model results. For example, the oedometer C14, in the North-Western area (Fig. 6.36), presents a compression index C_c and an initial void ratio decreasing with the depth; therefore, the correspondent oedometer modulus (in the case of dry and OC soils) results respectively of 3195 KN/m^2 at 4m depth, 8200 KN/m^2 at 6 m and 11355 KN/m^2 at 8 m (for NC soils the correspondent values are 885, 1516, 2275 KN/m^2, reported in figure 6.36). All these considerations have been performed to the model results interpretation reported in the following paragraphs.

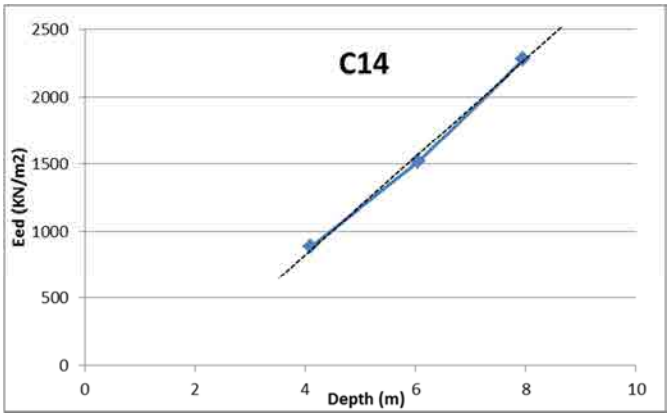

Figure 6.36: Oedometer C14; E_{ed} (dry, NC soils)

6.3.2. Sensibility analysis of the model

In the model computation, the degree of saturation (S_r) has been considered constant.

Thus, the influence of the retention curve defined for the partially saturated zone on the computed subsidence has been analyzed, considering three different degrees of saturation:

(1) $S_{r1} = 1$ *saturation of the material placed above the groundwater table;*

(2) $S_{r2} = 1 - 0.8\,tanh(2s)$ *partial saturation function of the soil suction (s);*

(3) $S_{r3} = 1 - 0.8\,tanh(20s)$ *partial saturation function of the soil suction (s).*

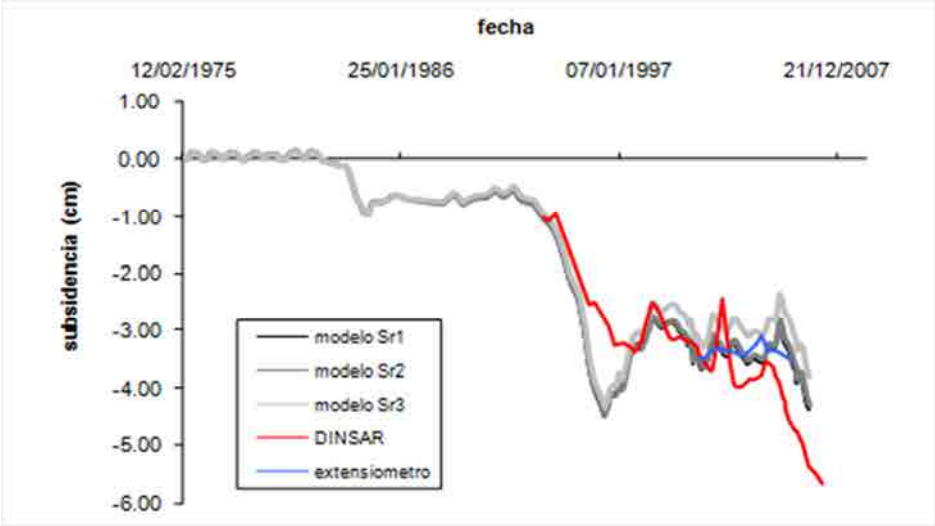

Figure 6.37: Influence of the retention curve in the model results

The time-dependent consolidation analysis has shown that the retention curves (obtained using the relation proposed by Lloret & Alonso, 1985) have a little influence on the computed vertical settlements. The non-linearity associated to the changes in the degree of saturation affects the bulk density (ρ) of the soil placed above the groundwater table, through the equation:

$$\rho = (1 - n)\rho_s + n \cdot S_r \cdot \rho_w \tag{6.1}$$

where *n* represents the porosity, ρ_s the density of the solid matrix and ρ_w the water density.

This variation of the weight of the partially saturated material has a reduced effect on the settlements' computation (Fig. 6.37).

To understand the influence on the models results of the chosen geotechnical and hydrogeological parameters, several different models have been reported in the following.

Considering the Tab. 6.6, for the metropolitan area of Murcia, the Young's modulus and the vertical permeability results to vary respectively between 7500 and 13000 KN/m^2 (15000 KN/m^2 in the peripheral area) and 3.87e^{-9} and 3.14e^{-10} m/s.

The example of the extensometer V8 (which is located between the sectors "*city center*", II, III of the Tables 6.1 and 6.6), has been reported.

Its simplified stratigraphic column is composed of clay between 0-19.3 m, sand: 19.3-21 m, gravel: 21-28.3 m (Fig. 6.33).

In particular, the parametrical analysis has been carried out for the deep model (up to the bottom of the surficial gravel layer) and for the shallow model (up to the extensometer's depth), considering the permeability constant in the clay layer (Fig. 6.38).

After that, the case of a higher permeability sandy-clay layer (which allows to simulate the good connection between aquifer and aquitard, confirmed by the evidences shown in the previous paragraphs), have been reported to show the great influence that it has on the shallow model results.

The shallow model results have been compared with the extensometers' measurements which represent the "*ground truth*" to validate the model. Moreover, the deep model results have been compared with the CPT's and SPN's time series (1995-2010 and 2008-2013).

In figure 6.38 A, B, C and D some examples of achieved models are reported:

- ⟶ A and C are referred to the deep model and have allowed to appreciate graphically the influence, respectively of K_y (A) and E (C);
- ⟶ B and D are referred to the shallow one, namely to the deformations of the first 15 m from the ground, considering homogeneous the permeability of the clay layer.

In order to quantify the influence of the vertical permeability and of the Young's modulus in the model results, the calculated total displacement relative to the third water level drop (ζ) has been used as dependent variable in this analysis.

Therefore, in figures 6.38 E and F, respectively the curves K_y-ζ, E-ζ for the deep model have been achieved.

In figures 6.38 G and H also the shallow model ones have been reported.

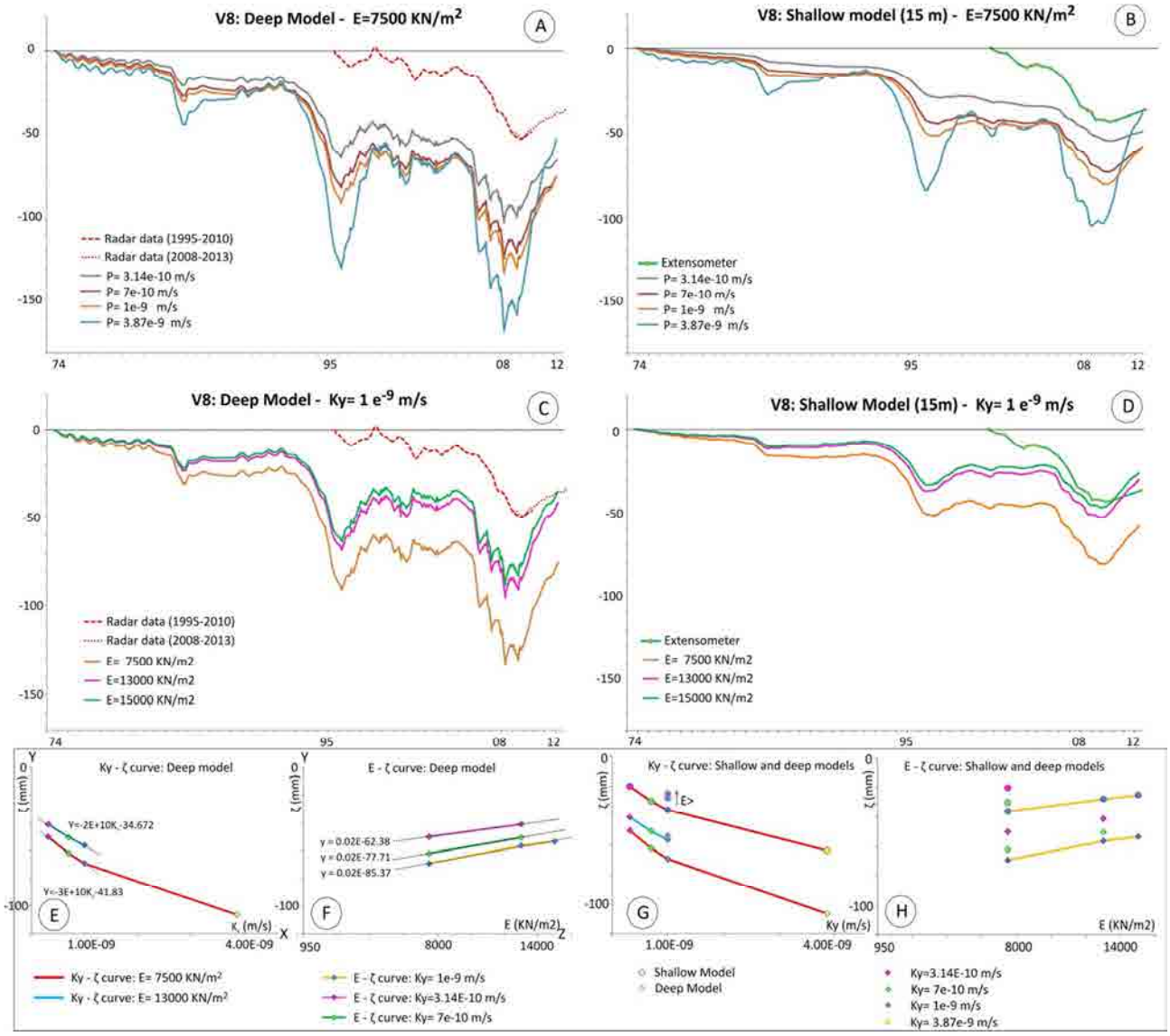

Figure 6.38. Analysis of the influence of E and Ky in the model

As it possible to note in 6.38 F, varying the K_y value between the minimum and the maximum in the range values found for the study area, the obtained E-ζ curves are parallels with a regression coefficient of 0.02 (0.015 for the shallow model). This means that the total displacement ζ variation will vary with ΔE independently from the chosen permeability. In this way it is possible to consider this equation:

$$\zeta = 0.02 \cdot E + b \tag{6.2}$$

where *b* represent the intercept in the plan E-ζ and varies in the range (-62; -85) mm for the deep model (between -31 and -44 for the shallow ones). This intercept is a function of the permeability and corresponds to the condition E=0 (that is to say that represents the influence of the permeability in the ζ computation).

In particular, plotting the intercept values versus the permeability, this results to vary with an almost linear relation; so, it is possible to consider:

$$b = -3 \cdot 10^{10} \cdot K_y - 52.46 \tag{6.3}$$

The following equation to achieve the total displacement has been obtained:

$$\zeta = 0.02 \cdot \mathrm{E} - 3 \cdot 10^{10} \cdot \mathrm{K_y} - 52.46 \tag{6.4}$$

This results have been achieved only to quantify the *sensibility* of the model to the parameters.

In particular, for V8 and in the thresholds' values of K_y and E introduced above ($K_y \in [3.14e^{-10};1e^{-9}$ m/s], two deep models having, as input, two Young's modulus with a difference of 5000 KN/m^2 (6667 for the shallow models) will have, as a result, a total displacement difference ($\Delta\zeta$) of 10 mm.

The same $\Delta\zeta$ difference can be achieved in two models having the same Young's modulus value, but a vertical permeability value difference of $3.33 \cdot 10^{-10}$ m/s.

Considering the uncertainty especially of the permeability values available to the model implementation and the great weight which it has demonstrated to have in the present paragraph, this considerations will be useful in the results analysis.

Another important consideration is related to the modelled columns, that is often corresponding to a not very detailed borehole's stratigraphy description. Therefore, as introduced above, only for three main materials the geotechnical and hydrological characterization is available.

The extensometer V8 has been chosen to the sensibility analysis because of the available information. In particular, the stratigraphic column is composed of clay between 0-13.8 m, **sandy clay: 13.8-19.3 m**, sands: 19.3-21 m, gravel: 21-28.3 m.

The oedometer modulus, E_{ed} (4.9-5.5 m), obtained by the oedometric curve analysis, is 6972 KN/m^2 (Par. 6.3.1.1.3.1).

Extensometer V8 is 450 m far from the multilevel piezometer P-45 from which the connection between aquifer and aquitard results to be good. The Lefranc's test results, carried out between 13.5-15 m, have found a vertical permeability equal to $K_y=2.03 \times 10^{-7}$ m/s; the vertical permeability achieved from laboratory tests results equal to $K_y=5.23\ 10^{-8}$ m/s.

For this reason, two models have been performed. In both the models, the Young's modulus of 7500 KN/m^2 introduced in table 6.6 has been used (Fig. 6.39).

The two models differ for the presence of the sandy-clay layer which, in most boreholes available in the study area, is not reported.

In particular, the grey line represents the model achieved considering an uniform clay layer between 0 and 19.3 m deep; the pink curve represents the real stratigraphic column where the sandy clay layer is between 13.8 and 19.3 m deep. To the pink model implementation, the sandy-clay layer's permeability has been estimated through the available Lefranc's and laboratory tests and, for both the available permeability values (to K_y=2.03x10^{-7} m/s; K_y=5.23 10^{-8} m/s), the overpressure dissipation has turned out to be, from the model computation, almost instantaneous; so, the lowest one has been used.

As evident in figure 6.39, the uncertainness related to the stratigraphic columns can cause very different results because of the underestimation of the permeability, especially of the soils above the gravel layer.

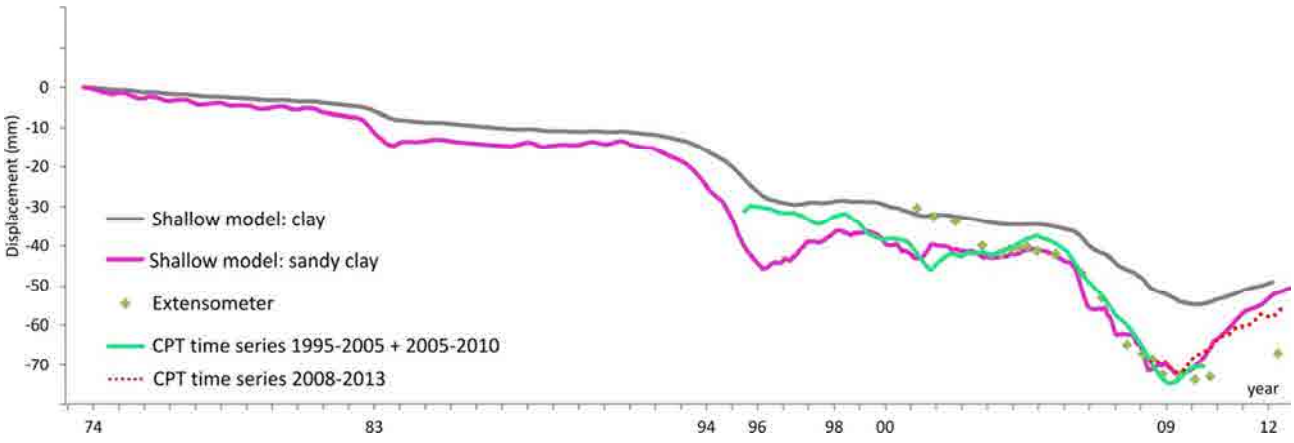

Figure 6.39: Comparison between subsidence models achieved for V8 considering the sandy clay layer (pink curve) and not considering it (grey curve); green rhombus represents the extensometric measures; in the figure, also displacement's time series detected by SAR have been reported. In particular, the time series obtained from three separated CPT processing (1995-05; 2005-10; 2008-2013) have been considered to show the best displacement estimation (see also paragraph 6.2.2.1.1).

The model absolute error for the extensometers V8 with respect to the pink model (obtained considering all the sufficient amount of available data) results of **3.5±3.8 mm** for the common monitoring period between 2001 and 2012.

To explain how the pore water overpressure dissipation changes when a sandy clay layer is present in the stratigraphic column, also the example of Ei-1 is reported.

The extensometer Ei-1 measures the deformations of the firsts 15 m deep. Ei-1 stratigraphy includes: 0-14 m of clay or sandy clay; **14-21.5 m of sandy clay**, 21.5-25 m of gravel, 25-29 m of sandy-clay and 29-34 m of gravel (Fig. 6.33). It is the same scheme of V8 extensometer.

No oedometer's tests are available to the characterization of the sandy-clay layer. However, Ei-1 case has been useful to analyse the pore water over-pressure dissipation mechanism in the case of presence of the sandy-clay layer between the extensometer base and the gravel layer. In fact, it has shown that, from an hydrogeological point of view, the sandy-clay layer is equitable to the sand; in many cases, it can reach the base of the instrument and, probably, the aquitard characterized by a lowest permeability is immediately up to the extensometer base.

The used Geho-Madrid code allows to compute the pore water pressure's time series in all the nodes of the used mesh of quadrilateral elements. In this case, the hydraulic boundary condition has been imposed up to the gravel layer bottom (to which the piezometer's measurements are referred) and the pore water pressure P_w has been computed up to the extensometer base (15 m). As it possible to note in figure 6.40, the pore water pressure computed through the model at **15 m**, considering the K_y=5.23x10^{-8} m/s, results to be equal to that calculated as a succession of hydrostatic pressures (as $P_w = g \cdot h_w$, with h_w computed respect to the depth of the extensometer's base). The available Lefranc's permeability for Ei-1 results of 1,14x10^{-6} m/s, but the same permeability value used for V8, obtained from laboratory test has been considered.

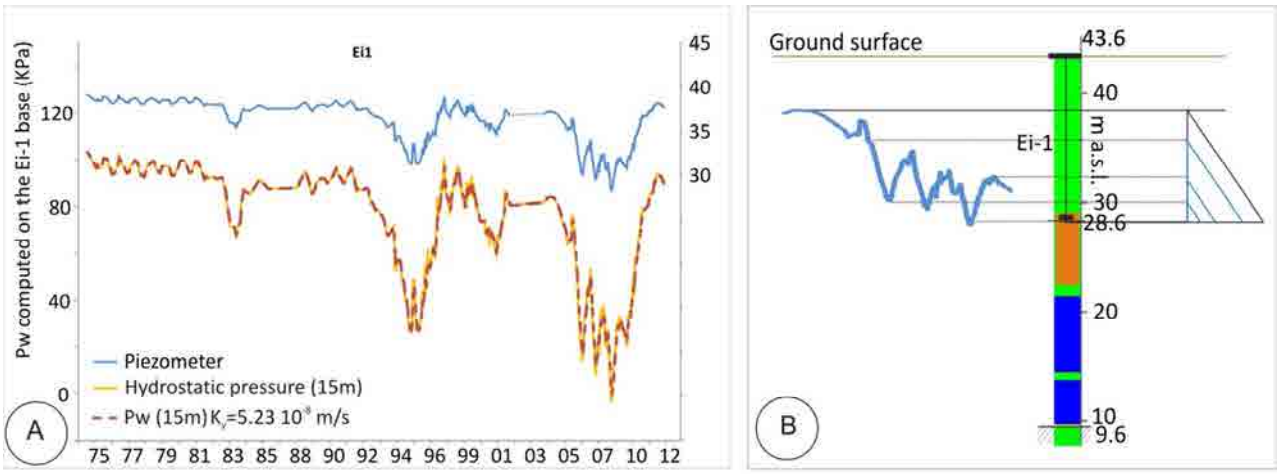

Figure 6.40: (A) Comparison between pore water pressure's time series on the extensometer's Ei-1 base: (1) computed through the model, using, as boundary condition, the piezometric variation imposed up to the bottom of the gravel layer (red curve); (2) computed as $g \cdot h_w$ (orange curve). (B) Schematic representation of the hydrologic observed mechanism (the hydrostatic pressures are referred to the extensometer's base).

The Ei-1 and V-8 examples (where the presence of the sandy-clay layer is reported in the stratigraphic column), represent the extreme cases where the aquifer reach the extensometer base. They are useful to understand the influence in the model results of a higher permeability layer (up to the gravel layer) also on displacements computed above it, namely affecting the low permeability clay layers of the firsts 15 m as in Fig. 6.39.

6.3.3. Model results and error computation

In this section, the results of the numerical model for the 24 extensometric columns (Fig. 6.4) are presented. The model has been carried out to obtain the aquitard deformation induced by groundwater's variations, only considering the compressible materials placed above the surficial gravel layer. For this reason, all the models are referred to a different depth and each stratigraphic column has been reported for a correct results interpretation.

For the model implementation, some preliminary considerations, have been done and are summarized in the following:

1. For all the achieved general models, the same Young's modulus has been used (E=7500 KN/m^2) which has been considered constant with the depth. This is an adequate value to the shallow model implementation because it is in agreement with that achieved from oedometric curves at a depth of 5-6 m. Nevertheless, in the deep model results, it causes an overestimation of the deepest deformations.

2. In the North-Western part of the study area (which include the "*city centre"*), the ground subsidence, measured both by radar and extensometers, has a lower magnitude respect to the southern part of the river; this is due to the depth of the gravel layer which has the top between 11 and 16 m to the ground surface (the thickness of the aquitard compressible materials is about 1/2 than that in the southern part of the river). Soil response to the water level changes results to be rapid and this is in according to the observed comparisons between the multilevel piezometer's data (i.e. P-2425, Fig. 6.6).

3. Furthermore, here, the fine-grained soils have suffered a pre-consolidation due to the presence of the ancient city walls and, in general, present a higher stiffness. This is also due to the great percentage of interbidded sand layers. Then, the few available oedometer curves show a lower initial void ratio (0.6) and an homogeneous higher stiffness for all the specimens below a depth of 4 m (values comparable to that found for specimens from other parts of the city at a depth of 11 m).

4. The most uncertainty for the model implementation is in the South-Eastern part of the city where the extensometers (V1, V6, V17 and Ei-4) are very far from the piezometer (more than 700 m) and V6 is 800 m far from the closest stratigraphic borehole.

5. For several extensometers, the elastic model will overestimate the ground level recuperation in the period 2008-12 because the plastic deformations have not been taken into account.

6. In the North-Eastern part of the city, the only available K_y value is of $1.55x10^{-10}$ m/s (near V-13), but a great variability of the vertical permeability is observed due to the presence of several sandy-clay layers. These is evident also in the comparisons between the three close extensometers V15, V14 and Ei6, which differ only for the sand thickness. Because of the few available data (detailed stratigraphy, permeability's values), for the deep models presented in Par. 6.3.3.1 only three materials (clay, sand and gravel) have been taken into consideration. For the shallow models computation this simplification brings to an underestimation of the surficial deformations. For this reason, in Par. 6.3.3.2 a model modification has been proposed, taking into account four materials (clay, sand, gravel and sandy clay).

7. Similarly, in the southern part of the river, the hydrological analysis carried out in the previous paragraphs, has shown a very good connection between aquifer and aquitard. Because of the few available permeability's values and the low detail of the stratigraphic descriptions (which, in most cases, do not distinguish clay and sandy-clay layers), the results achieved for V8 and Ei1 (Par. 6.3.2) have been useful to the implementation of the models of other columns located in the southern part of the city (Par. 6.3.3.2).

These considerations, as same as the few available oedometers' tests shown in paragraph 6.3.1.1.3.1, will be useful to the later results interpretation.

The validation of the deep models have been carried out through the comparisons with CPT's and SPN's radar data; nevertheless, the shallow models results have been compared with in situ measured displacements.

6.3.3.1. Deep models

The results of the numerical deep model for the 24 columns are presented (Figs. 6.41, 6.42, 6.43, 6.44).

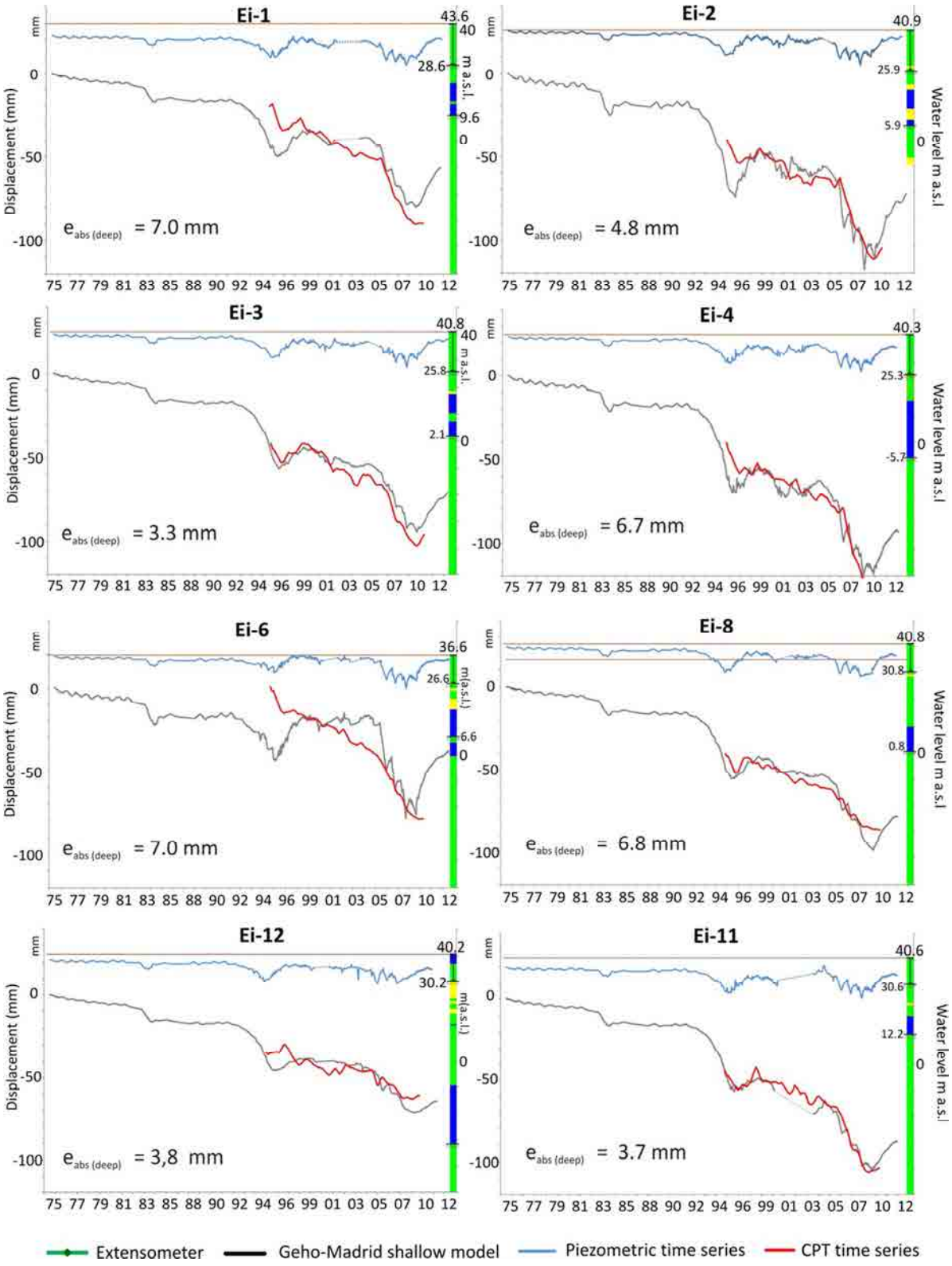

Figure 6.41: Piezometric levels, deep models and CPT's time series (1995-2010). The simplified stratigraphic column of the differential extensometers have been reported in the figure.

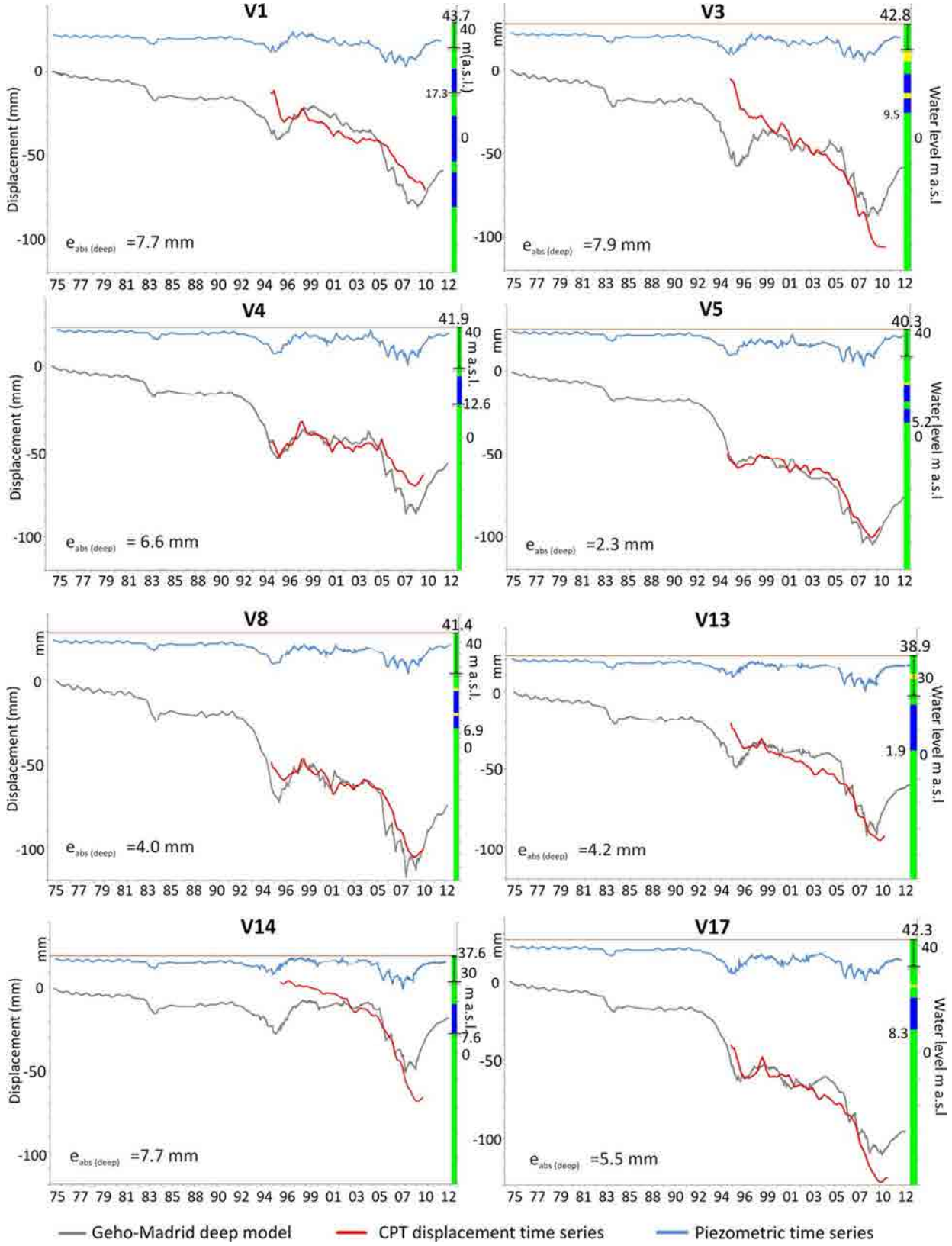

Figure 6.42 Piezometric levels, deep models and CPT time series (1995-2010). The simplified stratigraphic column of the rod extensometers have been reported in the figure.

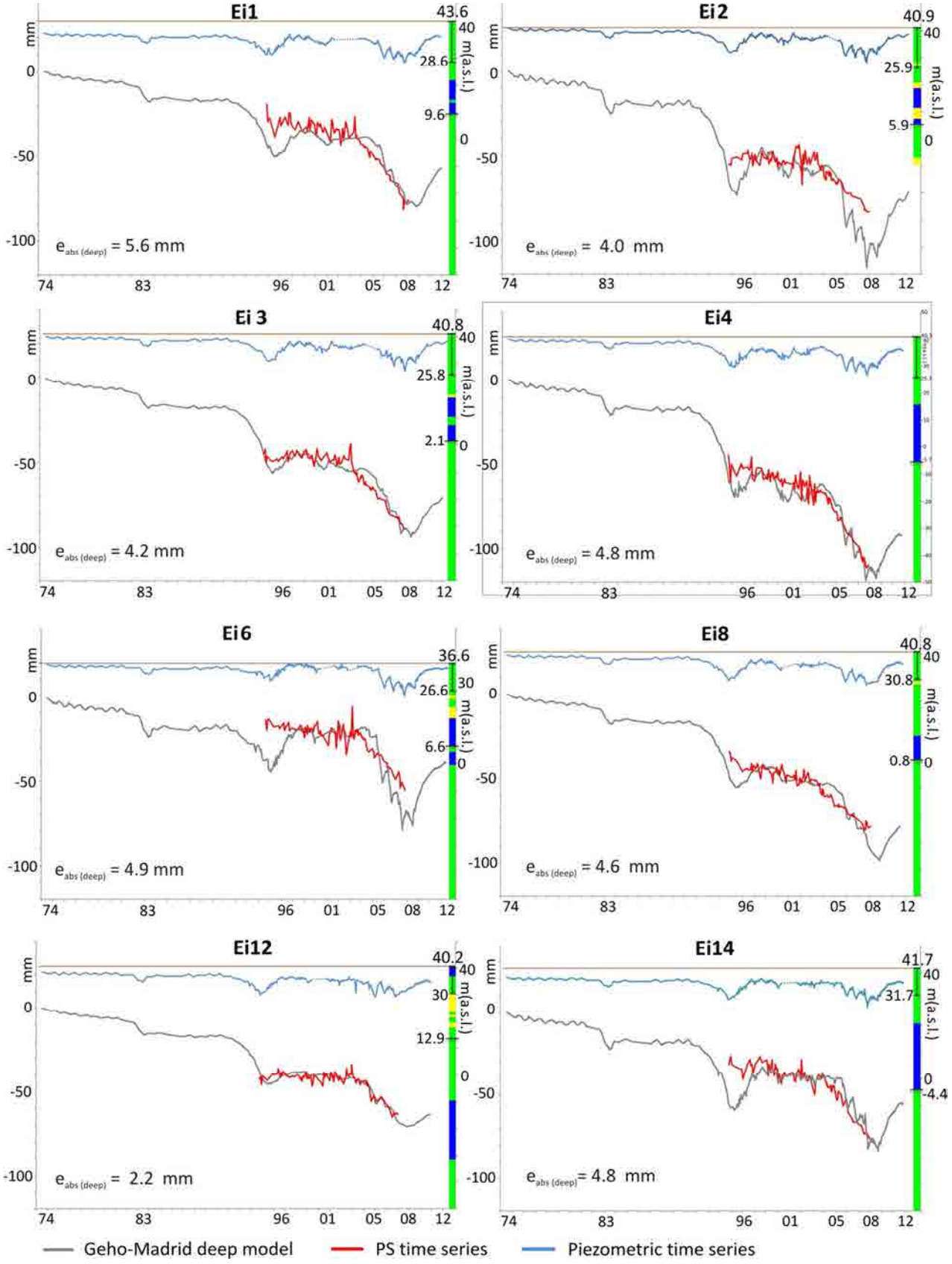

Figure 6.43 Piezometric levels, deep models and SPN time series (1995-2008). The simplified stratigraphic column of the differential extensometers have been reported in the figure.

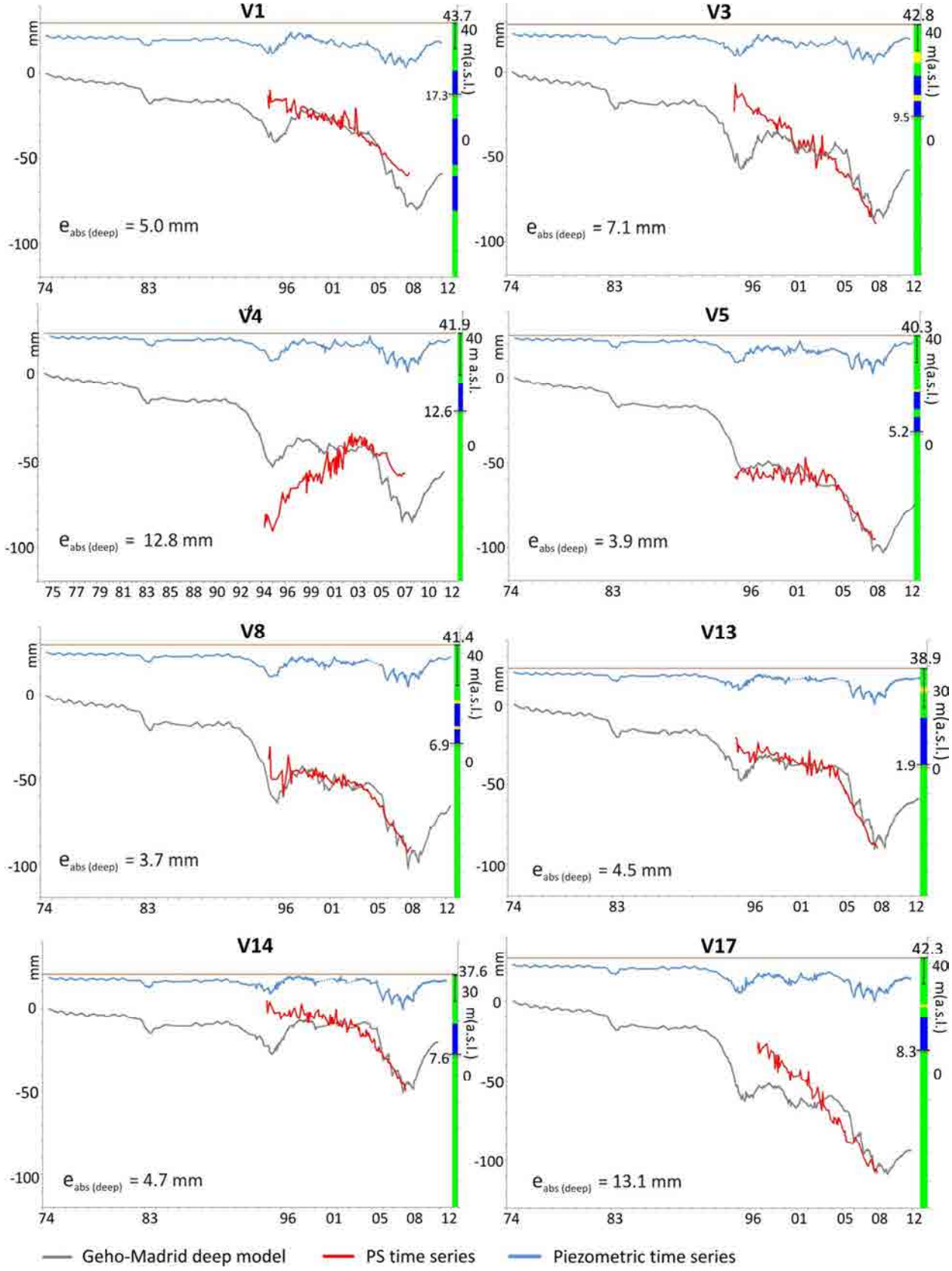

Figure 6.44 Piezometric levels, deep models and SPN time series (1995-2008). The simplified stratigraphic column of the rod extensometers have been reported in the figure.

The deep model carried out up to the gravel layer bottom has been compared with DInSAR displacement time series. In particular, Figs. 6.41 and 6.42 show the comparisons with CPT's data and Figs. 6.43 and 6.44 that with SPN's data.

To the deep model error's computation, both CPT's and SPN's time series have been considered. These two techniques, in fact, can achieve complementary results to the subsidence phenomenon analysis, as demonstrated in several works, like Tomás et al. (2013).

Following the approach proposed by Herrera et al. (2009), the PS closest to the extensometer has been selected avoiding PS located within building areas. Due to the few SAR images available for the period 1995-1996 (6 between July 1995 and November 1996), the SPN and the CPT algorithms could not monitor the highly non-linear subsidence behavior of the 1994-96 drought and 1996-98 recuperation. Therefore the first part of the time series has not been considered for the comparison with the model results.

However, in this case, the error calculation reported in table 6.7 is strongly influenced by the effects introduced by the significant dispersion shown in the PS's time series (σ=±9 mm on average, see Figs. 6.28, 6.43 and 6.45), if a fixed starting date (for both time series) is chosen. This would not even make possible the comparison of the error tables achieved using SPN's displacement time series with that relative to the CPT's results.

For this reason, the error computation has been performed using a vertical translation (Δ) of the radar curves (respectively CPT's and SPN's displacement measurements) over the other (the deep model curve).

Δ represents the vertical translation to apply to the time series, respect to the zero (which in both CPT and SPN curves corresponds to July 1995) to minimize the absolute error, namely to obtain the best fitting of the two time series (Fig. 6.45).

To better describe the problem, the case of Ei-2 has been showed in figure 6.45.

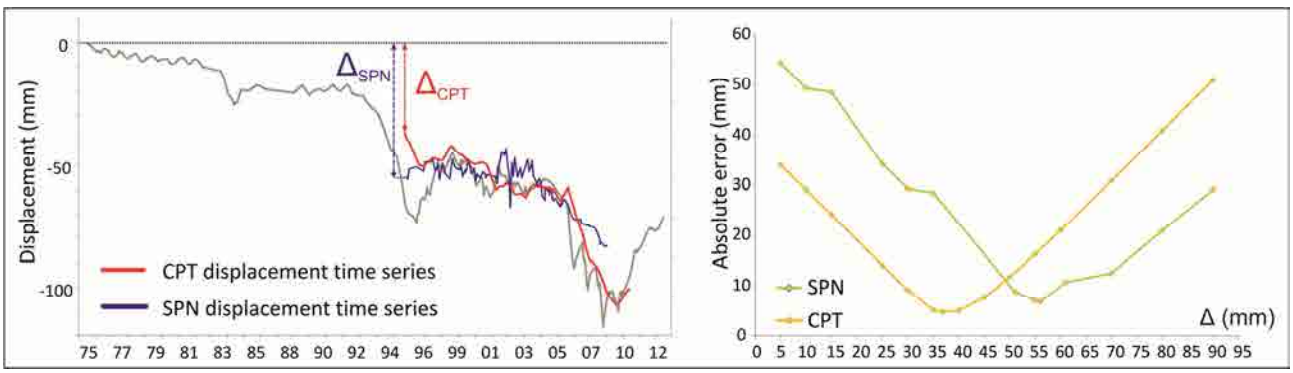

Figure 6.45: Minimum absolute error computation

According to figure 6.45, to obtain the best fitting between the CPT's displacement time series and the deep model curve, a translation of Δ_{CPT} = 37 mm has to be applied to the CPT curve; in this way, the absolute error results of 4.8±6 mm (Table 6.7) has been obtained; following the same criteria, the one achieved through SPN's time series results of 7.0±6.8 mm (Δ_{SPN} = 57 mm).

Observing figure 6.45 is possible to note the strong influence that the DInSAR curve position can have on the error calculation; this criteria has been performed in order to optimize the error computation, uniform the calculation for all the comparisons and reduce this influence.

The comparisons shown in Figs. 6.41, 6.42, 6.43 and 6.44 have been performed applying the Δ_{CPT} and Δ_{SPN} values obtained using this criteria.

In particular, the average absolute difference between deep model results and CPT's measured displacement time series has resulted of **5.9 ±6.2** mm (for the period 05/1997-05/2010) and that with the SPN ones of **5.9 ±4.4** mm (for the period 05/1997-12/2008).

(05/1997-05/2010)	CPT - deep model										
	Differential						Rod				
	Ext_depth	e_{abs}	σabs	Model_depth	δ		Ext_depth	e_{abs}	σabs	Model_depth	δ
	(m)	(mm)	(mm)	(m)	(m)		(m)	(mm)	(mm)	(m)	(m)
Ei-1	15	7.00	10.12	34	21.5	**V-1**	10	7.65	6.14	26	17.3
Ei-2	20	4.75	6.45	35	19.4	**V-3**	10	7.94	9.37	33	14.5
Ei-3	20	3.30	3.43	39	21.1	**V-4**	15	6.55	5.27	29	19
Ei-4	20	6.55	6.51	46	25	**V-5**	10	2.34	2.71	39	21.1
Ei-6	10	7.04	8.36	30	14.5	**V-6**	10	5.98	4.13	50	25.1
Ei7	10	9.21	7.18	25	14	**V-8**	15	4.02	4.20	35	19.3
Ei8	10	6.83	6.50	40	30.4	**V-13**	15	4.24	4.93	37	16.4
Ei9	10	7.86	6.43	22	7.5	**V-14**	10	7.69	9.59	30	19
Ei10	10	6.14	5.67	25	7.65	**V-15**	10	7.98	7.11	30	10.6
Ei11	10	3.73	7.35	28	20.5	**V-17**	10	5.54	4.72	34	21
Ei12	10	3.83	3.34	27	13.4						
Ei13	10	7.28	6.71	18	11.5						
Ei14	10	4.76	8.08	46	21.2						
Ei15	10	3.39	5.07	33	10.9						

(05/1997-12/2008)	SPN - deep model										
	Differential						Rod				
	Ext_depth	e_{abs}	σabs	Model_depth	δ		Ext_depth	e_{abs}	σabs	Model_depth	δ
	(m)	(mm)	(mm)	(m)	(m)		(m)	(mm)	(mm)	(m)	(m)
Ei-1	15	5.55	3.95	34	21.5	**V-1**	10	5.02	4.81	26	17.3
Ei-2	20	7.01	6.84	35	19.4	**V-3**	10	7.13	5.46	33	14.5
Ei-3	20	4.17	3.06	39	21.1	**V-4**	15	12.78	9.36	29	19
Ei-4	20	4.77	3.05	46	25	**V-5**	10	3.94	2.50	39	21.1
Ei-6	10	6.23	5.60	30	14.5	**V-6**	10	8.59	6.76	50	25.1
Ei7	10	5.22	4.09	25	14	**V-8**	15	3.66	2.68	35	19.3
Ei8	10	4.55	3.19	40	30.4	**V-13**	15	4.48	3.66	37	16.4
Ei9	10	5.55	5.94	22	7.5	**V-14**	10	4.74	3.34	30	19
Ei10	10	4.66	3.28	25	7.65	**V-15**	10	10.77	6.57	30	10.6
Ei11	10	4.43	3.47	28	20.5	**V-17**	10	13.01	6.86	34	21
Ei12	10	2.15	1.79	27	13.4						
Ei13	10	5.24	3.65	18	11.5						
Ei14	10	4.80	3.90	46	21.2						
Ei15	10	3.38	2.61	33	10.9						

Table 6.7: Error table of the comparison between DinSAR data and deep model's time series

The deep models corresponding to the minimum error calculated both with CPT's and SPN's time series are that referred to Ei-12 and V-5.

Taking this considerations into account, it is observed that the average cumulated displacement for all the *"deep"* modeled columns between 1974 and the end of 2012 is 72 mm (Tab. 6.8). During the three drought periods, subsidence rates vary between 8±3 and 11±3 mm/yr on average.

During the ground water level recuperation phase, the velocity vary in a range between 2 and 13 mm/yr (9.5±2.6 mm/yr on average) while in those periods which are not affected by droughts the subsidence rates are -0.7±0.8 mm/yr on average.

During the period comprised between 1975 and 1994, only one piezometer was available and therefore the model results can only be attributed to the different stratigraphy of every borehole and to the thickness of the soils interested by the change in the pore water pressure. Taking this into account, in 1984 the 3 m average water level drop produced an average modeled subsidence of 19±3 mm. Note that 50% of this displacement was produced in the 1983-1984 drought (Table 6.9). In 1996 the average water level drop of 8.3 m, resulted in 23±9 mm of cumulated displacement (53±12 mm since the 1974) on average.

In the 1994-96 period a greater amount of piezometers were used for the interpretation of the ground water level evolution. In the third drought period the water level variation between 4 and 10 m resulted in a computed settlement of 39±9 mm. Note that the highest values are found in the southern part of the city, coinciding with the extensometer records.

Differential Extensometers				Rod Extensometers			
	1982-84	1994-96	2006-09		1982-84	1994-96	2006-09
Ei-1	8.80	19.14	35.3	**V-1**	8.59	13.25	33.9
Ei-2	13.94	46.94	60.5	**V-3**	11.23	20.95	38.3
Ei-3	8.55	34.36	38.4	**V-4**	8.91	22.97	38.3
Ei-4	11.34	31.14	42.7	**V-5**	8.61	23.63	33.1
Ei-6	12.54	15.07	50.5	**V-6**	11.98	32.40	43.5
Ei7	8.88	16.84	35.8	**V-8**	11.20	40.03	50.2
Ei8	8.72	21.63	38.1	**V-13**	10.63	15.48	42.7
Ei9	9.60	25.98	37.7	**V-14**	8.56	9.95	35.1
Ei10	9.49	19.71	34.5	**V-15**	12.43	14.96	50.5
Ei11	8.38	26.42	36.3	**V-17**	9.33	28.32	37.8
Ei12	7.56	17.45	22.6				
Ei13	9.16	18.33	34.8				
Ei14	12.20	22.67	43.0				
Ei15	10.68	17.39	19.7				

Synthesis			
	1982-84	1994-96	2006-09
μ =	-10.05	-23.13	-38.88
σ =	1.69	8.84	8.61
max =	-13.94	-46.94	-60.46
min =	-7.56	-9.95	-19.74

Table 6.8: Deep model computed differential displacements in the three drought periods.

6.3.3.1.1. Spatial analysis of the deep model results

The deep model results have been interpolated through the IDW method (Fig. 6.46). This method has been chosen because of the few number of modelled column (24 points in 36 Km^2) which has not allowed the use of more sophisticated geostatistical algorithms. In particular, a 2D map of the cumulated displacements between April 2001 and December 2008 has been obtained.

In April 2001 the extensometric network was installed (phase I and II) and a very stable behavior was registered by the piezometers and the radar time series between 1997 and 2001 (see Par. 6.2.1.1). Moreover, in this period, the induced deformations can be considered predominantly elastic. Consequently, the period 2001-2009 has been chosen for a 2D analysis of the results because it also allows some spatial comparisons with the extensometers measurements. Therefore, in figure 6.46, also the interpolated maps of extensometric and radar data have been reported. In particular, in Fig. 6.46 a, all the CPT points have been considered in the interpolations, while, in Fig. 6.46 b, only that used in the mono-dimensional comparisons have been interpolated. For the interpolations of Figs. 6.46 b, c and d, it has been considered that no deformation is produced in the ranges that limit the VMSR.

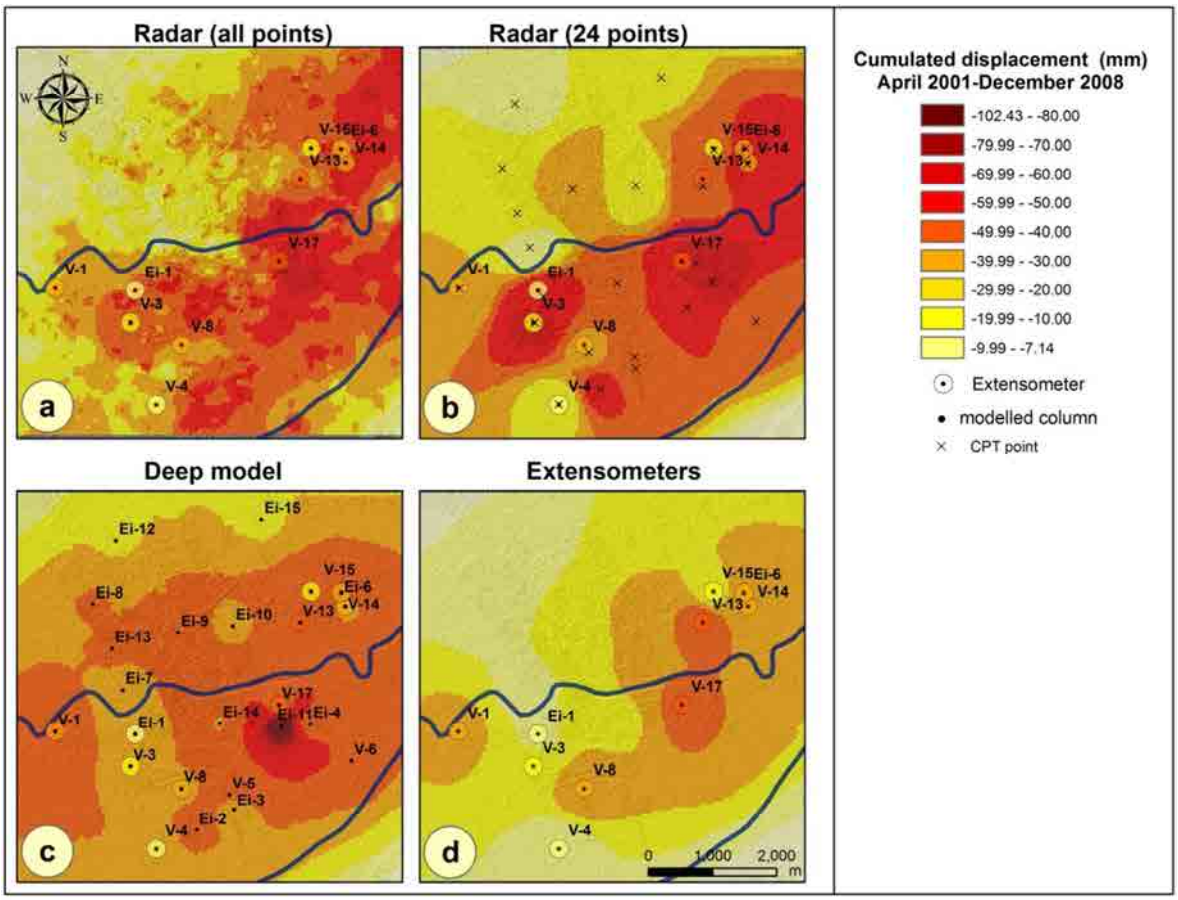

Figure 6.46: Maps of deformation, period 2001-09: IDW interpolations of CPT's cumulated displacements (a, b), model results (c) and extensometric data (d).

The spatial comparison between radar's and extensometers' measurements (figs. 6.46 a, d) shows that, in general, the radar registers a higher deformation (or at least of the same magnitude) than the extensometers, except for V-1. Here, the extensometer registers an initial settlement of 1 cm between the first two acquisition dates that generates this incongruence; in fact, as shown in Fig. 6.28, CPT's and SPN's time series seems to register the same deformation trend than the extensometer except for the first measured fall.

The spatial error has been computed as absolute difference between the cumulated displacement measured by SAR between 2001 and 2009 and the interpolated value extracted from the 2D model map. This error is computed using all the available SPN's and CPT's data and has turned out to be of **12.7±8** mm for the PS's data and of **12.3±8** mm for the CPT's data for the whole study area (fig. 6.46).

The spatial error is mostly due to:

- ⟶ the few number of modelled columns which did not allow to well estimate the local anisotropies,
- ⟶ the used interpolation technique,
- ⟶ the impossibility of the PS discrimination.

In fact, the PS could be placed on a building or on a street and the measured radar displacements could consist in the structural response to the ground deformation. In the mono-dimensional comparisons, PS located on the ground have been used, but, in a spatial interpolation, all the available data have been considered; therefore a probable under-estimation of the ground deformation has been obtained, especially in the urbanized area.

The spatial analysis, has also allowed understanding where the geotechnical model turns out to be not representative.

In this case, as also noted by the punctual comparisons shown in the previous paragraphs, the geotechnical parameters used in the model computation have resulted not representative in the North-Western part of the city. These comparisons have showed that the bi-linear deformation behaviour showed in most radar time series (Figs. 6.18), was not marked in that referred to the N-W part of the city (Figs. 6.29, 6.41).

Excluding the North-Western area from the error computation, the mean spatial error has resulted of 8.8±7 mm.

For this reason, a correction of the deep models for the North-Western part of the city have been carried out and reported in the following paragraph 6.3.3.1.2.

6.3.3.1.2. Deep model correction for the North-Western part of Murcia City

In the North-Western part of the city, the geotechnical and hydrogeological characterization used to the model implementation has not resulted representative of the phenomenon.

In particular, in this area, the SPN's and CPT's time series do not show a marked bi-linear behaviour (like that observed in the other part of the city) and the extensometers show a rapid response to the water level changes.

As described in paragraph 6.3.1.1.3.1, in this part of the city, the fine-grained soils have suffered a pre-consolidation due to the presence of the ancient city walls and, in general, present a higher stiffness also due to the great percentage of interbidded sand layers.

The few available oedometer curves show a lower initial void ratio (0.6) and a homogeneous higher stiffness for all the specimens below a depth of 4 m (values comparable to that found for specimens from other parts of the city at a depth of 11 m). In general E_{ed} varies between 8000 and 23000 KN/m^2; (reliably, the highest values are related to the presence of interbidded sand).

Considering the hypothesis of E constant with the depth, only the value of E_{ed}= 23000 KN/m^2 can be adopted to obtain a deformation magnitude comparable with that measured by SAR.

The results achieved for all the columns in the N-W part of the city have been showed in Fig. 6.47.

The comparisons in Fig. 6.47 correspond to a decrease of the average absolute error value of about 50% as shown in Table 6.9.

Models	Ei7		Ei8		Ei9		Ei13	
	e_{abs}	σ	e_{abs}	σ	e_{abs}	σ	e_{abs}	σ
E_{ed}=7500 KN/m^2	9.21	7.18	6.83	6.50	7.86	6.43	7.28	6.71
E_{ed}=23000 KN/m^2	5.32	3.00	3.10	4.20	5.86	8.31	3.31	5.15

Table 6.9: Comparisons between the absolute errors of the deep models (N-W part of Murcia city) achieved with the different stiffness values of 7500 and 23000 KN/m^2.

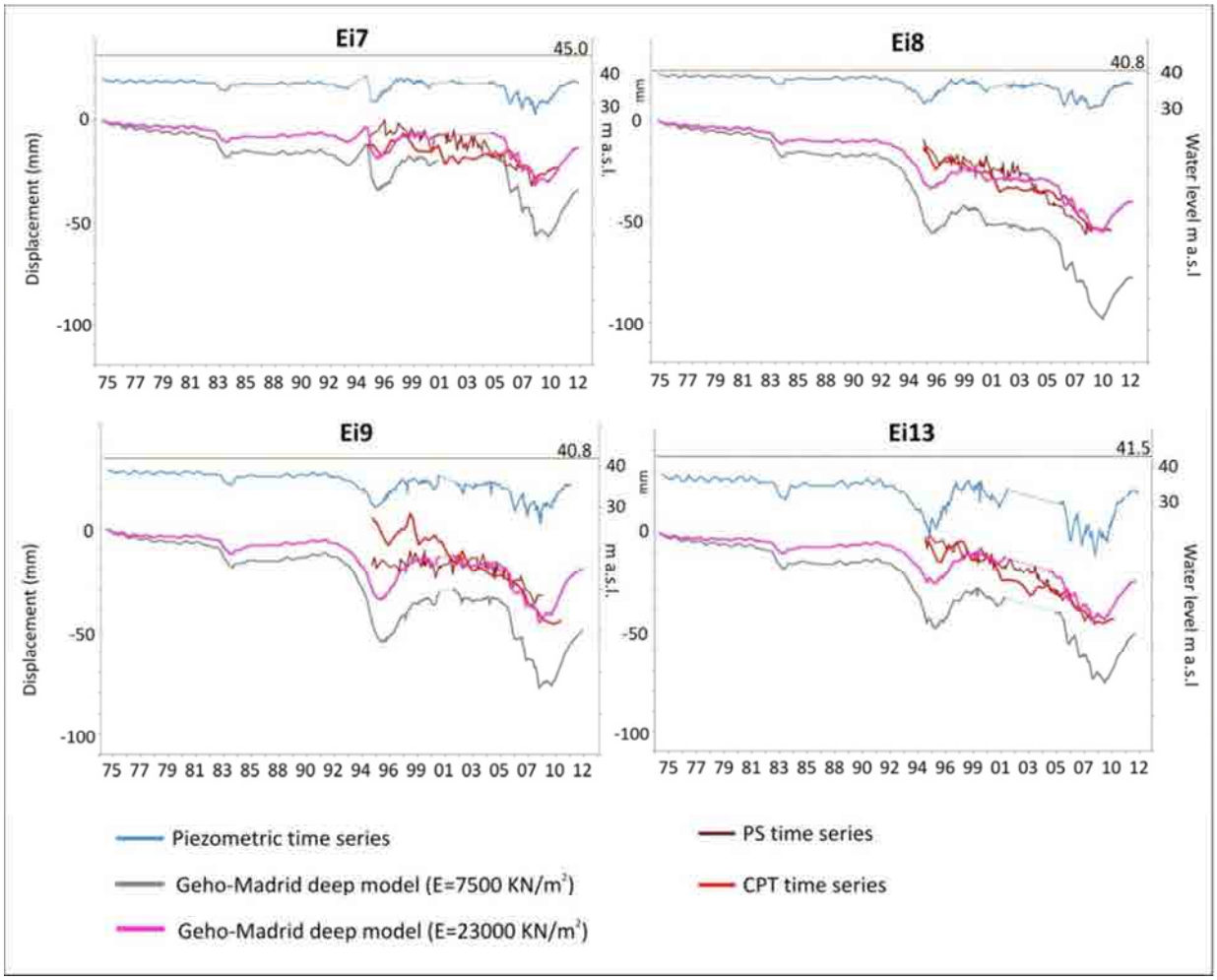

Figure 6.47: Deep models modified in the North-Western part of the city

6.3.3.2. Shallow models

In this section, taking into account the considerations reported in Par. 6.3.2, a new model has been proposed for the metropolitan area of Murcia, considering four materials: **clay, sand, sandy clay** and **gravel**.

The stratigraphic column simplification, used in the deep models' computation presented in the previous paragraph 6.3.3.1, in fact, has not allowed to justify the rapid deformations occurred in the firsts 10-20 m measured by the extensometers.

Through the in-depth analysis of the few available permeability in situ and laboratory tests, the presence of a higher permeability layer up to the gravel layer has been confirmed in the South of the river. However, the geological boreholes' descriptions are not homogeneous and, very often, do not discriminate clay and sandy-clay as described in Par. 6.3.3.

For example, in in the southern part of the river, the hydrological analysis carried out in the previous paragraphs has shown a very good connection between aquifer and aquitard (Par. 6.2.1.1).

In these part of the city, several Lefranc's permeability tests are available and aquitard permeability (between 12 and 15 m) results to vary between 2.03×10^{-7} m/s and $1{,}35 \times 10^{-5}$ m/s ($1{,}14 \times 10^{-6}$ m/s for Ei-1). This values are in agreement with the only available vertical permeability value, obtained through laboratory tests (which usually bring to a K_y of one order of magnitude less than the Lefranc's one), that results equal to $K_y = 5.23\ 10^{-8}$ m/s.

Using this K_y value in the V-8 and Ei-1 model results, shown in the paragraph 6.3.2, (where the sandy-clay layer is located between the extensometer base to the gravel layer top), the pore water overpressure dissipation has resulted instantaneous and its presence can completely vary the model results.

For this reason, V8 and Ei1 results' analysis has been useful to the implementation of the models of other columns located in the southern part of the city.

In fact, the extensometers Ei-2, Ei-3, V4, V5, V8 cover an area of 2.2×1.3 Km^2 where only 5 boreholes are available (see also the boreholes' location in Fig. 6.4). These boreholes are not very detailed and clay and sandy-clay layers are not distinguished in the stratigraphic description. For instance, the extensometer V5 is between two boreholes: S-28 (located at South, 300 m far) and S-10507 (located at North, 350 m far). According to the first one, 1.5 m of sandy-clay is present at a depth of 21 m; the second one reports the sandy clay layer between 13 and 18 m depth.

The same uncertainty occurs in V4, where only a piezometric borehole is available and simply reports clay between 0 and 19 m and gravel between 19 and 29.3 m.

For the extensometers Ei-2; Ei-3; V4, V5, as same as other cases where the same uncertainty occurs, the models have been achieved considering the information about the goodness of the aquitard-aquifer connection.

Only in the cases where the extensometers seems to observe a slow consolidation process (Ei1, V3, Ei6), also the model achieved considering a lower permeability clay layer below the extensometer base has been reported in figure 6.48. However, it has not resulted to well represent the extensometric measurements.

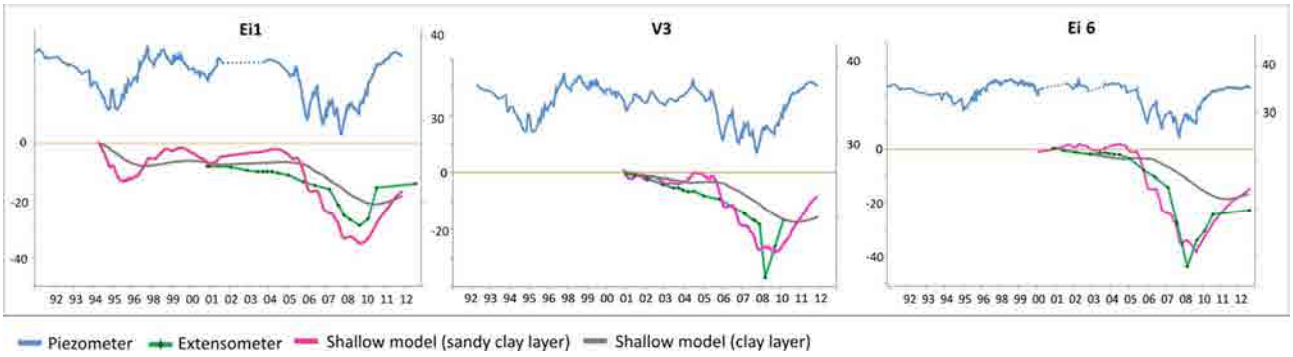

Figure 6.48: Comparisons between some shallow models achieved with or without the sandy-clay layers; see also V8 in Fig. 6.39.

Therefore, the shallow models' results shown in figures 6.49 and 6.50 have been carried out considering a higher permeability layer between the gravel and the extensometer base. The absolute error value of the comparison between the modelled column (shallow) and the correspondent extensometer's time series are shown in Table 6.10.

EXT-model											
	Differential						Rod				
	e_{abs}	σabs	Ext_depth	Gravel_d	δ		e_{abs}	σabs	Ext_depth	Gravel_d	δ
	(mm)	(mm)	(m)	(m)	(m)		(mm)	(mm)	(m)	(m)	(m)
Ei-1	5.87	3.37	15	22	21.5	**V-1**	6.08	4.57	10	17	17.3
Ei-2	1.03	1.13	20	23	19.4	**V-3**	3.91	3.25	10	18	14.5
Ei-3	1.93	1.97	20	23	21.1	**V-4**	5.40	4.94	15	19	19
Ei-4	2.21	1.04	20	25	25	**V-5**	6.75	2.36	10	23	21.1
Ei-6	2.67	2.67	10	20	14.5	**V-6**	8.62	8.80	10	25	25.1
Ei7	6.28	4.51	10	18	14	**V-8**	3.51	3.80	15	21	19.3
Ei8	4.86	4.39	10	31	30.4	**V-13**	6.47	4.57	15	18	16.4
Ei9	5.15	2.68	10	14	7.5	**V-14**	3.25	3.43	10	19	19
Ei10	7.50	6.94	10	13	7.65	**V-15**	7.61	6.38	10	20	10.6
Ei11	2.40	1.84	10	22	20.5	**V-17**	4.70	6.18	10	21	21
Ei12	3.28	2.69	10	27	13.4						
Ei13	4.13	2.05	10	13	11.5						
Ei14	8.67	4.98	10	21	21.2						
Ei15	3.59	2.94	10	14	10.9						

Table 6.10: Error table of the comparison between shallow model and extensometer's measurements

The average absolute error for all the measured displacement's time series with respect to the model is **4.8±3.8** mm for the common period between 2001-2012.

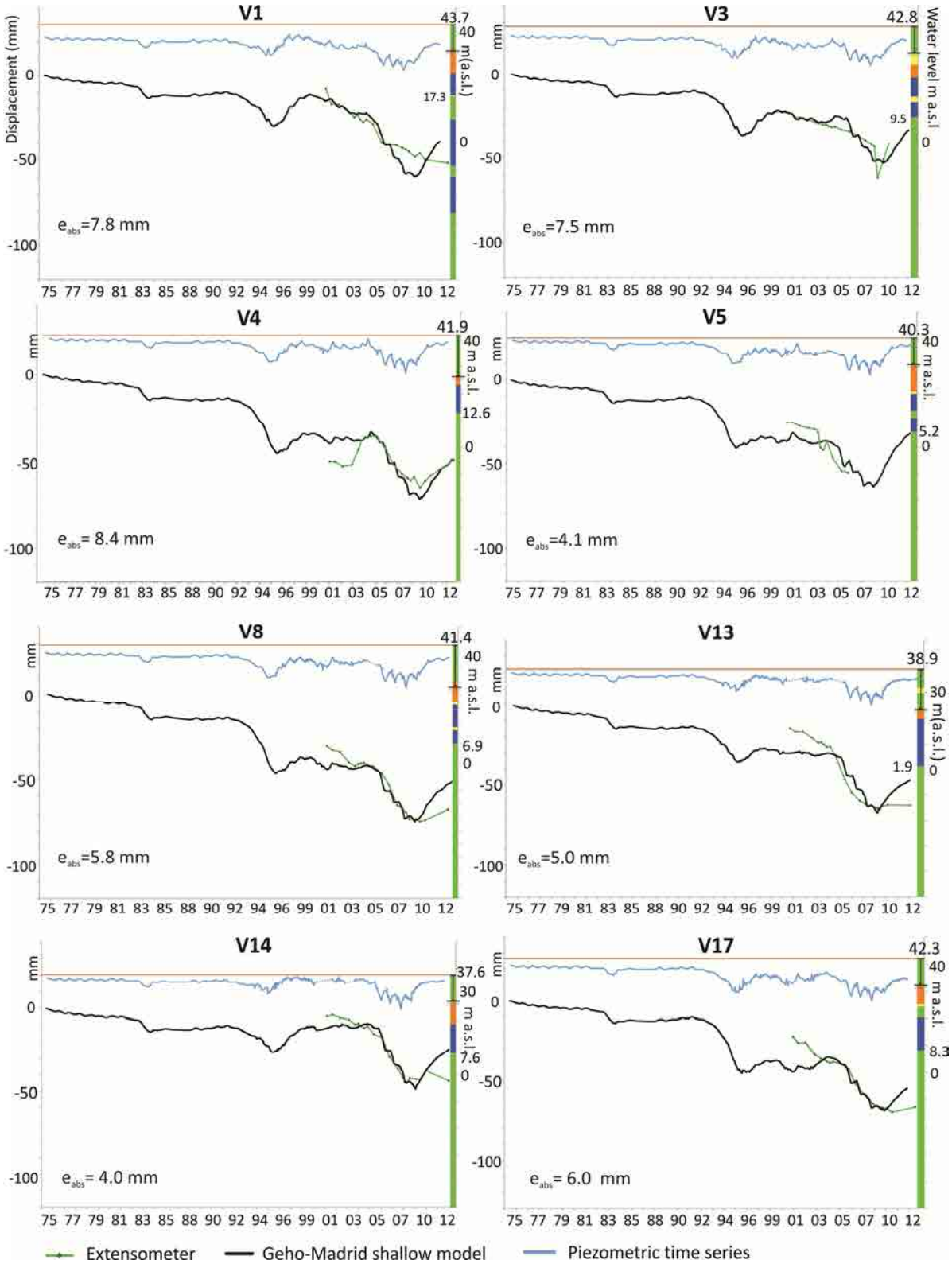

Figure 6.49: Comparisons between rod extensometer's data and shallow model's computed displacements

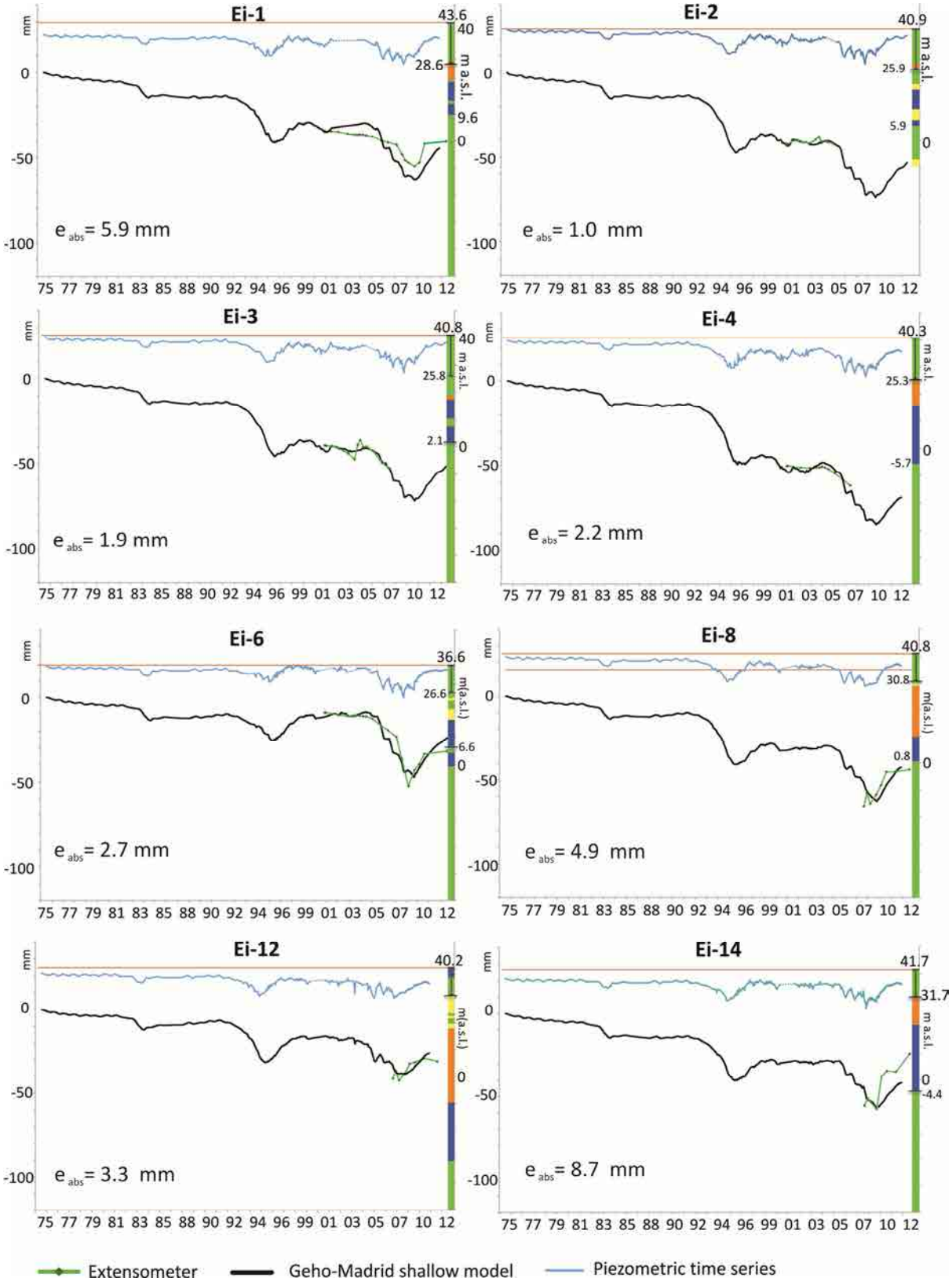

Figure 6.50: Comparisons between differential extensometer's data and shallow model's computed displacements.

In table 6.10, the extensometer's depth (*Ext_depth*), the gravel top's depth (*Gravel_d*) and the thickness of silt and clay layers up to the gravel layer (*δ*) have been reported to a correct results interpretation. The difference between Gravel_d and δ represents the sand thickness up to the gravel layer top. In the case of Ei-9, Ei-12, V15 and Ei-10, about 50% of compressible materials above the gravel top is constituted by sand.

The hypothesis considered in the shallow model computation (regarding the presence of a higher permeability layer between the extensometer base and the gravel layer) has resulted reliably on the bases of the obtained comparisons with in situ measurements.

As also observed through the comparisons between extensometric and radar's data, shown in Fig. 6.28, most of the occurred deformations interests the surficial soils.

In fact, the achieved shallow models present an average cumulated displacement between 1974 and 2012 of 56 mm. In this case, the three water level drops produced an average modelled displacements for the three subsidence periods respectively of -7±1 mm (1983-84), -18±6 mm (1993-96), -30±5 mm (2006-09); namely about 70% of that computed for the whole stratigraphic columns in Par. 6.3.3.1 (Tab. 6.8).

In particular, in many cases, extensometers and radar seem to register the same deformation (Ei2, Ei3, V1, V4, V8, V13, Fig. 6.28). This could mean that, in some cases, no deformations are occurring below the extensometer.

In this cases, the shallow model would represent by itself the subsidence phenomenon. Moreover, this cases could avoid the errors deriving from the simplified hypothesis of E_{ed} constant with depth which causes an overestimation of the deepest soils deformations.

In Fig. 6.51 the comparisons between the shallow model's results and in situ and radar data, show that, probably, in correspondence of V4 and V8 the deformations are affecting the first 10-15 m depth. In Ei-1's case, also the soils below the extensometer are suffering a consolidation. In this cases, the hydrogeological characterization is available (see Par. 6.3.1.1.3).

In all the other cases, it would be necessary a better geological, geotechnical and hydrogeological characterization of the stratigraphic columns to understand the depth of the soils interested by deformations.

However, these results have been useful to understand well the subsidence phenomenon mechanism in Murcia city, justifying the rapid response registered by the extensometers.

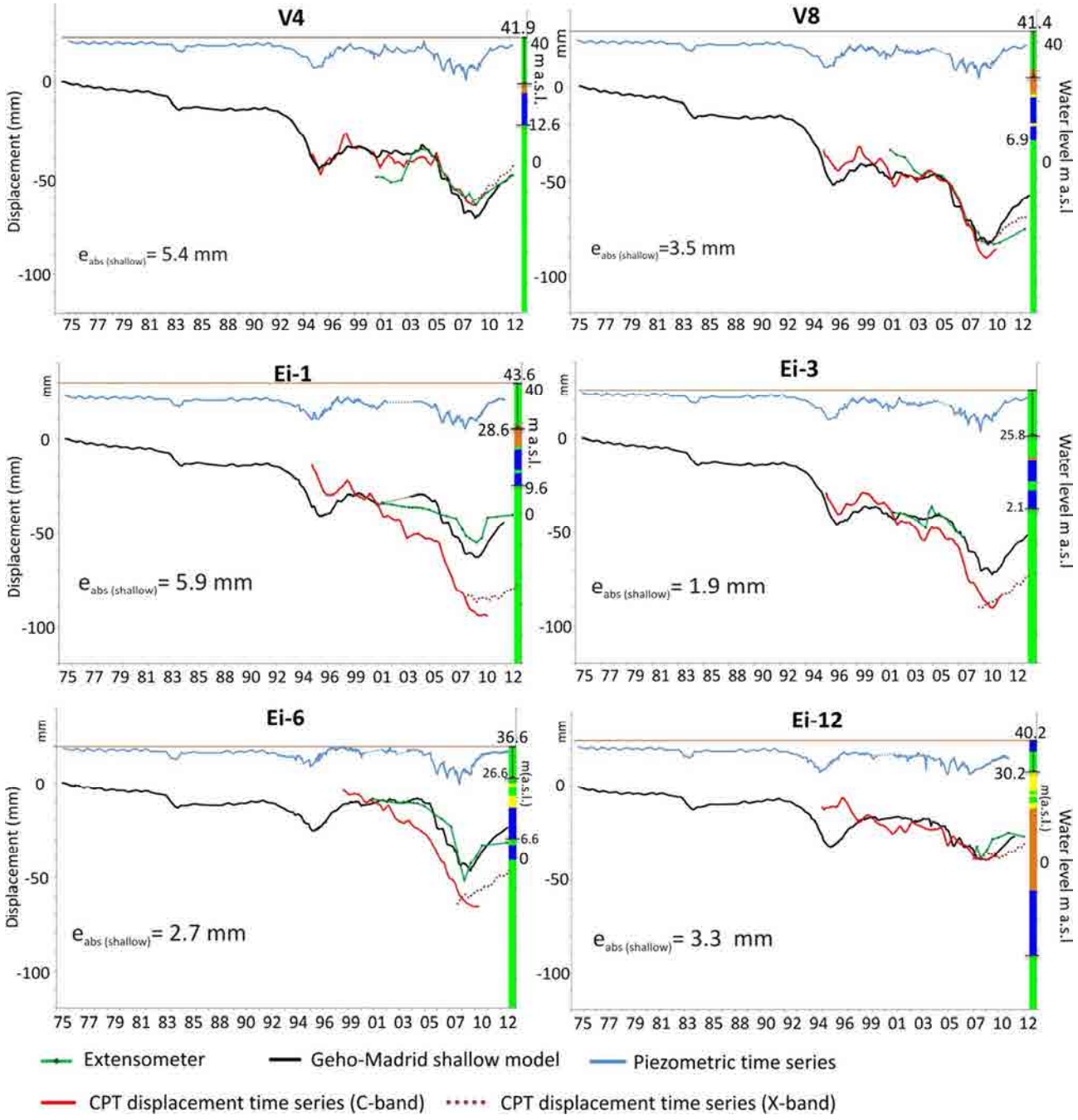

Figure 6.51: Comparisons between shallow model results, in situ and radar data

The shallow model's results (Figs. 6.49 and 6.50) obtained considering the sandy-clay presence, show a similar pattern of the temporal evolution of the displacement in respect to the deep ones (Figs. 6.41 and 6.42). In this case, the lower permeability of the deepest soils used was balanced by their underestimated stiffness (see also 6.3.2). Therefore, this analysis could represent the starting point to correct the deep model simplified hypothesis (in particular that regarding the soil stiffness constant with the depth).

6.3.3.3. Discussion

Before exploiting DInSAR data (CPT and SPN results) a statistical comparison between CPT DInSAR data and ground data (i.e. extensometers) has been performed.

As shown in paragraph 6.2.3.2.2, the compressible materials, in all the modelled boreholes, reach a higher depth respect to the installed extensometric boreholes.

The extensometers, in fact, are only measuring the deformations occurring in the first 10 to 20 m below the surface, whereas the radar measures the deformations affecting the whole aquifer system. In Fig. 6.28 and 6.29 the extensometer's measurements have been plotted and compared with the radar displacement's time series (1995-2010 and 2008-2013). The average difference (e) and absolute difference (e_{abs}) have been computed for the whole time series and for both the subsidence and uplift periods (Tabs. 6.4 and 6.5).

However, a difference of an order of millimeters between the CPT's time series and the extensometers is not significant enough to understand if the in situ monitoring network is representative of the phenomenon.

As described in paragraph 6.2.2.1.1, in fact, the time series' computation with the coherence-based method is affected by errors which have influence in the magnitude of the cumulated deformations; these are related to the coherence of every used interferogram and is very difficult to identify the images whose interferograms reduce the average coherence, increasing or reducing the noises and the errors in the computed final displacements.

After all, these comparisons show that the surficial deformations (measured by the extensometers) are very rapid in respect to the water level variations; moreover they demonstrate that most of the deformations are occurring in the firsts 10-20 meters from the ground surface; in fact, considering Fig. 6.31, the average of the maximum cumulated displacement measured by the extensometers is about 75% of the CPT one.

After the preliminary analysis, two geotechnical models have been performed: a "*shallow model"* up to the extensometer depth and a *"deep model"*, up to the surficial gravel layer bottom.

The deep model's validation has been achieved through the comparison with radar data and the shallow model one with in situ extensometric data. In particular, the comparison of the radar's time series with the "*deep model*" numerical simulations has allowed to understand if the generic parameters used in the model (Tab.6.4) and the simplified hypothesis introduced in paragraph 6.3.1.1, are reliable.

In particular, some very restrictive simplifications have been considered; among them, it is possible to highlight:

- ⟶ *the soil stiffness constant with the depth;*
- ⟶ *the soil elastic behavior;*
- ⟶ *the geotechnical and hydrogeological parameters constant in the whole urban area.*

To this aim, the absolute difference (e_{abs}) has been computed for the whole time series both of CPT's and SPN's results (Tab. 6.7). These two techniques, in fact, can bring to complementary results to the subsidence phenomenon analysis as demonstrated in several works, like Tomás et al., 2013.

Comparing the 24 deep model's computed displacement's time series with the DInSAR data (CPT and SPN) for the common monitoring periods, the average absolute difference between deep model's results and CPT's measured displacement time series has resulted of **5.9 ± 6.2** mm (for the period 05/1997-05/2010) and that with the SPN ones of **5.9 ± 4.4** mm (for the period 05/1997-12/2008).

Most of the modelled boreholes seems to well represent the phenomenon in terms of magnitude of the computed deformation and trends (Ei2, V3, V5, V6, V8, V13, V14, V4, V15, Ei1, Ei3, Ei4, Ei6, Ei11, Ei14, Ei15), whereas in the rest of them the CPT's time series seems to measure less deformation in respect to that computed with the model and having a different deformation trend (Ei-7, Ei-8, Ei-9, Ei-10, Ei-12, Ei-13, V-1).

Therefore, although the absolute error values for all the comparisons are of the order of few millimeters, an important anomaly has been identified. In fact, the geotechnical and hydrogeological parameters have resulted to be representative of the measured phenomenon for the whole study area, except in the North-Western part of the city. Here, in fact, the bi-linear deformation behavior observed in all the models in the period 1997-2009 has not resulted to correspond to that measured by SAR (in this part of the city the in situ measurements are only available after August 2008).

In particular, the deformations detected both through CPT and SPN algorithms (see Ei-7, Ei-8, Ei-9, Ei-10, Ei-12, Ei-13 and V-1 in Figs. 6.28 and 6.29) are characterized by an almost constant linear velocity, without significant trend changes. It is probably that this different behavior is due to their different stiffness. As introduced in the previous paragraphs, here, the fine-grained soils have suffered a pre-consolidation due to the presence of the ancient city walls (Tomas et al. 2011) and, in general, present a higher stiffness; this is also confirmed by the few available oedometer curves (Fig. 6.35) which show a lower initial void ratio (0.6) and a homogeneous higher stiffness for all the specimens below a depth of 4 m (values comparable to that found for specimens from other parts of the city at a depth of 11 m).

So, in the N-W part of the city, new deep models have been carried out considering a higher stiffness (Fig. 6.47). The final deep models' results will be used to obtain the phenomenon's deformation maps with the geostatistical techniques presented in Par. 6.4.

In general, we can state that the elastic model has provided good results for interpreting the Murcia city soils' behavior between 1996 and 2009 (period when the soils are over-consolidated). Nevertheless, it overestimate the ground level's recuperation for the period 2009-12 because the plastic deformations have not been taken into account. This is more evident for V13, V14, V15, V17, Ei-6 and V8 (where the third groundwater table's fall was more intense), than for Ei8, Ei13, Ei12, Ei10, Ei7, E1, V3 and Ei14 where the second and the third drop were of the same entity and a delay between the deformations and the piezometric measurements have not been registered.

The shallow model's results achieved considering three main materials (clay, sand and gravel) have not presented the rapid response observed in the extensometric measurements (Figs. 6.39 and 6.48).

This evidence has made it able to propose a variation in the models, considering four materials (clay, sand, sandy-clay and gravel) which allow to justify the rapid surficial soil responses measured by the extensometers. The presence of a sandy-clay layer up to the gravel layer is confirmed by several boreholes and its higher permeability is in according with the available in situ Lefranc's tests results.

These results have been useful to well understand the subsidence phenomenon mechanism in Murcia city, justifying the rapid response registered by the extensometers.

However, a hydrogeological and geotechnical characterization of the deepest soils is requested to improve these models. In fact, only three deep permeability's values, achieved through laboratory tests, are available (and not well distributed in the study area) and also the oedometric tests reach a depth of 11 m.

Therefore, up to the extensometer's depth, the soil characterization allows to obtain reliable computed displacements; an absolute error of **4.8±3.8** mm has been achieved from their comparisons with extensometric measurements (for the common period 2001-2012) but deriving from a hypothesis of the permeability values of the deepest soils which can be confirmed only in the South of the river.

Considering that about 75% of the displacement interests the extensometers' depth, the shallow model could characterize itself by the greatest part of the subsidence phenomenon; thanks to the comparisons between extensometers and radar data it could represent the starting point to correct the deep model simplified hypothesis regarding the soil stiffness constant with the depth.

6.4. Geostatistical analysis: Bidimensional model

In the previous paragraphs a one-dimensional modelling of the subsidence phenomenon affected the urban area of Murcia city has been presented. The one-dimensional analysis has been preferred to the two-dimensional one, considering the extension of the area of interest (36 square kilometers) versus the considered modelled depth (around 35 m). However the interpolation of the model results to obtain a 2D model of the phenomenon represents a critical point of the analysis.

In fact, through these maps is possible to have a clear vision of the spatial development and variability of the phenomenon and obtain information of the correlation with other variables in the space.

Another relevant possibility regards the use of the maps of deformation in the SAR images processing.

As described in chapter IV, in fact, the knowledge of the linear phase (function of the deformation) can allow to better estimate the no-linear part of deformation facilitating the convergence of the equation system of the CPT algorithm.

For this reason, the data interpolation become a very important topic in this part of the study and has been analyzed in the following paragraphs.

6.4.1. Geostatistical techniques: overview

Geostatistics is the application of statistical methods to geo-referenced data.

It allows the description of spatial patterns, quantitative modeling of spatial continuity and of sample semivariograms, spatial prediction and uncertainty assessment.

Several interpolation techniques have been proposed to obtain a spatial estimated representation of punctual values of a variable *z* available in *n* unsampled location *u*.

In particular, the simplest methods, called "*univariate*", as described in Goovaerts, 2010, are the Thiessen polygon (Thiessen, 1911) and the Inverse Distance Weighted, IDW (Bedient and Huber, 1992).

In the first case, to the unsampled location is assigned the record of the closest gauge. This is obtained drawing, around each gauge, a polygon of influence with the boundaries at a distance halfway between gauge pairs. In this case, the spatial variability of the variable is not taken into in account.

The IDW method is based on the principle that observations that are close to each other on the ground tend to be more alike than those further apart, hence observations closer to u should receive a larger weight.

The unknown variable is estimated as a weighted average of surrounding values, the weights being reciprocal to the square distances from the unsampled location (eq. 6.5).

$$z^*(u) = \frac{1}{\sum_{i=1}^{n(u)} \lambda_i(u)} \cdot \sum_{i=1}^{n(u)} \lambda_i(u) \cdot z(u_i) \qquad \text{with} \qquad \lambda_i(u) = \frac{1}{|u - u_i|^2} \tag{6.5}$$

In the IDW method, λ_i only depends on distance and does not take into account the spatial relationships among the samples.

For this reason, other geostatistical algorithms, are based on a model of the characterization of the spatial pattern of continuous and categorical soil attributes, represented by the semivariograms. Among them, the kriging interpolator is described.

The semivariogram analysis allows the study of the spatial behavior of the variable, namely its variance, anisotropy and influence zones. It is modelled starting from the experimental values to represent a random function, whereby the set of unknown values which is regarded as a set of spatially dependent random variables. Each datum *z(u_i)*, is then viewed as a particular realization of a random a variable *Z(u_i)*.

The semivariogram is computed as half average of the square difference of the values (z) which the variable has in a point (u_i) and in another having a distance *h* (called "*LAG number*") from the first one $(u_i + h)$:

$$\hat{\gamma}(h) = \frac{1}{2N(h)} \cdot \sum_{i=1}^{N(h)} [z(u_i) - z(u_i + h)]^2 \qquad \text{with} \qquad N \cdot h < |D|/2 \tag{6.6}$$

where *N(h)* is the number of pairs of data locations a vector *h* apart. *N* represents the number of LAGs considered in γ computation and usually is considered less than the dimension of the study area (D) divided for two times the LAG number.

In the Kriging algorithm, λ depends on the semivariogram and, for this reason, accounts for direction-dependent variability (*anisotropic spatial pattern*).

While the semivariogram allows describing spatial patterns, the interpolation algorithm, based on the modelled semivariogram, permits to predict the values of soil attributes at unsampled locations.

As described in Goovaerts, 1997, Kriging is a generalized least-square regression technique which allows one to account for the spatial dependence between observations, as revealed by the semivariogram, into spatial prediction.

As for the IDW algorithm, the unknown variable *z* at the unsampled location u is estimated as a linear combination of neighboring observations:

$$z^*(u) = \frac{1}{\sum_{i=1}^{n(u)} \lambda_i(u)} \cdot \sum_{i=1}^{n(u)} \lambda_i(u) \cdot z(u_i) \tag{6.7}$$

But, in the Kriging algorithms, weights λ_i are obtained by solving a system of linear equations which depend on the chosen method (*Ordinary kriging, Simple kriging, Universal kriging, Lognormal kriging*, etc.). The:

⟶ **Ordinary Kriging (OK)** assumes the stationarity of the first moment of all random variables: *E{Z(xi)}=E{Z(x0)}=m*, where m is unknown. The weights which solve the system of equation (6.8), in this case, minimize the estimation variance.

⟶ **Simple Kriging (SK)** assumes a known stationary mean: *E{Z(x)}=m*, where m is known.

⟶ **Universal Kriging (UK)** (also known as kriging with a trend model, KT) considers that the unknown local mean *m(u')* smoothly varies within each local neighborhood *W(u)* and the trend is modeled as a linear combination of functions $f_k(u)$.

$$m(u') = \sum_{k=0}^{K} a_k(u') \cdot f_k(u') \qquad \text{with} \quad a_k(u') \approx a_k \, \forall u' \in W(u) \tag{6.8}$$

The coefficients $a_k(u')$ are unknown and deemed constant within each local k neighborhood W(u).

⟶ **Indicator Kriging (IK)** uses indicator functions instead of the process itself, in order to estimate transition probabilities.

⟶ **Lognormal Kriging (LK)** interpolates positive data by means of logarithms.

The only information required by the kriging system are the semivariogram values for different LAGs and these are readily derived once a semivariogram model (*spherical, cubic, dampened, exponential,* …) has been fitted to experimental values (Goovaerts, 2010). In fact, for predictions, the empirical semivariogram is converted to a theoretic one by fitting a statistical model (curve) to describe its characteristics: *range, sill and nugget* (Fig. 6.52).

These describe the structure function, the autocorrelation and define the range or distance over which spatial dependence exists.

- The ***nugget*** is the semivariance at a distance 0.0, (the y –intercept);
- The ***sill*** is the value at which the semivariogram levels off (its asymptotic value);
- The ***range*** is the distance at which the semivariogram levels off (the spatial extent of structure in the data).

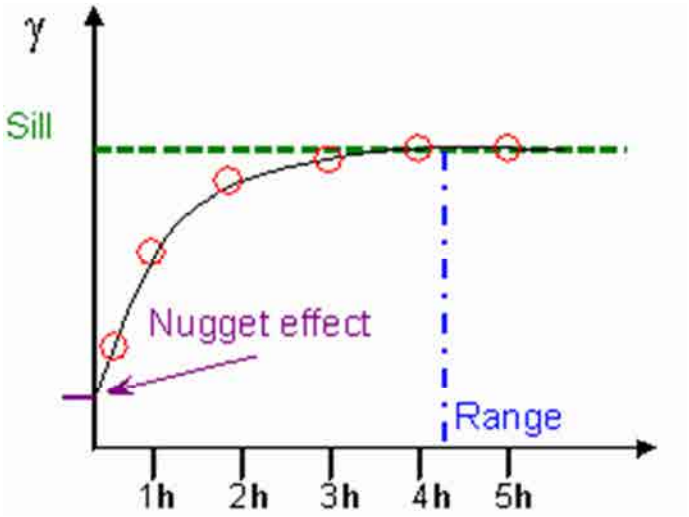

Figure 6.52: Semivariogram example

The main semivariogram models (Fig. 6.53) are:

a. Linear model: does not assume sill or range; in this case results:

$$\gamma(d) = c_0 + bd \tag{6.9}$$

b. Exponential:

$$\gamma(\mathrm{d}) = c_o + c[1 - \exp(-|d| / a)] \tag{6.10}$$

c. Spherical:

$$\gamma(\mathrm{d}) = \begin{cases} c_o + c[3d/2a) - (d^3 / 2a^3)], d \le a \\ c_o + c, d > a \end{cases} \tag{6.11}$$

d. Gaussian:

$$\gamma(\mathrm{d}) = c_o + c[1 - \exp(-d^2 / a^2)] \tag{6.12}$$

where c_0 = nugget; b = regression slope; a = range; c_0+ c = sill

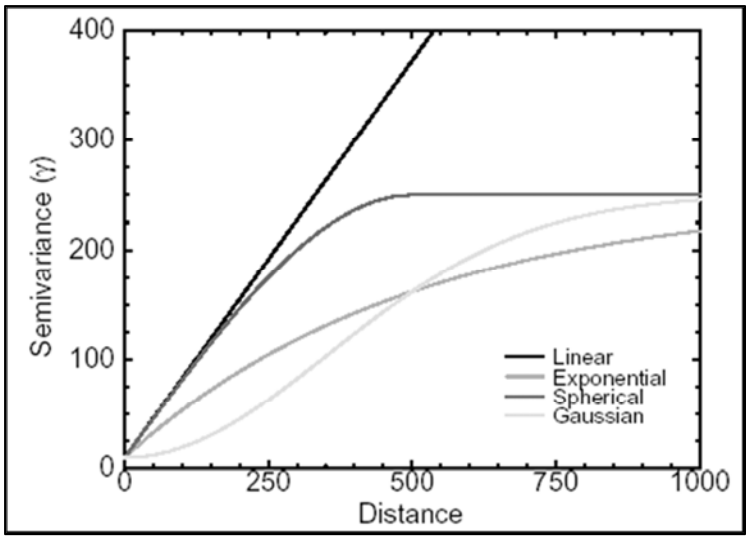

Figure 6.53: Main semivariogram models

As introduced above, to obtain the prediction value of a variable, to each Kriging algorithm, corresponds an equation system.

In the case of the *Ordinary Kriging*, the equations system is the following:

$$\begin{cases} \sum_{j=1}^{n(u)} \lambda_j(u) \cdot \gamma(u_i - u_j) - \mu(u) = \gamma(u_i - u) \\ \sum_{j=1}^{n(u)} \lambda_j(u) = 1 \end{cases} \qquad i = 1,\ldots,n(u) \tag{6.13}$$

In the event that the experimental values of a variable are too few to analyze their spatial variability, it is possible to consider several methods, belonging to the Kriging where the information of a densely distributed variable (for example the displacement radar data) is used to interpolate a variable having less known values (i.e. the ground-based data). In the case of use of radar data, these methods are called “for radar-gauge combination”.

In particular, ***Kriging with an external drift (KED)***, is a variant of the UK where the trend *m(u)* is modelled as a linear function of a smoothly varying secondary (external) variable *y(u)* instead of a function of the spatial coordinates:

$$m(u) = a_0(u) + a_1(u) \cdot y(u) \tag{6.14}$$

Another possibility in the employment of an external more densely sampled to improve the interpolation of sparsely sampled observations is represented by the ***Co-Kriging*** **(CK)** (Almeida and Journel, 1994).

Whereas Kriging with an External Drift uses the secondary exhaustive information only to inform on the shape of the trend of the primary variable, Co-Kriging exploits more fully the secondary information by directly incorporating the values of the secondary variable and measuring the degree of spatial association with the primary variable through the cross semivariogram (Goovaerts, 1999).

The methods described above have been effectively used to the rainfall data interpolation, integrating the densely-populated weather-radar observations. In particular, some examples can be found in Creutin et al., (1988), Azimi-Zonooz et al., (1989) where the Co-Kriging has been used and Raspa et al., (1997) where to combine in situ and radar information, the Kriging with an External Drift has been considered.

Another geostatistical methods for "radar-gauge combination" is the ***Ordinary Kriging of Radar Errors* (OKRE)**. As in the previous cases, the punctual values of a primary variable are regarded as measurements of true deformations, whereas radar is comprised as auxiliary information on the spatial distribution (Erdin, 2013). According to this method, is possible to obtain the interpolated map of deformations by subtracting a radar error map from the original interpolated radar map. In particular, the radar error map is carried out by interpolating the differences between radar and in situ data with the OK interpolator.

In the present thesis project, the geotechnical model results (considered as known deformations and available in 24 points) will be interpolated using the great amount of displacement data obtained through A-DInSAR techniques as "*secondary information*".

In the following, the mentioned methods for radar-gauge combination have been described, considering as variable the model deformation.

6.4.1.1. Kriging with External Drift (KED)

Deformation estimations using KED (eq. 6.15) are computed with the same expression introduced in OK method (Goovaerst, 1999):

$$z^*_{KED}(u_0) = \sum_{i=1}^{n} \lambda_i^{KED} \cdot z_G(u_i) \tag{6.15}$$

However, KED weights, λ_i^{KED}, are different from those used in the OK technique; in fact, the equation system of KED estimator (eqs. 6.16-6.18) has additional constraint to satisfy the new drift hypothesis and there are two auxiliary Lagrange multipliers μ_0 and μ_1:

$$\sum_{j=1}^{n} \lambda_i^{KED} \cdot C_R(u_i, u_j) + \mu_0 + \mu_1 \cdot z_R(u_i) = C_R(u_i, u_0), \qquad i = 1,2,\ldots,n \tag{6.16}$$

$$\sum_{j=1}^{n} \lambda_j^{KED} = 1 \tag{6.17}$$

$$\sum_{j=1}^{n} \lambda_j^{KED} \cdot z_R(u_j) = z_R(u_0) \tag{6.18}$$

where $z_G(u_i)$ and $z_R(u_i)$ are respectively deformation and radar observations at a given location and C_R is the covariance of the residuals $z_G(u_i) - m_G(u_i)$, where $m_G(u_i)$ is the deformation drift field.

The final constraint in the equations system 6.16, 6.17, 6.18, introduces the variability of the radar data into the interpolation process of the deformation values. This constraint means that deformation is weighted using the set of weights that add in the effect of estimating the radar value at the target point as the radar values at the deformation model locations were interpolated. Theoretically, KED requires that C_R, the covariance of the residuals $z_G(u_i) - m_G(u_i)$, to be inferred. This is not straight forward, because neither the trend (drift) nor the residuals are known a priori. Introducing the methodology proposed by Velasco et al. (2009): first a trend field $m_G(u_i)$ is estimated, at all target points from the radar field by OKRD and then residuals are computed by subtracting this estimated field from the radar one: $z_G(u_i) - m_G(u_i)$.

To summarize the methodology developed by Velasco et al. (2009) for obtaining estimated deformation fields using KED, we assume that the correlogram of the radar field is used to interpolate the rainfall field and the relationship between deformation model values and radar data is linear and high. Then:

1. Calculate a drift map from the radar field by OK for the whole estimation area, using only the radar data at the deformation model locations (24 points). The variogram of the deformation field for this step is computed from the complete radar field.
2. Calculate the radar field in the whole area using all the radar data available and the same variogram as in step 1.
3. Obtain the radar residual map by subtracting the drift map calculated in step (1) from the radar field computed in step (2).
4. Calculate the variogram of the residual map.
5. The KED algorithm can be used then to estimate deformation fields using deformation model values as the primary variable, radar data as the secondary variable and the radar residual variogram as the spatial variability model.

6.4.1.2. Co-Kriging (CK)

Co-Kriging methods are used to take advantage of the covariance between two or more regionalized variables that are related.

The unknown deformation value $z^*_{CK}(u_0)$ is a linear combination of n values of two or more regionalized variables. The general equation for two-variable co-kriging (eq. 6.19) for which input data are located only in correspondence of the 24 points where the displacement value is known:

$$z^*_{CK}(u_0) = \sum_{i=1}^{n} \lambda_i^{CK} \cdot z_{G_i} + \sum_{j=1}^{n} \beta_j \cdot z_{R_j}, \ldots\ldots \quad (6.19)$$

where $z^*_{CK}(u_0)$ = the deformation value estimated at the grid node; λ_i^{CK} = the undetermined weight assigned to the primary sample z_{Gi} which varies between 0 and 100%; z_{Gi} = the regionalized variable at a given location, with the same units as for the regionalized variable; z_{Rj} = the secondary regionalized variable that is co-located with the primary regionalized variable; z_{Gi}, with the same units as for the secondary regionalized variable; and β_j = the undetermined weight assigned to z_{Rj} and varies between 0 and 100%.

The estimate is unbiased, with the estimation variance minimized, and requires the following:

- ⟶ The spatial covariance model of the primary attribute (e.g., 24 model data).
- ⟶ The spatial covariance model of the secondary attribute (e.g., radar data).
- ⟶ The spatial cross-covariance model of primary and secondary attributes (e.g., model and radar data).

6.4.1.3. Ordinary Kriging of Radar Errors (OKRE)

The idea of *Ordinary Kriging of Radar Errors* (OKRE), (Erdin, 2013) is to interpolate observed radar errors at available deformation locations (determined by radar measurement minus model deformation values) by Ordinary kriging (OK).

The resulting radar error field is subsequently subtracted from the original radar field to obtain the deformation interpolated map: *Deformation = Radar – Radar error.*

The steps to follow are:

1. Compute the complete Radar field interpolating the radar values for each date.
   This is performed using the variogram modeled for the radar field. (To model the variogram, the radar dates have been classified depending on its behavior).
2. Compute the radar errors interpolating the errors (Radar – Modeled value) in the 24 points were modeled values are available.

   As it is not possible to have a robust variogram with 24 points the same variograms models for the radar are used. This simplification is suggested by Verworn and Haberlandt (2011) as Haberlandt (2007) have shown that there were no significant differences in the interpolation performance.

3. Compute the differences of radar values minus radar error.

6.4.3. Deep model results interpolation

As introduced in the previous, the generation of deformation maps is useful to understand the spatial development of a phenomenon and, specifically, in the present thesis, has allowed the improvement of the SAR images processing (as reported in Par. 6.5).

In the case of Murcia, DInSAR data are not available to achieve the deformation maps for the first and the second subsidence periods (1982-84 and 1995-96); to this analysis, it is possible to use the deep model validated results, as shown in Fig. 6.54. Here, in particular, the IDW method has been used.

As it possible to note, the evidences shown in Fig. 6.54 , achieved with the simplest interpolation algorithm are in according with the considerations made in the previous paragraphs (i.e. the higher deformations are occurring at South of the river, as also shown by extensometers' and radar's measurements; these higher deformations have a correspondence with the higher thickness of compressible materials and with the higher registered water level drop; see also Fig. 6.32).

However, the error introduced by the interpolation is significant, especially in those areas where in situ data are not available.

In the following, the cross-validation for the interpolated maps of Fig. 6.54 has been presented.

The sample of data have been partitioned into complementary subsets, performing the analysis on one subset (called the training set), and validating the analysis on the other subset (called the validation set or testing set).

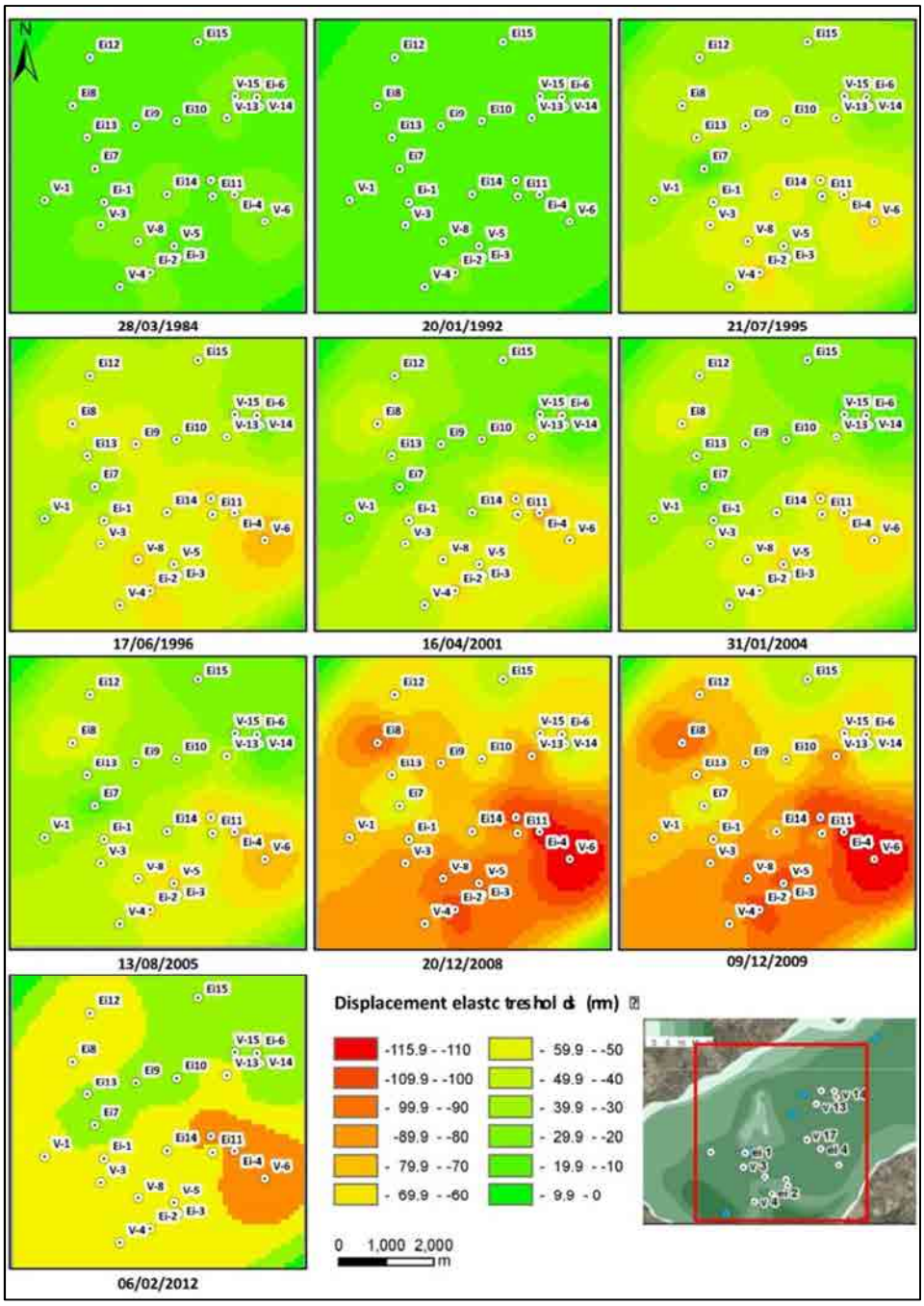

Figure 6.54: Deformation maps obtained from the deep model interpolation. The thickness of compressible materials, shown in Fig. 6.4 have been reported.

For each interpolation, a cross-validation table, containing the errors for all the couples of points used for the interpolation in function of their distance have been obtained. This table has been achieved for all the maps of Fig. 6.54.

In a second step, for each point considered in the interpolation, the distance from all the other points has been computed and the closest point has been selected. The distance of the couples of closest points have

been related to the cross-validation table. A plot of the error obtained for all the couples of closest points (and for each interpolation of Fig. 6.54) in function of the distance has been showed in Fig. 6.55.

Figure 6.55 shows an error increase for a distance higher than 600 m. This means that the interpolation error is even higher outside a buffer of 600 m from the modelled column.

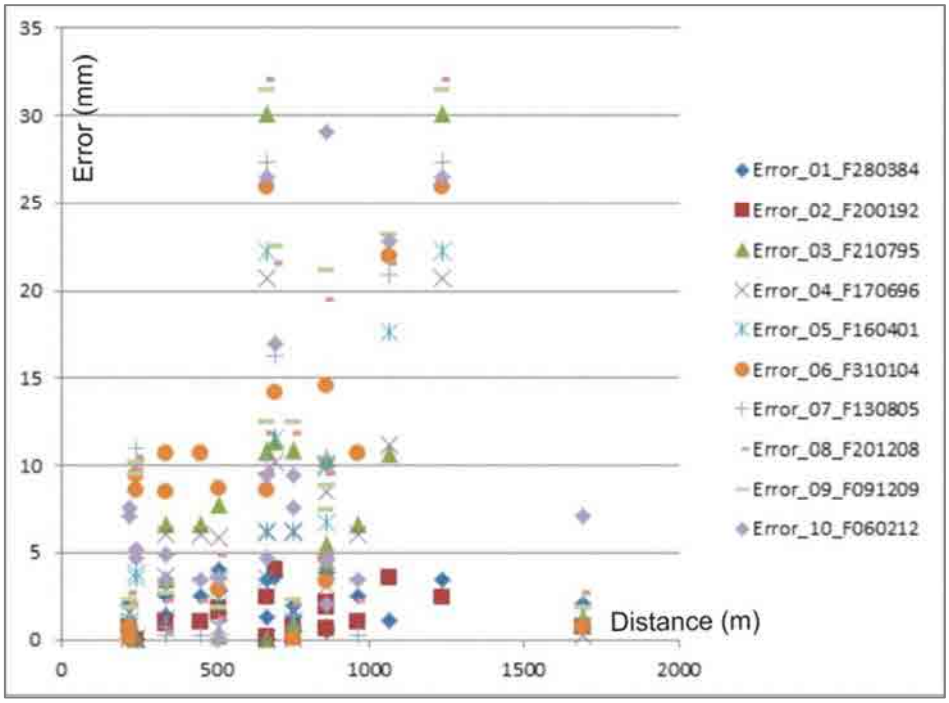

Figure 6.55: Error-distance graph

In any case, the generation of interpolated maps is useful to enhance the spatial analysis of the results, but the achieved interpolations strongly depend on the chosen estimator. For this reason, to a qualitative analysis of the phenomenon development, the IDW method has bring to reliable results, but, to their use in the CPT processing, a more sophisticate geostatistical algorithms has been taken into consideration.

In particular, the consultation of several scientific works concerning the comparisons between the geostatistical methods for radar-gauge combination (described in the previous), has brought to choose the OKRE to the model result interpolation presented in the following.

Above all, Erdin (2013) has pointed out the main differences between KED and OKRE methods. According to this work, KED interpolator brings to a better estimation of bias and mean error, while OKRE estimator is better is terms of low and high deformation distinction and to the representation of extreme values of deformation. The radar values are, hence, smoother by KED, favouring mean error and bias, and more sharp and rugged by OKRE, favouring a better estimation of the maximum deformation.

Therefore, among the methods described above, OKRE has been preferred and, (following the steps listed in Par. 6.4.1.3), the deep model interpolated maps have been achieved using all the radar data of the area of 6x6 Km^2 (Fig.6.20), for the period 1997-2009.

In fact, in the period 1995-1997, as described in the previous, only few SAR images are available and this have not allowed a good estimation of the ground up-lift. After 2009, the proposed elastic model has turned out to be inappropriate in some zones of the study area (see also Par. 6.3.3.3) where some plastic deformations occurred. Here, it overestimates the soil uplift in the period 2009-2012.

To the interpolations, the software ***Stanford Geostatistical Modeling Software (SGeMS)*** has been used.

It has been implemented at the University of Stanford and relies on the Geostatistics Template Library (GsTL) to implement its geostatistical routines, including the Kriging and multi-variate kriging methods. Furthermore, it allows taking into account the possible existing trends in the two direction of maximum anisotropy, performing a bi-directional variogram.

First of all, the correlation between the two variables has been analyzed (Fig. 6.56), by plotting the 24 displacement data computed with the model against that measured by the radar in all the dates (122 for the chosen period). The correlation coefficient obtained, 0.6, is considered here to be high enough to indicate that both variables are linearly related and radar data can be used to estimate deformations.

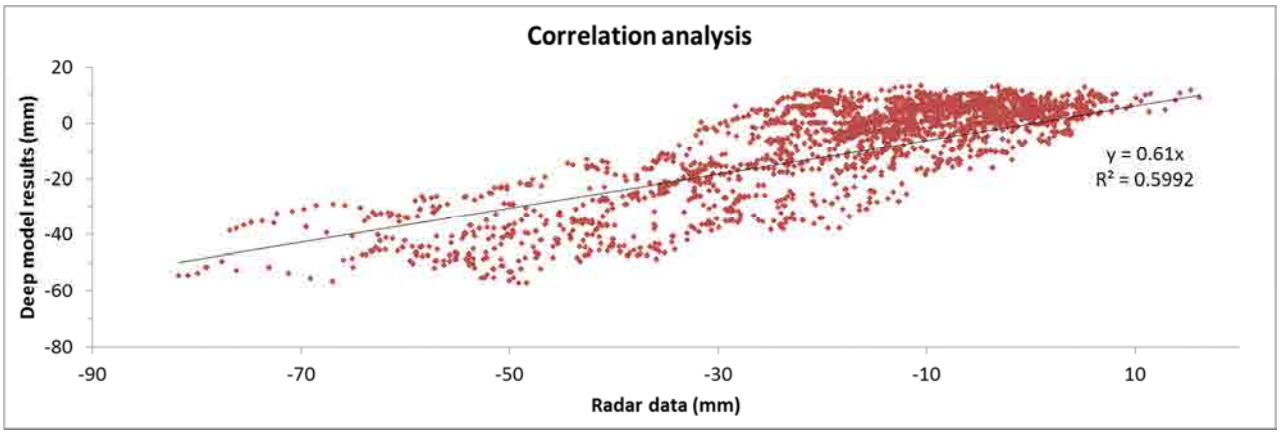

Figure 6.56: Correlation between deep model computed displacements and radar measurements

After that, as described in the point 1 of Par. 6.4.1.3, radar data (obtained using the CPT algorithm), have to be interpolated for each date (122 between 1997 and 2010) to obtain the complete Radar field. To this aim, the data spatial variability has been analyzed per year and the achieved modelled variograms have been used to the interpolations of the data in the intermediate dates.

Thus, first of all, the great amount of available radar data included in the study area of 36 Km^2 (Fig. 6.20) have been used to analyze the spatial anisotropies and existing trends in the occurred deformations and to model a bi-directional variogram.

At first, an *Omni-directional variogram* has been studied to choose the Lag number and the Lag separation.

It represents the average of the variograms achieved considering all the possibly directions. In this case, a spherical variogram model, obtained using a LAG of 200 m, a number of LAGs of 15 and a tollerance of 100 resulted to well fit the radar measures.

In a second step, the anisotropies have been analysed. To this aim, the directional variograms have been estimated in several directions (Fig. 6.57).

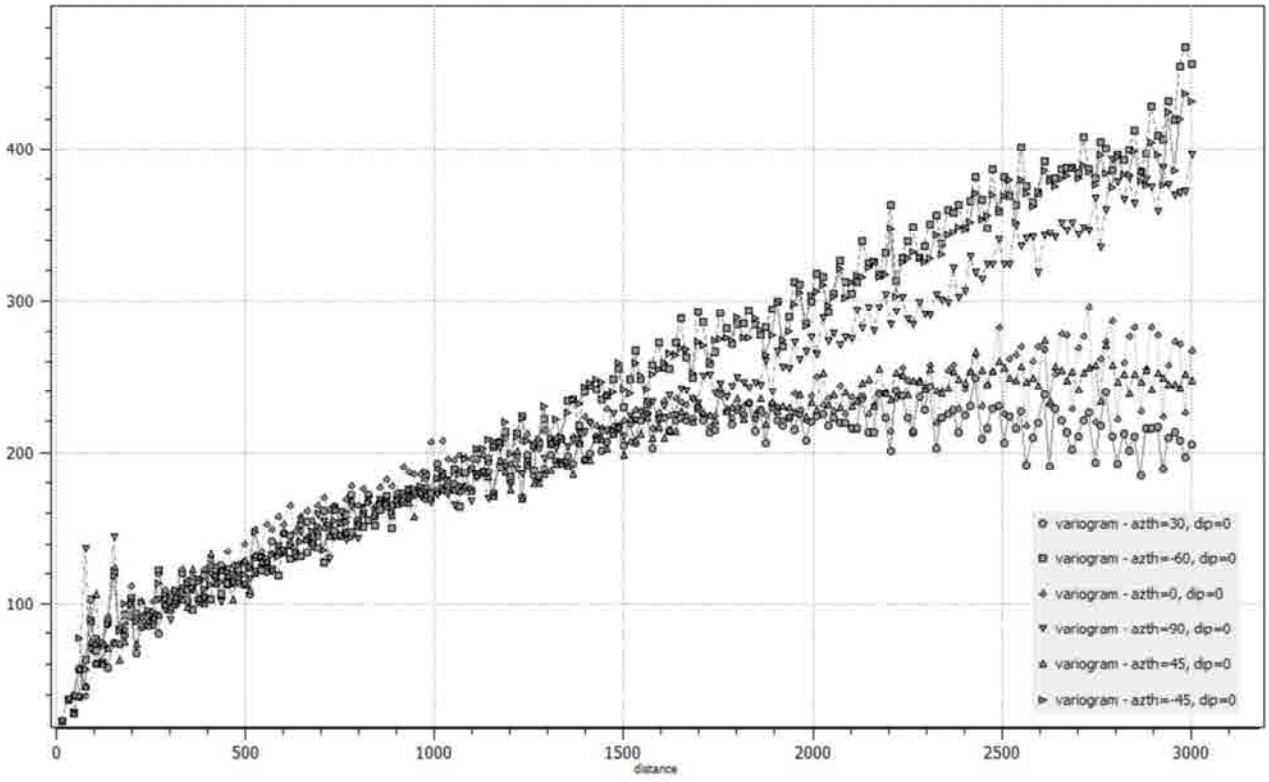

Figure 6.57: directional variograms analysis; x-axis=distance in the azimuth direction (m); y-axis=variance of the difference between radar data values at two locations whose distance is reported on the X-axis.

As described in the previous paragraphs, in the metropolitan area is registered a general up-lift in the periods 1997-2000 and 2009-12, a stable behavior between 2001 and 2005 and a subsidence phenomenon between 2005 and 2009.

Fig. 6.58 shows the phenomenon spatial variance per year which has been analyzed tacking into account these deformation phases.

In particular, an an-isotropic behaviour has been observed in the study area (Fig.6.58) only in the periods 1997-1999 and 2005-2010; in the stable period 2000-2005 the modelled variograms have turned out to be isotropic (Fig.6.59).

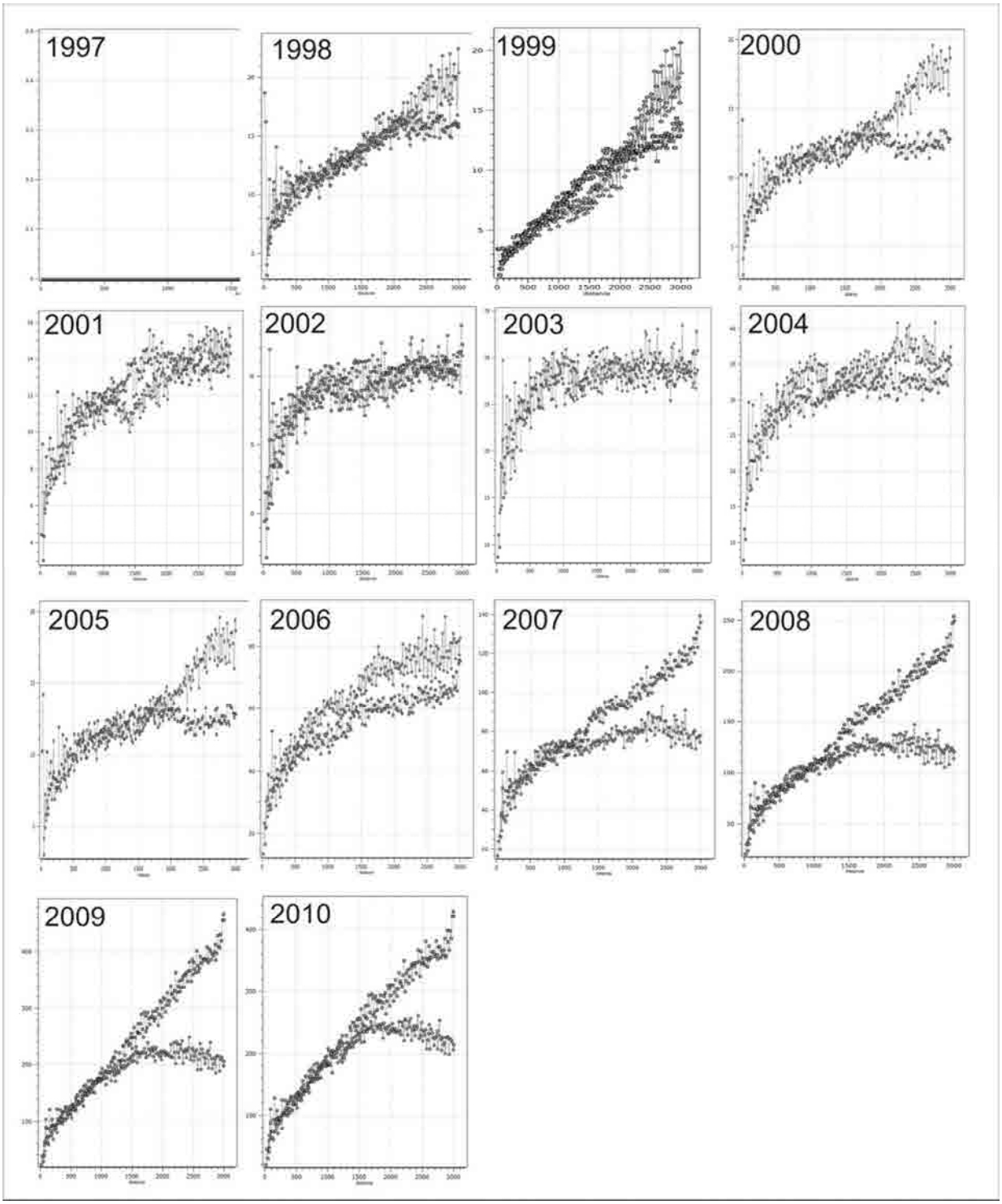

Figure 6.58: Anisotropy analysis: Bi-directional variograms (Azimuth: 30° and -60°); on Y-axis is represented the variance of the difference between radar data values at two locations whose distance is reported on the X-axis.

For both the periods when an an-isotropic behaviour has been observed (1997-1999 and 2005-2010), the directions of maximum anisotropy resulted to have an Azimuth respectively of 30° and -60° (Fig. 6.57).

These orthogonal directions corresponding to the maximum anisotropies have a geological correspondence because they coincide with the Segura river direction and with the VMSR axis.

This means that, along these directions, the maximum variogram differences are registered. In other words, thanks to the bi-directional variograms modelling in these two directions, the interpolation will take into account the deformation spatial variability in the two directions where it results more different: its anisotropy.

The modelled variograms are reported in Fig. 6.59 (period 1998-2004) and Fig. 6.60 (period 2005-2010).

Considering a spherical variogram model, the Range, the Nugget and Sill values have been modelled for all the experimental variograms, and have been reported in the Tab. 6.11.

As it possible to note in this table, in the period 1998-2004 a range of 1000 has been used to model the variogram in both the directions. This means that the influence zone of the variable is about 1 Km, namely that the samples are related up to this distance.

Furthermore, the intercept of the modelled variogram on the y-axes (nugget) vary between 2 and 15 mm; it means that close points in this period have a displacement difference of 0.2-1.5 cm. In the following period the displacement variance of close points increase to 2.5-5.0 cm.

	Azimuth 30°			**Azimuth -60°**		
	Range	**Nugget**	**Sill**	**Range**	**Nugget**	**Sill**
1997	1000	-	-	1000	-	-
1998	1000	5	7	1000	5	7
1999	1000	2	5	1000	2	5
2000	1000	5	7	1000	5	7
2001	1000	**5**	7	1000	**5**	7
2002	1000	10	10	1000	10	10
2003	1000	15	14	1000	15	14
2004	1000	15	18	1000	15	18
2005	1000	15	25	1000	15	25
2006	2000	25	50	1500	25	35
2007	1100	35	40	2500	35	70
2008	1100	40	73	6000	40	270
2009	1100	50	125	4000	50	370

Table 6.11: Variogram models' parameters

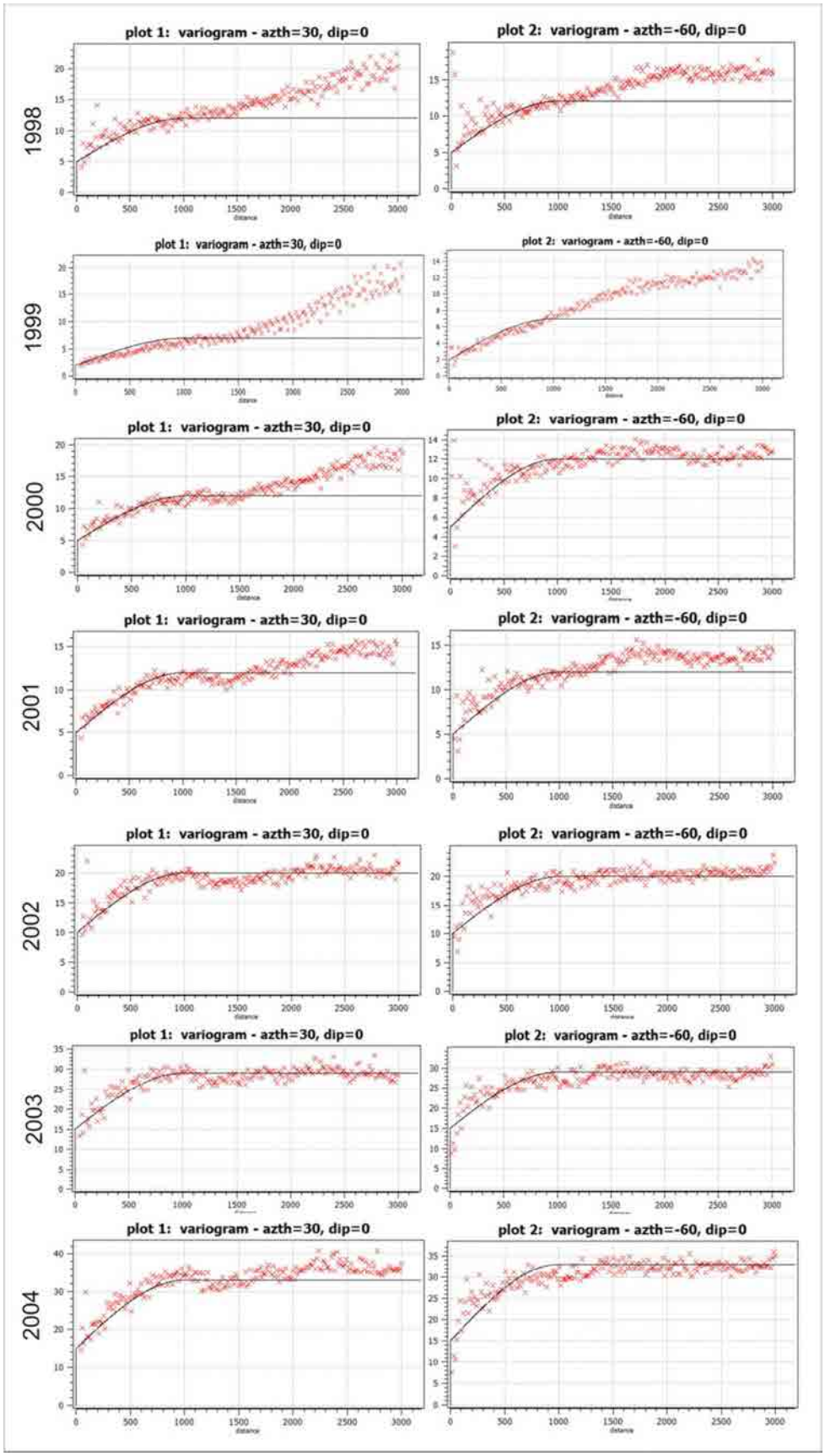

Figure 6.59: Bi-directional variograms (Azimuth: 30° and -60°); period 1998-2004.

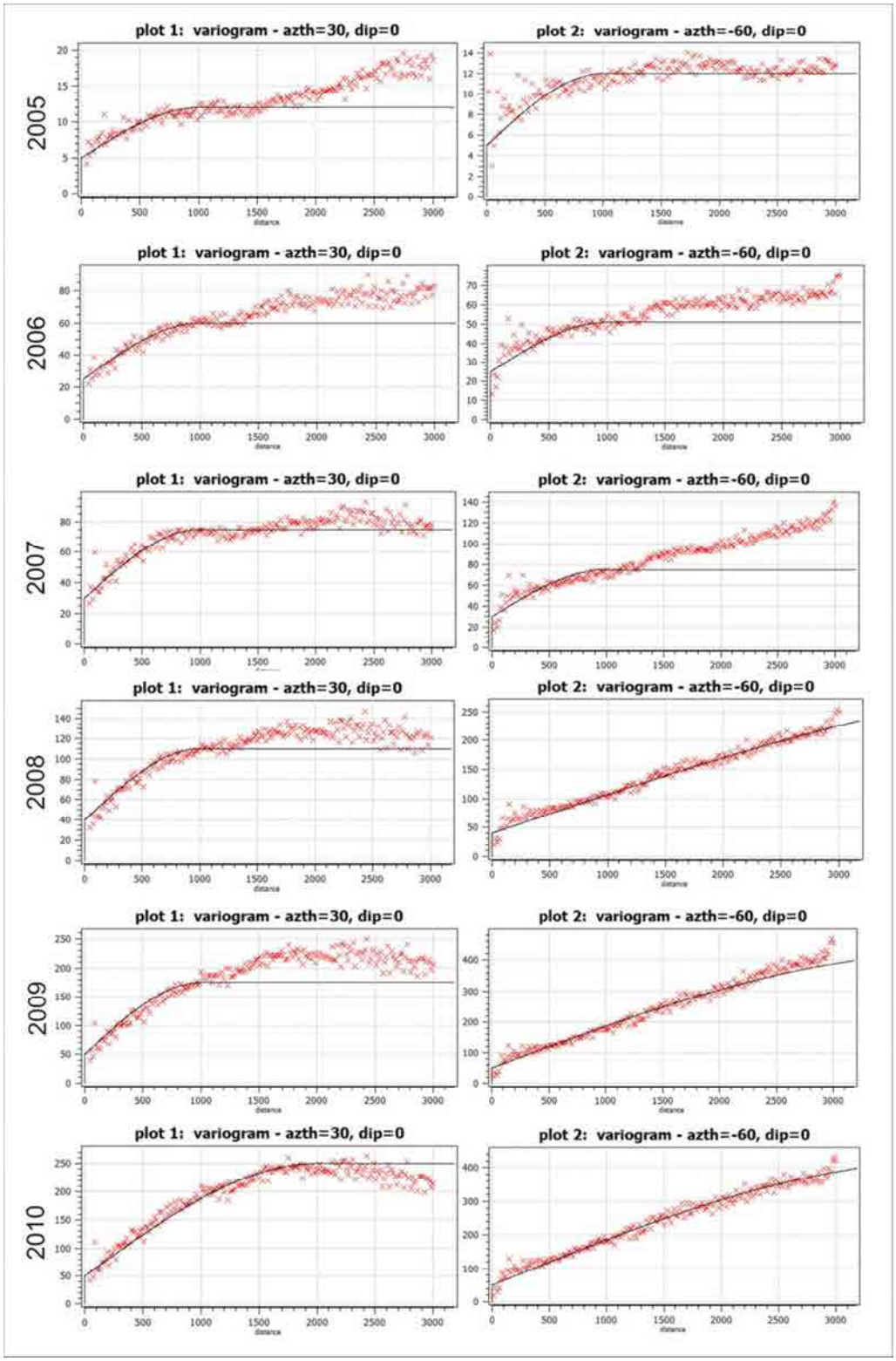

Figure 6.60: Bi-directional variograms (Azimuth: 30° and -60°); period 2005-2010.

Thus, according to the step 1 of Par. 6.4.1.3, radar data of the area of 6x6 Km^2 (Fig.6.20) have been interpolated (Fig. 6.61 a) through the *Ordinary Kriging method* (eq. 6.13) using the variogram models shown in Figs. 6.59 and 6.60 for the period 1997-2009.

The interpolation grid has a resolution of 60 m (correspondent to the resolution of CPT processing using a multilook 15x3). The Lower left corner (LLC) coordinates are (xLLC = 661891.5055 m, yLLC =4202718.82 m).

In a second step, radar errors (namely the difference between displacements measured by radar and computed by model in the 24 points) have been interpolated (Fig. 6.61 b).

As it is not possible to have a robust variogram with 24 points the same variograms models for the radar are used. This simplification is suggested by Verworn and Haberlandt (2011) that, as Haberlandt (2007), have shown that there were no significant differences in the interpolation performance.

Finally, the deep model deformation map has been obtained computing the differences of radar values minus radar error (Fig. 6.61 c).

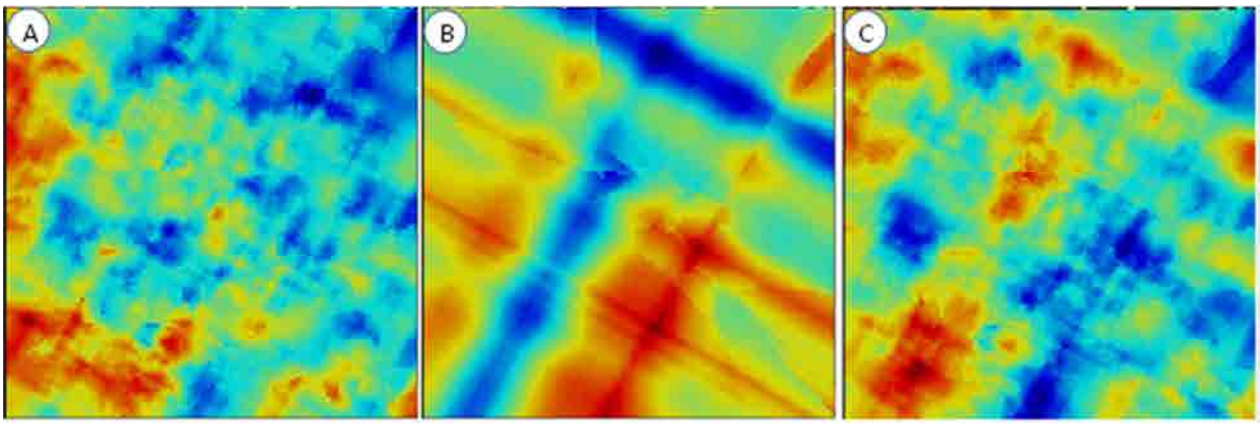

Figure 6.61: (A) Radar interpolation (OK), colour scale: red=4 mm and blue=-28 mm; (B) Radar error interpolation, colour scale: red=-2mm and blue=-32 mm; (C) Deep model interpolation (OKRE), colour scale: red=23 mm and blue=-15 mm.

Fig. 6.62 shows the deep model maps carried out through the OKRE method.

These maps have been used to obtain the linear-phase maps (Fig. 6.63) to introduce in the CPT processing, reported in Par. 6.5.

Here, also the linear-phase maps achieved through the IDW method have been reported (Fig. 6.63) in order to show the differences of the resulting maps achievable in relation to the different used estimator.

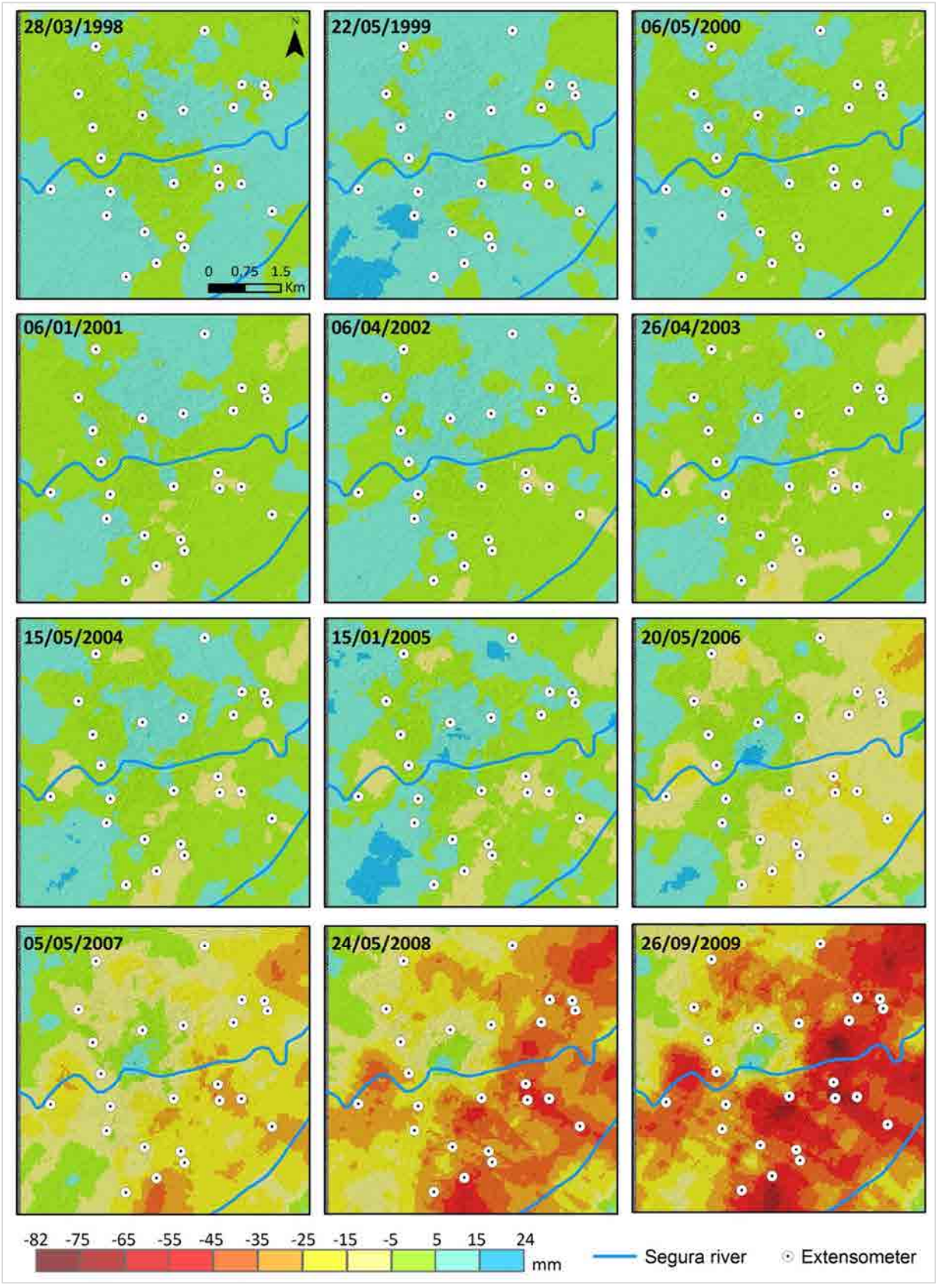

Figure 6.62: Deep model interpolated maps (OKRE)

6.5. CPT processing improving using the model computed deformation maps

As described in chapter IV (Par. 4.7), the CPT algorithm (Mora et al., 2003) includes a step to the evaluation of the linear and no-linear deformation components which compose $\Delta\varphi_{mov}$.

In particular, as explained in chapter IV, in order to estimate the linear part of the deformation from the phase information, the CPT algorithm has to apply a model adjustment to the data. After a pixel selection (based on the quality of the data correlation with the model), for the coherent selected pixels, the absolute linear velocity is evaluated through the interaction process represented in Fig. 4.18.

The statistical characteristics of each phase component depend on very different parameters (temporal or spatial baselines basically), which are separable through the linear phase analysis. For this reason, it is possible to use the phase modelling approach independently from the magnitude of each component.

If the linear displacement would be known, the algorithm would reach the convergence in the model adjustment with less variables. However, it does not mean that the model adjustment would be avoided because the evaluation of the topographic error is also a product of this step; in fact, the linear processing is necessary also even if no linear displacement component is present.

In Murcia case study, the validated geotechnical model results have been interpolated through IDW and OKRE technique, as shown in Par. 6.4 to obtain the displacements' maps (see Figs. 6.54 and 6.62).

The linear-phase is related to displacement rate as shown in the equation 4.19. Therefore, the linear-phase maps have been achieved for the period 1997-2009 (Fig. 6.63) and introduced in the CPT processing. In particular, Fig. 6.63 shows the comparison between some of the linear phase maps obtained through the IDW method and the OKRE one. It is evident that the used estimator could have a great influence on the generated maps and, for this reason, those obtained with the OKRE have been considered.

The spatial comparison of the achieved processing results has not changed respect to that shown in Fig. 6.19. The time series comparisons have shown some differences, due to the better estimation of the no-linear part of the deformation (Fig. 6.64). In particular, Fig. 6.64 shows the results achieved in the three different processing, described in paragraph 6.2.2.1.1, namely:

- ⟶ using all the images between 1995 and 2010 (yellow curve);
- ⟶ separating the processing considering the three periods 1995-05, 2005-10 and 2009-2013 where the linear velocity results to be very different (blue curve);
- ⟶ using the deformation maps achieved through the geotechnical model (red curve).

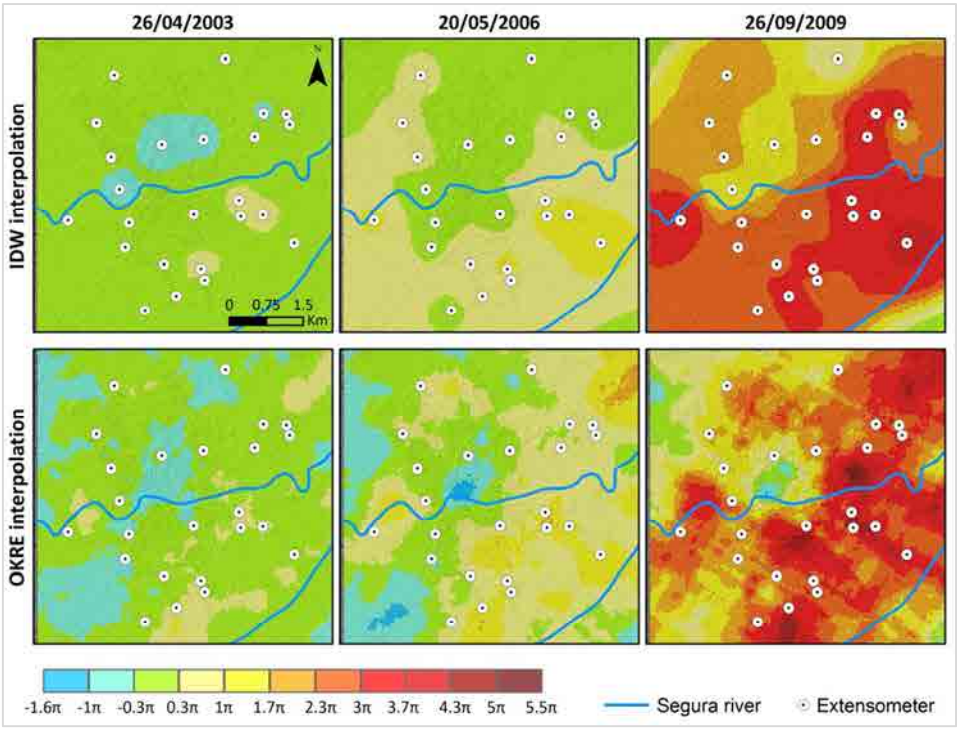

Figure 6.63: Linear phase maps obtained from the deep model interpolation (trough IDW and OKRE methods).

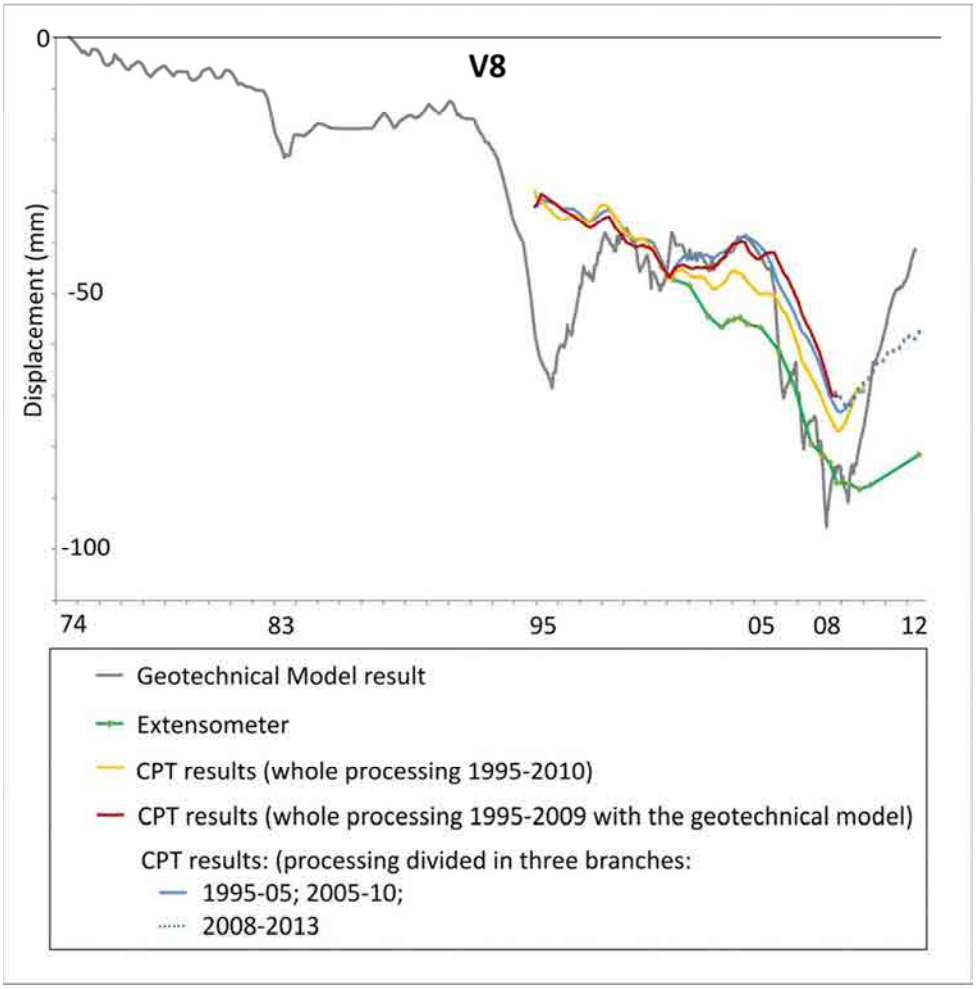

Figure 6.64. CPT results' comparisons.

According to figure 6.64, in the processing results obtained using all the available images for the period 1995-2010, the more stable period (2001-05) seems to be subsiding. This occurs because the algorithm extracts from the interferograms pairs an unique linear part of the phase $\Delta\varphi_{mov}$, which, between the 1995 and the 2010, does not well appreciate the change in the deformation trends.

In the case of a processing divided in two elaborations (blue curve), the two different behaviors are well interpreted and the processing results seem to well calculate also the non-linear part of the deformation.

In the third case, where the model 2D maps have been used, the results are characterized by a time series having a good correspondence with the blue curve.

So, the use of these models in the processing can allow to obtain a better estimation of the no-linear velocity; in particular, they can permit to obtain the same estimation of the no-linear part of the deformation achieved separating the processing in the different branches having similar linear velocities.

In the case of a phenomenon, characterized by "n" changes in the velocity trends, this method can avoid to separate the process in "*n"* different branches.

As explained in paragraph 6.2.2.1.1, this also avoids problems related to the different coherent pixels selected in the "*n"* processing; in fact, for each of the "n" processing, the same pixel will have a different mean coherence in relation to the coherence of the considered interferograms. This means, in other words, that the same pixel could be selected only in some of the "n" processing and this make difficult the results' analysis.

A further improvement of the 2D model, for example considering more modelled columns and tacking into account the plastic deformations occurred in the recuperation phase, could bring to an additional enhancement of the linear-phase maps and of the processing results.

6.6. Telese Terme case study: introduction

TeleseTerme plain is affected by subsidence and sinkholes phenomena due to the geological and hydrogeological settings.

The underground water circulation, in fact, provokes piping phenomena in the surficial fine-grained soils and, because of chemical characteristics and physical properties of the water, may also activate processes of accelerated travertine's corrosion.

In the study area (Fig, 6.65) no in situ monitoring networks are available and the Advanced DInSAR Interferometry techniques represent the only possibility to the natural hazard (in this case relative to subsidence and sinkholes phenomena) evaluations.

For this reason, a first analysis of the phenomenon (in terms of magnitude and location) has been achieved thanks to the available DInSAR data (Par. 6.6.2).

In particular a processing of the available SAR images between 2003 and 2010 acquired by ENVISAT satellite has been carried out through the Coherent Pixel Technique and the results have been compared with available PS SAR data (for the period 2002-2008).

The availability of the PS data has allowed, in addition to the validation of the CPT processing results, also some analysis of the structural response of a building, affected by severe structural fractures, to the displacement detected by SAR. To this kind of analysis, in fact, the SBAS techniques' results (corresponding to a pixel resolution of 60x60 m for the chosen multilook), turn out to be less effective than the PS ones, Herrera et al. (2012).

The knowledge of the deformation's evolution of the area has allowed to organize a more focused future monitoring through traditional techniques of relief (with the help of geophysical methodologies).

Since the zone affected by sinkhole phenomena is located in urbanized area, microgravity method was preferred to other geophysical methodologies. In fact, seismic, magnetic and electromagnetic techniques are strongly influenced by urban noise and this produces a low value of signal to noise ratio.

6.6.1. Study area settings

6.6.1.1.Geological and hydrogeological settings

Telese Terme is a small town located in the Benevento province.

The Telese Terme plain is characterized by a very complex stratigraphy (alternating levels of travertine, alluvial-marshy and pyroclastic deposits), that allows the occurrence of a groundwater circulation with overlapping aquifers (Celico, 1978, 1983, Corniello and de Riso 1986; Esposito et al., 2003). These aquifers are locally in pressure and, because of chemical characteristics and physical properties of the water, they may activate processes of accelerated travertine's corrosion; as a consequence, cavities or erosion processes can occur along the groundwater's preferential flow-paths, sometimes associated with piping phenomena.

Accordingly, the Telese valley is characterized by the presence of several sinkholes, created by different causal factors and located in the municipalities of Solopaca and Telese Terme. The latter hosts the largest network of collapse sinkholes of the entire Southern Apennine chain, as regards the summit area of a highly karstified carbonate relief (Montepugliano). Moreover, in the plain and in the vicinity of the western urban area, in 2002 and 2006 two sinkholes occurred, the first of which of large dimensions.

Differently from those occurred at Montepugliano, the recent sinkholes affected alluvial-marshy deposits (Fig. 6.65), Upper Pleistocene – Holocene in age, intercalated with discontinuous travertine layers; this succession was deposited in a palaeo-depression, whose overall depth is unknown, but certainly higher than 30 m from ground level. Sometimes, the available boreholes revealed the presence of an epiclastic component represented by a fine, well-sorted, prevailingly loose sand of pyroclastic origin, susceptible to liquefaction under dynamic loading. In addition to the piping phenomena involving the soils, travertines are prone to the formation of cavities, due to the accelerated corrosion caused by aggressive groundwater. The whole sequence, therefore, is under saturated conditions and is characterized by a pronounced lateral and vertical heteropy, where local hydraulic gradients and erosional processes concur to the formation of underground voids below the water table.

According to the recent *sinkhole project*, carried out by the Campania region, Telese Terme has been classified as "area of attention" because of the sinkhole hazard.

In addition to the cave collapse sinkholes located on the "Montepugliano" mountain, there are some other sinkholes in the plain classified as *"cover subsidence sinkholes"*. According to the studies of the sinkhole project, they were caused by the presence of the multilayer sulphurous groundwater that is very aggressive and locally in pressure.

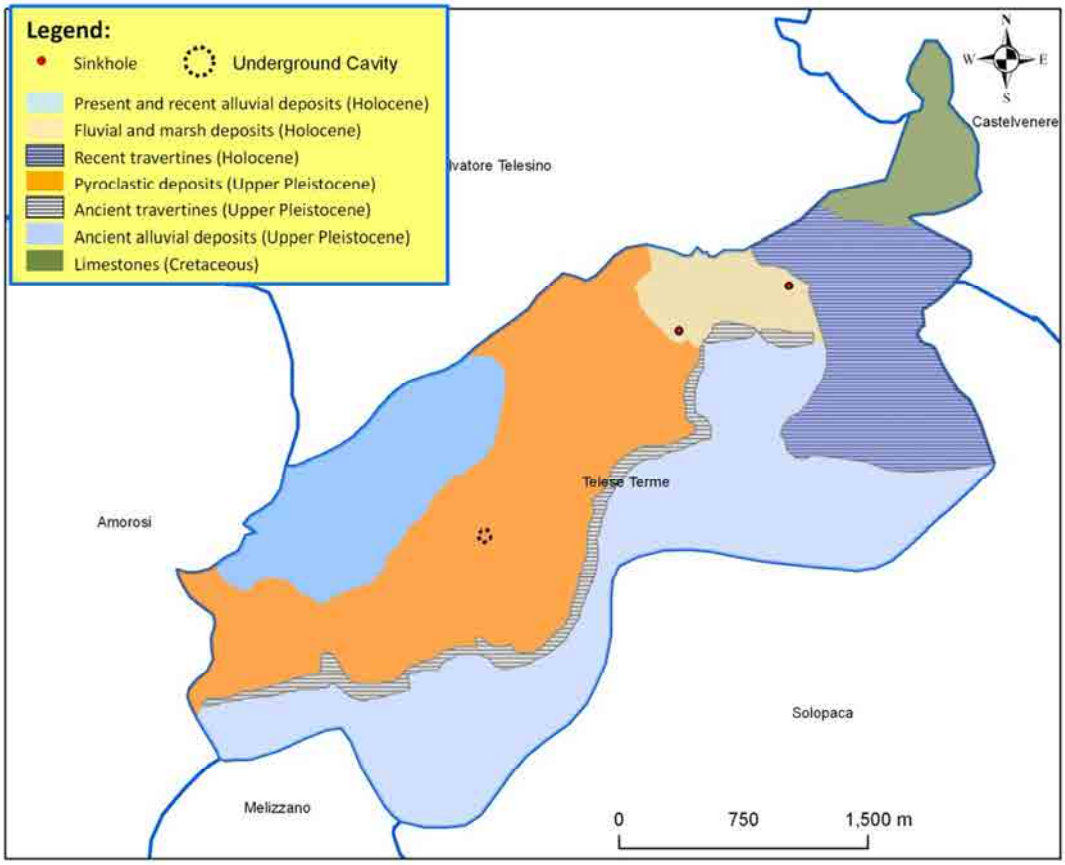

Figure 6.65: Geological Map of Telese Terme .

In particular, the study area includes two zones, where in 2002 and 2006 two cover subsidence sinkholes occurred (Figs. 6.65 and 6.66).

Figure 6.66: Sinkhole occurred in Telese Terme urban area in 2002

In the sinkhole project was stressed that *"in the case of areas affected by sinkholes occurred in incoherent soils, an accurate reconstruction of the geological and hydrogeological model of the subsurface is requested"*. For this reason an updated of the geological characterization has been requested by the institutions but is not still available.

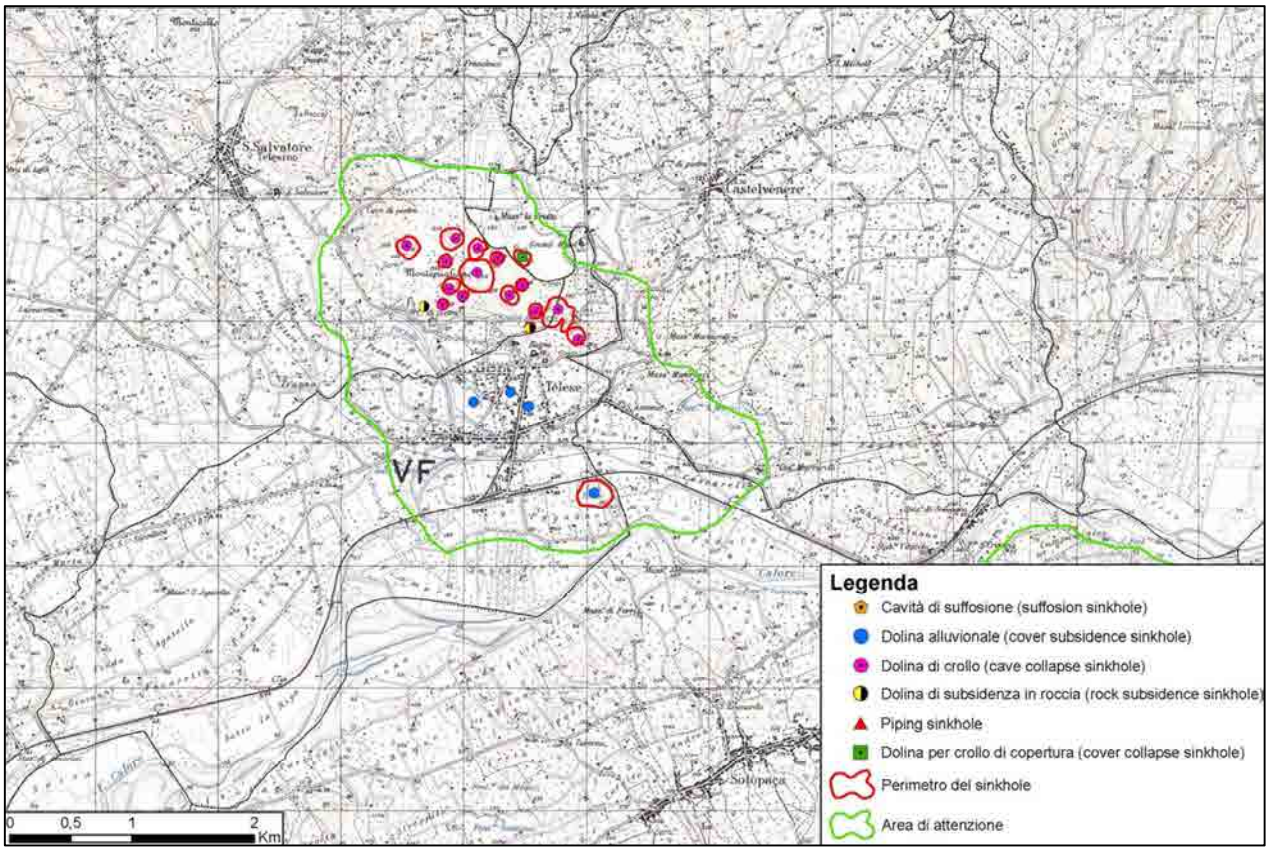

Figure 6.67: Sinkholes identified in the project carried out by the Campania region (extract from attachment 7 of the "sinkhole project" - in Italian).

After an initial analysis of the available technical documents and scientific papers, a geological database has been implemented. However, from the stratigraphic columns' analysis, a very complex context has been found in the study area, characterized by a great spatial variability of the underground soils.

A significant example is represented by the area where a sinkhole occurred in 2006 (Fig. 6.68); here, in three boreholes having a distance of about 5 m, a very different stratigraphies have been found (Fig. 6.68). The travertine's bedrock found in the borehole **S1** between a depth of 24.5 and 31 m, has not been found in the borehole **S2** where only cinerite is present between 2 and 31 m and in **S7** which includes a clay layer from 17 to 33 m deep.

These anisotropies influence the groundwater flow which can trail the fine-grain most permeable soils or provoke the travertine corrosion due to their chemical aggressive characteristics.

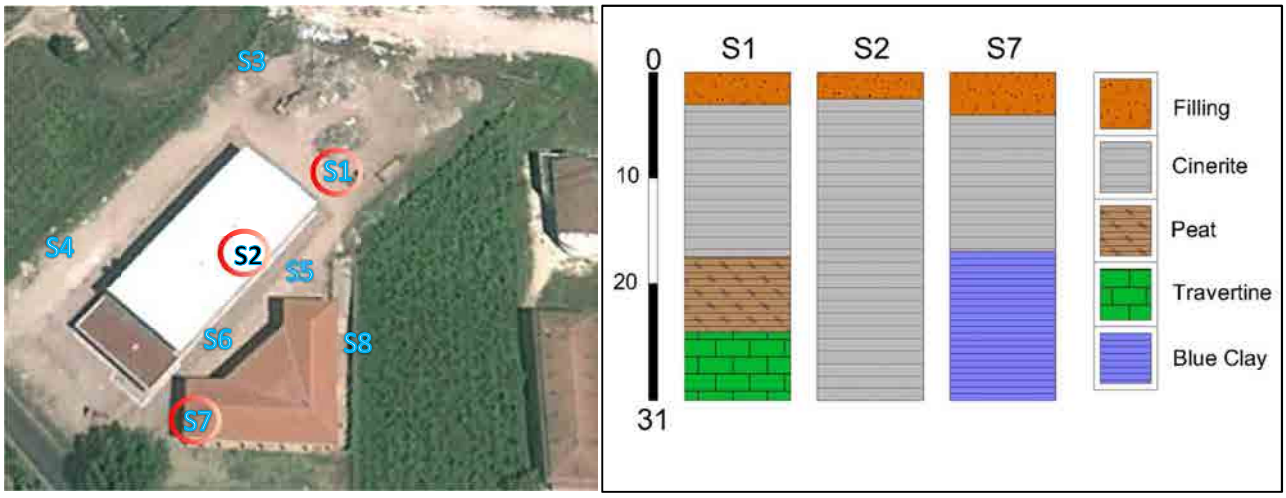

Figure 6.68: Stratigraphic columns in correspondence of the sinkhole occurred in 2006

In the study area, several faults have been detected. The most important is the "*Montepugliano-Monte Pizzuto*" fault which cross Telese Terme along the NW-SE direction generating a clear hydro-geochemical and thermic anomaly.

The hydrogeological settings present a succession of overlapping aquifers. Some piezometric measurements have been carried out in the study area, but they are referred to different aquifers in relation to the different wells' depth. The surficial wells in the urban area (up to 10 m) have been empty since the earthquake that occurred in 1980; before it, in most of them, the water reached the ground surface (less than 1 m to the ground).

6.6.2. A-DInSAR monitoring

The subsidence phenomenon which affects Telese Terme, has never been monitored through in situ techniques, except for some private studies which have not been accessible for consultation.

Therefore, A-DInSAR results, in the study area, represent the only possible way to analyse the phenomenon development, since 1992.

Thanks to a specific agreement with the Italian Ministry of Environment (MATTM), the ERS1-2 and ENVISAT images of the study area, for the periods 1992-2000 and 2002-2010, respectively, have been obtained. Accordingly, forty-seven images (track 358 – frame 819), acquired over ascending orbits of the ENVISAT satellite systems, and covering the time interval from January 2003 until July 2010, have been processed through the CPT technique (Fig. 6.69). Sixty-five interferograms characterized by a maximum perpendicular

baseline of 250 m and temporal baseline varied between 35 and 210 days have been used.

The achieved results have been validated through the comparison with PS available data (Fig. 6.69), processed In the framework of the project *"Piano Straordinario di Telerilevamento Ambientale"* (PST-A).

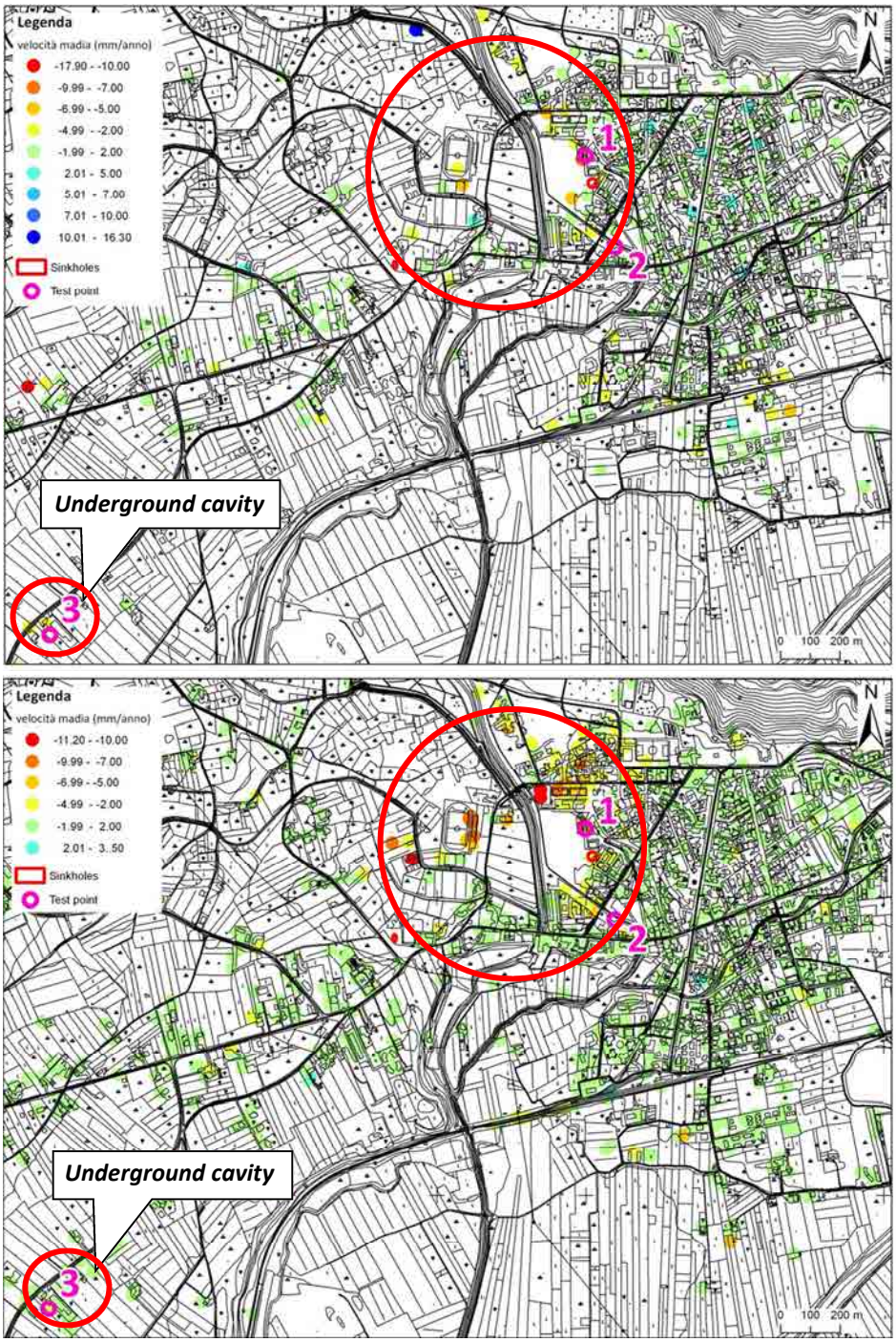

Figure 6.69: CPT processing results (above); PS DInSAR data (below)

Figure 6.69 shows three test points located in the study area which have been analysed in the following.

In particular:

⟶ two critical buildings (test points 1 and 2), which present different structural problems related to their different foundations;

⟶ an underground cavity (test point 3) which has been discovered in the area and where both the DInSAR results have detected a localized subsidence phenomena.

6.6.2.1. Results analysis

Figure 6.70 shows an interpolation of the available SAR data carried out through the IDW method.

The spatial points density achieved with both the techniques does not allow to obtain an interpolation reliable in the whole area, but only in the urban area.

Here, the performed spatial analysis (Fig. 6.70), shows that the subsidence phenomenon (detected by both CPT's and PS's results) corresponds to the fluvial and marshy deposits (Fig. 6.65).

Figure 6.70: IDW interpolation of PS DInSAR data

The line of demarcation between the city centre and the subsiding area corresponds to a strong change in the underground soils stratigraphy; specifically, the urban area is based upon an uniform travertine bedrock whose presence is variable in the left peripheral subsiding area.

This part of the city, in fact, was a marsh and recently has been reclaimed for urban expansion.

Here, a forensic analysis carried out by Calcaterra et al., 2009 is available.

According to this study, most of the buildings which are affected by structural fractures (filled in red in Fig. 6.71) are located where a deformation gradient has been found through DInSAR data. This can indicate the occurrence of differential settlements or distortions (Cascini et al., 2006, 2013, Tomàs et al., 2012).

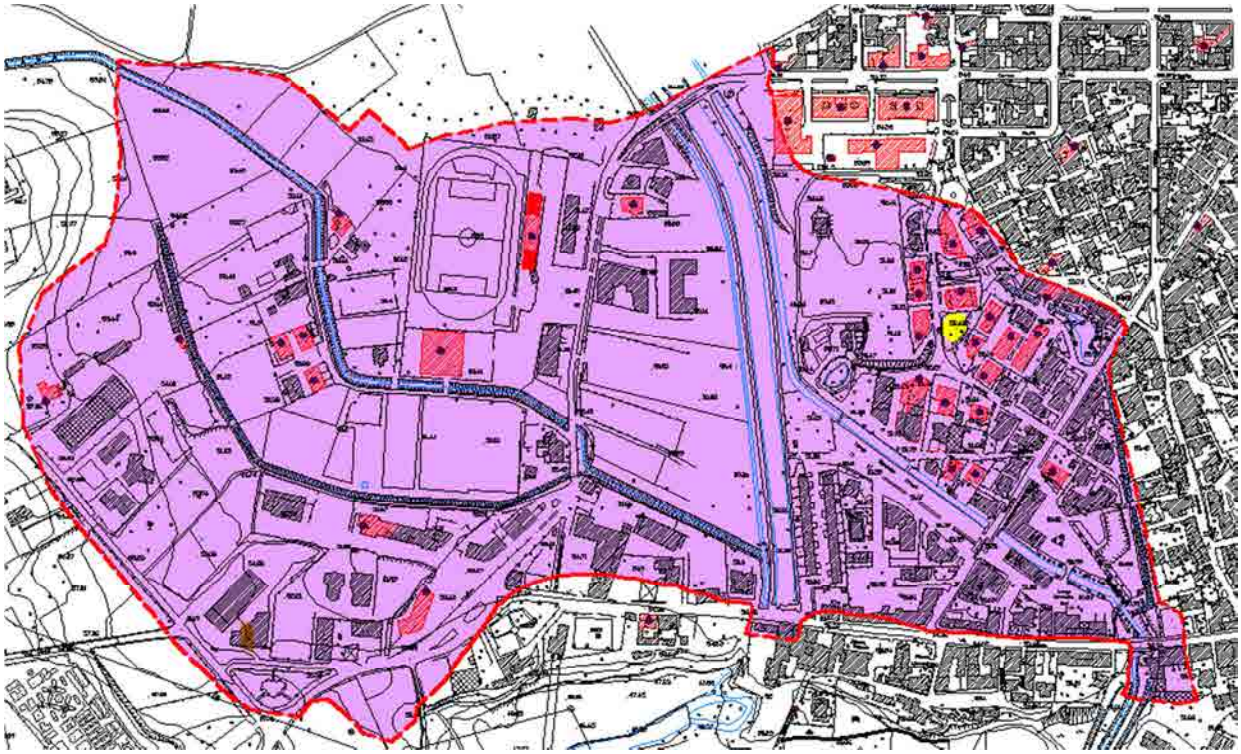

Figure 6.71: Forensic analysis extracted from Calcaterra et al., (2009)

For a detailed analysis of the reliability of this evidence, some test points have been taken into consideration (Fig. 6.69) and presented in the following paragraph.

6.6.3. Structural analysis

In a first part of the analysis, a multi-pass DInSAR algorithm to control the evolution of the structural damage of buildings, located in a subsiding urbanized area, has been tested.

In particular, the maximum differential settlement and the maximum angular distortion for the two considered buildings, have been calculated. To this aim, the methodology based on *Conditional Gaussian Simulation* (CGS) proposed in Sanabria et al. (under review) to calculate multiple equi-probable realizations of subsidence has been followed.

According to this method, through the interpolation of the total displacements cumulated along the observation period, is possible to verify if the obtained maximum differential settlement and maximum angular distortion exceed the serviceability limit states (Fig. 6.72).

This could allow to mitigate the risk in an area where a monitoring system does not exist using the remote sensing technique as a complementary tool for the forensic analysis of structures.

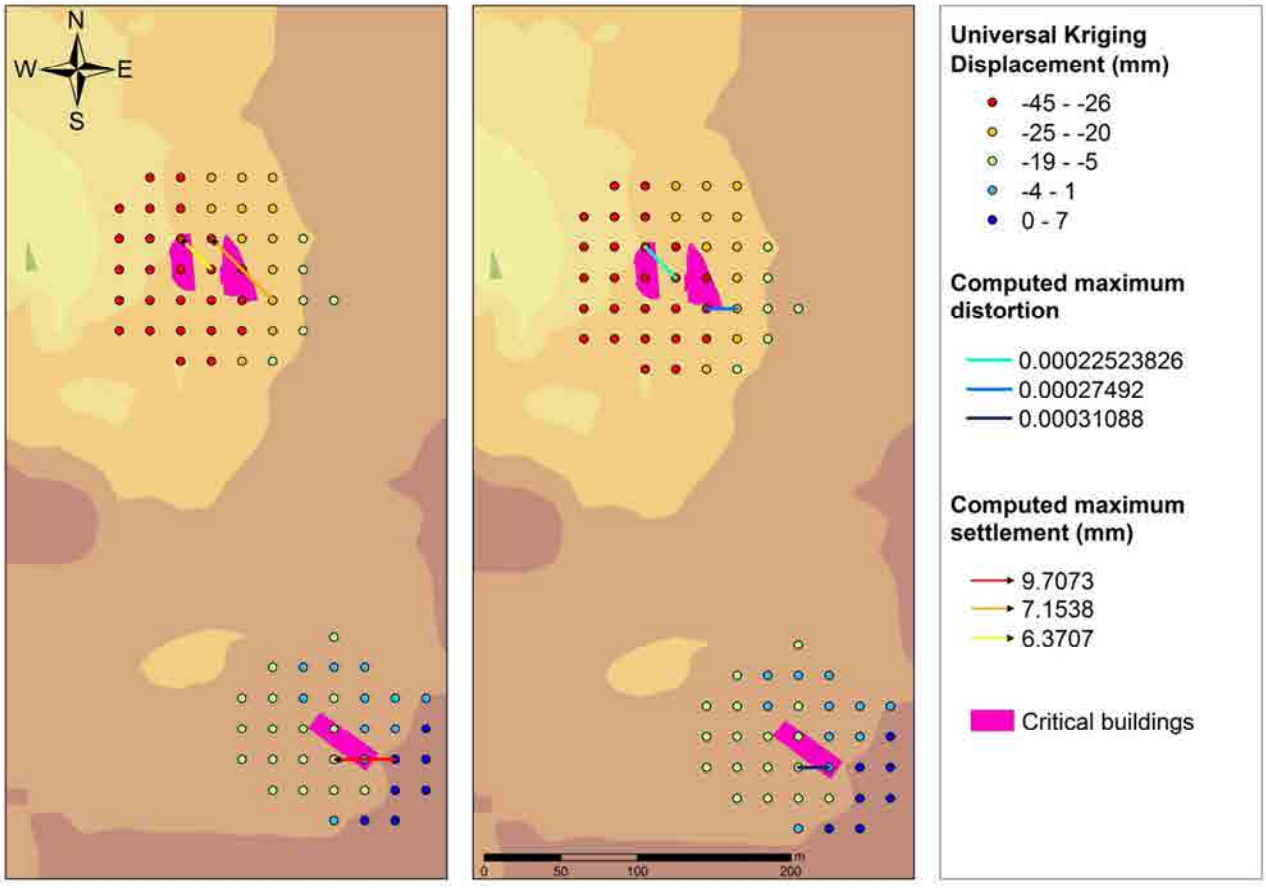

Figure 6.72: Maximum differential settlement and maximum angular distortion computed for the two considered buildings.

The available PS data have been interpolated through the Universal Kriging algorithm. The kriging interpolated values have been extracted (Fig. 6.72) using a grid with cells of 20x20 m (function of the ENVISAT images' resolution).

The obtained results are compatible with the field evidences. In particular the building in the upper part of figure 6.72 (test point 1 in figure 5.69), having pile foundations, is subject to a rotation of the whole structure in the direction of the maximum distortion shown in figure 6.72. In this case, the building is not affected by damages.

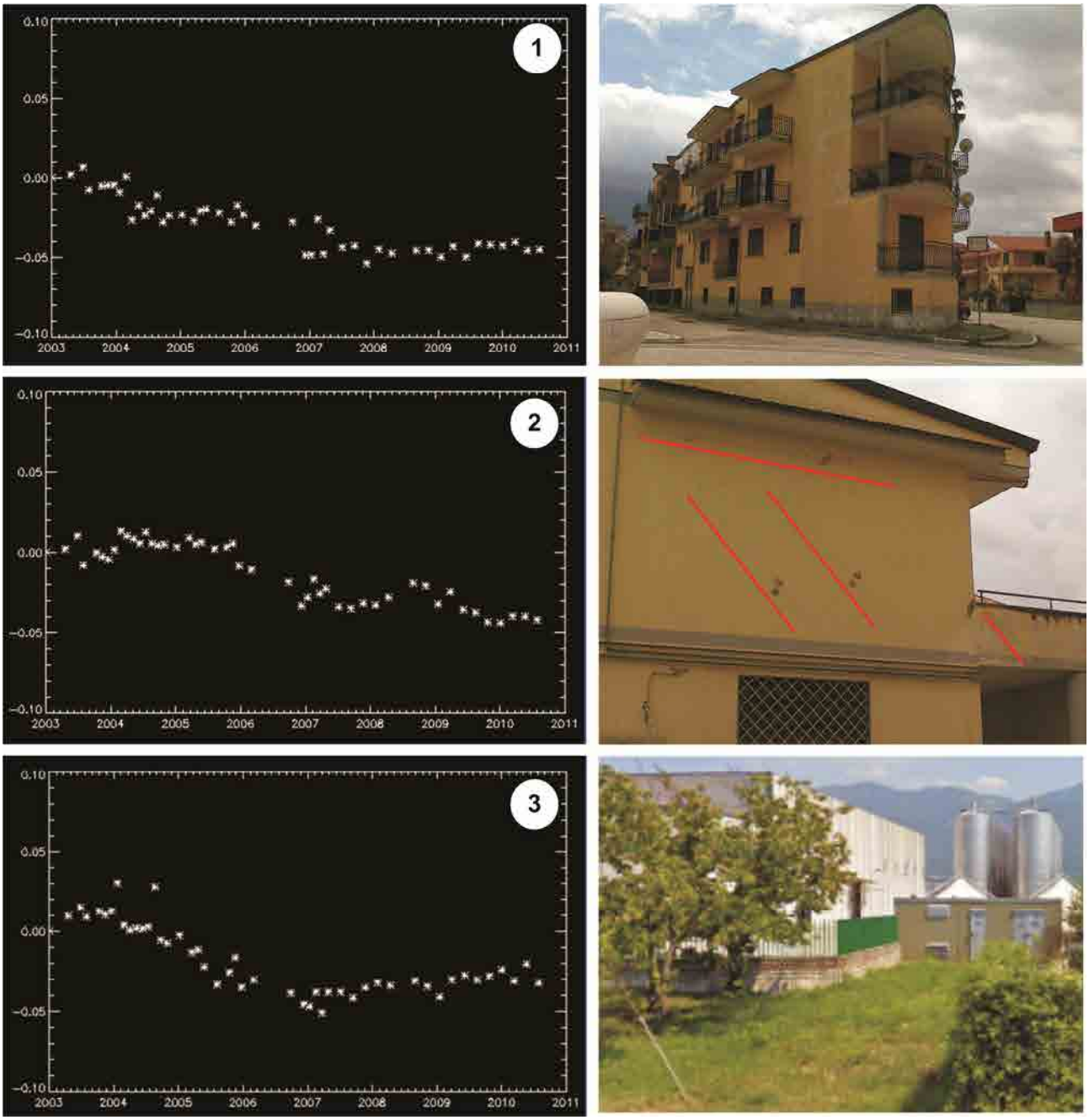

Figure 6.73: Some examples of buildings affected by structural problems: Displacements (m) detected by SAR (on the left)

The second test point (corresponding to the building in the lowest part of figure 6.72) has shown important structural fractures and has been partially evacuated.

In this case, using the differential settlements and the maximum distortion values achieved from PS SAR data, its structural response has been obtained and compared with the limit states.

The main uncertainty related to the obtained results, regards the availability only of SAR images acquired by C-band sensors. In this case, in particular, the use of PS SAR data has been preferred to the CPT results due to the achievable pixel resolution. In fact, the pixel resolution obtained through the CPT technique, for the used multilook (15x3), is equal to 60x60 m. Nevertheless, the PS technique, differently from the SBAS techniques, works at full resolution.

In this case, CPT results, , have turned out to be useful to the spatial analysis of the phenomenon, but not to the punctual comparisons and analysis showed in the paragraph 6.6.3.1.

6.6.3.1. Structural model

In this section, the forensic and structural analysis for the building n°2 in figure 6.69, has been presented.

The structure was built in 2002 and, since its edification, has manifested problems related with the subsidence phenomenon.

In this case, in particular, the structural problems are related to two factors:

- → a geological component, due to the incoherent high permeability soils and to the underground water flow which causes piping phenomena;
- → a structural component, due to the inadequate project and structural dimensioning.

The structure presents cracks distributed in all the rooms and floors. In particular, the most extended are located in the double-longitudinal end of the building (Fig. 6.74).

The central part of the structure is still inhabited and here, the cracks are less diffused and extended.

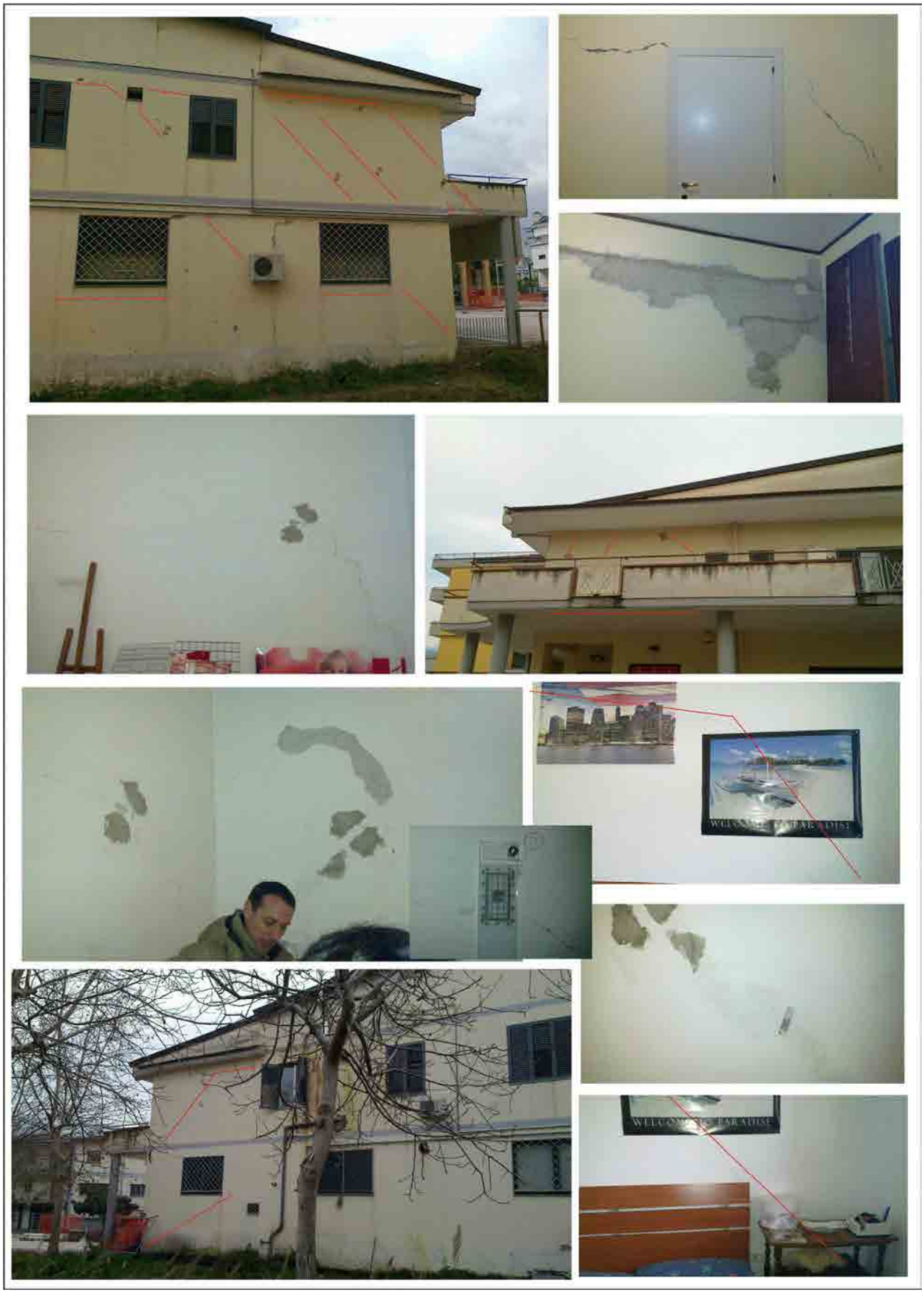

Figure 6.74: Forensic analysis of the building n°2

The structure is constituted by frames with orthogonal reinforced concrete beam and pillars.

In order to calculate the stress acting on the structure, a three-dimensional model of the building through the software SAP2000 v.14 has been performed.

Using the available technical reports and project plans, it has been possible to define the dimensional and mechanical characteristics of beam and pillars which constitutes the structure.

Figure 6.75 shows the project plan and prospective drawings.

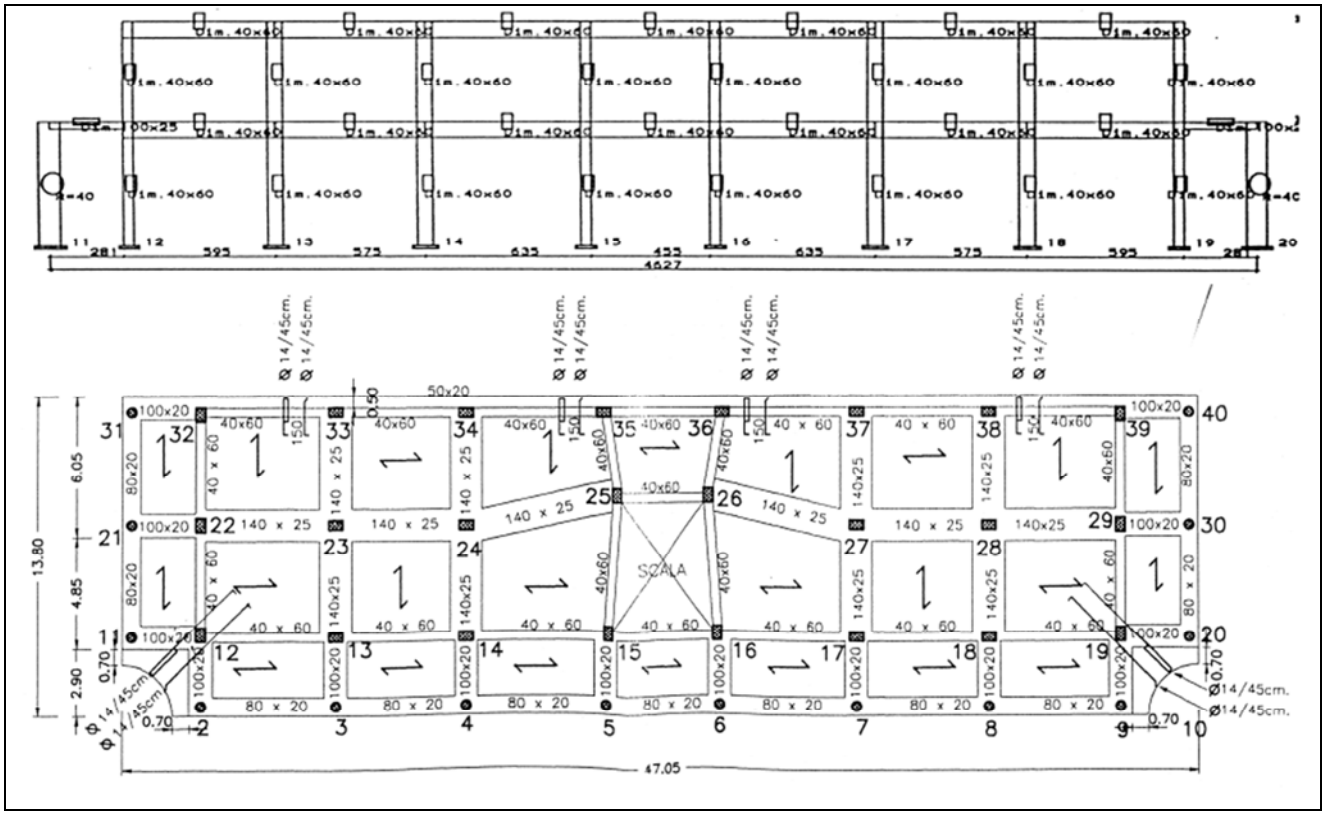

Figure 6.75: Prospective drawing (above); plan of the first floor (below)

The concrete used in the building is the *"Rck 250"* (specific weight Υ=2500 Kg/m^3) having the maximum permissible normal and tangential strain respectively equal to σ_{max}= 85 Kg/cm^2; τ_{max}=16.86 Kg/cm^2 and τ_{min}=5.33 Kg/cm^2. The normal and tangential elastic modulus are respectively 284605 Kg/cm^2 and 123741 Kg/cm^2.

Figure 6.76 shows the structural scheme of the building, including 4 frames in the *x*-direction and 10 in the *y*-direction. Beams and pillars have been modelled as “BEAM” elements. The interaction between the structure and the ground has been modelled using constraints; in particular the pillar bases have been blocked. In the technical relation, the plankeds result to be “collaborating surfaces of 4 cm” and, for this reason, it has been possible to characterize them with an infinite stiffness along their plain surface. In order to do that, to each node of the structure a DIAPHRAM constraint has been assigned.

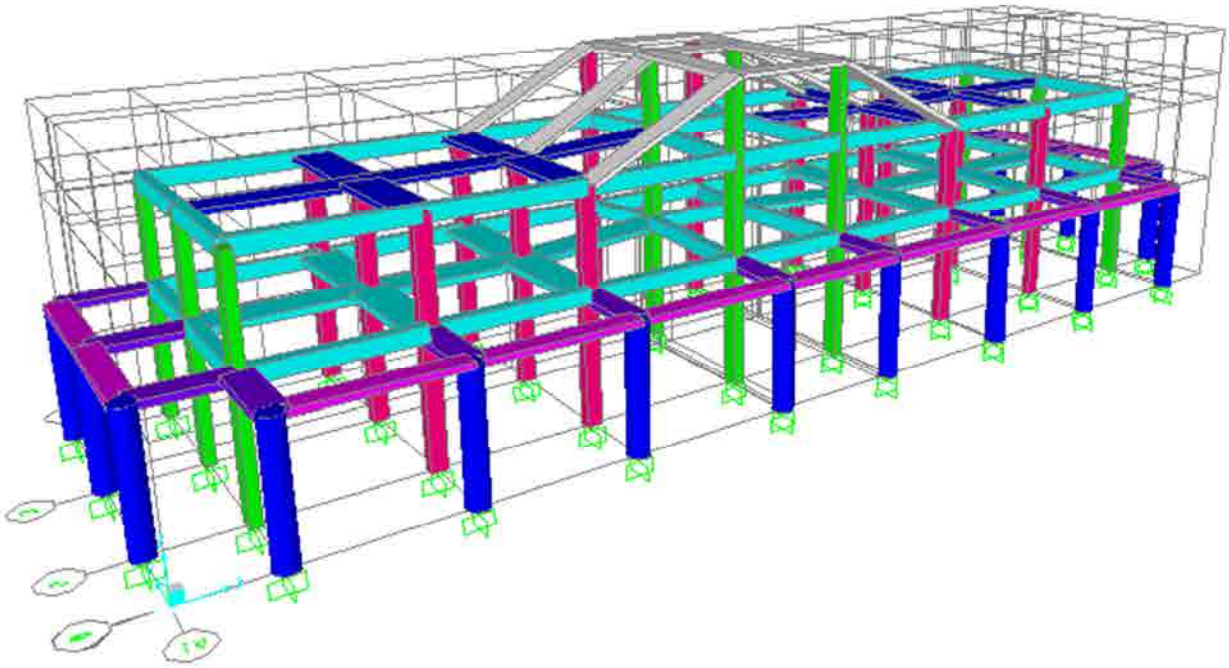

Figure 6.76: Geometric models of the building

After the implementation of the geometric model of the building (Fig. 6.76), the loading conditions have been introduced. In particular, in addition to the loads due to the structure elements weight, the differential settlements measured through PSI-DInSAR techniques have been considered.

Specifically, the differential settlements have been achieved form the PS’s displacements time series, referred to the period 2002-2010.

The software gives as output, for each “beam” element, the normal and tangential stress, shear and moment diagrams (Fig. 6.77).

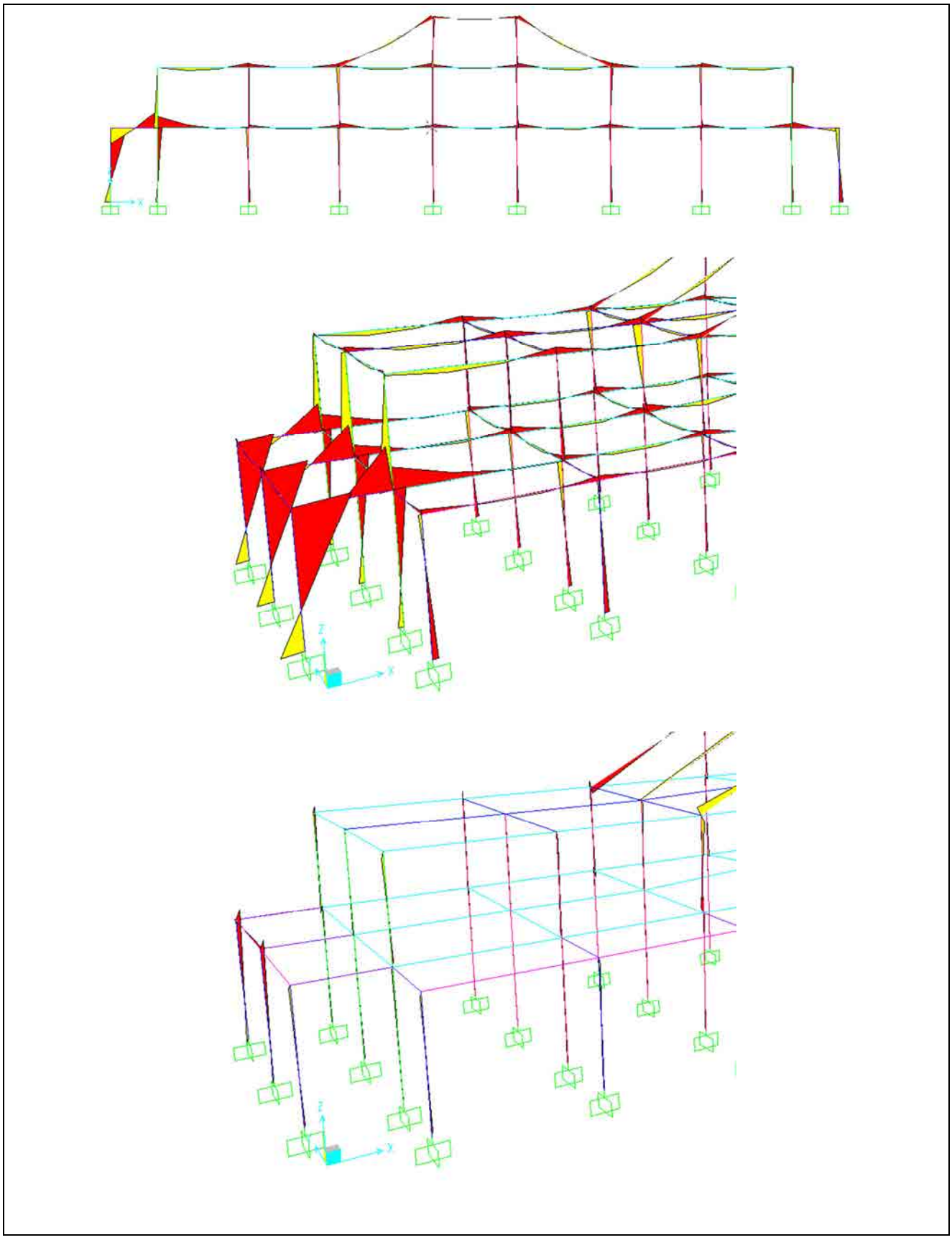

Figure 6.77: Computed momentum diagrams

The obtained strains have been compared with the limit states through the software EC2 (implemented by the Professor Aurelio Ghersi, University of Catania); the elements for which the limit states results to be overpassed, have been highlight in figure 6.78.

In particular, the beam and pillar of the extreme frames result to overpass the limit states; this is in according to the forensic analysis reported in the previous.

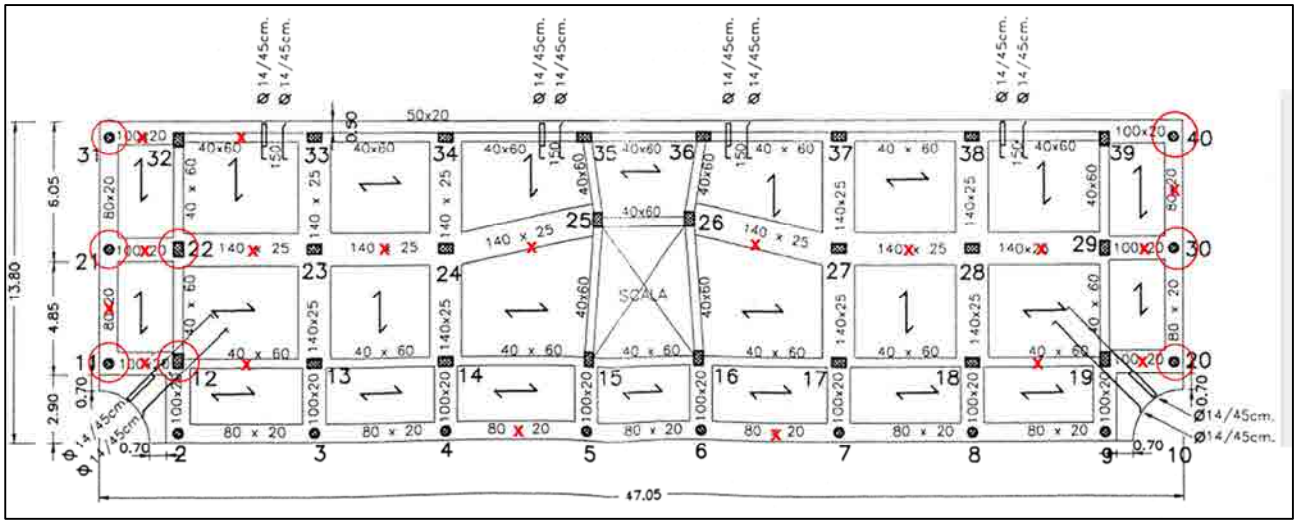

Figure 6.78: structural analysis results

6.6.4. Geophysical surveys

In the third test point, a localized subsidence, detected by SAR data, corresponds to an underground cavity, individuated through geological surveys.

In Telese Terme area, these cavities can be generated both in the cover due to piping phenomena, than in the travertine bedrock, caused by its corrosion due to the underground sulphurous water.

In the study area, several geophysical surveys have been carried out during the years, in order to analyse the possible occurrence of sinkhole phenomena and their causes. The gravity exploration, based on the identification of anomalies in the Earth's gravity field by measuring the gravity acceleration, allows to define any inhomogeneity generated by sources at different densities in the subsurface structure, such as underground voids.

In particular, in September 2006, after the last cover collapse sinkhole occurred in the plain, some geo-electrical investigations were carried out.

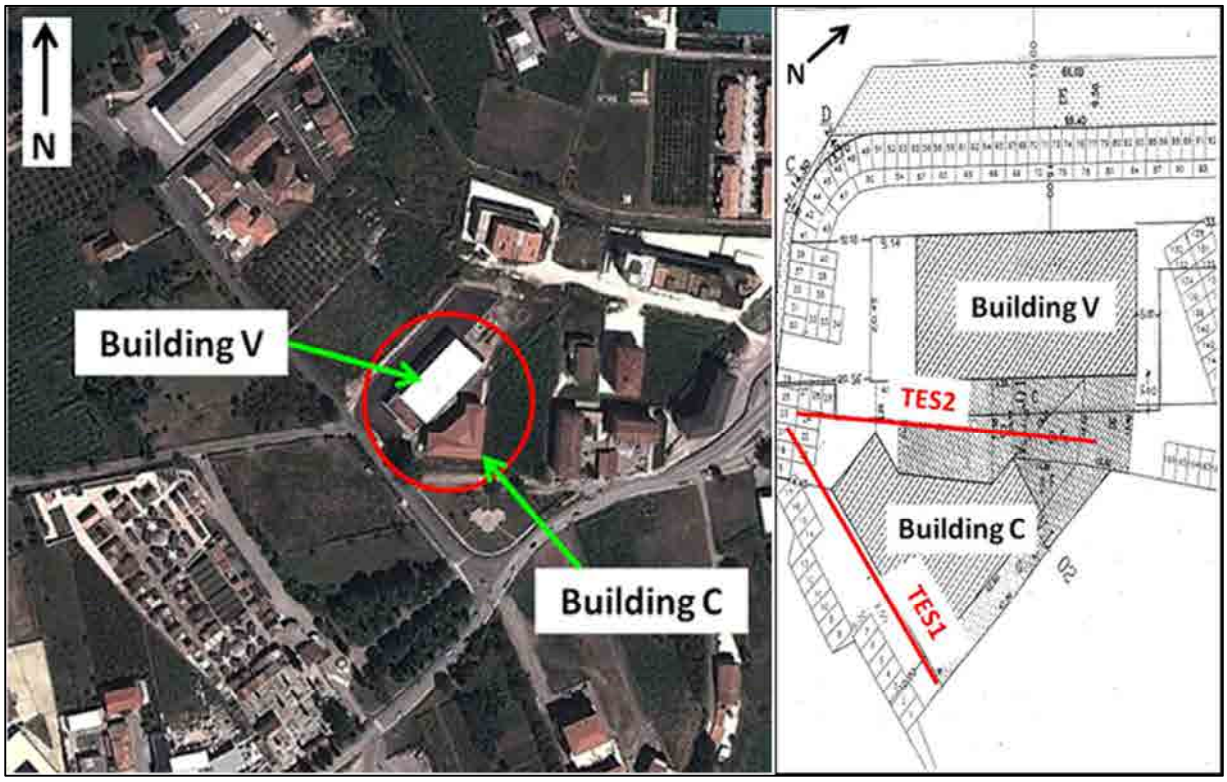

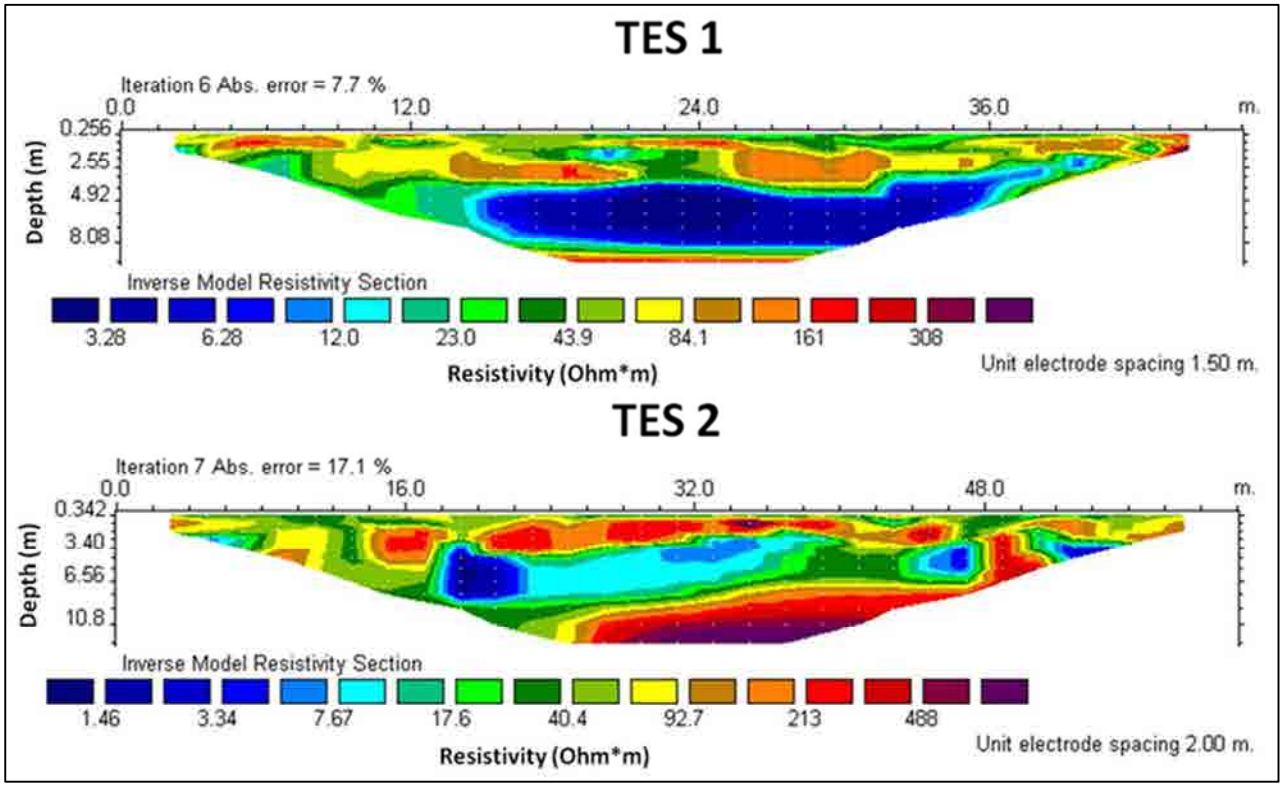

Figure 6.79: Location of geo-electrical profiles of the area affected by a sinkhole in 2006; geoelectrical tomographies TES1 and TES2.

The geophysical explorations were solicited to determine the presence of other unknown underground cavities near the buildings C and V (Fig. 6.79); see also the stratigraphic columns shown in Fig. 6.68.

Based on geological information, geophysical models of the known cavities were made.

Establishing the physical and geometrical characteristics of the voids, it was possible compute the amplitudes and wavelengths of the expected geophysical signal, in order to establish the procedures of the executive acquisition phase.

Data were collected with a multi-electrode georesistivimeter, (model A3000-E, M.A.E. Ltd). Fig. 6.79 shows the results of two geoelectrical tomographies: TES1 and TES2.

TES 1 is located in correspondence of the known collapsed void. The models of underground resistivity distribution were computed by RES2DINV software. In both the tomography in figure 6.79, the stratigraphy is plane-parallel. The shallow layer has a thickness of about 3 m and resistivity values ranging between 15 Ohms*m and 200 Ohm*m. The central layer has a thickness of 5 m and it is very conductive. The deepest layer is characterized by high resistivity values greater than 300 Ohm*m.

Taking into account the profile TES1, in the first layer, it is possible to note a discontinuity characterized by low resistivity values; this discontinuity is located between 16 m and 25 m along the profile and it represents the collapsed cavity. The central very conductive layer could represent the void filled with water and much more extended in depth than on the topographic surface.

Furthermore, **TES 2** profile, shows, in the upper layer, two small areas of discontinuity characterized by low resistivity values. These areas are located along the profile between 18-20 m and between 46-48 m; they may be zones of preferential drainage of surface water. Also in this case, the central layer is very conductive and it could represent the void filled with water.

Another geophysical campaign has been provided for in order to investigate the area around the test point 3 introduced in paragraph 6.6.2.1 (Figs. 6.69 and 6.73c) and to analyse the possible evolution of the underground cavity.

In particular, microgravity method was preferred to other geophysical methodologies. In fact, seismic, magnetic and electromagnetic techniques are strongly influenced by urban noise and this produces a low value of signal to noise ratio.

To a detailed description of the used technique, is possible to consult Castiello G. (2010).

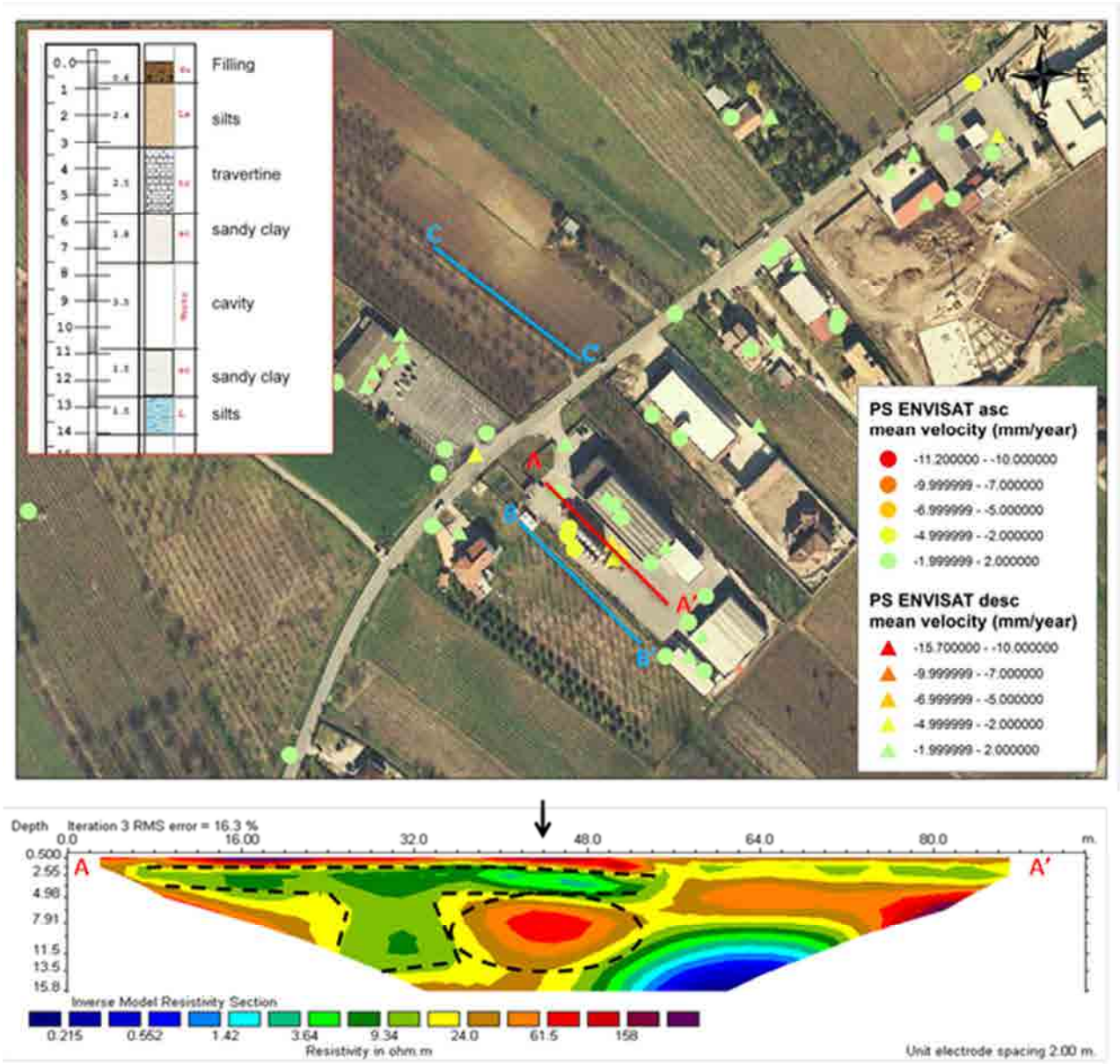

Figure 6.80: Geo-electrical profiles RES_2 acquired using the configuration Wenner-Schlumberger.

Figure 6.80 shows two principal anomalies (represented with dotted lines); the black arrow in the figure indicates the ubication of the reported stratigraphic column.

The green anomaly is characterized by low resistivity values, while the red one corresponds to higher resistivity values and has been found at the void depth.

However, the resistivity measurements have still to be interpreted because of the great humidity of the underground soils in the period when they have been carried out.

Probably, the high resistivity values are not due to the presence of water in the underground cavity and it could mean that it is not expanding.

The only available piezometric boreholes in this area, intercept the deep aquifer and the information of the surficial overlapped one is not available. In correspondence of the arrow, the water level, measured in 2012, resulted at a depth of 27 m respect to the ground surface.

In the event that the underground cavity is not expanding, the subsidence localized phenomenon could be due to the consolidation of the surficial soils (filling and silt) under the loading of the wine silos.

The displacement time series detected by SAR (Fig. 6.73), show the maximum subsidence a the no-rainy period 2006-2008 with a little recuperation in the following period. It could confirm the hypothesis that the subsidence cause is not related to the presence of the cavity.

6.6.5. Discussion

In Telese Terme case study, the deficiency of data, both geological and hydrogeological does not allow a complete employment of DInSAR data.

In fact:

- No in situ data are available to their validation,
- Too few data are available to discretize the millimetre displacements detected, as shown in the case of the underground cavity; here, in particular, the subsidence phenomenon detected by SAR can be due to the development of the cavity or, more reliably, to a consolidation process.

At the same time, the displacements detected by SAR, have resulted an useful tool to understand the causes-effect mechanisms which bring to the structural fractures of the building insisting in the study area. In this case, they could represents the only monitoring system to use to the subsidence risk mitigation.

CHAPTER VII

Conclusions

CHAPTER VII. Conclusions

Natural hazards are the result of naturally occurring processes that have operated throughout Earth's history. The potential to be harmed by natural hazard represents the "*vulnerability to natural hazards*". The main natural hazards are landslides, subsidence, earthquakes, volcanic eruptions, tsunami, and floods. They can cause loss of life or property and their relationship with humans represents the risk.

Risk is a statement of probability that an event will cause a certain amount of damage. The minimization of risk is called *hazard mitigation*. The natural hazard prediction or monitoring can reduce the related risk (and the vulnerability) (Thuro et al., 2009). In some cases, humans can influence natural disasters or directly generate them. In any case, knowing their development and cause-effect mechanism is possible to plan some measures to reduce their effects.

The technological progress has provided new techniques to the Earth monitoring, among which remote sensing occupies a prominent position.

In particular, *Remote Sensing DInSAR techniques* have demonstrated to be powerful investigation tools for their high spatial and multi-temporal coverage, fast data acquisition, and overall low costs (Tomàs et al., 2013). Thanks to the recent development of the sensor technology, it has been employed as a monitoring system for various instability phenomena, such as volcanic eruptions, earthquakes, landslides, subsidence, sinkholes, and it has been proficiently used for the related risk assessment. Risk assessment aids decision makers and scientists to compare and evaluate potential hazards, set priorities on what kinds of mitigation are possible and on where to focus resources and further studies. A remote sensing monitoring system, as demonstrated also in the present thesis project, allows the integration of conventional techniques, if available, and the knowledge of unmonitored phenomena also in the past. The so obtained information about the historical development of a phenomenon, permit to understand its cause-effect mechanism or to correlate the measured deformations with other monitored variables, if directly correlated with the phenomena occurrence. The use of these techniques yields to a monitoring of wide areas characterized by a millimeter accuracy and it results to be particularly effective if these areas show deformations with a predominant vertical component, as in the case of subsidence and sinkholes.

The aim of the present work, in particular, has been to test the applicability of the innovative Advanced DInSAR techniques in the natural risk mitigation related to subsidence phenomena. Specifically, this study has been devoted to verify the suitability of DInSAR techniques as complementary tools for subsidence monitoring by comparing the interferometric results with conventional ground-based data (as shown also in Herrera et al., 2008, 2009; Tomàs et al., 2010, 2011). After the test of this methodology in an area where

in situ data are available, it has been possible to consider admissible the use of this approach in another area, affected by similar phenomena, where a monitoring network does not exists.

For this reason, two test sites have been chosen, both located within alluvial plains and affected by subsidence phenomena: Telese Terme where no monitoring network has been installed in spite of the great amount of damaged buildings located in the urban area; Murcia where subsidence has caused damage to structures and infrastructures with an estimated cost of more than 50 million euros. In this second case, institutions have required studies since '90s. For this reason, 20 years of monitoring data are available which have allowed the implementation of an integrated monitoring system based upon satellite DInSAR, conventional field techniques and geotechnical data.

In particular, in Murcia city, the correlation of the temporal evolution of ground surface displacement measures (radar and in situ) and the piezometric groundwater level variation have been analysed to determine mechanisms and critical states of failure; this has permitted to implement a finite element model (FEM) of the phenomenon. Therefore, two models have been carried out: one up to the end of the gravel layer (called *"deep model"*) and one up to the extensometers' base (called *"shallow model"*). The results of the model implemented up to the base of the surficial gravel layer (where the water pumping takes place) have been compared with DInSAR displacements time series. In fact the displacements estimated through these techniques represent the whole deformation of the stratigraphic column. These comparisons have allowed the individuation of local anomalies of the stiffness values, and have permitted a better model calibration.

Moreover, the shallow model results have been compared with the extensometer measurements which represent the so called "*ground truth*". However, the comparison between the displacements calculated through the achieved model up to the extensometers depth and their time series has showed the occurrence of vertical anisotropies of the permeability. This hypothesis has been verified, analysing the available Lefranc's tests and the most detailed stratigraphic columns. Thus, a new model has been proposed achieving an absolute error of 4.8±3.8 mm in its comparisons with in situ data, for the common period between 2001-2012. The proposed numerical model will allow the prediction of possible future deformations and the consequences of any piezometric level variation in the study area. This is necessary to better plan the subsequent water resources exploitation and the land use management.

As to the Telese Terme case study, radar measured displacements have allowed to understand the spatial extension of the phenomenon, its magnitude as same as its historical development. In fact, a remote sensing monitoring system allows the knowledge of unmonitored phenomena also in the past. This has permitted the individuation of the causes which provoked damage for some *"test buildings"*.

For one of them, a structural model has been implemented; in this case, radar data have been used to verify whether its structural response to the displacements detected by SAR corresponds to the overpassing of the limit states. The model results have been compared with the forensic analysis achieved in situ.

For the two considered test sites, DInSAR data, achieved by means of two different techniques (SBAS and PS techniques) have been available. The choice of the best algorithm to use depends on the phenomenon to study. In fact, these methods can be used to deal with different problems, in function of their characteristics and spatial extension. In particular, the pixel selection methods based on amplitude criteria work at *"full resolution*", (namely, it allows keeping the original resolution of the SAR image), while coherence-based methods work at lower ground resolution depending on the multilook set. This means that the pixel selection involves an averaging of adjacent pixels of the original image with the consequent degradation in spatial resolution (Tomàs et al., 2013).

As referred by Herrera et al. (2012), in fact, DInSAR applications for built areas and infrastructures require very high resolutions to obtain information on individual buildings rather than an averaged subsidence rate for an area including several constructions. At the same time, if the subsidence phenomenon to observe is localized in an area of few kilometres, the coherence-based methods bring to an appropriate compromise between resolution and electromagnetic response stability. These techniques are, in fact, more effective in the study of spatially restricted subsidence phenomena but cannot effectively be used to structural analysis.

In the two case studies shown in the present work, the topic regarding the DInSAR techniques differences has been addressed. In particular, in the Murcia case study, where ground-based data have been compared with DInSAR displacement measurements, the coherence-based method has resulted to well represent ground movements. In this case, the main problem in the use of PS data has concerned the choice of the PS to compare with in situ measures and CPT results. In the Murcia metropolitan area, in fact, most of the PS correspond to structures. Therefore, their measured displacement regarded the structural response to ground movements and not its estimation. CPT results are maps with a pixel resolution of 60x60 m (for the chosen multilook of 3x15).

Therefore, following the approach proposed by Herrera et al. (2009), the PS closest to every extensometer has been selected on the ground and compared also with CPT displacement time series. In the C-band image processing validation, the average value of the absolute difference between the two time series for 24 points (near the extensometer boreholes) has resulted of 5.8±4.8 mm and their difference of 0.1±6.4 mm on average.

Another problem to take into account in the pixel choice regards the possible geocoding errors; these shifts of DInSAR maps is typical and make very difficult this selection. However, the achieved CPT processing results have not showed spatial shifts and the CPT time series have resulted to correctly estimate the ground displacements, as demonstrated by the comparison with in situ data shown in the chapter VI.

Also in the Telese Terme case study, a good correspondence between PS and SBAS results has been found; both DInSAR results have been useful for the spatial analysis of the subsidence phenomenon. In particular, they have allowed to understand the subsidence spatial correspondence with the fluvial marshy deposits. Furthermore, they have permitted to individuate a stable area in the eastern side of the city due to the existence of a stiff travertine bedrock. This has justified the occurrence of a deformation gradient which has provoked structural damage to buildings. In order to analyze in detail the structural response to the displacement detected by SAR, the PS-based method has resulted more effective. Therefore, available PS DInSAR data have been used to verify whether the structure serviceability limit states have been overpassed.

The principal limitation, in this study, has regarded the unavailability of X-band SAR images. As shown in Herrera et al. (2010), in fact, X-band-based PS density is at least ten times higher than the PS density provided by C-band satellites. This would have permitted a more accurate analysis of the differential settlements and distorsions which provoked the structural damage. In any case, even though PS radar data acquired by C-band satellites have been used, a reliable result has been obtained. In fact, the achieved model results have turned out to be coherent with the forensic analysis evidences carried out in situ.

Therefore, in this case, the principal requirement to this kind of analysis was an acceptable PS density in correspondence of the building to analyze. This can be reached also using C-band images even though, to an in-depth analysis, the number of PS provided by X-band images is more adequate.

At the same time, in the case of Telese Terme, the cause of the structural failure is related to the existence of a gradient of deformation (due to the geological setting). For this reason, also the approach proposed by Sanabria et al. (under review) has brought to reliable values of the different settlement and angular distortion to be considered in the model. Input data of the algorithm proposed by Sanabria et al. (under review), are interpolated displacement maps. Therefore, using this approach, PS-based or coherence-based DInSAR results would be both used to this kind of analysis bringing to coherent results.

Finally, the proposed work has allowed to critically analyze constraints and advantages of this technique in the field of subsidence monitoring. In particular, also for the achieved CPT DInSAR processing, several tests have been done to fully understand the influence of the used parameters on the final results.

Moreover, the geotechnical model results have been interpolated through the Ordinary Kriging Radar Errors (OKRE) technique. The achieved deformation maps have been used in the processing to allow the algorithm to better estimate the no-linear part of the phase. This approach has permitted to obtain a good estimation of the displacement time series without separating the processing in different branches (not characterized by a linear velocity trend changes).

Considering the results so far obtained, it can be stated that all the proposed approaches could be conveniently applied to other scenarios affected by similar phenomena.

In the case of Murcia city, the use of DInSAR data have allowed to understand the cause-effect mechanism of the phenomenon, to analyze the aquifer-aquitard connection trough piezometric comparisons, to achieve geotechnical and hydrogeological parameters, such as the storage coefficients (Tomàs et al., 2011). Moreover, it has also permitted to identify local anomalies, like areas where soils have an higher stiffness.

All that demonstrates that DInSAR techniques can really be considered as a reliable tool to the natural risk mitigation because they allow assessments about the phenomenon characterization and analysis and, at the same time, can supply to the total unavailability of monitoring networks.

7.1. Future research development

In the Murcia case study, the continuation of the research will regard the implementation of an elasto-plastic model as to better characterize the last soil uplift related to the water recuperation phase; the up-to-dated extensometric and piezometric data will support this analysis. The model results will be validated with the Terrasar-X image processing, following the integrated approach shown in the present thesis. The final geotechnical model results will be interpolated through the Ordinary Kriging Radar Errors (OKRE) technique (as in the present thesis) and the results will be compared with that achieved with other techniques, like the Kriging with External Drift (KED). The obtained elasto-plastic model deformation maps will be used to improve the DInSAR processing both of C-band and X-band images as described in the present project.

In the Telese Terme case study, the structural analysis presented in this work will be applied to other buildings in the study area affected by similar problems. It would be interesting to test the proposed analysis in areas where X-band images are available.

References

References

- Alberotanza L., Conchetto E., Donnici S., Barbero R.S., Zambon G. (2002). “Informational elements for monitoring land elevation at the historical building sites of an urban area in assessing a change in their reuse”. J. Cult. Herit. 3, 15-20.

- Akagi, T. (1992). “National contributions by TC12 land subsidence committee members”. Japan. Proc. 12th Int. Conf. Soil Mech. and Found. Eng., Río de Janeiro, 13-18 August, 5, 3205-3206.

- Aragòn, R., Garcìa-Aròstegui, J. L., Lambàn, J., Hornero, J., Fernàndez-Grillo A.I. (2004). “Impacto de la explotaciòn intensiva de aguas subterràneas en la ciudad de Murcia (Espana), anàlisis hidrogeològico”. Proc. 23th International Congress of IAH-ALHSUD, 11–14 October 2004, Zacatecas, Mexico, 2622–2624, (on CDROM), (in Spanish).

- Arnaud, A., Adam, N., Hanssen, R., Inglada, J., Duro, J., Closa, J., Eineder, M. (2003). “ASAR ERS interferometric phase continuity”. IEEE Int. Geosci. Remote Sens. Symp., IGARSS 2003, Toulouse, 21-25 July, 2, 1133-1135.

- Autin WJ (2002). “Landscape evolution of the Five Islands of south Louisiana: scientific policy and salt dome utilization and management”. Geomorphology 47(2–4):227–244. doi:10.1016/s0169-555x(02)00086-7.

- Avallone A., Zollo A., Briole P., Delacourt C., and Beauducel F. (1999). “Subsidence of Campi Flegrei (italy) detected by SAR interferometry. Geophysical research letters”. Vol. 26., No. 15., pp. 2303-2306.

- Ashrafianfar N., Hebel H.P. Busch W. (2011). “Monitoring of mining induced land subsidence – differential SAR Interferometry and persistent scatterer Interferometry using TERRASAR-X data in comparison with ENVISAT data”. Proc. 4th TerraSAR-X Science Team Meeting, 14-16 February 2011 DLR, Oberpfaffenhofen, Germany.

- Azimi-Zonooz, A., W.F. Krajewski, D.S. Bowles and D.J. Seo, (1989). “Spatial rainfall estimation by linear and non-linear cokriging of radar-rainfall and raingage data”. Stochastic Hydrol. Hydraul., 3, pp. 51-67.

- Baldi P., Casula G., Cenni N., Loddo F., and Pesci A. (2009). “GPS-based monitoring of land subsidence in the Po Plain (Northern Italy)”. Earth and Planet. Sci. Lett., 288, pp. 204-212.

- Berardino P., Fornaro G., Lanari R., Sansosti E. (2002). “A new algorithm for surface deformation monitoring based on small baseline differential SAR interferograms”. IEEE Transactions on Geoscience and Remote Sensing, 40 (11): 2375-2383.

- Bergado, D.T., Khaw, L.G., Nutalaya, P., Balasubramaniam, A.S. (1987). “Subsidence effects on infra-structures and settlement predictions in the AIT Campus, Chao Phraya Plain, Thailand. Groundwater effects in Geotechnical Engineering”. Proc. 9th Eur. Conf. Soil Mech. and Found. Eng., Dublín, 31 Au-

gust-3 September, 1, 277-284.

- Berardino P., Fornaro G., Lanari R., Sansosti E. (2002). “A new algorithm for surface deformation monitoring based on small baseline differential SAR interferograms”. IEEE Transactions on Geoscience and Remote Sensing, 40(11), 2375-2383.

- Bedient, P. B. and Huber W. C., (2008). “Hydrology and Floodplain Analysis”, 4th Ed. Prentice-HallPublishing Co., Upper Saddle River, NJ, 2008, 795 pp.

- Bertoni W., Carbognin L., Gatto P. and Mozzi G. (1973). “Note interpretative preliminari sulle cause della subsidenza in atto a Ravenna”, C.N.R., Lab. per lo Studio della Dinamica delle Grandi Masse, Tech. Rep. 65, Venezia**.**

- Biot, M. (1956). “General solutions of the equations of elasticity and consolidation for a porous material”. Journal of applied mechanics.

- Biot, M. A. (1941). “General theory of three-dimensional consolidation”, J.Appl. Phys., 12, 155–164.

- Birkle, P., Schneider, J.F. (1998). “Hydrogeological aspect of the Basin of Mexico City – A summary”. Felsbau 6, 435-441.

- Bitelli, G., Bonsignore, F., Unguendoli, M. (2000). “Levelling and GPS networks to monitoring ground subsidence in the Southern Po Valley”. J. Geodyn. 30, 355-369.

- Blanco, P., Mallorquí, J.J., Duque, S., Navarrete, D. (2006). “Advances on DInSAR with ERS and ENVISAT data using the Coherent Pixels Technique (CPT)”. IEEE Int. Geosci. Remote Sens. Symp., IGARSS 2006, Denver, Colorado, July 31-August 2004, 4, 1898-1901.

- Blanco P., Mallorquı J. J., Navarrete D., Duque S., Sanz Marcos J., Prats P., Romero R., Dominguez J., Carrasco D., Broquetas T. (2005). “Application of the Coherent Pixels Technique to the Generation of Deformation Maps with ERS and ENVISAT Data”. International Geoscience and Remote Sensing Symposium, 2005. IGARSS’05. Vol 3, pp:1983-1986.

- Bock, O., Thom, C. (2001). “Sub-cm measurement with the wide-angle airborne laser ranging system”. Surv. Geophys. 22, 537-548.

- Bouwer, H. (1977). “Land subsidence and craching due to ground-water deplection”. Ground Water 15, 358-364.

- Bru, G.; Herrera, G.; Tomás R.; Duro, J.; De la Vega, R. & Mulas, J. (2013) . “Control of deformation of buildings affected by subsidence using PSI techniques: the Murcia city case of study”. Journal of Structural and Infrastructure Engineering. Volume 9, Issue 2, 2013. Ed. Taylor and Francis. England DOI:10.1080/15732479.2010.519710 pages 188-200. (Published online: 22 Sep 2010).

- Bru, G.; Herrera, G.; Tomás R.; Duro, J.; De la Vega, R. & Mulas, J. (2010). "Control of deformation of buildings affected by subsidence using PSI techniques: the Murcia city case of study". Journal of Structural and Infrastructure Engineering.(on line) Ed. Taylor and Francis. England.

- Buchignani V., Leva D., Nico G., Rivolta C. (2004). "Interferometria Sar da terra per il monitaraggio di un fenomeno di sprofondamento (sinkhole) in Toscana". 1° Seminario sullo stato dell'arte sullo studio dei fenomeni di sinkhole e ruolo delle amministrazioni statali e locali nel governo del territorio. APAT, Roma, 20 – 21 Maggio

- Burbey, T.J. (2001). "Stress-strain analyses for aquifer-system characterization". Ground Water 39, 128-136.

- Calcaterra D., Esposito A., Fuschini V., Galluccio F., Giulivo I., Nardò S., Russo F., Terranova C. (2009) – "L'utilizzo della tecnica Psinsar™ per l'individuazione ed il monitoraggio di sinkholes in aree urbanizzate della Campania: i casi di Telese Terme (Bn) e Sarno (Sa)". Atti Conv: "I Sinkholes. Gli sprofondamenti catastrofici nell'ambiente naturale ed in quello antropizzato". Roma 3-4 Dicembre 2009, 931-948.

- Calderhead A.I., Therrien R., Rivera A., Martel R., Garfias J. (2011). "Simulating pumping-induced regional land subsidence with the use of InSAR and field data in the Toluca Valley". Mexico, Advances in Water Resources, Volume 34, Issue 1, Pages 83-97, ISSN 0309-1708, http://dx.doi.org/10.1016/j.advwatres.2010.09.017.

- Caramanna G., Ciotoli G., Nisio S. (2008). "A review of natural sinkhole phenomena in Italian plain areas". Natural Hazard, 45 (2), pp. 145-172.

- Carbognin, L., Gatto, P., Mozzi, G., Gambolati, G. (1979). "Land subsidence of Ravenna and its similarities with the Venice cases. En: Saxena, S.K. (ed.). Evaluation and prediction of subsidence". Proc. of the Int. Conf., Pensacola Beach, Florida, January 1978, Am. Soc. Civil Eng., New York, 254-266.

- Carbognin, L., Gatto, P., Mozzi, G., Ricceri, G. (1978). "Subsidenza e ambiente". Atti del Convegno 'I Problemi della subsidenza nella politica del Territorio o della difesa del suolo'. Pisa, 3-12.

- Carbognin, L., Gatto, P., Mozzi, G., Gambolati, G., Ricceri, G. (1977). "New trends in the subsidence of Venice". Land subsidence Symposium. Int. Ass. Hydrological Science, Proc. 2nd Int. Symp. Land Subsidence, Anaheim, 13-17 December, 65-81.

- Carminati, E., Martinelli, G. (2002). "Subsidence rates in the Po Plain, northern Italy: the relative impact of natural and anthropogenic causation". Eng. Geol. 66, 241-255.

- Caramanna G., Ciotoli G., Nisio S. (2008). "A review of natural sinkhole phenomena in Italina plain areas". Nat. Hazards 45: 145-172.

- Casagrande, A., (1936). "The determination of the Pre-Consolidation Load and its Pratical Significance". Proc. " 1st ICSMFE, Harward University Cambridge, Mass., vol.3, D-34,pp. 60-64.

- Cascini L., Peduto D., Reale D., Arena L., Ferlisi S., Verde S. and Fornaro G. (2013). "Detection and monitoring of facilities exposed to subsidence phenomena via past and current generation SAR sensors". Journal of Geophysics and Engineering 10 064001. doi:10.1088/1742-2132/10/6/064001.

- Cascini L., Ferlisi S., Peduto D., Fornaro G., Manunta M., (2007a). "Analysis of a subsidence phenomenon via DInSAR data and geotechnical criteria". Rivista Italiana di Geotecnica, 41(4), 50-67.

- Cascini, L., Di Nocera, S., Ferlisi, S., Fornaro, G. & Peduto, D., (2007b). "A land subsidence study via DInSAR technique over large urbanized areas". Urban Remote Sensing Joint Event URS 2007, Parigi. 1 1-13 April 2007. IEEE 1-4244-0712-5/07.

- Cascini L., Ferlisi S., Fornaro G., Lanari R., Peduto D., Zeni G., (2006). "Subsidence monitoring in Sarno urban area via multitemporal DInSAR technique". International Journal of Remote Sensing, 27(8), 1709-1716.

- Cassiani G., and Zoccatelli C. (2000). "Towards a reconciliation between laboratory and in-situ measurements of soil and rock compressibility". in Land Subsidence, Proceedings of VI International Symposium on Land Subsidence, vol. II, edited by L. Carbognin et al., pp. 3 – 15, La Garangola, Padua, Italy**.**

- Castiello G. (2010). "Microgravimetria in ambito urbano". Phd thesis (in Italian).

- Casu, F., Manzo, M., Lanari, R. (2006). "A quantitative assessment of the SBAS algorithm performance for surface deformation retrieval from DInSAR data". Remote Sensing of Environment, 102(3-4), 195–210, doi:10.1016/j.rse.2006.01.023.

- Celico P. (1983). "Idrogeologia dei massicci carbonatici, delle piane quaternarie e delle aree vulcaniche dell'Italia centro-meridionale (Marche e Lazio meridionali, Abruzzo, Molise e Campania)". Quaderni Casmez, 4(2), 225 pp., Roma.

- Celico P. (1978). "Schema idrogeologico dell'Appennino Carbonatico Centro-Meridionale". Memorie e Note dell'Istituto di Geologia Applicata dell'Università di Napoli.

- Cerón, J.C., Pulido, A. (1996). "Groundwater problems resulting from CO_2 pollution and overexploitation in Alto Guadalentín aquifer (Murcia, Spain)". Environmental Geology 28, 223–228.

- Chan Y. K., Koo V. C. (2008). "An introduction to Syntethic Aaperture Radar (SAR)". Progress In Electromagnetics Research B, Vol. 2, pp. 27–60.

- CHS, (2007). "Nuevas aportaciones al conocimiento hidrogeológico".

- Colesanti, C., Ferretti, A., Prati, C., and Rocca, F. (2003). "Monitoring landslides and tectonic motions with the Permanent Scatterers Technique". Eng. Geol., Special Issue on Remote Sensing and Monitoring of Landslides, 68, (1–2), 3–14, 2003.

- Corapcioglu, M.Y. (1984). “Land subsidence a state of the art review. Fundamentals of Transport Phenomena in Porous Media”. En: Bear and M. Y. Corapcioglu (Ed.), NATO ASI Series E.82, Martinus Nijhott Publishers, 369-444.

- Corniello A., De Riso R. (1986). “Idrogeologia e idrochimica delle sorgenti dell’agro Telesino (Benevento)”. Geol. Appl. e Idrog., 21, 52-84.

- Costantini M., Falco S., Malvarosa F., Minati F., (2008). “A new method for identification and analysis of persistent scatterers in series of SAR images,” in Proc. Int. Geosci. Remote Sensing Symp.(IGARSS), Boston MA, USA, 7-11 July 2008, pp. 449- 452.

- Crosetto M., Biescas E., Duro J., Closa J., Arnaud A. (2008). “Generation of advanced ERS and envisat interferometric SAR products using the Stable Point Network technique”. Photogramm Eng Remote Sens74 (4) : 443–451.

- Creutin, J.D., G. Delrieu and T. Lebel, (1988). “Rain measurement by raingage-radar combination: a geostatistical approach”. J. Atm. and Oceanic Tech., 5(1), pp. 102-115.

- Curlander J.C., R.N. McDounough, (1991). “Synthetic Aperture Radar, Systems and Signal Processing”. John Wiley&Sons, NewYork.

- D’Amato Avanzi G., Giannecchini R., Puccinelli A., Verani M. (2004). “Assetto geologico e pericolosità da sinkholes in aree urbane: il caso di Camaiore (Toscana, Italia)”. 1° seminario sullo stato dell’arte dei fenomeni di sinkholes e ruolo delle amministrazioni statali e locali nel governo del territorio. Roma, 20-21 Maggio 2004, 331-346.

- De Justo, J.L., Vázquez, N.J., De Justo, E. (2003). “Subsidencia en suelos saturados y parcialmente saturados. Aplicación al caso de Murcia”. Ingeniería Civil 132, 103-108.

- De Justo J.L., Vázquez N.J., De Justo E. (2002). “Rozamiento negativo en pilotes producidos por la subsidencia en Murcia”. Ingeniería Civil 125, 95-103.

- De Justo, J.L., Vázquez, N.J. (1999). Subsidencia en Murcia I. Soluciones explícitas para el asiento unidimensional. Ingeniería Civil 115, 63-77.

- Del Greco O., Garbardino E., Oggeri C. (2004). “A multidisciplinary approach for the evaluation of the “Bottegone” subsidence (Grosseto, Italy)”. In: Hack R., Azzam R.,; Charlier R., (eds) Engineering geology for infrastructure planning in Europe, an European perspective, vol. 1, 685-693.

- De Simone P and Viggiani C, (1978). “Consolidation of a thick aquitard due to ground water withdrawal”. En Evaluation and Prediction of Subsidence. Ed. S.K.Saxona. Eng. Found. Conf. ASCE, Pensacola, p. 358-372.

- Di Martire D., (2013). “Application of DInSAR data for slow-moving landslides monitoring”. (PHD

thesis).

- Doerry A.W. (2008). “Reflectors for SAR Performance Testing”. SANDIA REPORT SAND 2008-0396 Unlimited Release Printed January 2008.

- Doglioni C. (1993). “Some remarks on the origin of foredeeps”. Tectonophysics 228(1–2):1–20**.**

- Duro J., Closa J., Biescas E., Crosetto M., Arnaud A. (2005). “High Resolution Differential Interferometry using time series of ERS and ENVISAT SAR data”. Proc. of the 6th. Geomatic Week Conference, February 2005, Barcelona, Spain (CDROM).

- Erdin, R. (2013). “Geostatistical methods for hourly radar-gauge combination: An explorative, systematic application at MeteoSwiss”. Scientific Report MeteoSwiss, 92, 58 pp.

- Esposito L., Celico P., Guadagno F.M., Aquino S. (2003). “Aspetti idrogeologici del territorio sannita”. Con saggio cartografico alla scala 1:100.000. Techne Edt. Napoli, pp. 58.

- Ferretti A., Savio G., Barzaghi R., Borghi A., Musazzi S., Novali F., Prati C. and Rocca F. (2007). “Sub-millimeter Accuracy of InSAR Time Series: Experimental Validation”. IEEE Transactions On Geoscience And Remote Sensing, VOL.45, NO.5, MAY 2007.

- Ferretti A., Colesanti C., Prati C., Rocca F. (2001a). “Comparing GPS, optical levelling and Permanent Scatterers”. IEEE International Geoscience and Remote Sensing Symposium, IGAARS, Sydney (Australia), 9-13 Luglio 2001, vol. 6, Pagine 2622-2624.

- Ferretti, A., Prati, C. & Rocca F. (2001b). “Permanent Scatterers in SAR Interferometry”. IEEE Trans. Geoscience And Remote Sensing, 39(1), 8–20.

- Ferretti, A., Prati, C. & Rocca F. (2000). “Nonlinear Subsidence Rate Estimation Using Permanent Scatterers in Differential SAR Interferometry”. IEEE Trans. Geoscience And Remote Sensing, 38(5), 2202–2212.

- Figueroa, E., Germán. E. (1977). “Subsidence of the city of Mexico. A historical review”. Land Subsidence Symposium. Int. Ass. Hydrological Science, Proc. 2nd Int. Symp. Land Subsidence, Anaheim, 13-17 De- cember, 35-3.

- Folloni, G., Russo, P., Radicioni, F. (1996). “La subsidenza del territorio bolognese dal 1983 al 1993”. INARCOS 571, 400-413.

- Galloway, D.L., Hoffmann, J., (2007). "The application of satellite differential SAR interferometry-derived ground displacements in hydrogeology”. Hydrogeol. J. 15, 133–154.

- Galloway, D.L., Hudnut, K.W., Ingebritsen, S.E., Philips, S.P., Peltzer, G., Rogez, F., Rosen, P.A., (1998). “Detection of aquifer system compaction and land subsidence using interferometric synthetic aperture

radar, Antelope Valley, Mojave Desert, California". Water Resour. Res. 34, 2573–2585.

- Galve, J., Gutiérrez, F., Lucha, P., Bonachea, J., Remondo, J., Cendrero, A., Gutiérrez, M., Gimeno, M., Pardo, G., Sánchez, J. (2009). "Sinkholes in the salt-bearing evaporite karst of the Ebro River valley upstream of Zaragoza city (NE Spain): Geomorphological mapping and analysis as a basis for risk management". Geomorphology, 108, 145–158.

- Gambolati, G., Teatini, P., Tomasi, L., Gonella, M. (1999a). "Coastline regresion of the Romagna region, Italy, due to natural and anthropogenic land subsidence and sea level rise". Water Resour. Res. 35, 163- 184.

- Gambolati G., Teatini P., and Tomasi L. (1999b). "Stress-strain analysis in productive gas/oil reservoirs, Int. J. Numer. Anal. Methods Geomech. 23, pp. 1495 – 1519**.**

- Gambolati G., and Teatini P. (1998). "Numerical analysis of land subsidence due to natural compaction of the Upper Adriatic Sea basin. In: CENAS, Coastline evolution of the upper Adriatic Sea due to sea level rise and natural and anthropogenic land subsidence". Kluwer Academic Publishing, Water Science & Technology Library N. 28, pp 103–131.

- Gambolati G., Ricceri G., Bertoni W., Brighenti G., and Vuillermin E. (1991). "Mathematical simulation of the subsidence of Ravenna". Water Resour. Res., 27(11), pp. 2899 – 2918.

- Gambolati, G., Freeze, R.A. (1973). "Mathematical simulation of the subsidence of Venice". Water Resour. Res. 9, 721-733.

- García, J; Martínez, M; Mulas, J,; y Rodríguez, J. (2003). "Analisis numerico mediante simulacion de un proceso de subsidencia ligado a consolidacion por explotacion de aguas subterraneas en el area metropolitanea de Murcia". Asociación de Ingeniería Geológica Española. (AIGE). Boletín informativo. nº 0 (Octubre). Dep. legal A.S. 4.145-2003. Págs 14-19.

- Goovaerts P., (2010). "Performance comparison of geostatistical algorithms for incorporating elevation into the mapping of precipitation". Proceeding at Geocomputation. 1999, http://www.geovista.psu.edu/sites/geocomp99/Gc99/023/gc_023.htm.

- Goovaerts P., (1999). "Geostatistics in soil science: state-of-the-art and perspectives", Geoderma, Volume 89, Issues 1–2, April 1999, Pages 1-45, ISSN 0016-7061, http://dx.doi.org/10.1016/S0016-7061(98)00078-0.

- Guerrero, J.; Gutiérrez, F.; Bonachea, J. & Lucha, P. (2008). "A sinkhole susceptibility zonation based on paleokarst analysis along a stretch of the Madrid-Barcelona high-speed railway built over gypsum- and salt-bearing evaporites (NE Spain)". Eng. Geol., 102, 62-73.

- Gumiel, J.C., García-Aróstegui, J.L., Hornero, J., Aragón, R., Fabregat, V. Fernández-Grillo, A.I., Moreno, M.T. (2001). "Evaluación mediante teledetección de superficies agrícolas y estimación de demandas de

agua en la Vega Media del Segura (Murcia)". VII Simp. de Hidrogeol. En: Hidrogeología y Recursos Hidráulicos, AEH-IGME, Madrid, XXIII, 71-81.

- Gutiérrez F., Galve J.P., Lucha P., Castañeda C., Bonachea J., Guerrero J. (2011). "Integrating geomorphological mapping, trenching, InSAR and GPR for the identification and characterization of sinkholes: A review and application in the mantled evaporite karst of the Ebro Valley (NE Spain)". Geomorphology 134, 2011, 144–156, doi:10.1016/j.geomorph.2011.01.018.

- Gutiérrez F, Galve J, Lucha P, Bonachea J, Jorda´ L, Jorda´ R (2009). "Investigation of a large collapse sinkhole affecting a multi-storey building by means of geophysics and the trenching technique (Zaragoza city, NE Spain)". Environ Geol 58(5):1107–1122. doi: 10.1007/s00254-008-1590-8.

- Gutiérrez, F., Calaforra, J. M., Cardona, F., Orti, F., Duran, J. J., Garay, P. (2008). "Geological and environmental implications of the evaporite karst in Spain". Environ. Geol., 53,951-965.

- Haberlandt U., (2007). "Geostatistical interpolation of hourly precipitation from rain gauges and radar for a large-scale extreme rainfall event ". Journal of Hydrology, 332(1-2): 144-157

- Hanssen, R. F. (2003). "Subsidence monitoring using contiguous and PSInSAR: quality assessment based on the precision and reliability". Proc. 11th FIG Sym. Def. Measur., Santorini, Grecia, 2003.

- Hanssen, R.F. (2001). "Radar interferometry. Data interpetation and error analysis". Kluwer Academic publisher, Holanda, 308 pp.Hazards Earth Syst. Sci., 13, 2425-2440, doi:10.5194/nhess-13-2425-2013, 2013.

- Helm, D.C. (1976). "One-dimensional simulation of aquifer system compaction near Pixley, California, Part 2, stress-dependent parameters". Water Resour. Res. 12, 375-391.

- Herrera G., Álvarez Fernández, M. I., Tomás Jover R., González Nicieza, C., López Sánchez, J. M., Álvarez Vigil A. E. (2012) Forensic analysis of buildings affected by mining subsidence based on Differential Interferometry (Part III). Eng Fail Anal 24:67–76. doi: 10.1016/j.engfailanal.2012.03.003.

- Herrera G., Tomás R., Monells D., Centolanza G., Mallorquí J.J., Fernando Vicente, F. Navarro,V.D. Lopez-Sanchez J.M. Sanabria, M., Cano M. & Mulas, J. (2010). "Analysis of subsidence using Terrasar-1 X data: Murcia case study". Elsevier Editorial System. Engineering Geology. Springer. Alemania. Vol: 116 284-295.

- Herrera, G., Tomás, R., Lopez-Sanchez, J.M., Delgado, J., Vicente, F., Mulas, J., Cooksley, G., Sánchez, M., Duro, J., Arnaud, A., Blanco, P., Duque, S., Mallorquí, J.J., Vega-Panizo, R., Monserrat, O., (2009a). "Validation and comparison of advanced differential interferometry techniques: Murcia metropolitan area case study". ISPRS Journal of Photogrammetry and Remote Sensing 64, 501–512.

- Herrera, G., Fernández, J.A., Tomás, R., Cooksley, G., Mulas, J., (2009b). "Advanced interpretation of subsidence in Murcia (SE Spain) using A-DInSAR data modelling and validation". Natural Hazards and Earth System Science 9, 647–661.

- Herrera, G., Tomás, R., Lopez-Sanchez, J.M., Delgado, Vicente, F., Mulas, J., Cooksley, G., Sanchez, M., Duro, J., Arnaud, A., Blanco, P., Duque, S., Mallorquí, J.J., (2008). "Comparison of Advanced Differential Interferometry Techniques: Murcia metropolitan area case study". ISPRS Journal of Photogrammetry and Remote Sensing.

- Hoffman, J. (2003). "The application of satellite radar interferometry to the study of land subsidence over developed aquifer systems". PhD Thesis, University of Stanford, 211 pp.

- Hoffmann J, Galloway DL, Zebker HA (2003). "Inverse modelling of interbed storage parameters using land subsidence observations, Antelope Valley, California". Water Resour Res 39(2): 1031. DOI 10.1029/2001WR001252.

- Holzer, T.L. (1981). "Preconsolidation stress of aquifer systems in areas of induced land subsidence". Water Res. 17, 693-704.

- Hooke R. (1676). "Introduction to Scientific Inference". (book) London, England.

- Hu, R.L., Yue, Z.Q., Wang, L.C., Wang, S.J. (2004). "Review on current status and challenging issues of land subsidence in China". Eng. Geol. 76, 65-77.

- Hueckel, T., Cassiani G., Tao F., Pellegrino A., and Fioravante V. (2001). "Effect of aging on compressibility of oil/gas bearing sediments and their subsidence". J. Geotech. Eng., 127(11), pp. 926 – 938.

- IGME, (2002). "Estudio hidrogeológico de la unidad Vega Media y Baja del Segura".

- IGME, (2001a). "Seguimiento y control instrumental de asentamientos del terreno en el área metropolitana de Murcia".

- IGME, (2001b). "Estudio hidrogeológico del acuífero de las Vegas Media y Baja del Segura y su relación con los cauces naturales y artificiales de su territorio".

- IGME, (2000a). "Estudio geotécnico para el análisis, prevención y corrección de la patología constructiva derivada del cambio en las condiciones del subsuelo en la ciudad de Murcia".

  IGME, (2000b). "Estudio geotécnico del Subsuelo del Área Metropolitana de Murcia".

- Ishii, M., Kuramochi, F., Endo, T. (1977). "Recent tendencies of the land subsidence in Tokio". Land Sub- sidence Symposium. Int. Ass. Hydrological Science, Proc. 2nd Int. Symp. Land Subsidence, Anaheim, 13- 17 December, 25-34.

- Ireland, R.L., Poland, J.F., Riley, F.S. (1984). "Land subsidence in the San Joaquin Valley, California, as 1980". U.S. Geological Survey Professional paper, 437-I, 93 pp.

- ITGE & CPTOP, (2000). “Estudio Geotécnico para el análisis prevención y correción de la patología derivada de los cambios en el subsuelo de la Ciudad de Murcia. Informe inédito. 208 p.

- JANBU, N. (1987). “Subsidence due to ground water and oil withdrawal”. IX ECSMFE, Dublín, Vol. 1, p. 303-307.

- Kappel WM, Yager RM, Todd MS (1999). “The Retsof Salt Mine Collapse”. In: Galloway DL, Jones DR, Ingebritsen SE (eds) Land Subsidence in the United States, vol 1182., US Geological Survey CircularUS Geological Survey, Reston, pp 111–120.

- Jensen, J.R. (2000). “Remote Sensing of the Environment”. Prentice-Hall, Upper Saddle River, New Jersey.

- Lanari R., Mora O., Manunta M., Mallorquí J.J., Berardino P., Sansosti E., (2004). “A small-baseline approach for nvestigating deformations on full-resolution differential SAR interferograms”. IEEE Transactions on Geosciences and Remote Sensing, 42 (7), pp. 1377-1386.

- Lanari R., Mora O., Manunta M., Mallorqui J.J., Berardino P., Sansosti E. (2004). “A small-baseline approach for investigating deformations on full-resolution differential SAR interferograms”. IEEE Transactions on Geoscience and Remote Sensing, 42(7), 1377-1386.

- Lancellotta R., 1993.”Geotecnica”. Zanichelli (book).

- Lewis, R.W., Scherefler, B.A. (1998). “The finite element methods in the static and dynamic deformation and consolidation of porous media”. John Wiley and Sons Ltd, Baffins Lane, Chichester, England, 508 pp.

- Lloret A., Alonso E.E. (1985). “State surfaces for partially saturated soils”. Proc. Of the XI International Conference on Soil Mechanics Foundation Engineering, San Francisco, CA, Vol. 2, pp. 557-562.

- Lu P., Casagli N., Catani F., Tofani V. (2012). “Persistent Scatterers Interferometry Hotspot and Cluster Analysis (PSI-HCA) for detection of extremely slow-moving landslides”. International Journal of Remote Sensing, 33(2), pp. 466-489.

- Mancini F, Stecchi F, Zanni M, Gabbianelli G (2009). “Monitoring ground subsidence induced by salt mining in the city of Tuzla (Bosnia and Herzegovina)”. Environ Geol 58(2):381–389. doi:10.1007/s00254-008-1597-1.

- Martínez, M., Mulas, J., Herrera, G., Aragón, R. (2004). “Efectos de una subsidencia moderada por extracción de agua subterránea en Murcia, España”. Proc. XXXIII Congress of IAH-ALHSUD, Conf. on Groundwater Flow Understanding from local to regional scales, Zacatecas, Mexico, 11-15 October, CD ROM.

- Marturià, J., Mora, O., Xifre, D., Martínez, P., Roca A., (2006). “DInSAR Techniques versus High

Topographic Leveling Surveys: The Subsidence Phenomena in Sallent". European Congress on Regional Geoscientific Cartography and Information Systems, vol. II, pag. 53-57.

- Mattavelli L., Novelli L., and Anelli L. (1991). "Occurrence of hydrocarbons in the Adriatic basin. In: Spencer AM (ed) Generation, accumulation and production of Europe's hydrocarbons". Special Publication of European Association of Petroleum Geoscientists No. 1, Oxford University Press, Oxford (UK), pp. 369–380.

- Meisina C., Zucca F. , Notti D., Colombo A., Cucchi A., Savio G., Giannico C., Bianchi M., (2008). "Geological Interpretation of PSInSAR Data at Regional Scale". Sensors 2008, 8, 7469-7492; DOI: 10.3390/s8117469

- Mihalinec Z., Ortolan Z., (2008). "Landslide ''Granice'' in Zagreb (Croatia). In: Chen Z, Zhang J-M, Ho K,Wu F-Q, Li Z-K (eds) Landslides and engineered slopes: From the past to the future". Proceedings of the tenth international symposium on landslides and engineered slopes. Taylor & Francis, Xi'an, pp 1587–1593.

- Mora, O. (2004). "Advanced differential SAR techniques for detection of terrain and building displacements". Tesis doctoral, Universidad Politécnica de Barcelona, 182 pp.

- Mora O., Mallorqui J.J., Broquetas A. (2003). "Linear and Non-linear Terrain Deformation Maps from a Reduced Set of Interferometric SAR Images". IEEE Transactions on Geoscience and Remote Sensing, 2003.

- Mulas, J. Aragón, R., Clemente A.A., (2010). "La subsidencia del terreno en la ciudad y área metropolitana de Murcia: Modelización, seguimiento y control", (coord. Madrid: Instituto Geológico y Minero de España y Consejería de Obras Públicas y Ordenación del Territorio de la Comunidad Autónoma de la Región de Murcia). Book

- Mulas, J. (2007). "Subsidencia en Murcia. Análisis hidrogeológico y geotécnico". Jornada Técnica la Investigación geológica base de la ordenación del território, Murcia, 13 Febrero. Inédito.

- Mulas, J., Martínez, M., Herrera, G., Rodriguez, A., Sanz, M. A., Lozano, A., Alcaraz, M. (2005). Seguimiento y control instrumental de la subsidencia del terreno en Murcia: Fase II, Instituto Geológico y Minero de España, 150 pp. (In spanish).

- Mulas, J., Crosetto, M., Biescas, E., Herrera, G. (2004). "Estimación de la subsidencia del Área Metropolitana de Murcia mediante Interferometría Radar". Instituto Geológico y Minero de España, Madrid, 38 pp.

- Mulas, J., Aragón, R., Martínez, M., Lambán, J., García-Arostegui, J.L., Fernández-Grillo, A.I., Hornero, J., Rodríguez, J., Rodríguez, J.M., (2003). "Geotechnical and hy-drological analysis of land subsidence in Murcia (Spain)". Proc. 1ª International Confer-ence on Groundwater in Geological Engineering, 22-26 September, Bled, Slovenia, 50, 249-252.

- Mulas, J.; Martínez M.; Rodriguez, J.; Rodriguez, J.M. y SERVIGIS (2002). “Utilización de un SIG en los estudios geotécnicos para la determinación de los asentamientos por descenso del nivel freático. Aplicación en el Área Metropolitana de Murcia”. II Jornadas sobre Sistemas de Información Geográfica en Riesgos Geológicos y Medio Ambiente pag 1241-1252.. Ed. Publicación del Instituto Geológico y Minero de España. Serie: Medio Ambiente. Riesgos Geológicos. Nº3. I.S.B.N. 84-7840-458-9.

- Mulas, J., Pardo, J. M., Martìnez, M., Rodriguez, A., Peral, F.,Jimènez, A., and Alcaraz, M. (2001). “Seguimiento y control instrumentalde la subsidencia del terreno en Murcia: Fase I, Instituto Geològico y Minero de Espana, 120 pp., 2001.

- Nakagawa, H., Murakami, M., Fujiwara, S., Tobita, M. (2000). “Land subsidence of the Nothern Kanto Plañís caused by ground water extraction detected by JERS-1 SAR interferometry”. IEEE Int. Geosci. Remote Sens. Symp., IGARSS 2000, Hawaii, 24-28 July, 5, 2233 – 2235.

- Nisio S., Graciotti R. & Vita L. (2004). “I fenomeni di sinkhole in Italia: terminologia, meccanismi genetici e problematiche aperte”. Atti Conv. “Stato dell’arte sullo studio dei fenomeni di sinkholes e ruolo delle amministrazioni statali e locali nel governo del territorio Roma 20-21 maggio 2004”, 557-572.

- Oppikofer T., Jaboyedoff M., Blikra L.H. & Derron M.-H., (2008). “Characterization and monitoring of the Aknes landslide using terrestrial laser scanning”. Proc. 4th Canadian Conference on Geohazards: From Causes to Management, pp. 211-218.

- Pardo J. M.; Lozano A ; Herrera G.; Mulas J. y Rodríguez A. (2013). “Instrumental monitoring of the subsidence due to groundwater withdrawal in the city of Murcia (Spain)” Environ Earth Sci DOI 10.1007/s12665-013-2710-7. Springer-Verlag Berlin Heidelberg.

- Pardo J. M., Herrera G., Rodríguez A., Mulas J. (2007). “Últimas propuestas en la monitorización instrumental de la subsidencia en Murcia”. XII Congreso Internacional de Energía y Recursos Minerales. Oviedo, 7 a 11 de Octubre de 2007.

- Peral, F., Rodrìguez, A., and Mulas J., (2004). “Control of subsidence with borehole exten-someters and surveying measurements in Murcia (Spain)”. Proceedings ISC-2 on Geotechnical and Geophysical Site Characterization, 15–19 October, Rotterdam, Holland, 1171–1176, 2004.

- Perna, S.; Zamparelli, V.; Pauciullo, A.; Fornaro, G. (2013). "Azimuth-to-Frequency Mapping in Airborne SAR Data Corrupted by Uncompensated Motion Errors," Geoscience and Remote Sensing Letters, IEEE , vol.10, no.6, pp.1493,1497, Nov. 2013 doi: 10.1109/LGRS.2013.22607.

- Pipia, L., Aguasca, A., Fabregas, X., Mallorquí, J.J., López-Martinez, C., Marturià, J. (2007a). “Mining induced subsidence monitoring in urban áreas with a Ground-Based SAR”. Urban Remote Sensing Joint Event, Paris, 11-13 april, 1-5.

- Placzek, D. (1989). “Methods for the calculation of ssttlements due to ground-water lowering”. Proc.

12th Int. Conf. Soil Mech. and Found. Eng., Río de Janeiro, 13-18 August, 3, 1813-1818.

- Pipia, L., Fabregas, X., Aguasca, A., Lopez-Martinez, C., Mallorqui, J.J., Moraline, O. (2007b). "Polarimetric temporal information for urban deformation map retrieval". Proc. IEEE Int. Geosci. Remote Sens. Symp., IGARSS 2007, Barcelona, 23-28 July, 2, 192-195.

- Plank S., Singer J., Thuro K. (2013). "Assessment of number and distribution of persistent scatterers prior to radar acquisition using open access land cover and topographical data", ISPRS Journal of Photogrammetry and Remote Sensing, Volume 85, November 2013, Pages 132-147, ISSN 0924-2716, http://dx.doi.org/10.1016/j.isprsjprs.2013.09.001.

- Poland, J.F., Lofgren, B.E., Ireland, R.L., Pugh, R.G. (1975). "Land Subsidence in the San Joaquin Valley, Califonia as of 1972". U.S. Geological Survey Professional Paper 437-H, 78 pp.

- Polselli P. (2005). "Relazione tra fenomeni di sprofondamento, risalite di fluidi mineralizzati e sismicità in alcune aree di studio dell'italia centro-meridionale". ISPRA – Stage thesis (in italian).

- Prati C., A. Ferrett, Perissin D., (2010). "Recent advances on surface ground deformation measurement by means of repeated space-borne SAR observations". J. Geodyn., 49, 161–170, doi:10.1016/j.jog.2009.10.011.

- Prokopovich NP (1979). "Genetic classification on land subsidence". Paper presented at the international conference on evaluation and prediction of subsidence, Pensacola Beach

- Prinzl, F., Nutalaya, P. (1987). "Land subsidence in the Bangkok region: Reasons, effects and results of recent measurements. Groundwater effects in Geotechnical Engineering". Proc. 9th Eur. Conf. Soil Mech. and Found. Eng., Dublín, 31 August-3 September, 1, 323-326.

- Puche A., (1996). "Evolución piezométrica de Murcia. Consecuencias geotécnicas" (Master thesis, in spanish).

- Raspa, G., M. Tucci and R. Bruno, (1997). "Reconstruction of rainfall fields by combining ground raingauges data with radar maps using external drift method". In: E.Y. Baafi, N.A. Schofield (Eds.). Geostatistics Wollongong '96, Kluwer Academic Publishers, Dordrecht, pp. 941-950.

- Raspini, F., Loupasakis, C., Rozos, D., and Moretti, S., (2013). "Advanced interpretation of land subsidence by validating multi-interferometric SAR data: the case study of the Anthemountas basin (Northern Greece)". Nat. Hazards Earth Syst. Sci., 13, 2425-2440; doi:10.5194/nhess-13-2425-2013.

- Ricceri, G., Butterfield, R. (1974). "An analysis of compressibility data from a deep borehole in Venice". Geotechnique 2, 175-191.

- Ricceri, G., Favaretti,, M. (1992). "National contributions by TC12 land subsidence committee members Italy". Proc. 12th Int. Conf. Soil Mech. and Found. Eng., Río de Janeiro, 13-18 August, 5, 3214-3216.

- Riley, F.S. (1984). “Developments in borehole extensometry. In Jonson, A.I.; Carbognin, L; and Ubertini, L. (Editors)”, Proc. of the Third Int. Symp. of Land Subsidence, Venice, 19-25 March, 151, 169-186.

- Riley, F.S. (1969). “Análisis of borehole extensometer data from central California”. En Tison, L.J. (Ed.). Land subsidence, 2, 423-431.

- RIVERA, A. e t al. (1991). “Nonlinear modelling of groundwater flow and total subsidence of the Mexico City aquifer-Aquitard system”. 4th Int. Symp. on Land Subsidence, Houston, IAHS Publ. nº 200, 45-58.

- Rodríguez Ortiz, J.M., Mulas, J. (2002). “Subsidencia generalizada en la ciudad de Murcia (España)”. En: Ayala, J. y Olcina Coords.: Riesgos Naturales, Editorial Ariel, 459-463.

- Rodríguez Jurado, J., Martínez Corbella, M., Mulas, J., Rodríguez Ortiz, J.M., (2000). “Establecimiento de un modelo geológico para el estudio de la subsidencia por rebajamiento del nivel freático. Geotemas 1, 155–158.

- Salvioni G. (1957). “I movimenti del suolo nell’Italia centro-settentrionale”. Boll. di Geodesia e Scienze Affini, I.G.M., anno XVI, Firenze**.**

- Sanabria, M. P., Guardiola-Albert, C., Tomás, R., Herrera, G., Prieto, A., Sánchez, H., and Tessitore, S. “Subsidence activity maps derived from DInSAR data: Orihuela case study”. Nat. Hazards Earth Syst. Sci. Discuss., 1, 5365-5402, doi:10.5194/nhessd-1-5365-2013, 2013.

- Sato, H.P., Abe, K., Ootaki, O. (2003). “GPS-measured land subsidence in Ojiya City, Niigata Prefecture, Japan”. Eng. Geol. 67, 379-390.

- Sarabandi, K., and T. C. Chiu, (1995). “An optimum corner reflector for calibration of imaging radars”. IEEE Trans. Antennas Propagation, submitted for publication.

- Shi, X., Xue, Y., Wu, J., Ye, S., Zhang, Y., Wei, Z., Yu, J. (2007). “Characterization of regional land subsidence in Yangtze Delta, China: the example of Su-Xi-Chang area and the city of Shanghai”. Hydrogeol. J. 16, 593-607.

- Schmidt, D.A., and R. Bürgmann, (2003). “Time dependent land uplift and subsidence in the Santa Clara valley, California, from a large InSAR data set”. J. Geophys. Res., 108, doi:10.1029/2002JB002267, 2003.

- Schrefler B. A., Ricceri G., Achilli V., Fabris M., and Laloui L. (2008). “Actual problems in the study of soil dynamics of the Upper Adriatic Sea”. Soc. Geol. It., Vol. 2, pp. 1-3.

- Schrefler, B.A., Lewis, R.W., Norris, V.A. (1977). “A case of study of the surface subsidence of the Pole-sine area”. Int. J. Numer. Anal Met. 1, 377-386.

- Scott, R.F. (1979). “Subsidence – A review. En: Saxena, S.K. (ed.). Evaluation and prediction of

subsidence". Proc. of the Int. Conf., Pensacola Beach, Florida, January 1978, Am. Soc. Civil Eng., New York, 1-25.

- Sottile R. (2010). "Problematiche geologiche legate agli sprofondamenti in area urbana. L'esempio della città di Palermo: Rifugi antiaerei, Canali sotterranei, Cavità antropiche". Master degree thesis (in italian).

- Stramondo S., Bozzano F., Marra F., Wegmuller U., Cinti F.R., Moro M., Saroli M. (2008). "Subsidence induced by urbanisation in the city of Rome detected by advanced InSAR technique and geotechnical investigations". Remote Sensing of Environment 112 (2008) 3160–3172, doi:10.1016/j.rse.2008.03.008

- Strozzi, T., Tosi, L., Wegmüller, U., Werner, C., Teatini, P., Carbognin, L. (2003). "Land subsidence monitoring service in the lagoon of Venice". Proc. IEEE Int. Geosci. Remote Sens. Symp., IGARSS 2003, Toulouse, 21-25 July, 1, 212 – 214.

- Strozzi, T., Wegm¨uller, U., Tosi, L., Bitelli, G., and Spreckels, V. (2001). "Land Subsidence Monitoring with Differential SAR Interferometry,Photogramm, Eng. Rem. S., 67(11), 1261–1270, 2001.

- Strozzi, T., Wegmüller, U. (1999). "Land subsidence in Mexico City Mapped by ERS Differential SAR Interferometry". Proc. IEEE Int. Geosci. Remote Sens. Symp., IGARSS 1999, Piscataway, New Jersey, 28 June-2 July, 4, 1940-1942.

- Teatini P., Tosi L., and Strozzi T. (2011). "Quantitative evidence that compaction of Holocene sediments drives the present land subsidence of the Po Delta, Italy". J. geophys. Res, Vol. 116., B08407.

- Teatini P., Ferronato M., Gambolati G., and Gonella M. (2006). "Groundwater pumping and land subsidence in the Emilia-Romagna coastland, Italy: Modeling the past occurrence and the future trend". Water Resour. Res., Vol. 42, W01406**.**

- Teatini P., Ferronato M., Gambolati G., Bertoni W., and Gonella M. (2005a). "A century of land subsidence in Ravenna, Italy". Environ. Geol., 47 (6), pp. 831 – 846.

- Teatini P., Tosi L., Strozzi T., Carbognin L., Wegmuller U., and Rizzetto F., (2005b). "Mapping regional land displacements in the Venice coastland by an integrated monitoring system". Remote Sens. Environ., 98(4), 403-413.

- Terzaghi, Karl; Peck, Ralph; Mesri, Gholamreza (1996). "Soil Mechanics in Engineering Practice (3rd Edition)". (Article 16.9) Wiley-Interscience

- Terzaghi K. (1923). "Die Berechnung der Durchlässigkeitziffer des Tones aus dem Verlauf der hydrodynamischen Spannungs- erscheinungen". Akad Wissensch Wien Sitzungsber Math-naturwissensch Klasse IIa 142(3/4), pp 125–138

- Tessitore S.; Herrera G.; Fernández-Merodo J.A.; Tomás R.; Sánchez J.M.; Mallorqui J.J.; Mulas J.;

Cooksley G.; Ramondini M. and Calcaterra D. (2013). “Subsidence numerical modeling due to ground water extraction integrating advanced DInSAR, in situ monitoring and geotechnical data: Murcia case study”. 15th Annual conference of the International Association for Mathematical Geosciences. 2nd – 6th September 2013, Madrid.

- Tomás R.; Romero R.; Mulas J.; Marturia J,; Mallorquı J.; Lopez-Sanchez J.M. ; Herrera G.; Gutierrez J.; González P.J.; Fernandez J.; Duque S.; Concha-Dimas A.; Cocksley G.; Castaneda C.; Carrasco D. y Blanco. P. (2013). “Radar interferometry techniques for the study of ground subsidence phenomena: a review of practical issues through cases in Spain”.Environmental Earth Sciences. Received: 4 September 2012 / Accepted: 16 March 2013 Springer-Verlag Berlin Heidelberg 2013(revista del SCI) DOI 10.1007/s12665-013-2422-z

- Tomás R., García-Barba J., Cano M., Sanabria M. P., Ivorra S., Duro J., Herrera G. (2012). “Subsidence damage assessment of a Gothic church using differential interferometry and field data”. Structural Health Monitoring. 01/2012; 11(6):751-762.

- Tomas R., Herrera G., Cooksley G., Mulas J., (2011). “Persistent Scatterer Interferometry subsidence data exploitation using spatial tools: The Vega Media of the Segura River Basin case study”. Journal of Hydrology, Volume 400, Issues 3–4, 11 April 2011, Pages 411-428, ISSN 0022-1694, http://dx.doi.org/10.1016/j.jhydrol.2011.01.057.

- Tomás, R., Herrera, G., Delgado, J., Lopez-Sanchez, J.M., Mallorquí, J.J., Mulas, J., (2010). “A ground subsidence study based on DInSAR data: Calibration of soil parameters and subsidence prediction in Murcia City (Spain)”. Engineering Geology 111, 19-30.

- Tomás R., Herrera G., Delgado J., Lopez-Sanchez J.M. , Mallorquí J.J., Mulas J. (2010a). “A ground subsidence study based on DInSAR data: Calibration of soil parameters and subsidence prediction in Murcia City (Spain)”. Engineering Geology 111 (2010) 19–30.

- Tomás R., Herrera G., Lopez-Sanchez J.M. , Mallorquí J.J., Mulas J. (2010b). “Monitorización de la subsidencia del terreno de la Vega Media del río Segura mediante Interferometría SAR Diferencial Avanzada”. Ingenieria Civil. Nº 158 CEDEX. . 93-102.

- Tomàs, R. (2009). “Estudio de la subsidencia de la ciudad de Murcia mediante interferometría SAR diferencial avanzada”. Ph. D thesis, unpublished, 2009 (in Spanish).

- Tomás R., Herrera G.,. Delgado J,. Lopez-Sanchez J.M ,. Mallorquí J. J, Mulas J. (2009). ”A model for predicting ground subsidence in Murcia (Spain) based on DInSAR data . Engineering Geology. Vol:111, 19- 30. Ed. Elsevier Holanda.

- Tomás, R.; Márquez, Y.; López-Sanchez, J.M.; Delgado,J.; Blanco, P.; Mallorquí, J.J.; Martínez, M.; Herrera, G; y Mulas, J. (2006). Monitorizacion de la subsidencia del terreno en la Vega Media Del Rio Segura mediante interferometria SAR differencial (DInSAR)”. Geogaceta 39 Sociedad Geológica de España. 107-110.

- Tomas, R.; Márquez, Y.; López – Sánchez, J.M.; Delgado, J.; Blanco, P.; Mallorquí, J.J.; Martínez, M.; Herrera, G.; Mulas, J. (2005). "Mapping ground subsidence induced by aquifer overexploitation using advanced Differential SAR Interferometry: Vega Media of the Segura River (SE Spain) case study". Remote Sensing of Environment 98 (2005) 269 – 283. Elsevier

- Tomás R., Márquez Y., Lopez-Sanchez J.M., Delgado J., Blanco P., Mallorquí J.J., Martínez M., Herrera G., Mulas J., (2005a) - "Mapping ground subsidence induced by aquifer overexploitation using advanced Differential SAR Interferometry: Vega Media of the Segura River (SE Spain) case study". Remote Sensing of Environment, Volume 98, Issues 2–3, 15 October 2005, Pages 269-283, ISSN 0034-4257, http://dx.doi.org/10.1016/j.rse.2005.08.003.

- Thuro, K. and Schubert, W. (2009), "Monitoring, interpretation, and predictation. Messen, Interpretieren und Prognose. Geomechanik Tunnelbau, 2: 214. doi: 10.1002/geot.200990017

- Travelletti J., Oppikofer T., Delacourt C., Malet J.-P., Jaboyedoff M. (2008). "Monitoring landslide displacements during a controlled rain experiment using a long-range terrestrial laser scanning (TLS)". International Archives of Photogrammetry and Remote Sensing, 37 (Part B5), pp. 485-490.

- Ulaby, F.T., R.K. Moore, and A.K. Fung (1982). "Physical mechanisms and empirical models for scattering and emission". In Microwave Remote Sensing: Active and Passive, Vol. II: Radar Remote Sensing and Surface Scattering and Emission Theory. Addison-Wesley Publishing Co., Inc.: 816-921.

- UNE (1994). "Geotecnia, UNE 103-405-94. Ensayo de consolidación unidimensional de un suelo en edómetro". Asociación Española de Normalización y Certificación (AENOR), Madrid, 10 pp.

- UNESCO (1984). "Guidebook to studies of land subsidence due to ground-water withdrawal". Prepared for the International Hydrological Programme, working group 8.4. J.F. Poland (Ed.), USA. Disponible en: http://wwwrcamnl.wr.usgs.gov/rgws/Unesco/

- Vázquez, J.N., De Justo, J.L. (2002a). "La subsidencia en Murcia. Implicaciones y consecuencias en la edificación". Ed. COPOT, Murcia. 262 pp.

- Vázquez, J.N., De Justo, E. (2002b). "Subsidencia unidimensional no lineal de un suelo saturado. Aplicación al Casco Urbano de Murcia". Bol. Soc. Esp. Mec. Suelos e Ing. Geot. 146, 3-8.

- Vázquez, J.N. (2001). "Cálculo de la subsidencia unidimensional debido a los descensos de nivel piezométrico. Aplicación al casco urbano de Murcia y los efectos sobre los edificios". Tesis doctoral, Universidad de Sevilla, 455 pp.

- Velasco-Forero C. A., Sempere-Torres D., Cassiraga E.F., Gómez-Hernández J. J. (2009). "A non-parametric automatic blending methodology to estimate rainfall fields from rain gauge and radar data". Advances in Water Resources, Volume 32, Issue 7, July 2009, Pages 986-1002, ISSN 0309-1708, http://dx.doi.org/10.1016/j.advwatres.2008.10.004.

- Verworn, A., Haberlandt U., (2011). “Spatial interpolation of hourly rainfall effect of additional information, variogram inference and storm properties”. - Hydrol. Earth Syst. Sci., 15: 569-584.

- Wegmüller, U., Strozzi, T., Bitelli, G. (1999). “Validation of ERS differential SAR interferometry for land subsidence mapping: the Bologna Case study”. Proc. IEEE Int. Geosci. Remote Sens. Symp., IGARSS 1999, Piscataway, New Jersey, 28 June-2 July, 2, 1131-1133.

- Wu Y (2003). “Mechanism analysis of hazards caused by the interaction between groundwater and geo-environment”. EnvironGeol 44(7):811–819. doi:10.1007/s00254-003-0819-9

- Xia Y., Kaufmann H., and Guo X.F. (2004). “Landslide monitoring in the Three Georges Area using D-InSAR and corner reflectors”. Photogrammetric Engineering and Remote Sensing, 70/10, 1167-1172.

- Yamamoto, S. (1996). “Recent trends of land subsidence in Japan”. Int. J. Rock Mech. Min. 33, 297.

- Yerro A., Corominas J., Monells D., Mallorquí J. J., (2014). “Analysis of the evolution of ground movements in a low densely urban area by means of DInSAR technique”, Engineering Geology, Volume 170, 20 February 2014, Pages 52-65, ISSN 0013-7952, http://dx.doi.org/10.1016/j.enggeo.2013.12.002.

- Yin J.H., Zhu H.H., Jin W., (2008). “Monitoring of soil nailed slopes and dams using innovative technologies. In: Chen Z, Zhang J-M, Ho K, Wu F-Q, Li Z-K (eds) Landslides and engineered slopes: from the past to the future”. Proceedings of the tenth international symposium on landslides and engineered slopes. Taylor &Francis, Xi’an, pp 1361–1366.

- Young, I. “A Course of Lectures on Natural Philosophy and the Mechanical Arts (4 vols.)”, reprint of 1807 edition, with foreword by N. J. Wade, Thoemmes, Bristol, 2002. Peacock G. & Leitch J. (eds.), Miscellaneous Works of the Late Thomas Young, reprint of 1855 edition, Thoemmes, Bristol, 2003. Peacock’s 1855 biography and the 1845 Kelland edition of Young's Lectures (which unfortunately omitted the 1807 edition’s mathematical supplements) are also available as free downloads from Google Books. There is a copy of the Thoemmes edition of Young’s Lectures in the Institution of Structural Engineers Library

- Zhang, Y., Xue, Y-Q, Wu, J-C, Ye, S-J, Wei, Z-W, Li, Q-F, Yu, J. (2007a). “Characteristics of aquifer system deformation in the Southern Yangtse Delta, China”. Eng. Geol. 90, 160-173.

- Zhang, Y., Xue, Y-Q., Wu, J-C., Ye, S-J., Li, Q-F. (2007b). “Stress-strain measurements of deforming aquifer system that underlie Shangai, China”. Environ. Eng. Geosci. XIII, 217-228.

Annexes

Annex I: CPT processing

List of images and interferograms used for processing Murcia city

C-band images: 149

Date - Satellite

19950721 ers1
19950826 ers2
19950930 ers2
19951104 ers2
19960706 ers2
19961019 ers2
19970412 ers2
19970517 ers2
19970726 ers2
19970830 ers2
19971004 ers2
19971108 ers2
19980117 ers2
19980328 ers2
19980711 ers2
19980919 ers2
19981128 ers2
19990313 ers2
19990417 ers2
19990522 ers2
19990730 ers1
19990731 ers2
19990903 ers1
19990904 ers2
19991009 ers2
19991113 ers2
19991218 ers2
20000122 ers2
20000226 ers2
20000506 ers2
20000610 ers2
20000715 ers2
20000819 ers2
20000923 ers2
20001028 ers2
20001202 ers2
20010106 ers2
20010804 ers2
20010908 ers2
20011013 ers2
20011117 ers2
20011222 ers2
20020302 ers2
20020406 ers2
20020720 ers2
20020824 ers2

20021102 ers2
20021207 ers2
20030111 ers2
20030322 envi
20030322 ers2
20030426 ers2
20030809 ers2
20031018 envi
20031122 ers2
20031227 envi
20040131 envi
20040131 ers2
20040306 envi
20040306 ers2
20040515 ers2
20040619 envi
20040619 ers2
20040724 ers2
20040828 ers2
20041002 ers2
20041106 envi
20041106 ers2
20041211 envi
20041211 ers2
20050115 envi
20050115 ers2
20050219 envi
20050219 ers2
20050326 envi
20050326 ers2
20050430 envi
20050604 envi
20050604 ers2
20050709 ers2
20050813 envi
20050813 ers2
20050917 envi
20050917 ers2
20051022 ers2
20051126 envi
20051126 ers2
20051231 envi
20051231 ers2
20060204 ers2
20060311 ers2
20060415 envi
20060520 ers2
20060624 envi
20060624 ers2
20060729 ers2
20060902 ers2
20061007 envi
20061007 ers2
20061111 ers2

20070331 envi
20070331 ers2
20070505 ers2
20070609 ers2
20070714 ers2
20070818 ers2
20071027 ers2
20071201 ers2
20080105 envi
20080105 ers2
20080209 envi
20080315 envi
20080315 ers2
20080419 envi
20080524 envi
20080524 ers2
20080628 envi
20080628 ers2
20080802 envi
20080802 ers2
20080906 envi
20080906 ers2
20081011 envi
20081115 envi
20081220 envi
20081220 ers2
20090228 envi
20090404 envi
20090404 ers2
20090509 envi
20090509 ers2
20090613 envi
20090613 ers2
20090718 envi
20090827 ers2
20090926 envi
20090926 ers2
20091031 envi
20091031 ers2
20091205 envi
20091205 ers2
20100213 envi
20100213 ers2
20100320 ers2
20100424 envi
20100424 ers2
20100529 envi
20100529 ers2
20100703 ers2

Master image: 20071027 ers2

C-band interferograms: 405

Image 1	-	image 2	spatial baseline
19950721 ers1	-	19960706 ers2	-228.702
19950721 ers1	-	19970517 ers2	139.482
19950721 ers1	-	19970726 ers2	66.6011
19950721 ers1	-	19971004 ers2	-188.715
19950721 ers1	-	19980328 ers2	162.55
19950826 ers2	-	19970517 ers2	-137.247
19950826 ers2	-	19970726 ers2	-207.464
19950826 ers2	-	19980117 ers2	147.326
19950826 ers2	-	19980328 ers2	-112.662
19950930 ers2	-	19951104 ers2	175.554
19950930 ers2	-	19961019 ers2	156.824
19950930 ers2	-	19970412 ers2	51.7262
19951104 ers2	-	19960706 ers2	169.23
19951104 ers2	-	19961019 ers2	-19.2338
19951104 ers2	-	19970412 ers2	-131.87
19951104 ers2	-	19970830 ers2	123.462
19951104 ers2	-	19971004 ers2	210.624
19960706 ers2	-	19961019 ers2	-188.428
19960706 ers2	-	19970830 ers2	-45.8012
19960706 ers2	-	19971004 ers2	58.4772
19961019 ers2	-	19970412 ers2	-112.838
19961019 ers2	-	19970830 ers2	142.294
19961019 ers2	-	19971004 ers2	229.659
19961019 ers2	-	19990417 ers2	-102.721
19970412 ers2	-	19990417 ers2	36.1021
19970412 ers2	-	19990730 ers1	104.871
19970517 ers2	-	19970726 ers2	-76.5881
19970517 ers2	-	19980328 ers2	23.6007
19970517 ers2	-	19981128 ers2	115.115
19970517 ers2	-	19990313 ers2	32.3223
19970517 ers2	-	19990522 ers2	90.8926
19970517 ers2	-	19990903 ers1	136.572
19970517 ers2	-	20000122 ers2	-31.6824
19970726 ers2	-	19980328 ers2	98.435
19970726 ers2	-	19981128 ers2	192.921
19970726 ers2	-	19990313 ers2	95.9146
19970726 ers2	-	19990522 ers2	159.244
19970726 ers2	-	19990731 ers2	-239.5
19970726 ers2	-	19990903 ers1	213.931
19970726 ers2	-	19991218 ers2	-231.549
19970726 ers2	-	20000122 ers2	48.4627
19970830 ers2	-	19971004 ers2	93.638
19970830 ers2	-	19990417 ers2	-244.813
19970830 ers2	-	19990730 ers1	-149.897
19970830 ers2	-	19990731 ers2	100.399
19970830 ers2	-	19991113 ers2	28.1603
19970830 ers2	-	19991218 ers2	138.364
19970830 ers2	-	20000506 ers2	25.3009
19971004 ers2	-	19990730 ers1	-239.338

19971004 ers2 - 19990731 ers2	49.7058
19971004 ers2 - 19991113 ers2	-63.9874
19971004 ers2 - 19991218 ers2	47.1251
19971004 ers2 - 20000506 ers2	-89.9925
19971108 ers2 - 19980117 ers2	-220.171
19971108 ers2 - 19980711 ers2	-39.215
19971108 ers2 - 19980919 ers2	28.0451
19971108 ers2 - 19990904 ers2	-106.961
19971108 ers2 - 19991009 ers2	210.512
19971108 ers2 - 20000226 ers2	-36.5892
19971108 ers2 - 20000610 ers2	-55.6764
19980117 ers2 - 19980711 ers2	213.112
19980117 ers2 - 19980919 ers2	243.185
19980117 ers2 - 19981128 ers2	-178.349
19980117 ers2 - 19990522 ers2	-194.963
19980117 ers2 - 19990903 ers1	-147.203
19980117 ers2 - 19990904 ers2	128.505
19980117 ers2 - 20000226 ers2	196.848
19980117 ers2 - 20000610 ers2	210.857
19980328 ers2 - 19981128 ers2	98.1293
19980328 ers2 - 19990313 ers2	-45.3571
19980328 ers2 - 19990522 ers2	66.0831
19980328 ers2 - 19990903 ers1	115.888
19980328 ers2 - 20000122 ers2	-55.2495
19980328 ers2 - 20000819 ers2	22.2854
19980328 ers2 - 20001028 ers2	-84.9566
19980328 ers2 - 20001202 ers2	-198.59
19980711 ers2 - 19980919 ers2	36.7012
19980711 ers2 - 19990904 ers2	-88.1993
19980711 ers2 - 19991009 ers2	213.788
19980711 ers2 - 20000226 ers2	-16.7703
19980711 ers2 - 20000610 ers2	-16.503
19980711 ers2 - 20010106 ers2	-107.177
19980919 ers2 - 19990904 ers2	-123.908
19980919 ers2 - 19991009 ers2	184.43
19980919 ers2 - 20000226 ers2	-48.965
19980919 ers2 - 20000610 ers2	-53.6319
19980919 ers2 - 20010106 ers2	-141.23
19981128 ers2 - 19990313 ers2	-103.728
19981128 ers2 - 19990522 ers2	-77.312
19981128 ers2 - 19990903 ers1	30.8606
19981128 ers2 - 20000122 ers2	-143.918
19981128 ers2 - 20000819 ers2	-86.3355
19981128 ers2 - 20001028 ers2	-179.295
19990313 ers2 - 19990522 ers2	103.713
19990313 ers2 - 19990903 ers1	131.059
19990313 ers2 - 20000122 ers2	-45.2739
19990313 ers2 - 20001028 ers2	-83.1069
19990313 ers2 - 20001202 ers2	-192.895
19990417 ers2 - 19990730 ers1	99.7708
19990417 ers2 - 20000923 ers2	12.4152
19990417 ers2 - 20011013 ers2	218.953
19990522 ers2 - 19990903 ers1	77.6949
19990522 ers2 - 20000122 ers2	-121.844

19990522 ers2 - 20000819 ers2	-78.7496
19990522 ers2 - 20001028 ers2	-146.505
19990730 ers1 - 19990731 ers2	249.637
19990730 ers1 - 19991113 ers2	176.443
19990730 ers1 - 20011013 ers2	128.822
19990731 ers2 - 19991113 ers2	-79.2757
19990731 ers2 - 19991218 ers2	88.1077
19990731 ers2 - 20000506 ers2	-83.974
19990731 ers2 - 20001202 ers2	143.056
19990731 ers2 - 20011013 ers2	-214.078
19990731 ers2 - 20011117 ers2	237.052
19990903 ers1 - 20000122 ers2	-167.235
19990903 ers1 - 20001028 ers2	-200.325
19990904 ers2 - 20000226 ers2	73.5236
19990904 ers2 - 20000610 ers2	83.3233
19990904 ers2 - 20010106 ers2	-20.0676
19990904 ers2 - 20010908 ers2	220.304
19991009 ers2 - 20000226 ers2	-229.82
19991009 ers2 - 20000610 ers2	-218.893
19991009 ers2 - 20010908 ers2	-234.264
19991113 ers2 - 19991218 ers2	110.361
19991113 ers2 - 20000506 ers2	-32.9839
19991113 ers2 - 20001202 ers2	220.535
19991113 ers2 - 20011013 ers2	-173.486
19991218 ers2 - 20000506 ers2	-136.888
19991218 ers2 - 20001028 ers2	242.712
19991218 ers2 - 20001202 ers2	157.812
20000122 ers2 - 20000819 ers2	57.5941
20000122 ers2 - 20001028 ers2	-35.1901
20000122 ers2 - 20001202 ers2	-147.867
20000226 ers2 - 20000610 ers2	28.1491
20000226 ers2 - 20000715 ers2	116.382
20000226 ers2 - 20010106 ers2	-92.5886
20000226 ers2 - 20010908 ers2	165.701
20000226 ers2 - 20020824 ers2	81.9642
20000506 ers2 - 20001202 ers2	226.38
20000506 ers2 - 20011013 ers2	-140.802
20000506 ers2 - 20020302 ers2	-211.182
20000610 ers2 - 20000715 ers2	101.22
20000610 ers2 - 20010106 ers2	-103.273
20000610 ers2 - 20010908 ers2	186.487
20000610 ers2 - 20020824 ers2	77.3767
20000715 ers2 - 20010106 ers2	-204.461
20000715 ers2 - 20010908 ers2	-190.707
20000715 ers2 - 20020824 ers2	-47.5994
20000819 ers2 - 20001028 ers2	-91.6455
20000819 ers2 - 20001202 ers2	-205.323
20000923 ers2 - 20010804 ers2	-191.651
20000923 ers2 - 20011013 ers2	215.637
20001028 ers2 - 20001202 ers2	-112.941
20001028 ers2 - 20011117 ers2	-173.843
20001202 ers2 - 20011117 ers2	136.972
20010106 ers2 - 20010908 ers2	227.501
20010106 ers2 - 20020824 ers2	174.373

20010804 ers2 - 20020302 ers2	206.232
20010908 ers2 - 20020824 ers2	148.731
20011013 ers2 - 20021102 ers2	-188.987
20011222 ers2 - 20040515 ers2	-126.872
20011222 ers2 - 20040619 ers2	178.869
20020302 ers2 - 20030111 ers2	170.519
20020406 ers2 - 20030426 ers2	-123.812
20020406 ers2 - 20040828 ers2	-167.748
20021207 ers2 - 20040724 ers2	-54.0206
20030322 envi - 20040306 envi	142.867
20030322 envi - 20040619 envi	168.895
20030322 envi - 20041106 envi	225.346
20030322 envi - 20050917 envi	157.978
20030322 envi - 20051126 envi	160.983
20030426 ers2 - 20040828 ers2	-48.2899
20030426 ers2 - 20050219 ers2	-215.231
20030426 ers2 - 20051022 ers2	178.226
20030809 ers2 - 20040515 ers2	-93.5415
20031018 envi - 20031227 envi	70.3373
20031018 envi - 20040131 envi	80.3182
20031018 envi - 20050430 envi	149.146
20031122 ers2 - 20041002 ers2	28.5412
20031227 envi - 20040131 envi	52.3834
20031227 envi - 20050430 envi	91.4694
20040131 envi - 20050430 envi	75.9719
20040306 envi - 20040619 envi	26.5044
20040306 envi - 20041106 envi	82.6488
20040306 envi - 20041211 envi	134.788
20040306 envi - 20050813 envi	188.767
20040306 envi - 20050917 envi	42.8635
20040306 envi - 20051126 envi	23.3278
20040306 envi - 20051231 envi	-104.289
20040306 envi - 20060415 envi	199.521
20040515 ers2 - 20050115 ers2	205.308
20040515 ers2 - 20051022 ers2	-247.059
20040619 envi - 20041106 envi	57.4604
20040619 envi - 20041211 envi	107.73
20040619 envi - 20050813 envi	161.336
20040619 envi - 20050917 envi	-54.2314
20040619 envi - 20051126 envi	-10.2751
20040619 envi - 20051231 envi	-124.644
20040619 envi - 20060415 envi	174.952
20040724 ers2 - 20051231 ers2	151.36
20040828 ers2 - 20041002 ers2	-125.032
20040828 ers2 - 20050219 ers2	-189.159
20040828 ers2 - 20051022 ers2	156.7
20040828 ers2 - 20070505 ers2	109.525
20041106 envi - 20041211 envi	55.2508
20041106 envi - 20050115 envi	245.237
20041106 envi - 20050813 envi	110.058
20041106 envi - 20050917 envi	-83.9795
20041106 envi - 20051126 envi	-67.0073
20041106 envi - 20051231 envi	-181.787
20041106 envi - 20060415 envi	117.514

20041106 ers2 - 20061111 ers2	166.042
20041211 envi - 20050115 envi	199.204
20041211 envi - 20050604 envi	207.63
20041211 envi - 20050813 envi	53.3841
20041211 envi - 20050917 envi	-141.163
20041211 envi - 20051126 envi	-115.757
20041211 envi - 20051231 envi	-226.837
20041211 envi - 20060415 envi	79.0955
20041211 ers2 - 20050604 ers2	12.9512
20050115 envi - 20050604 envi	50.7741
20050115 envi - 20050813 envi	-155.191
20050115 envi - 20060415 envi	-128.311
20050219 envi - 20050326 envi	109.703
20050219 envi - 20061007 envi	-59.2725
20050326 envi - 20061007 envi	-142.119
20050326 ers2 - 20060902 ers2	-163.294
20050430 envi - 20060624 envi	237.749
20050430 envi - 20070331 envi	186.281
20050604 envi - 20050813 envi	-156.626
20050604 envi - 20060415 envi	-151.184
20050604 envi - 20080105 envi	97.577
20050709 ers2 - 20060311 ers2	71.6708
20050813 envi - 20050917 envi	-195.653
20050813 envi - 20051126 envi	-168.719
20050813 envi - 20060415 envi	65.5659
20050813 envi - 20080315 envi	-71.2647
20050917 envi - 20051126 envi	57.9155
20050917 envi - 20051231 envi	-135.718
20050917 envi - 20060415 envi	190.422
20050917 envi - 20080315 envi	122.892
20050917 envi - 20080524 envi	62.3163
20051022 ers2 - 20070505 ers2	-57.0939
20051022 ers2 - 20080628 ers2	226.562
20051126 envi - 20051231 envi	-113.631
20051126 envi - 20060415 envi	185.21
20051126 envi - 20080315 envi	105.929
20051126 envi - 20080524 envi	3.78374
20051126 envi - 20080628 envi	-101.891
20051126 envi - 20080802 envi	-104.744
20051126 ers2 - 20061111 ers2	-107.746
20051231 envi - 20080209 envi	-220.75
20051231 envi - 20080315 envi	219.809
20051231 envi - 20080419 envi	-193.009
20051231 envi - 20080524 envi	117.411
20051231 envi - 20080628 envi	45.656
20051231 envi - 20080802 envi	39.2635
20051231 envi - 20080906 envi	-192.041
20051231 ers2 - 20061216 ers2	-92.4492
20060415 envi - 20080105 envi	234.085
20060415 envi - 20080315 envi	-79.2681
20060415 envi - 20080524 envi	-181.415
20060415 envi - 20081011 envi	-133.539
20060415 envi - 20081220 envi	42.2642
20060520 ers2 - 20080524 ers2	46.556

20060624 envi - 20070331 envi	-66.9231
20060624 envi - 20080209 envi	75.556
20060624 envi - 20080419 envi	105.369
20060624 envi - 20080906 envi	110.66
20060624 envi - 20081115 envi	183.495
20060624 envi - 20090228 envi	138.088
20060902 ers2 - 20061007 ers2	-218.981
20061007 envi - 20080105 envi	-178.369
20070331 envi - 20080209 envi	124.414
20070331 envi - 20080419 envi	151.103
20070331 envi - 20080906 envi	152.486
20070331 envi - 20081115 envi	239.982
20070331 envi - 20090228 envi	197.07
20070331 envi - 20090404 envi	-117.692
20070331 envi - 20090613 envi	159.708
20070331 envi - 20090926 envi	-201.688
20070331 envi - 20091205 envi	235.617
20070331 ers2 - 20070818 ers2	-170.901
20070505 ers2 - 20080628 ers2	249.141
20070609 ers2 - 20080524 ers2	180.173
20071027 ers2 - 20080105 ers2	-60.7626
20071027 ers2 - 20081220 ers2	-87.6822
20071201 ers2 - 20080105 ers2	219.865
20071201 ers2 - 20081220 ers2	172.406
20080105 envi - 20081220 envi	-193.026
20080105 ers2 - 20081220 ers2	-47.5256
20080209 envi - 20080419 envi	28.0483
20080209 envi - 20080628 envi	228.765
20080209 envi - 20080802 envi	224.957
20080209 envi - 20080906 envi	33.0912
20080209 envi - 20081115 envi	115.994
20080209 envi - 20090228 envi	75.8365
20080209 envi - 20090404 envi	-242.045
20080209 envi - 20090613 envi	37.4032
20080209 envi - 20090718 envi	215.859
20080209 envi - 20091205 envi	111.236
20080209 envi - 20100213 envi	-135.421
20080209 envi - 20100424 envi	36.3249
20080315 envi - 20080524 envi	-102.156
20080315 envi - 20080628 envi	-206.617
20080315 envi - 20080802 envi	-209.92
20080315 envi - 20081011 envi	-58.6048
20080315 envi - 20081220 envi	116.988
20080315 envi - 20090509 envi	-64.5597
20080315 envi - 20090718 envi	-219.364
20080315 envi - 20091031 envi	-33.2031
20080315 envi - 20100529 envi	-79.1179
20080419 envi - 20080628 envi	203.983
20080419 envi - 20080802 envi	199.758
20080419 envi - 20080906 envi	5.42002
20080419 envi - 20081115 envi	93.0457
20080419 envi - 20090228 envi	60.6028
20080419 envi - 20090613 envi	29.1799
20080419 envi - 20090718 envi	191.116

20080419 envi - 20091205 envi	85.7404
20080419 envi - 20100213 envi	-162.923
20080419 envi - 20100424 envi	6.62196
20080524 envi - 20080628 envi	-106.106
20080524 envi - 20080802 envi	-108.757
20080524 envi - 20081011 envi	51.8431
20080524 envi - 20081115 envi	-218.352
20080524 envi - 20081220 envi	219.638
20080524 envi - 20090509 envi	39.5318
20080524 envi - 20090718 envi	-118.68
20080524 envi - 20091031 envi	81.2651
20080524 envi - 20091205 envi	-221.775
20080524 envi - 20100529 envi	23.7836
20080628 envi - 20080802 envi	-3.69042
20080628 envi - 20080906 envi	-204.32
20080628 envi - 20081011 envi	149.635
20080628 envi - 20081115 envi	-113.083
20080628 envi - 20090228 envi	-157.987
20080628 envi - 20090509 envi	142.052
20080628 envi - 20090613 envi	-193.557
20080628 envi - 20090718 envi	-13.3104
20080628 envi - 20091031 envi	179.875
20080628 envi - 20091205 envi	-117.641
20080628 envi - 20100424 envi	-197.902
20080628 envi - 20100529 envi	129.583
20080802 envi - 20080906 envi	-199.972
20080802 envi - 20081011 envi	153.562
20080802 envi - 20081115 envi	-109.702
20080802 envi - 20090228 envi	-155.093
20080802 envi - 20090509 envi	145.491
20080802 envi - 20090613 envi	-190.156
20080802 envi - 20090718 envi	-10.6127
20080802 envi - 20091031 envi	183.913
20080802 envi - 20091205 envi	-113.728
20080802 envi - 20100424 envi	-193.625
20080802 envi - 20100529 envi	132.413
20080906 envi - 20081115 envi	96.0617
20080906 envi - 20090228 envi	67.4452
20080906 envi - 20090613 envi	38.6768
20080906 envi - 20090718 envi	192.397
20080906 envi - 20091205 envi	87.346
20080906 envi - 20100213 envi	-164.892
20080906 envi - 20100424 envi	6.90283
20080906 ers2 - 20090509 ers2	163.236
20080906 ers2 - 20090926 ers2	192.183
20080906 ers2 - 20091205 ers2	-180.324
20081011 envi - 20081220 envi	173.704
20081011 envi - 20090509 envi	-11.4249
20081011 envi - 20090718 envi	-162.235
20081011 envi - 20091031 envi	30.4896
20081011 envi - 20100529 envi	-33.2949
20081115 envi - 20090228 envi	-46.4302
20081115 envi - 20090613 envi	-80.4894
20081115 envi - 20090718 envi	100.223

20081115 envi - 20091205 envi	-11.1892
20081115 envi - 20100424 envi	-87.5573
20081115 envi - 20100529 envi	242.076
20081220 envi - 20090509 envi	-181.05
20081220 envi - 20091031 envi	-144.061
20081220 envi - 20100529 envi	-195.968
20090228 envi - 20090613 envi	-37.0795
20090228 envi - 20090718 envi	144.945
20090228 envi - 20091205 envi	47.0037
20090228 envi - 20100213 envi	-206.596
20090228 envi - 20100424 envi	-57.4269
20090404 envi - 20090926 envi	-84.6771
20090404 envi - 20100213 envi	106.881
20090509 envi - 20090718 envi	-154.904
20090509 envi - 20091031 envi	41.9344
20090509 envi - 20100529 envi	-18.5274
20090509 ers2 - 20090926 ers2	71.4962
20090613 envi - 20090718 envi	180.711
20090613 envi - 20091205 envi	77.2478
20090613 envi - 20100213 envi	-169.918
20090613 envi - 20100424 envi	-29.8293
20090718 envi - 20091031 envi	192.768
20090718 envi - 20091205 envi	-104.756
20090718 envi - 20100424 envi	-185.062
20090718 envi - 20100529 envi	142.241
20090926 envi - 20100213 envi	191.73
20091031 envi - 20100529 envi	-59.9883
20091205 envi - 20100213 envi	-246.525
20091205 envi - 20100424 envi	-79.7447
20091205 envi - 20100529 envi	245.597
20100109 ers2 - 20100213 ers2	211.78
20100213 envi - 20100424 envi	169.448

X-band images: 117

Date - Satellite

20080718 tsx1
20080809 tsx1
20080820 tsx1
20080831 tsx1
20080911 tsx1
20080922 tsx1
20081003 tsx1
20081014 tsx1
20081025 tsx1
20081105 tsx1
20081116 tsx1
20081208 tsx1
20081219 tsx1
20090110 tsx1

20090201 tsx1
20090212 tsx1
20090223 tsx1
20090306 tsx1
20090317 tsx1
20090328 tsx1
20090408 tsx1
20090419 tsx1
20090430 tsx1
20090511 tsx1
20090522 tsx1
20090602 tsx1
20090624 tsx1
20090705 tsx1
20090716 tsx1
20090727 tsx1
20090807 tsx1
20090829 tsx1
20090909 tsx1
20090920 tsx1
20091012 tsx1
20091023 tsx1
20091114 tsx1
20091125 tsx1
20091206 tsx1
20091217 tsx1
20091228 tsx1
20100108 tsx1
20100119 tsx1
20100130 tsx1
20100210 tsx1
20100221 tsx1
20100304 tsx1
20100315 tsx1
20100326 tsx1
20100406 tsx1
20100417 tsx1
20100428 tsx1
20100509 tsx1
20100520 tsx1
20100622 tsx1
20100703 tsx1
20100725 tsx1
20100805 tsx1
20100816 tsx1
20100907 tsx1
20100918 tsx1
20100929 tsx1
20101112 tsx1
20101123 tsx1
20101215 tsx1
20101226 tsx1
20110106 tsx1
20110117 tsx1

20110128 tsx1
20110208 tsx1
20110219 tsx1
20110302 tsx1
20110313 tsx1
20110324 tsx1
20110404 tsx1
20110415 tsx1
20110426 tsx1
20110507 tsx1
20110529 tsx1
20110609 tsx1
20110620 tsx1
20110701 tsx1
20110712 tsx1
20110723 tsx1
20110803 tsx1
20110814 tsx1
20110905 tsx1
20111008 tsx1
20111019 tsx1
20111121 tsx1
20111213 tsx1
20111224 tsx1
20120104 tsx1
20120115 tsx1
20120126 tsx1
20120206 tsx1
20120217 tsx1
20120228 tsx1
20120310 tsx1
20120412 tsx1
20120423 tsx1
20120504 tsx1
20120515 tsx1
20120709 tsx1
20120731 tsx1
20120811 tsx1
20120822 tsx1
20120902 tsx1
20120913 tsx1
20121005 tsx1
20121016 tsx1
20121027 tsx1
20121107 tsx1
20121118 tsx1
20121129 tsx1
20121210 tsx1
20121221 tsx1

Master image: 20100622 tsx1

X-band interferograms: 308

Image 1	–	image 2	spatial baseline
20080718 tsx1		20080820 tsx1	-141.166
20080718 tsx1		20080911 tsx1	81.2888
20080718 tsx1		20080922 tsx1	-114.385
20080718 tsx1		20081105 tsx1	8.70475
20080718 tsx1		20081219 tsx1	31.5997
20080718 tsx1		20090306 tsx1	-52.6382
20080809 tsx1		20080820 tsx1	152.356
20080809 tsx1		20080831 tsx1	57.4665
20080809 tsx1		20081025 tsx1	30.6086
20080820 tsx1		20080831 tsx1	-94.8896
20080820 tsx1		20080922 tsx1	30.8819
20080820 tsx1		20081003 tsx1	-48.7600
20080820 tsx1		20081014 tsx1	23.4409
20080820 tsx1		20090110 tsx1	-40.2733
20080831 tsx1		20081003 tsx1	46.7116
20080831 tsx1		20081025 tsx1	-26.8733
20080831 tsx1		20081116 tsx1	24.5953
20080911 tsx1		20081219 tsx1	-49.7166
20080911 tsx1		20090212 tsx1	-38.0465
20080911 tsx1		20090317 tsx1	-38.8292
20080922 tsx1		20081014 tsx1	-15.0406
20080922 tsx1		20090201 tsx1	4.28065
20080922 tsx1		20090306 tsx1	62.5229
20081003 tsx1		20081116 tsx1	-25.7510
20081003 tsx1		20081208 tsx1	-13.2843
20081003 tsx1		20090110 tsx1	12.0672
20081014 tsx1		20090110 tsx1	-63.6439
20081014 tsx1		20090201 tsx1	12.7132
20081014 tsx1		20090430 tsx1	-36.3352
20081025 tsx1		20081116 tsx1	50.9723
20081025 tsx1		20090223 tsx1	35.1662
20081105 tsx1		20081219 tsx1	24.1879
20081105 tsx1		20090306 tsx1	-58.3746
20081116 tsx1		20081208 tsx1	12.9808
20081116 tsx1		20090223 tsx1	-18.4109
20081208 tsx1		20090110 tsx1	21.6470
20081208 tsx1		20090223 tsx1	-25.5938
20081208 tsx1		20090408 tsx1	-16.4898
20081219 tsx1		20090212 tsx1	11.7282
20081219 tsx1		20090317 tsx1	12.9444
20081219 tsx1		20090727 tsx1	-47.8749
20090110 tsx1		20090328 tsx1	10.8225
20090110 tsx1		20090408 tsx1	-36.8372
20090110 tsx1		20090430 tsx1	27.3179
20090110 tsx1		20090602 tsx1	-13.2511
20090201 tsx1		20090306 tsx1	60.1962
20090201 tsx1		20090419 tsx1	-12.9122
20090201 tsx1		20090430 tsx1	-44.4521
20090201 tsx1		20090624 tsx1	49.7861

20090201 tsx1 20090716 tsx1 7.09028
20090212 tsx1 20090317 tsx1 -7.19481
20090223 tsx1 20090408 tsx1 11.7961
20090223 tsx1 20090807 tsx1 -60.7754
20090306 tsx1 20090624 tsx1 -27.0557
20090306 tsx1 20090727 tsx1 34.5807
20090317 tsx1 20090727 tsx1 -57.9447
20090317 tsx1 20090829 tsx1 -50.5091
20090328 tsx1 20090430 tsx1 19.7394
20090328 tsx1 20090511 tsx1 8.66590
20090328 tsx1 20090602 tsx1 -22.4207
20090408 tsx1 20090522 tsx1 6.87520
20090408 tsx1 20090602 tsx1 23.6023
20090408 tsx1 20090807 tsx1 -69.2737
20090419 tsx1 20090430 tsx1 -32.6831
20090419 tsx1 20090705 tsx1 10.3145
20090419 tsx1 20090716 tsx1 17.2334
20090430 tsx1 20090511 tsx1 -13.0262
20090430 tsx1 20090705 tsx1 38.7563
20090430 tsx1 20090909 tsx1 -26.3591
20090430 tsx1 20091114 tsx1 12.6192
20090511 tsx1 20090602 tsx1 -27.5087
20090511 tsx1 20090909 tsx1 -17.9100
20090522 tsx1 20090602 tsx1 18.0963
20090522 tsx1 20090807 tsx1 -74.9021
20090522 tsx1 20090909 tsx1 41.1516
20090522 tsx1 20091125 tsx1 36.6950
20090522 tsx1 20091206 tsx1 -44.6278
20090602 tsx1 20090909 tsx1 24.2695
20090624 tsx1 20090716 tsx1 -42.7173
20090624 tsx1 20090727 tsx1 53.8279
20090624 tsx1 20090920 tsx1 -22.6162
20090624 tsx1 20091023 tsx1 25.1796
20090705 tsx1 20090716 tsx1 16.4051
20090705 tsx1 20091114 tsx1 -26.6963
20090716 tsx1 20090920 tsx1 24.8604
20090716 tsx1 20091012 tsx1 18.3058
20090716 tsx1 20091114 tsx1 -37.2272
20090727 tsx1 20090829 tsx1 7.46637
20090727 tsx1 20091023 tsx1 -35.4340
20090807 tsx1 20091228 tsx1 6.85108
20090829 tsx1 20091023 tsx1 -42.8766
20090829 tsx1 20100221 tsx1 45.4488
20090829 tsx1 20100406 tsx1 -22.6502
20090829 tsx1 20100417 tsx1 -21.9892
20090909 tsx1 20091114 tsx1 36.6982
20090909 tsx1 20091125 tsx1 -8.69107
20090920 tsx1 20091012 tsx1 -13.9271
20090920 tsx1 20091023 tsx1 28.4231
20091012 tsx1 20091023 tsx1 38.5270
20091012 tsx1 20091114 tsx1 -54.3942
20091012 tsx1 20100108 tsx1 -31.2167
20091012 tsx1 20100130 tsx1 -28.5410
20091012 tsx1 20100315 tsx1 30.1249

20091023 tsx1 20100315 tsx1 -12.2090
20091023 tsx1 20100406 tsx1 20.2689
20091114 tsx1 20091125 tsx1 -35.8605
20091114 tsx1 20100108 tsx1 23.3286
20091114 tsx1 20100119 tsx1 21.4115
20091114 tsx1 20100326 tsx1 -35.5067
20091125 tsx1 20091206 tsx1 -79.9132
20091125 tsx1 20100326 tsx1 5.01706
20091125 tsx1 20100520 tsx1 -51.1248
20091206 tsx1 20091217 tsx1 -9.65252
20091206 tsx1 20100520 tsx1 28.8074
20091217 tsx1 20091228 tsx1 -23.0560
20091217 tsx1 20100509 tsx1 -5.72668
20091217 tsx1 20100520 tsx1 35.4190
20091228 tsx1 20100509 tsx1 17.9649
20100108 tsx1 20100119 tsx1 -5.58538
20100108 tsx1 20100130 tsx1 13.1901
20100119 tsx1 20100130 tsx1 11.3840
20100119 tsx1 20100326 tsx1 -56.4447
20100119 tsx1 20100622 tsx1 -38.3653
20100119 tsx1 20100816 tsx1 -11.3007
20100130 tsx1 20100315 tsx1 47.7449
20100130 tsx1 20100428 tsx1 36.7574
20100130 tsx1 20100816 tsx1 -22.1283
20100210 tsx1 20100304 tsx1 -83.2579
20100210 tsx1 20100929 tsx1 -7.46883
20100221 tsx1 20100304 tsx1 17.1579
20100221 tsx1 20100417 tsx1 -65.8491
20100221 tsx1 20100725 tsx1 -15.2577
20100304 tsx1 20100725 tsx1 -20.4454
20100304 tsx1 20100929 tsx1 76.0704
20100315 tsx1 20100406 tsx1 31.3844
20100315 tsx1 20100428 tsx1 -15.9619
20100315 tsx1 20100703 tsx1 22.8390
20100326 tsx1 20100520 tsx1 -52.9864
20100326 tsx1 20100622 tsx1 21.7829
20100326 tsx1 20100918 tsx1 -12.2178
20100406 tsx1 20100417 tsx1 10.8126
20100406 tsx1 20100703 tsx1 -12.0989
20100417 tsx1 20100703 tsx1 -12.2567
20100417 tsx1 20100725 tsx1 64.4753
20100428 tsx1 20100703 tsx1 34.2823
20100428 tsx1 20100816 tsx1 -57.4403
20100428 tsx1 20101123 tsx1 -9.83204
20100509 tsx1 20100520 tsx1 38.4734
20100509 tsx1 20100805 tsx1 28.0599
20100520 tsx1 20100805 tsx1 -10.5805
20100520 tsx1 20100918 tsx1 42.4929
20100622 tsx1 20100816 tsx1 32.2936
20100622 tsx1 20100907 tsx1 15.6343
20100622 tsx1 20100918 tsx1 -33.5946
20100703 tsx1 20100725 tsx1 76.6703
20100703 tsx1 20101123 tsx1 -43.4500
20100703 tsx1 20101215 tsx1 32.2391

20100703 tsx1 20110106 tsx1 11.2294
20100725 tsx1 20100929 tsx1 93.1393
20100725 tsx1 20101215 tsx1 -44.4467
20100725 tsx1 20110128 tsx1 -3.73876
20100805 tsx1 20100918 tsx1 52.8346
20100805 tsx1 20110219 tsx1 15.8891
20100816 tsx1 20100907 tsx1 -17.2184
20100816 tsx1 20101112 tsx1 11.4481
20100816 tsx1 20101123 tsx1 47.6969
20100907 tsx1 20100918 tsx1 -43.1608
20100907 tsx1 20101112 tsx1 27.7229
20100907 tsx1 20101226 tsx1 -32.3650
20100918 tsx1 20101226 tsx1 17.3156
20100918 tsx1 20110219 tsx1 -38.7133
20100929 tsx1 20110128 tsx1 -93.3067
20101112 tsx1 20101123 tsx1 36.2619
20101112 tsx1 20101226 tsx1 -59.8368
20101112 tsx1 20110117 tsx1 22.5563
20101112 tsx1 20110415 tsx1 -10.3805
20101123 tsx1 20110106 tsx1 49.1771
20101123 tsx1 20110117 tsx1 -14.2503
20101123 tsx1 20110302 tsx1 9.14031
20101215 tsx1 20110106 tsx1 -27.2227
20101215 tsx1 20110128 tsx1 44.0863
20101215 tsx1 20110208 tsx1 -17.9182
20101215 tsx1 20110313 tsx1 28.9312
20101215 tsx1 20110426 tsx1 2.78523
20101226 tsx1 20110219 tsx1 -46.0208
20101226 tsx1 20110404 tsx1 -9.21045
20101226 tsx1 20110415 tsx1 58.6629
20110106 tsx1 20110208 tsx1 15.2050
20110106 tsx1 20110302 tsx1 -45.7573
20110106 tsx1 20110324 tsx1 13.3171
20110117 tsx1 20110302 tsx1 19.9277
20110117 tsx1 20110415 tsx1 -21.8928
20110128 tsx1 20110313 tsx1 -17.5619
20110208 tsx1 20110324 tsx1 -6.54027
20110208 tsx1 20110426 tsx1 18.8751
20110219 tsx1 20110404 tsx1 40.3349
20110219 tsx1 20110529 tsx1 13.6300
20110219 tsx1 20110814 tsx1 -150.927
20110302 tsx1 20110324 tsx1 46.7804
20110302 tsx1 20110415 tsx1 -41.3138
20110302 tsx1 20110609 tsx1 2.42402
20110313 tsx1 20110426 tsx1 -26.8759
20110313 tsx1 20110712 tsx1 -22.9932
20110324 tsx1 20110426 tsx1 25.4158
20110324 tsx1 20110609 tsx1 -44.3569
20110324 tsx1 20110723 tsx1 11.3317
20110324 tsx1 20110803 tsx1 -31.4237
20110404 tsx1 20110415 tsx1 64.4822
20110404 tsx1 20110507 tsx1 11.4880
20110404 tsx1 20110529 tsx1 -26.8271
20110404 tsx1 20110620 tsx1 54.8431

20110415 tsx1 20110609 tsx1 43.7269
20110415 tsx1 20110620 tsx1 -11.2722
20110415 tsx1 20110905 tsx1 29.1028
20110426 tsx1 20110712 tsx1 6.19573
20110426 tsx1 20110723 tsx1 -22.7960
20110507 tsx1 20110529 tsx1 -27.5816
20110507 tsx1 20110620 tsx1 54.1239
20110507 tsx1 20110701 tsx1 -11.8180
20110529 tsx1 20110701 tsx1 19.4712
20110529 tsx1 20111121 tsx1 -131.333
20110529 tsx1 20120104 tsx1 12.5578
20110609 tsx1 20110803 tsx1 12.9639
20110609 tsx1 20110905 tsx1 -24.6148
20110620 tsx1 20110701 tsx1 -61.6267
20110620 tsx1 20110905 tsx1 34.5156
20110620 tsx1 20111008 tsx1 14.9920
20110620 tsx1 20111224 tsx1 -16.6722
20110701 tsx1 20111224 tsx1 47.4799
20110701 tsx1 20120104 tsx1 -9.05244
20110701 tsx1 20120115 tsx1 30.3367
20110712 tsx1 20110723 tsx1 -28.9884
20110712 tsx1 20111019 tsx1 -35.6122
20110712 tsx1 20120126 tsx1 -5.06393
20110712 tsx1 20120228 tsx1 60.4667
20110723 tsx1 20110803 tsx1 -39.2982
20110723 tsx1 20111019 tsx1 -11.3247
20110803 tsx1 20110905 tsx1 -36.4965
20110803 tsx1 20111019 tsx1 28.3684
20110803 tsx1 20120217 tsx1 -24.0087
20110814 tsx1 20111121 tsx1 33.2161
20110905 tsx1 20111008 tsx1 -19.5514
20110905 tsx1 20120217 tsx1 12.5338
20111008 tsx1 20111213 tsx1 -12.9101
20111008 tsx1 20111224 tsx1 -31.5750
20111008 tsx1 20120217 tsx1 29.3009
20111019 tsx1 20120126 tsx1 30.5615
20111019 tsx1 20120217 tsx1 -50.5987
20111019 tsx1 20120515 tsx1 -7.58683
20111121 tsx1 20120104 tsx1 143.659
20111121 tsx1 20120412 tsx1 132.092
20111213 tsx1 20111224 tsx1 -20.3520
20111213 tsx1 20120217 tsx1 39.8481
20111213 tsx1 20120310 tsx1 19.5657
20111224 tsx1 20120115 tsx1 -24.0040
20111224 tsx1 20120206 tsx1 -26.0006
20111224 tsx1 20120310 tsx1 39.6576
20120104 tsx1 20120115 tsx1 35.8518
20120104 tsx1 20120206 tsx1 30.3020
20120104 tsx1 20120412 tsx1 -11.5772
20120104 tsx1 20120504 tsx1 -5.82186
20120115 tsx1 20120206 tsx1 -7.23025
20120126 tsx1 20120228 tsx1 64.9057
20120126 tsx1 20120515 tsx1 -35.4536
20120206 tsx1 20120310 tsx1 61.5200

20120206 tsx1 20120504 tsx1	-35.4371
20120206 tsx1 20120822 tsx1	4.16711
20120206 tsx1 20120913 tsx1	24.6734
20120217 tsx1 20120310 tsx1	-20.4181
20120217 tsx1 20120423 tsx1	-0.973848
20120217 tsx1 20120515 tsx1	45.1306
20120310 tsx1 20120423 tsx1	19.4484
20120310 tsx1 20120811 tsx1	16.1658
20120310 tsx1 20120913 tsx1	-37.6767
20120412 tsx1 20120504 tsx1	7.22659
20120412 tsx1 20120731 tsx1	-4.46925
20120412 tsx1 20121005 tsx1	-52.3582
20120423 tsx1 20120515 tsx1	46.0598
20120423 tsx1 20120709 tsx1	10.4419
20120423 tsx1 20120811 tsx1	-3.84841
20120504 tsx1 20120731 tsx1	-10.8392
20120504 tsx1 20120822 tsx1	36.4092
20120504 tsx1 20120902 tsx1	23.5129
20120515 tsx1 20120709 tsx1	-36.1682
20120515 tsx1 20121221 tsx1	25.7621
20120709 tsx1 20120811 tsx1	-12.4564
20120709 tsx1 20121221 tsx1	61.9025
20120731 tsx1 20120902 tsx1	31.5646
20120731 tsx1 20121005 tsx1	-51.4086
20120731 tsx1 20121107 tsx1	-41.8288
20120811 tsx1 20120913 tsx1	-53.4635
20120811 tsx1 20121016 tsx1	-42.4546
20120811 tsx1 20121129 tsx1	-25.9758
20120811 tsx1 20121221 tsx1	74.2993
20120822 tsx1 20120902 tsx1	-13.8764
20120822 tsx1 20120913 tsx1	22.8784
20120822 tsx1 20121027 tsx1	-6.50235
20120902 tsx1 20121027 tsx1	10.4084
20120902 tsx1 20121118 tsx1	6.01535
20120913 tsx1 20121016 tsx1	17.1288
20120913 tsx1 20121027 tsx1	-26.8637
20121005 tsx1 20121107 tsx1	10.4103
20121005 tsx1 20121210 tsx1	10.5690
20121016 tsx1 20121027 tsx1	-38.3864
20121016 tsx1 20121129 tsx1	23.1194
20121027 tsx1 20121118 tsx1	-6.46093
20121107 tsx1 20121210 tsx1	-4.35383
20121129 tsx1 20121221 tsx1	94.6509